

CERN-LHCC-2015-NNN
CMS-TDR-MMM
ISBN 978-92-9083-396-3
Draft V05-00
4 February 2015

CMS TECHNICAL DESIGN REPORT FOR THE MUON ENDCAP GEM UPGRADE

This report describes both the technical design and the expected performance of the Phase-II upgrade, using Gas Electron Multiplier (GEM) detectors, of the first endcap station of the CMS muon system. The upgrade is targeted for the second long shutdown (LS2) of the CERN LHC and is designed to improve the muon trigger and tracking performance at high luminosity. The GEM detectors will add redundancy to the muon system in the $1.6 < |\eta| < 2.2$ region, where the amount of detection layers is lowest while the background rates are highest and the bending of the muon trajectories due to the CMS magnetic field is small. GEM detectors have been identified as a suitable technology to operate in the high radiation environment present in that region. The first muon endcap station will be instrumented with a double layer of triple-GEM chambers in the $1.6 < |\eta| < 2.2$ region. The detector front-end electronics uses the custom designed VFAT3 chip to provide both fast input for the level-1 muon trigger and full granularity information for offline muon reconstruction. This document describes the design of detectors, electronics, and services. The expected performance of the upgraded muon system is discussed in the context of several benchmark physics channels. The document also presents the plan - including the project schedule, cost, and organization - for the detector construction, testing, and integration into the CMS detector.

10 **Editors**

11 A. Colaleo, A. Safonov, A. Sharma and M. Tytgat

12 **Chapter Editors**

13 M. Abbrescia, P. Aspell, L. Benussi, S. Bianco, O. Bouhali, A. Cimmino, A. Colaleo, G. De Lent-
14 decker, P. Giacomelli, J. Hauser, K. Hoepfner, M. Hohlmann, P. Karchin, A. Lanaro, M. Maggi,
15 A. Marinov, A. Safonov, A. Sharma and M. Tytgat

16 **Language Editors**

17 M. Hohlmann and P. Karchin

18 **Cover Design**

19 S. Cittolin

20 **Acknowledgments**

21 We would like to thank the technical staff from the various institutions for the design, R&D
22 and testing of all components of this upgrade.

23 We acknowledge the warm support received from the CMS management team and the CMS
24 offline and computing projects.

DRAFT

25 Contents

26	1 Introduction	1
27	1.1 Motivations for the GE1/1 muon detector upgrade	1
28	1.2 GEM technology and GE1/1 system overview	4
29	1.3 Readiness for production and installation	7
30	1.4 Structure of the TDR	9
31	2 GE1/1 GEM Chambers	11
32	2.1 Technology overview	11
33	2.1.1 Requirements on GE1/1 chamber performances and design specifications	11
34	2.1.2 Electron transport in GE1/1 gas mixtures	14
35	2.1.3 Choice of GEM technology for GE1/1 as motivated by other experiments	17
36	2.2 GE1/1 prototyping results	18
37	2.2.1 R&D program on full-size GE1/1 prototypes	18
38	2.2.2 Performance measurements and simulation studies	19
39	2.2.3 Considerations for environmentally-friendly counting gas mixtures . . .	30
40	2.3 Technical design of GE1/1 chambers for CMS	35
41	2.3.1 GEM foil design and production technology	35
42	2.3.2 Validation of chamber materials	37
43	2.3.3 Mechanical design	42
44	2.3.4 Foil stretching	47
45	2.3.5 Gas distribution within chamber	50
46	2.3.6 On-chamber HV distribution to GEM foils and drift electrode	51
47	3 Electronics	57
48	3.1 Electronics system overview	57
49	3.2 The VFAT3 front-end ASIC	59
50	3.2.1 The analog front-end	60
51	3.2.2 Variable latency data path	61
52	3.2.3 Fixed latency trigger path	63
53	3.2.4 Slow control	64
54	3.3 The GEM electronic board (GEB)	64
55	3.4 The opto-hybrid and optical links	65
56	3.4.1 The gigabit transceiver (GBT) and the versatile link	65
57	3.4.2 Trigger path to the CSC	68
58	3.5 The back-end electronics	68
59	4 Data Acquisition and Trigger	71
60	4.1 Introduction	71
61	4.2 Tracking data flow	71
62	4.3 Trigger data flow	72
63	4.4 Data rate simulations	74
64	4.5 DAQ firmware and software	75

65	4.5.1	MP7 and μ TCA control	75
66	4.5.2	Firmware	75
67	4.5.3	Overview of the online software	75
68	4.5.4	Testing and integration	76
69	5	Chamber production, quality control and quality assurance	79
70	5.1	GE1/1 component production and assembly overview	79
71	5.2	Component production and quality control	81
72	5.3	Chamber assembly at production sites	82
73	5.3.1	Assembly site requirements	82
74	5.3.2	Assembly site readiness present status	82
75	5.3.3	Single GE1/1 chamber assembly	84
76	5.3.4	Flatness and planarity check and monitoring	85
77	5.3.5	Single GE1/1 chamber commissioning	85
78	5.4	superchamber assembly and production at CERN	86
79	5.4.1	Cosmic ray tests (QC ₈)	86
80	5.5	Database	86
81	6	System Performance	97
82	6.1	Background evaluation and modeling the high luminosity environment	99
83	6.1.1	Evaluation of the backgrounds due to long-lived neutrons	100
84	6.1.2	Implementation of the GE1/1 system in the CMSSW framework	104
85	6.1.3	Summary of the GE1/1 detector hit rates	105
86	6.2	Muon trigger performance	106
87	6.2.1	Integrated local CSC-GEM L1 trigger	107
88	6.2.2	Muon trigger performance in Phase 1	109
89	6.2.3	HL-LHC trigger performance	111
90	6.3	Muon reconstruction performance	114
91	6.3.1	Integration of the GE1/1 detector into the common CMS muon recon- struction	115
92	6.3.2	GE1/1 impact on muon performance	116
94	7	Integration and Installation in CMS	121
95	7.1	Introduction	121
96	7.2	Mechanical aspects and alignment	122
97	7.2.1	Description of the GE1/1 location	122
98	7.2.2	Position monitoring and alignment	124
99	7.3	Power system	126
100	7.3.1	HV power system	126
101	7.3.2	LV power system	130
102	7.4	Readout, control and power lines	131
103	7.4.1	Optical links and architecture	131
104	7.5	Cable routing	132
105	7.6	Gas system	133

106	7.7	Cooling system	136
107	7.8	Proposal for radiation monitoring with RADMONs	139
108	8	Controls and Monitoring	141
109	8.1	Introduction	141
110	8.2	Detector control system	141
111	8.2.1	GEM detector control system	142
112	8.2.2	GEM finite state machine	143
113	8.2.3	Electronic controls and monitoring	144
114	8.3	Data quality monitoring system	146
115	8.3.1	Architecture of the GEM DQM system	146
116	8.3.2	Data certification	147
117	8.3.3	DQM graphical user interfaces	148
118	8.4	Database management system for the GEM project	148
119	9	Project Organization, Responsibilities, Planning and Costs	149
120	9.1	Participating institutes	149
121	9.2	Project organization	151
122	9.3	Role of the Project Manager and Management Team	153
123	9.4	GEM Technical Coordination Team	154
124	9.5	Role of the Resource Manager	154
125	9.6	Organization of Construction work	154
126	9.7	Meetings	155
127	9.8	Construction schedule	157
128	9.9	Costs	157
129	9.9.1	Expected funding, cost sharing and profile	162
130	A	The GE1/1 Slice Test	163
131	A.1	Introduction	163
132	A.2	Detector configuration	164
133	A.3	Front-end electronics and data-acquisition	165
134	B	Integrated Charge Estimation	167
135	C	GE1/1 Project 3D Views	169
136		References	179

DRAFT

137 Chapter 1

138 Introduction

139 **Editors:** J. Hauser, K. Hoepfner

140 **Contributors:** A. Colaleo, J. Hauser, M. Hohlmann, A. Safonov, K. Hoepfner, P. Aspell, A.
141 Marinov, A. Conde Garcia

142 1.1 Motivations for the GE1/1 muon detector upgrade

143 The CMS muon subdetector was originally designed as a highly hermetic and redundant sys-
144 tem that employs three detection technologies [1]. Precision measurements and Level 1 (L1)
145 triggering are provided by drift tubes (DT) in the barrel, covering acceptances up to $|\eta| < 1.2$,
146 and cathode strip chambers (CSC) in the endcaps covering $1.0 < |\eta| < 2.4$. Additionally, resis-
147 tive plate chambers (RPC) provide redundant trigger and coarse position measurement in both
148 barrel and endcap regions, but were not implemented beyond $|\eta| > 1.6$ due to concerns about
149 their capability to handle the high background particle rates.

150 Chapter 4 of the CMS Phase 2 Upgrade Technical Proposal [2] (TP) describes the motivations
151 and plans for improvements to the muon system that will be necessary to maintain the high
152 level of performance achieved during Run 1 in the challenging environment of the high lumi-
153 nosity LHC collider (HL-LHC). One of these improvements is the installation of an additional
154 set of muon detectors, GE1/1, that use gas electron multiplier (GEM) technology in the first
155 endcap muon station in order to maintain or even improve the forward muon triggering and
156 reconstruction in the region $1.6 < |\eta| < 2.2$ in the face of high luminosity. This Technical
157 Design Report document describes the GE1/1 project in great detail. The document is to be
158 published shortly after the TP, because of the already well-advanced state of the GE1/1 project
159 and the early schedule for installation that is proposed for Long Shutdown 2 (LS2, approxi-
160 mately 2018-2019). The GE1/1 muon detector station is shown in the quadrant cross-section of
161 CMS in Figure 1.1. Since forward RPCs were envisioned in the original conception of the CMS
162 muon system, space for the installation of GE1/1 detectors already exists within CMS. The pro-
163 posed GEM detectors have been shown to operate well at rates far above those expected in the
164 forward region under HL-LHC conditions.

165 In CMS terminology, this muon station is designated GE1/1, where the letter G indicates the
166 GEM technology, the letter E indicates this is an endcap muon station, the first “1” indicates
167 that it is part of the first muon station encountered by particles from the interaction point, and
168 the second “1” indicates that it is the first ring of muon chambers going outward in radius from
169 the beam line.

170 The greatest benefit of the GE1/1 muon station is to improve the L1 muon trigger during LHC
171 running before the installation of a new silicon tracker and its associated track trigger in LS3.

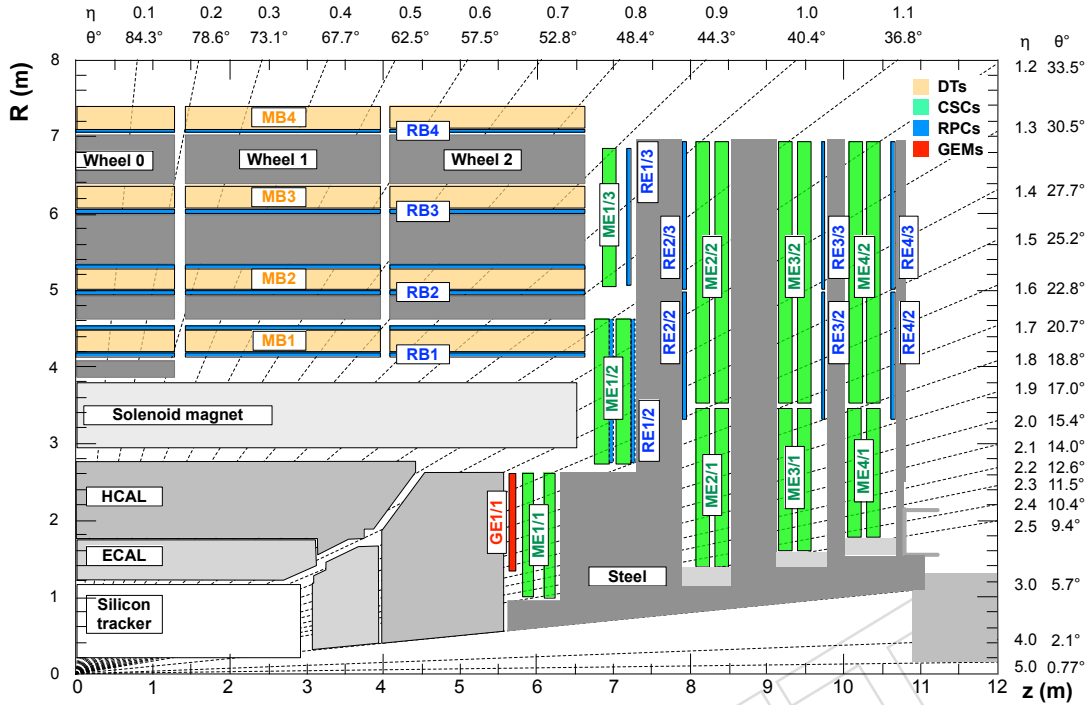


Figure 1.1: A quadrant of the $R - z$ cross-section of the CMS detector, highlighting in red the location of the proposed GE1/1 detector within the CMS muon system.

172 The bending of muons within the CMS solenoid is largest at the position of the first muon station; the bending is much less at subsequent muon stations because the magnetic field lines bend around in the endcap flux return. At this critical position, the GE1/1 chambers in conjunction with the existing CSC station ME1/1 effectively multiply by a factor of 2.4–3.5 the path length traversed by muons within the first muon station over that of the 6 layers of the ME1/1 CSC chambers alone (11.7 cm). The increased path length, in turn, significantly improves the L1 stand-alone muon trigger momentum resolution. With the improved resolution, the L1 muon trigger threshold can be maintained at a low p_T value, so that the efficiency for capturing interesting physics processes such as $H \rightarrow \tau^+ \tau^-$ can be kept high. The single muon trigger rate curves before and after the GE1/1 upgrade are shown in Figure 1.2.

182 The $H \rightarrow \tau^+ \tau^-$ decay is an important channel for probing the Higgs coupling to leptons and to the third particle family. Among the various tau decay channels, the leptonic decays yield a relatively clean signal, provided these events can actually be triggered efficiently given the low average lepton p_T of ≈ 25 GeV. Simulations show that the kinematic acceptance for $H \rightarrow \tau^+ \tau^-$ signal events to pass the L1 trigger will increase by 20(40)% if the trigger threshold can be lowered from 20 GeV to 15(10) GeV. Similar arguments apply to bosonic Higgs decays, $H \rightarrow VV$, such as $H \rightarrow W^+ W^- \rightarrow 2\mu 2\nu$. Additional justification for a low- p_T muon trigger may derive from the B-physics program of CMS.

190 After the new silicon tracker and the track trigger for CMS will have been commissioned in LS3, they will be used in coincidence with the L1 muon trigger to form a “combined muon trigger,” where the momentum resolution for most muons from the primary event vertex will be set by the very high resolution achieved by the track trigger. The GE1/1 and other planned new muon stations will be used to maintain excellent position matching with the track trigger, and the stand-alone muon trigger will run in parallel with the combined muon trigger but at a higher p_T threshold. The stand-alone muon trigger will provide high efficiency for displaced

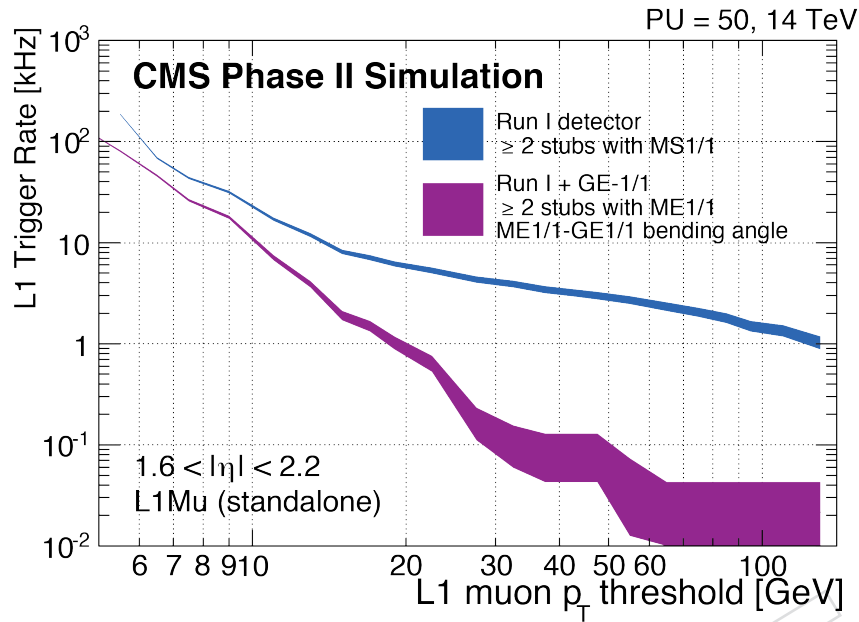


Figure 1.2: L1 muon trigger rates before and after the GE1/1 upgrade at a luminosity of $2 \times 10^{34} \text{ cm}^{-2} \text{ s}^{-1}$, for constant efficiency of 94%. MS1/1 denotes the first endcap muon station L1 trigger in both cases, i.e. with CSC-only or with the combination CSC and GEM trigger information.

197 muons and exotic particles as well as a backup for the combined muon trigger to maintain
198 highest overall muon trigger efficiency.

199 Besides GE1/1, the CMS Phase 2 muon upgrade plans include later installation, during LS3,
200 of a second station of GEM detectors (GE2/1), and third (RE3/1) and fourth (RE4/1) stations
201 of improved RPC (iRPC) detectors. The additional forward muon detectors will increase the
202 average number of muon hits along a forward track up to about the same level that is already
203 present in the barrel muon region of CMS. This is a minimal requirement for handling HL-
204 LHC conditions, given that in the forward region the background particle rates are higher and
205 magnetic bending power is much reduced. The new forward muon stations provide additional
206 redundancy that will be important for continued good operation of the forward muon system
207 if any of the forward muon detectors suffer degradation due to the high particle rates and large
208 radiation doses from the HL-LHC luminosity, or the long passage of time during the HL-LHC
209 era. Offline, the new muon stations will be incorporated into the muon identification, improv-
210 ing the reconstruction efficiency and the momentum resolution. High muon reconstruction
211 efficiency is important for analyses such as $Z \rightarrow \mu^+ \mu^-$ and $H \rightarrow ZZ \rightarrow 4\mu$ where all final state
212 muons need to be reconstructed for the full kinematic event reconstruction. For example, 18%
213 of the $Z \rightarrow \mu^+ \mu^-$ (with $p_T > 15 \text{ GeV}$) events and 27% of the $H \rightarrow 4\mu$ (with $p_T > 5 \text{ GeV}$) events
214 have at least one muon at $1.6 < |\eta| < 2.2$.

215 In summary, the proposed GE1/1 upgrade targets the following improvements:

- 216 • The combined CSC-GEM operation allows measuring the bending angle at trigger
217 level, thus strongly reducing the rate of mis-measured muons driving the trigger
218 rate.
- 219 • Improve tracking performance in the high-rate environment where the background
220 rates of all types are highest and the magnetic bending power is reduced.

- As part of the overall Phase 2 forward muon improvement plan, establish sufficient redundancy in the difficult region $1.6 < |\eta| < 2.2$, by adding detector planes using the space originally foreseen for RPC detectors which were not built due to concerns about hit rate capability.

1.2 GEM technology and GE1/1 system overview

In the Station GE1/1 we propose to install 72 ten-degree chambers per endcap of CMS. For charged-particle detection, the GE1/1 muon upgrade employs gas electron multipliers[3] (GEMs). GEMs exploit electron amplification that occurs within a gas medium inside narrow holes that perforate a thin polyimide foil in a hexagonal pattern. The GEM foil is clad on both sides with thin conductive layers of copper. A voltage of a few hundred volts is applied across the two layers which creates a strong electric field (60-100 kV/cm) inside the holes that causes electron-ion avalanches in the gas. An arrangement of three cascaded GEM foils, commonly known as a “Triple-GEM detector” (see Figure 1.3), allows for modest high voltage and gas amplification across each individual foil to avoid electrical breakdown problems, yet provides a high total charge amplification factor (up to 10^5). This is because the gains of the individual foils multiply to produce the total gain. The amplified charge induces a signal on the electrodes that are finely segmented in the muon bending direction (ϕ) to make the detector position-sensitive; the induced charges are read out by sensitive electronics. The chambers are segmented in 384 strips in ϕ , over 10 degree which means that each strip cover $450 \mu\text{rad}$.

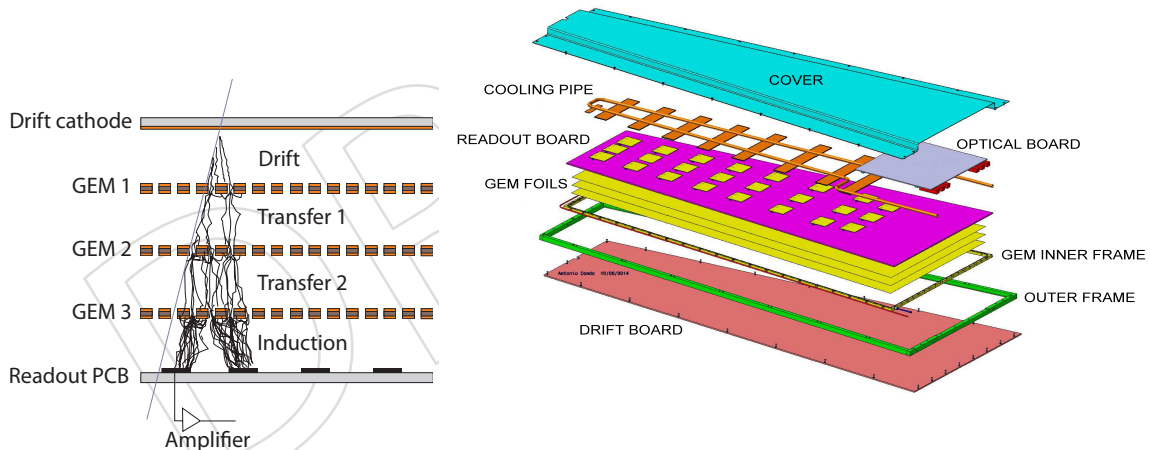


Figure 1.3: Left: By cascading three GEM foils, the amplification per stage can be kept modest to avoid electric breakdown problems. Right: Exploded view of the mechanical design of a Triple-GEM chamber.

In the GE1/1 muon system, a pair of such Triple-GEM chambers is combined to form a “super-chamber” (see Figure 1.4 left) that provides two measurement planes in the muon endcap that complement the existing ME1/1 detectors and maximizes the detection efficiency. Each super-chamber covers a $\approx 10^\circ$ sector, so that 72 superchambers are required (36 in each endcap) to form a ring of superchambers that gives full azimuthal coverage. The superchambers alternate in ϕ between long ($1.55 < |\eta| < 2.18$) and short ($1.61 < |\eta| < 2.18$) versions, as dictated by the mechanical envelope of the existing endcap. These η ranges maximize the GE1/1 coverage within the limits of that envelope. In most cases in this document, the coverage of GE1/1 will

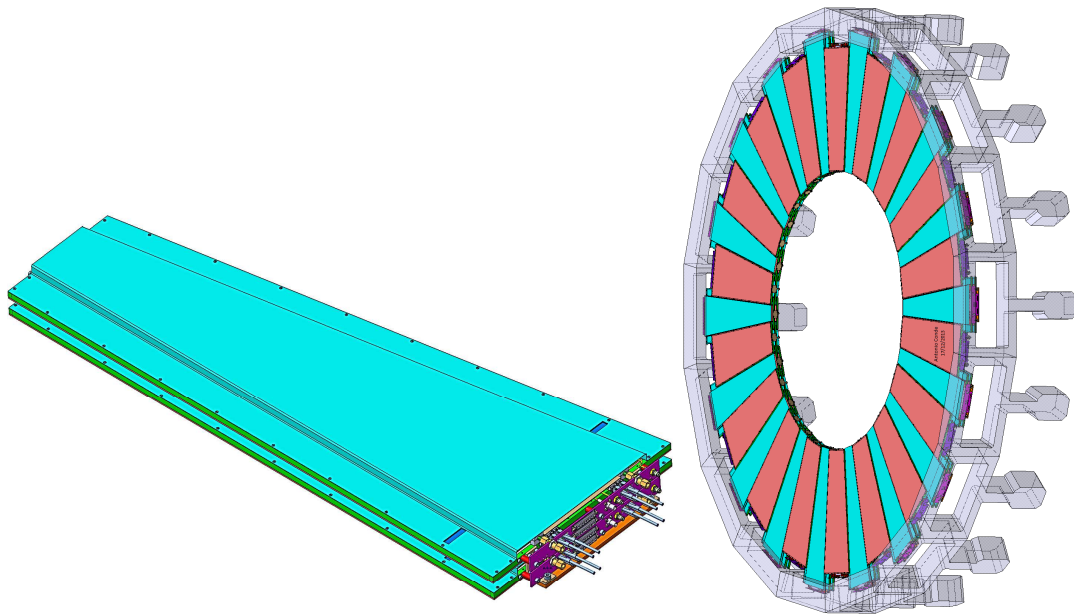


Figure 1.4: Left: A pair of GEM chambers form a superchamber. Right: Long and short chambers are combined to maximize the instrumentation within given mechanical constraints in the endcap.

248 be quoted approximately as $1.6 < |\eta| < 2.2$. Each endcap holds 18 long and 18 short super-
 249 chambers. One endcap is depicted in Figure 1.4 (right). The superchambers will be installed in
 250 slots originally foreseen for RPC chambers, in the gap between the hadron calorimeter and the
 251 CSC ME1/1 chambers in the YE1 “nose” (see Figure 1.5). This geometry is also implemented
 252 in detector simulations used for various performance studies.

253 The performances of several generations of GE1/1 prototypes were studied in great detail in
 254 a series of beam tests at CERN and Fermilab and with x-ray sources over a five-year R&D
 255 period. Figure 1.6 shows the most recent prototype, which is essentially equivalent to the
 256 proposed final production chamber. It was demonstrated that the detector response varies not
 257 more than 15% across the entire chamber. At the same time, detection efficiencies of 97-98%
 258 were achieved, depending on gas mixture and type of readout. With binary-output readout,
 259 an acceptable angular resolution of $131 \mu\text{rad}$ has been measured, which is close to the intrinsic
 260 resolution expected for the binary readout. Timing measurements of a prototype operated with
 261 Ar/CO₂/CF₄ 45:15:40 demonstrate that 97% of all hits are attributed to the correct 25 ns bunch
 262 crossing.

263 The GE1/1 front-end electronics is well advanced in its design cycle. Improvements are being
 264 made to the existing 128-channel VFAT2 ASIC chip, and the resulting VFAT3 design, detailed
 265 in Chapter 3, is expected to be submitted for a first fabrication near the end of 2015. A sec-
 266 ond submission is foreseen in 2016 if necessary. The full VFAT3 production is expected to be
 267 launched by early 2017.

268 The first prototype versions of the GEM Electronics Board (GEB) shown in Figure 1.3 and the
 269 OptoHybrid (OH) board detailed in Chapter 3 have already been designed, manufactured and
 270 tested. These are the first of a three step prototyping plan. The second step is currently in
 271 its design phase and expected to be complete by early 2015. Prototyping steps one and two

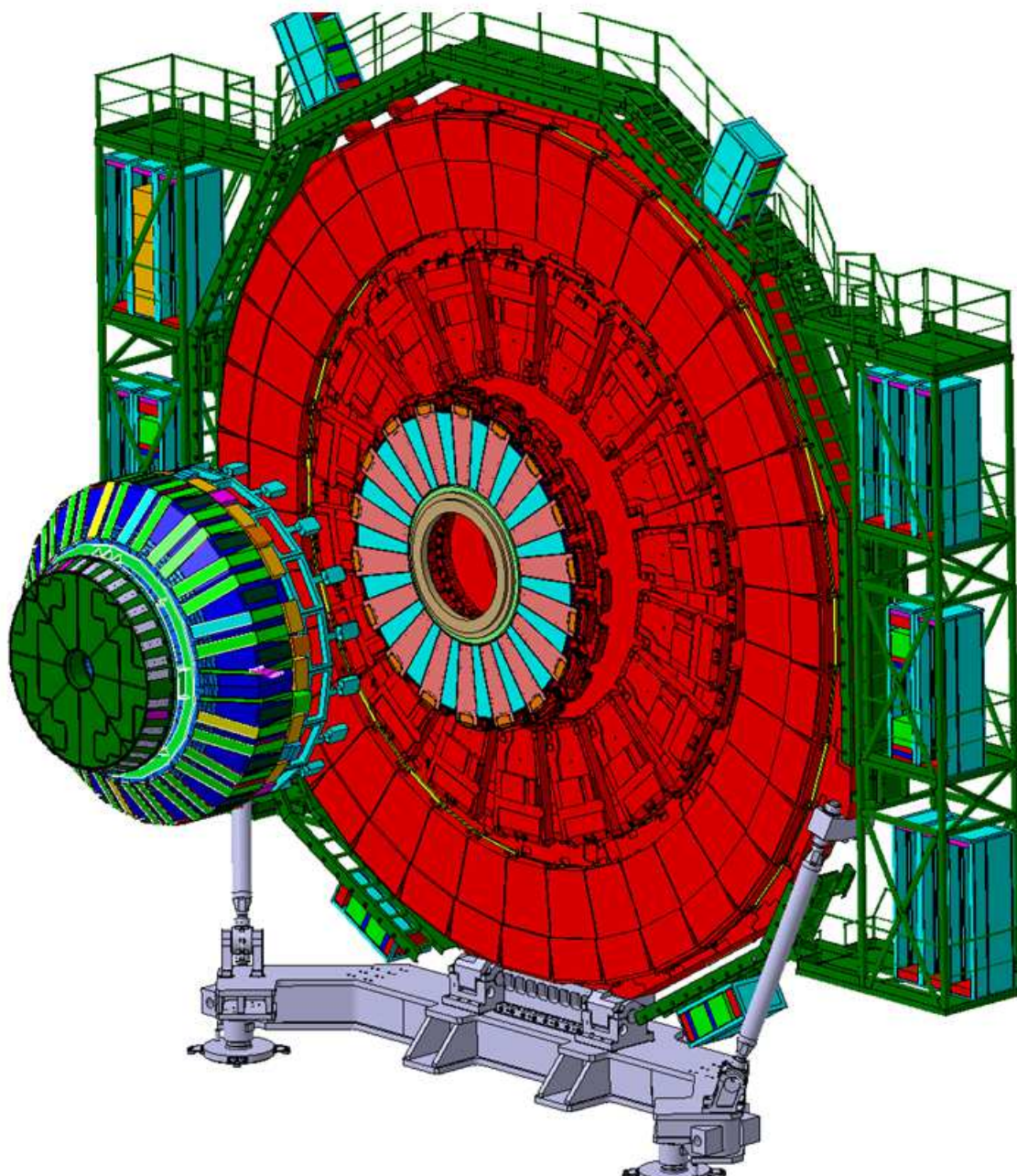


Figure 1.5: First CMS muon endcap station where the inner ring is equipped with 18 long and 18 short triple GEM superchambers.



Figure 1.6: Most recent GE1/1 chamber prototypes (top left) in the uniformity test stand, (top right) ready for CSC-GEM integration tests and (bottom) latest version of Optohybrid mounted on detector.

272 use the VFAT2 chip which already exists and is readily available. The third prototyping step
273 will incorporate the VFAT3 chip and the GigaBit Transceiver (GBT). The GBT is expected to be
274 available for initial prototype tests in 2015. The design of the OptoHybrid and GEB boards for
275 the third prototype step is expected to start during 2015.

276 For the off-detector electronics, we will use the μ TCA standard and the CMS MP7 and AMC13
277 μ TCA boards. Data will be transmitted between the on- and off-detector electronics through
278 optical fibers using the CERN GBT protocol. In 2014 the first prototypes of the Opto-hybrid
279 and GEB have already been successfully read out with a μ TCA GLIB board together with an
280 AMC13. In 2015 the system will be tested with the MP7 board replacing the GLIB.

281 1.3 Readiness for production and installation

282 Small GEM detectors have demonstrated excellent rate capability and robustness in the past.
283 To cover the much larger areas that are required for CMS, new technologies for production of
284 large-size GEM detectors had to be developed. Within the CMS GEM R&D effort, cost-effective
285 production of large GEM foils over 1m long was demonstrated and the resulting chambers have
286 been extensively tested in beams. A novel technique has recently been developed where three
287 foils are mounted into a single stack under tension, keeping a constant inter-GEM spacing.
288 Since no gluing is involved, a large-size chamber can be quickly assembled by two people in
289 about two to three hours; it can also be easily re-opened for maintenance.

290 Chamber production can be launched as soon as the project is approved. Six chamber produc-
291 tion and testing sites (BARC, INFN Bari, CERN, FIT, UGent, and INFN LNF) have been under
292 preparation for a couple of years. Building 186 at CERN is being developed as a center for
293 GE1/1 chamber quality control, integration, and final testing. A cosmic-ray test stand has been
294 built there which allows testing of up to 10 superchambers in terms of long-term HV stabil-

295 ity; it will also allow for scans of gain, efficiency, and angular resolution over a large area of
 296 the chambers. It is estimated that the production of the 72 superchambers for the first muon
 297 endcap station will easily be completed within two years. In LS2 the full GE1/1 station with
 298 detectors, electronics, and full DAQ chain would be installed and fully integrated into CMS.

299 The slots for insertion into the endcap nose already exist and integration and installation stud-
 300 ies for the existing CMS muon high- η envelope have been performed in order to ensure smooth
 301 installation. The needed technical services have been studied and detailed understanding of
 302 cooling, cabling, and gas distribution has been worked out. Several trials with mechanical
 303 demonstrators were successfully completed within this envelope. Figure 1.7 shows the most
 304 recent installation of an assembly of one long and two short GE1/1 superchambers in CMS.
 305 The routing of services, gas pipes and cables was also successfully demonstrated.

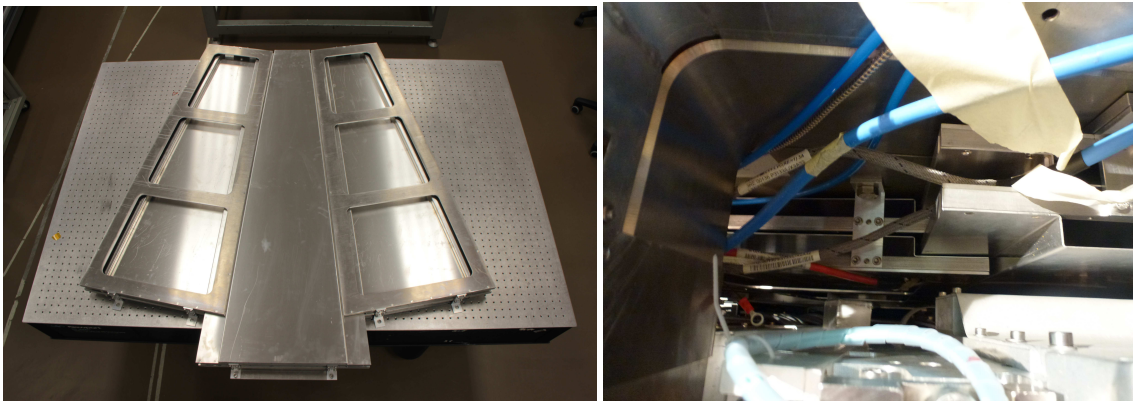


Figure 1.7: Installation test with an assembly of real-sized long and short dummy chambers.

306 The small charge signals on the GE1/1 electrodes are amplified, digitized, and further pro-
 307 cessed by custom designed 128-channel ASIC circuits. A new front-end ASIC design based on
 308 the previous success of the binary-readout VFAT2 chip was developed to match the required
 309 particle rates and trigger precision. The transport of data between the GEM on-detector elec-
 310 tronics and the off-detector DAQ system will be via optical fibres. CERN-based common design
 311 projects such as the GBT chip set, Versatile link and GLIB/MP7 μ TCA systems can provide the
 312 radiation tolerant optical communication system required.

313 Each single GEM chamber is treated as an individual unit from an electronics system point of
 314 view. The GEM chamber is segmented in both ϕ and η ; the baseline for LS2 is segmentation of
 315 three in ϕ and eight in η creating a maximum of 24 individual detector segments. Each of these
 316 segments is further subdivided into 128 strips and read out by one 128-channel front-end chip.
 317 Each GEM chamber consequently has up to 24 front-end chips and channels organised in three
 318 columns. The system is designed such that one optical fibre can read out the tracking data from
 319 one GEM column, while all trigger data are carried out by a dedicated additional fibre. A single
 320 GEM chamber has three optical fibres to take the tracking and trigger data to and from the CMS
 321 GEM DAQ system. The data from the VFAT chips are sent to the GEB which delivers power
 322 and communication signals to and from the VFAT hybrid as well as providing the connection
 323 to the GEM strips. From the GEB, data are transmitted to one FPGA board, called the GEM
 324 OptoHybrid (OH), located on the wide end of the GEM module. One of the main components
 325 of the OH is a Xilinx Virtex 6 FPGA, which has been shown to be radiation-hard to levels at
 326 least two orders of magnitude higher than the expected radiation dosage.

327 The GEM trigger data will be sent to the CSC Trigger Mother Board (TMB) located in the ex-
 328 perimental cavern (UXC55) while the trigger and the tracking data will be sent to the GEM

329 off-detector electronics located in the service cavern (USC55). In the CSC TMB, the GEM trig-
330 ger data will be combined with the CSC data to make combined local muon stubs, which will
331 improve the endcap muon L1 trigger efficiency. In the GEM off-detector electronics, the track-
332 ing data will be transferred to the CMS DAQ system, and trigger data will be processed by a
333 trigger algorithm and transferred to the L1 endcap muon track finder. The GEB and the OH
334 boards have been designed and are undergoing tests in the laboratory and a test beam, while
335 all off-detector electronics devices are commercial off-the-shelf components.

336 In summary,

- 337 • R&D to build large-size triple GEM chambers is completed. Integration into CMS
338 has been worked out and tested successfully with dummy chambers.
- 339 • Several chamber production sites are being prepared and provide sufficient capacity
340 to produce the necessary 72 superchambers plus spares within two years.
- 341 • Design of the electronics for readout, trigger, and DAQ is in an advanced stage.
342 First prototypes of various components are being integrated with the latest chamber
343 prototypes.
- 344 • The objective for LS2 is to be ready with the full GE1/1 station and integrate it into
345 CMS.

346 1.4 Structure of the TDR

347 The organization of this TDR is as follows.

348 Chapters 2–5 cover details of the chambers and their associated electronics. Details of the
349 GEM chambers and their measured performance are described in Chapter 2. The front-end
350 on-chamber electronics and the trigger path to the CSC are described in Chapter 3. In Chapter
351 4, the data flow and the DAQ system are discussed. Chapter 5 covers the detailed aspects of
352 chamber production and quality assurance.

353 Chapter 6 presents in detail the challenging conditions expected during HL-LHC operation, the
354 expected performance of the forward muon detector and the beneficial aspects of the GE1/1
355 upgrade, based on simulation studies.

356 Chapters 7–9 discuss “practical” matters: Chapter 7 presents various issues that will arise in in-
357 tegrating the GE1/1 detectors in CMS, such as installation procedures, power, gas and cooling
358 systems. Chapter 8 discusses controls and monitoring that are needed for the proper operation
359 of this detector. Chapter 9 discusses the project organization, schedules, and estimated costs.

360 Three appendices are included: Appendix A discusses a Slice Test consisting of 4 supercham-
361 bers that are expected to be installed in CMS at the end of 2016, while Appendix B contains
362 details of the estimated charge per unit area that is expected to be accumulated on the GE1/1
363 chamber electrodes during the lifetime of the HL-LHC. Engineering drawings for the GE1/1
364 Project are added in Appendix C as a reference.

DRAFT

365 Chapter 2

366 GE1/1 GEM Chambers

367 **Editors:** L. Benussi, M. Hohlmann

368 **Contributors:** N. Amapane, P. Aspell, A. Barnac, P. Barria, B. Dorney, L. Benussi, V. Bhopatkar,
369 O. Bouhali, S. Colafranceschi, A. Conde, R. De Oliveira, M. Hohlmann, G. de Lentdecker, A.
370 Marinov, T. Maerschalk, J. Merlin, A. Sharma, G. Saviano, M. Tytgat, and A. Zhang

371 2.1 Technology overview

372 A Gas Electron Multiplier [3] is a thin metal-clad polymer foil chemically perforated by a high
373 density of microscopic holes. The polyimide (Kapton by DUPONT Co. or Apical by KANEKA
374 Co.) used as the bulk material of the foil is $50\ \mu\text{m}$ thick and has a dielectric constant of 3.5; it
375 is clad on both sides with $5\ \mu\text{m}$ of copper. As shown in Figure 2.1 (left), the GEM holes are
376 truncated double cones with the larger (outer) diameters around $70\ \mu\text{m}$ and the smaller (inner)
377 diameter around $50\ \mu\text{m}$; they are spaced with a pitch of $140\ \mu\text{m}$ in a hexagonal pattern.

378 A triple-GEM chamber consists of a stack of three GEM foils placed at a relative distance of
379 a few mm and immersed in a counting gas mixture. The voltage applied between the two
380 copper-clad surfaces of a foil produces an electric field as high as $\sim 80\ \text{kV/cm}$ in the GEM hole
381 as seen in Figure 2.1 (right). The electrons produced by a charged particle passing through the
382 chamber due to ionization of the counting gas drift towards the holes and once they start to
383 experience the very intense electric field in the holes, they acquire enough kinetic energy to
384 produce secondary ionization in the gas. This produces an electron avalanche process, which
385 induces an electrical signal on the readout strips. A schematic view of this operation principle
386 is given in Figure 2.2, which also defines the drift region, two transfer regions, and induction
387 region within the triple-GEM chamber.

388 Typical dimensions of the different regions in a triple-GEM detector are: Drift region of 3 mm
389 between drift cathode and first GEM, spaces of 1 mm and 2 mm in the electron transfer gaps
390 between GEM foils, and a 1 mm space in the signal induction region (Figure 2.2). A standard
391 gas mixture for operating a triple-GEM detector is Ar/CO₂ 70:30. For CMS, we have also
392 evaluated Ar/CO₂/CF₄ 45:15:40, which is the gas that was used by LHCb for triple-GEMs
393 during the data taking period in 2010-2012[4].

394 2.1.1 Requirements on GE1/1 chamber performances and design specifications

395 The desired trigger and physics performances outlined in the introduction and detailed in
396 chapter 6 impose the following fundamental requirements on the detection performance of
397 the GE1/1 chambers:

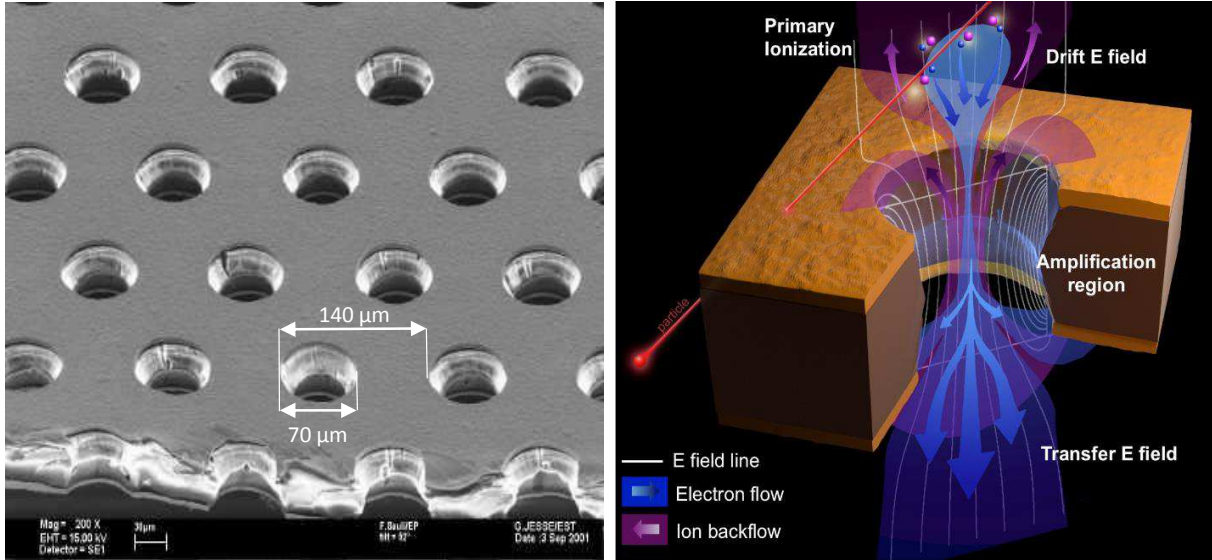


Figure 2.1: Scanning Electron Microscope (SEM) picture of a GEM foil (left)[3] and schematic view of the electric field lines (white), electron flow (blue), and ion flow (purple) through a bi-conical GEM hole (right). The outer diameters of the hole are 70 μm and the inner diameter is 50 μm ; the hole pitch is 140 μm .

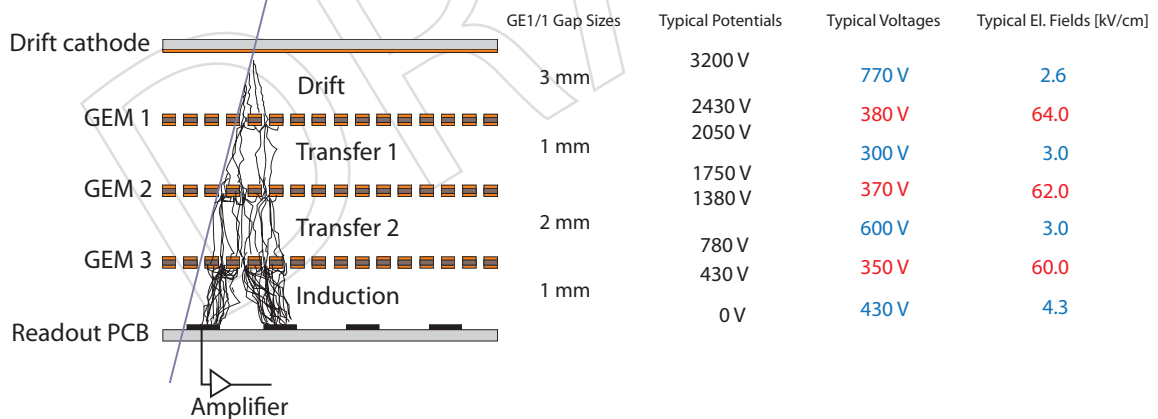


Figure 2.2: Principle of operation of a generic triple-GEM chamber and definition of drift, transfer, and signal induction gap regions within the detector[3]. The columns on the right give the actual gap sizes in the GE1/1. They also list typical values for electric potentials on the seven electrodes and typical values for voltages and electric fields across the four gaps (blue) and the three foils (red) if the nominal potential of 3200 V for operation in Ar/CO₂ 70:30 is applied to the drift cathode.

- 398 • Maximum geometric acceptance within the given CMS envelope.
- 399 • Rate capability of 10 kHz/cm² or better.
- 400 • Single-chamber efficiency of 97% or better for detecting minimum ionizing particles.
- 401 • Angular resolution of 300 μ rad or better in the azimuthal direction.
- 402 • Timing resolution of 10 ns or better for a single chamber.
- 403 • Gain uniformity of 15% or better across a chamber and between chambers.
- 404 • No gain loss due to aging effects after 200 mC/cm² of integrated charge.

405 We briefly review the rationale for these requirements. Clearly, maximum acceptance will yield
 406 maximum physics yield. The maximum expected hit rate within the GE1/1 acceptance is about
 407 5 kHz/cm² for HL-LHC running at 14 TeV and 5×10^{34} cm⁻²s⁻¹. Multiplying with a safety fac-
 408 tor of two then requires a hit-rate capability of 10 kHz/cm². With 97.0% individual chamber
 409 efficiency, a “superchamber” that contains two chambers will have an efficiency above 99.9%
 410 when the signals from the two chambers are combined as a logical OR. An azimuthal resolu-
 411 tion of 300 μ rad or better will not significantly smear the difference $\Delta\phi = \phi_{GE1/1} - \phi_{ME1/1}$ of
 412 the angular muon positions measured in GE1/1 and ME1/1. Consequently, a resolution of that
 413 magnitude will enable the trigger to discriminate high- p_T muons from low- p_T muons reliably.
 414 For a binary readout, 300 μ rad resolution corresponds to a pitch of $\sqrt{12} \cdot 300 \mu\text{rad} = 1040 \mu\text{rad}$
 415 for trigger strips. At the outer radius ($r = 2.6$ m) of the GE1/1 chambers, this azimuthal reso-
 416 lution of 300 μ rad corresponds to a 0.8 mm resolution in the azimuthal $\hat{\phi}$ direction. Since two
 417 chambers can provide independent timing information that can also be combined with timing
 418 provided by the CSCs, a time resolution of 10 ns or better for a single chamber is sufficient to
 419 reliably match GE1/1 hits to ME1/1 stubs in time when running with a 25 ns bunch crossing
 420 time at the LHC. A uniform chamber response will ensure that there are no geometrical trigger
 421 or reconstruction biases. The gain of a single GEM foil typically varies across the foil surface
 422 by 5-8% due to intrinsic variations in hole diameters that stem from the production process[5].
 423 The corresponding typical gain variation in a triple-GEM detector is $\sqrt{3}$ times larger, i.e. about
 424 10-15%. The chambers should not incur significant additional response non-uniformities due
 425 to any other factors. The chambers must be able to integrate a charge of 200 mC/cm² over
 426 their lifetime without any gain loss or other loss in response. The charge expected to be inte-
 427 grated in the GE1/1 sector at highest η over 20 years of operation at the HL-LHC is about 100
 428 mC/cm². A calculation of this estimated integrated charge value is given in appendix B. The
 429 stated requirement of 200 mC/cm² includes an additional safety factor of two.

430 In addition, several technical constraints and requirements need to be taken into account in the
 431 chamber design. As a baseline, it must be possible to operate the chambers using only counting
 432 gases that have low global warming impact. The material budget must be low enough so that
 433 multiple scattering within the GE1/1 itself will not affect the muon track measurement in the
 434 GE1/1–CSC trigger. Sufficiently small readout segmentation in η , i.e. along the readout strips,
 435 is needed so that the GE1/1–CSC trigger can remove CSC ghosts effectively when reconstruct-
 436 ing events with multiple muon hits in a CSC chamber. The chambers must be designed so that
 437 a superchamber is less than 10 cm thick and will easily fit into the available slot in the muon
 438 endcap nose. The on-chamber service interfaces must be laid out so that pre-existing cabling
 439 and tubing infrastructure can be used effectively.

440 The resulting basic parameters and specifications for the construction of the GE1/1 triple-GEM
 441 chambers and their operation in CMS are compiled in Table 2.1.

Specification / Parameter	GE1/1
Detector technology	Gaseous detector; micro-pattern gas detector (MPGD)
Charge amplification element	GEM foil (triple, cascaded, tensioned at ≈ 5 N/cm)
Number of chambers in overall system	144 (72 in each endcap)
Chamber shape (active readout area)	Trapezoidal; opening angle 10.15°
Active area overlap in adjacent chambers	2.6 mrad (corresponds to 5.7 readout strip pitches)
Short chamber dimensions (active vol.)	L: 106.1 cm (center line), W: (23.1 - 42.0) cm, D: 0.7 cm
Long chamber dimensions (active vol.)	L: 120.9 cm (center line), W: (23.1 - 44.6) cm, D: 0.7 cm
Total chamber thickness	D: 3.5 cm
Active readout area	0.345 m^2 (short ch.); 0.409 m^2 (long ch.)
Active chamber volume	2.6 liters (short ch.); 3 liters (long ch.)
Radial distance from beam line	130.2 cm (at inner edge of active readout area)
Geometric acceptance in η	1.61 - 2.18 (short ch.); 1.55 - 2.18 (long ch.)
Signal readout structure	Truly radial readout strips
Readout strip dimensions	230 μrad angular strip width; 463 μrad angular pitch
Number of η -segments in readout	8
Number of readout strips per η -segment	384
Number of readout strips per chamber	3,072
Counting gas mixtures	Ar/CO ₂ 70:30 or Ar/CO ₂ /CF ₄ 45:15:40
Nominal operational gas flow	1 chamber volume per hour
Number of gas inlets	1
Number of gas outlets	1
Nominal HV applied to drift electrode	3200 V (Ar/CO ₂); 4000 V (Ar/CO ₂ /CF ₄)
Nominal operational gas gain	$1-2 \times 10^4$
Demonstrated rate capability	100 MHz/cm ²

Table 2.1: Main specifications and parameters for the design and operation of the GE1/1 chambers.

2.1.2 Electron transport in GE1/1 gas mixtures

We briefly discuss the intrinsic electron transport parameters of Ar/CO₂/CF₄ 45:15:40 and Ar/CO₂ 70:30 gas mixtures. Triple-GEM detectors have been operated successfully in high-rate environments using Ar/CO₂/CF₄ 45:15:40 in the LHCb experiment[4] and Ar/CO₂ 70:30 in the TOTEM experiment[6]. These two gas mixtures have also been used extensively during the GE1/1 R&D phase and consequently are candidate gas mixtures for operating the GE1/1 in CMS. The Ar/CO₂/CF₄ 45:15:40 mixture combines a high drift velocity due to its high CF₄ content with a small Lorentz angle, similar to that of Ar/CO₂. Since CMS has a magnetic field of 3 T at the location of the GE1/1 chambers, we review the effect of a magnetic field and the effect of the angle between the E-field and B-field on the charge transport.

A general discussion of transport properties in gaseous detectors can be found, for example, in Ref. [7]. When electrons and ions in a gas are subjected to an electric field, they drift along the electric field lines on the average, but individual electrons can deviate from that average due to scattering in collisions with atoms and molecules in the gas. This leads to longitudinal diffusion of the drifting electron cloud along the field lines and to its transverse diffusion across the field lines. The scattering process in each direction is approximately Gaussian on a microscopic scale. An electric field affects the transverse and longitudinal diffusion differently and so two diffusion coefficients σ_L and σ_T are used to quantify the diffusions. In cold gases such as carbon dioxide, the diffusion is small and the drift velocity is low and unsaturated at electric field

461 strengths that are typically used in gaseous detectors. Warm gases such as argon have stronger
 462 diffusion and slower drift velocities, but when they are mixed with polyatomic/organic gases
 463 with vibrational and rotational modes, the diffusion is reduced in most cases and the drift
 464 velocity is increased.

465 In the presence of both an electric field and a magnetic field, the Lorentz force deflects electrons
 466 between collisions so that they drift effectively at an angle, called the Lorentz angle, relative to
 467 the electric field (Figure 2.3). The diffusion transverse to the drift direction is reduced in this
 468 case, while the longitudinal diffusion is basically unchanged (Figure 2.4). Too large a Lorentz
 469 angle worsens the spatial resolution; however, a small Lorentz angle may improve the spatial
 470 resolution due to enhanced charge sharing among the readout strips. Knowledge of the Lorentz
 471 angle is important so that the spatial resolution can be optimized by correcting for this effect.

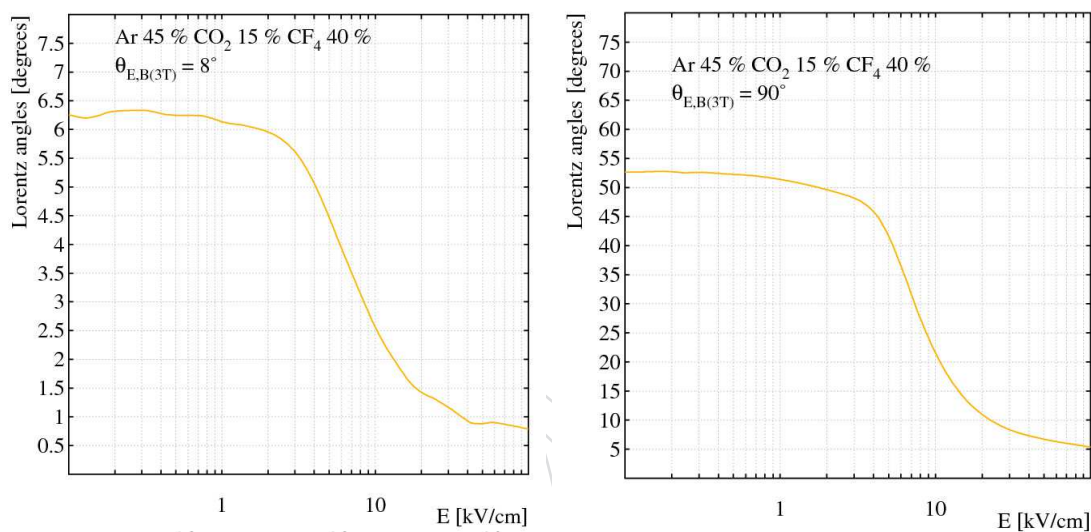


Figure 2.3: Lorentz angles as a function of electric field for Ar/CO₂/CF₄ 45:15:40 at B=3T obtained with the GARFIELD simulation suite[8]. The angles are shown for $\angle(\vec{E}, \vec{B}) = 8^\circ$ (left) as given in the GE1/1 and for a maximum angle $\angle(\vec{E}, \vec{B}) = 90^\circ$ (right).

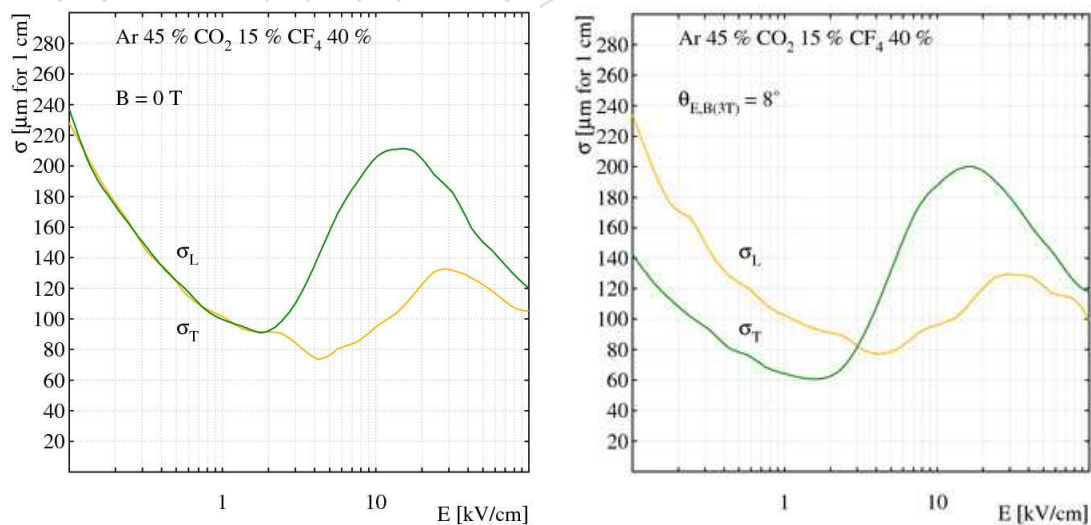


Figure 2.4: Longitudinal (σ_L) and transverse (σ_T) diffusion coefficients in Ar/CO₂/CF₄ 45:15:40 without magnetic field (left) and at B=3T with $\angle(\vec{E}, \vec{B}) = 8^\circ$ (right) obtained with GARFIELD.

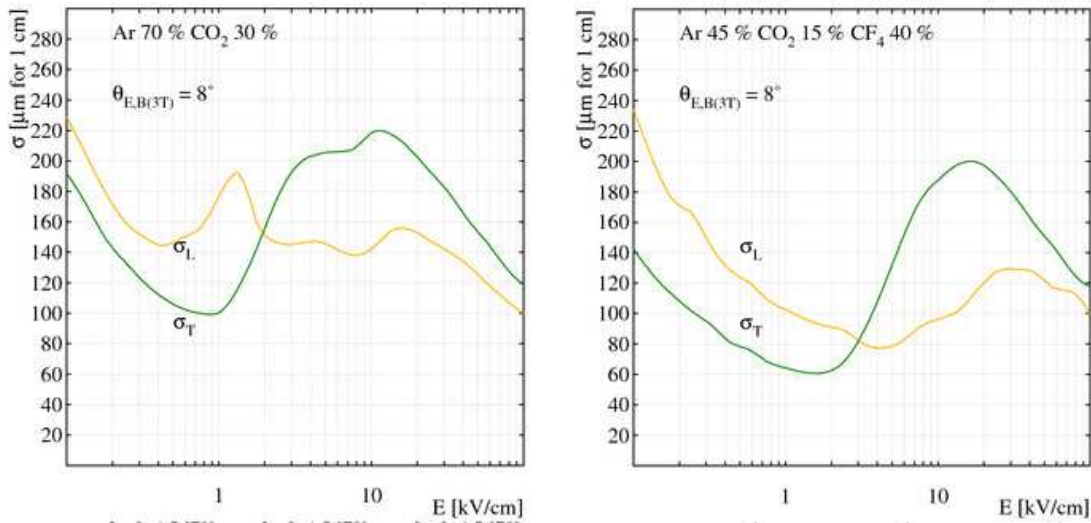


Figure 2.5: Longitudinal (σ_L) and transverse (σ_T) diffusion coefficients for the two gas mixtures of interest for GE1/1 operation at $B=3T$ and with angle $\angle(\vec{E}, \vec{B}) = 8^\circ$.

472 Figure 2.5 shows the diffusion coefficients for the two gas mixtures of interest as a function
 473 of the electric field for the specific angle $\angle(\vec{E}, \vec{B}) = 8^\circ$. This is the maximum angle between
 474 electric drift field lines in the GEM and magnetic field lines produced by the CMS solenoid at
 475 the location of the GE1/1. The diffusion in Ar/ CO_2 / CF_4 is lower, as expected, due to higher
 476 polyatomic gas content; both CF_4 and CO_2 have vibrational modes which lower the diffusion.
 477 Simulation studies done by LHCb[4] for different gas mixtures show that the Ar/ CO_2 / CF_4
 478 45:15:40 mixture is a significantly faster gas due to the addition of the CF_4 gas (Figure 2.6). CF_4
 479 is advantageous in a high-rate environment because it enables high-rate capability due to its
 480 high drift velocity but it suffers from electron attachment. CO_2 is added to “cool” the electrons
 481 which reduces the electron attachment that occurs with CF_4 .

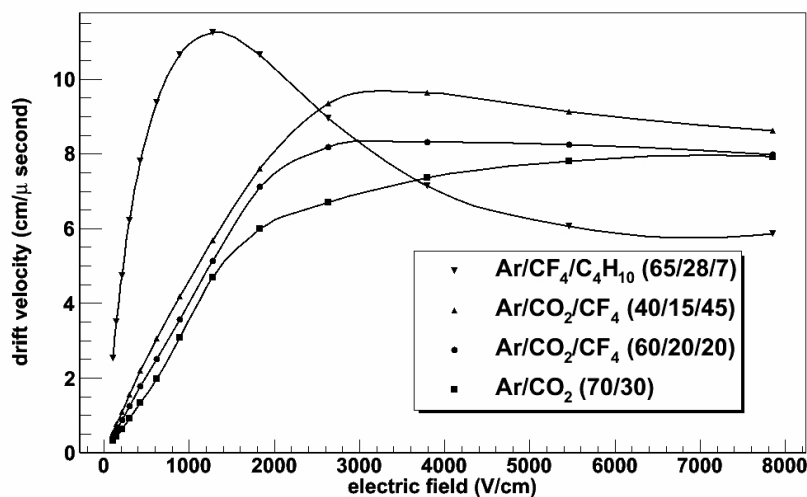


Figure 2.6: Electron drift velocities as a function of electric field from simulation studies by LHCb for various gas mixtures including the GE1/1 candidate gas mixtures.

2.1.3 Choice of GEM technology for GE1/1 as motivated by other experiments

We briefly review the experience with GEM technology that exists within the community. GEM detectors have been successfully operated long-term in several major high energy and nuclear physics experiments, i.e. COMPASS, PHENIX, STAR, TOTEM, and LHC-b. The main features of the GEM applications in those experiments are highlighted below.

- **COMPASS:** This is the pioneering experiment for GEM technology. It is the first high-rate experiment to use GEM detectors[9]. Running at the CERN SPS, COMPASS has been employing 22 medium-size (30 cm × 30 cm) triple-GEM detectors with 3/2/2/2 mm gap sizes in 11 inner tracking stations. Detectors are operated with Ar/CO₂ 70:30 at a gas gain around 8,000 and are read out with two-dimensional Cartesian strips and APV25 chips[10]. The detectors operate at rates up to 2.5 MHz/cm², which corresponds to roughly 1000 times the expected rate for the CMS GE1/1. Operating with two OR'ed GEM trackers, each tracking station has an efficiency of 97.5%. A single COMPASS GEM achieves about 70 μm spatial resolution and 12 ns time resolution. During the 2002-2007 running period the detectors accumulated total charges around 200 mC/cm² without any gain drop while in earlier bench tests with x-rays 700 mC/cm² had been collected without any observed gain loss. COMPASS also operated five small-size GEM trackers with 1 mm² pixel readout[11] that were exposed to muon rates up to 12 MHz/cm² in the 2008/09 COMPASS runs and achieved 7 ns time resolution.
- **PHENIX:** This experiment operated 20 medium-size triple-GEM detectors at RHIC as a “hadron-blind” detector system[12] for electron identification. A special feature of this system was a reverse bias of the HV between drift mesh and first GEM, which desensitized the GEM to charged particles, while a CsI coating on the first GEM made the detector sensitive to Cherenkov radiation from electrons. The detector was operated in pure CF₄ and achieved a hadron rejection factor of 50 in the 2010 PHENIX run.
- **STAR:** Since late 2012, STAR has been operating 24 medium-size triple-GEM detectors read out with r-φ strips and APV25 chips as a forward tracker[13] at RHIC. GEM foils are shaped as circular quadrants and were produced industrially in the USA.
- **TOTEM:** This experiment employs 20 medium-size triple-GEM detectors of semi-circular shape that are read out with concentric strips and radial pads and VFAT2 chips[14]. These detectors form two T2 telescopes for charged-particle tracking and triggering in the very forward region at the LHC. They were exposed to a total fluence of a few 10¹³/cm² particles during the 2012 LHC run and had sustained a total ionizing dose of about 5 × 10⁴ Gy by the end of the 2012 LHC run while performing as expected[6].
- **LHCb:** The LHCb experiment employs 12 pairs of medium-size triple-GEM detectors with 3/1/2/1 mm gap sizes as the inner section of the LHCb M1 muon station, which is located in immediate vicinity of the beam pipe. Using a pad readout, this GEM system produces input for the LHCb L0 muon trigger. Unusual for a muon station, this subdetector is located in front of the calorimeters rather than behind them. Consequently, it sustains rather high rates for a muon detector of up to 500 kHz/cm². It operates with an Ar/CO₂/CF₄ 45:15:40 gas mixture that is one of the mixtures being considered for the CMS GE1/1. Read out with TDCs and running at a gain around 4,300, the GEMs have a time resolution of 4 ns when the signals from two paired detectors are logically OR'ed and an efficiency of 97-99% in a 20ns

529 time window. The most irradiated LHCb GEM detector has integrated about 120
 530 mC/cm^2 during the 2010-12 LHC running period without signs of aging[4]. This
 531 value happens to correspond closely to the GE1/1 requirement for 20 years of run-
 532 ning at the HL-LHC (see section 2.1.1).

533 This strong track record for GEMs in high-rate applications for HEP and NP experiments
 534 demonstrates that GEMs represent a mature and robust technology for high-rate experiments.
 535 The CMS GE1/1 project represents the next major step in the evolution of GEM detector sys-
 536 tems by going from systems with a small number of medium-size detectors to a large number
 537 of large-size detectors; it builds mainly upon the more recent experiences with the LHCb and
 538 TOTEM GEMs.

539 2.2 GE1/1 prototyping results

540 2.2.1 R&D program on full-size GE1/1 prototypes

541 The crucial first step in the 5-year R&D program that led to this design report was a demonstra-
 542 tion that large-area GEM foils can indeed be manufactured reliably and that triple-GEM detec-
 543 tors built with such foils can satisfy the performance requirements listed in section 2.1.1. Five
 544 generations of prototype detectors (Figure 2.7) were built and tested in 2010-14 with one gener-
 545 ation being developed every year based on the experience with the previous generation[15–18].
 546 Since the GE1/1 prototype performances discussed below are obtained from tests of different
 547 prototype generations, we briefly review the evolution of the GE1/1 detector prototypes.

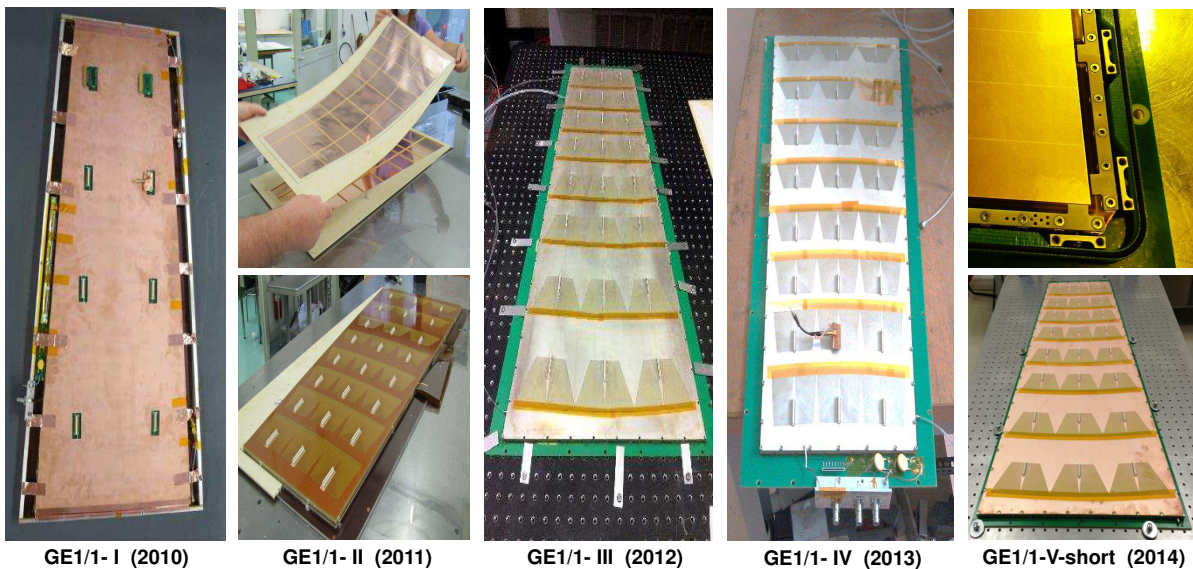


Figure 2.7: Five generations of GE1/1 prototype chambers constructed and tested by the GEM collaboration in 2010-2014. The split figures for GE1/1-II and GE1/1-V demonstrate the evolution from construction using spacer frames to purely mechanical stretching of GEM foils without any spacers.

548 The GE1/1-I prototype was the first 1m-class GEM detector ever constructed and operated[15].
 549 Components were glued together and spacer ribs were used to keep the GEM foils apart; it had
 550 only 8 readout sectors total. In the GE1/1-II the readout segmentation was increased to 24 sec-
 551 tors arranged in eight η -partitions and three columns. Each η -partition comprised 384 radial

strips with $455 \mu\text{rad}$ angular pitch. The foil gap configuration was changed from 3/2/2/2 mm to 3/1/2/1 mm to speed up the signal[16]. The GE1/1-III prototype was the first detector in which foils were stretched purely mechanically against the outer detector frame, but this frame was made from several pieces and was glued to the drift board[17]. This generation was also the first prototype to use a miniaturized ceramic high voltage divider for powering. When bolting the readout board onto the outer frame in this design, the O-ring acted as a fulcrum creating a torque on the board as the bolts were tightened. This caused the readout board to deform slightly after assembly, which in turn caused a response non-uniformity across that chamber prototype as the foil gap sizes were not kept uniform enough. In the GE1/1-IV prototype, before assembly both readout and drift boards were pre-bent in the direction opposite to the bowing observed in the GE1/1-III in an attempt to compensate for the bending that occurs after assembly. They were bolted to the outer frames and sealed with O-rings making the GE1/1-IV the first large-area GEM detector produced without gluing any components. Consequently, it could be assembled in a few hours[19]. While the pre-bending technique works in principle, it is not deemed reliable enough for future mass production purposes and it is a time-consuming production step. Instead, the problem has been rectified in the GE1/1-V prototype design by tensioning the foils against independent “pull-out” pieces (see Figure 2.7 top right). The drift and readout boards are now bolted onto the pull-out pieces. The outer frame is made from a single piece and only serves as a wall for the gas volume; it is sealed against readout and drift boards with O-rings. This final prototype design with a few improvements of details is being adopted as the final design of the GE1/1 triple-GEM chambers, which is described in detail in this report (see sec. 2.3).

2.2.2 Performance measurements and simulation studies

The performances of the different generations of GE1/1 prototypes were studied in a series of beam tests at CERN in 2010[15], 2011[16], and 2012[17], and at Fermilab in 2013[18]. The beam tests at CERN focused on measuring the performance when the chambers were operated with the Ar/CO₂/CF₄ 45:15:40 gas mixture and read out with binary-output VFAT2 front-end chips[14], whereas in the Fermilab beam test the chambers were operated with Ar/CO₂ 70:30 and read out with analog APV25 front-end chips[10] that produce full pulse height information. The APV25 chips are mounted on small hybrid boards for use with the scalable readout system[20, 21] developed by the RD51 collaboration.

In addition to this multi-year experimental effort, the GEM collaboration has mounted an extensive GEM simulation effort, which is described below in section 2.2.2.5.

2.2.2.1 Measurements of detector gain and response uniformity

Gas gain:

The gas gain was measured for each GE1/1 prototype generation. Typically, for this measurement a high-rate X-ray generator is used to irradiate the GEM chamber. The gas gain can then be calculated from measured hit rates and anode currents. For example, gain measurements performed at CERN for a GE1/1-IV operated at different high voltages applied to the drift electrode are shown in Figure 2.8 for both Ar/CO₂ 70:30 and Ar/CO₂/CF₄ 45:15:40 counting gases. The typical exponential dependence of the gas gain on HV is evident. The plot also shows the hit rates observed in the GE1/1-IV for a fixed rate of incident X-rays, which feature the beginnings of rate plateaus where the chamber starts operating with full efficiency.

Response uniformity:

An X-ray generator is also employed to study the response uniformity across the detector[19].

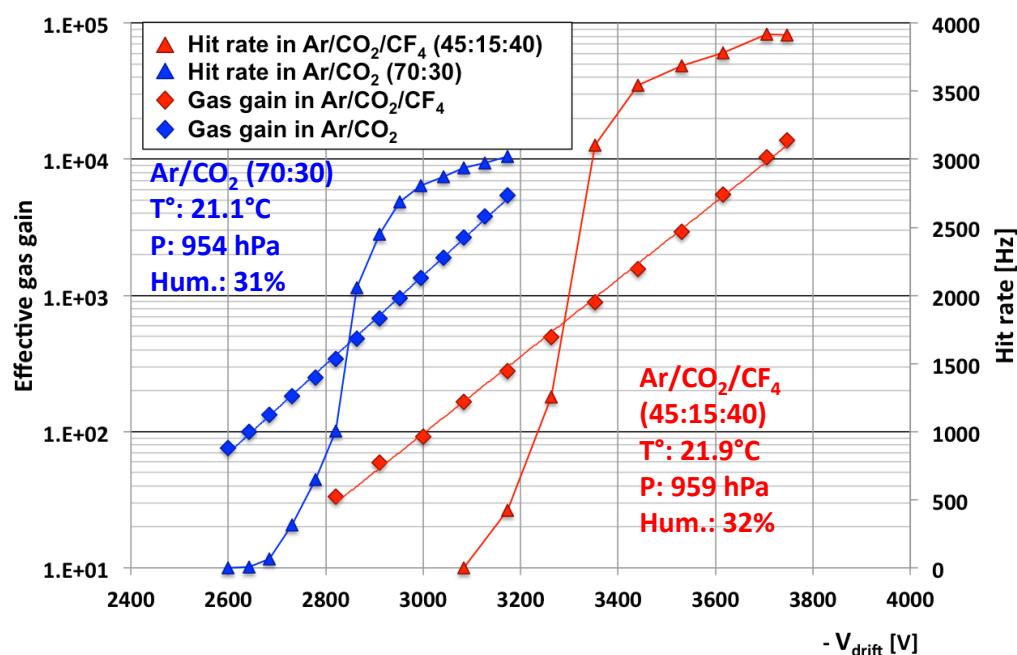


Figure 2.8: Measured gas gains (diamonds) and hit rates (triangles) as a function of high voltage applied to the drift electrode of a GE1/1-IV. Measurements with Ar/CO₂ 70:30 (blue) and with Ar/CO₂/CF₄ 45:15:40 (red) gas mixtures are displayed. The log scale (left) applies to the gain whereas the rates are plotted on a linear scale (right).

597 Figure 2.9 shows results from a GE1/1-III scan as an example. The variation of the peak posi-
 598 tion in the pulse charge distributions is taken as a measure of the response uniformity. From
 599 the data shown in Figure 2.9 (right) we conclude that the response varies not more than 15%
 600 across the detector in this slice. Corresponding measurements for the GE1/1-V are currently in
 601 progress.

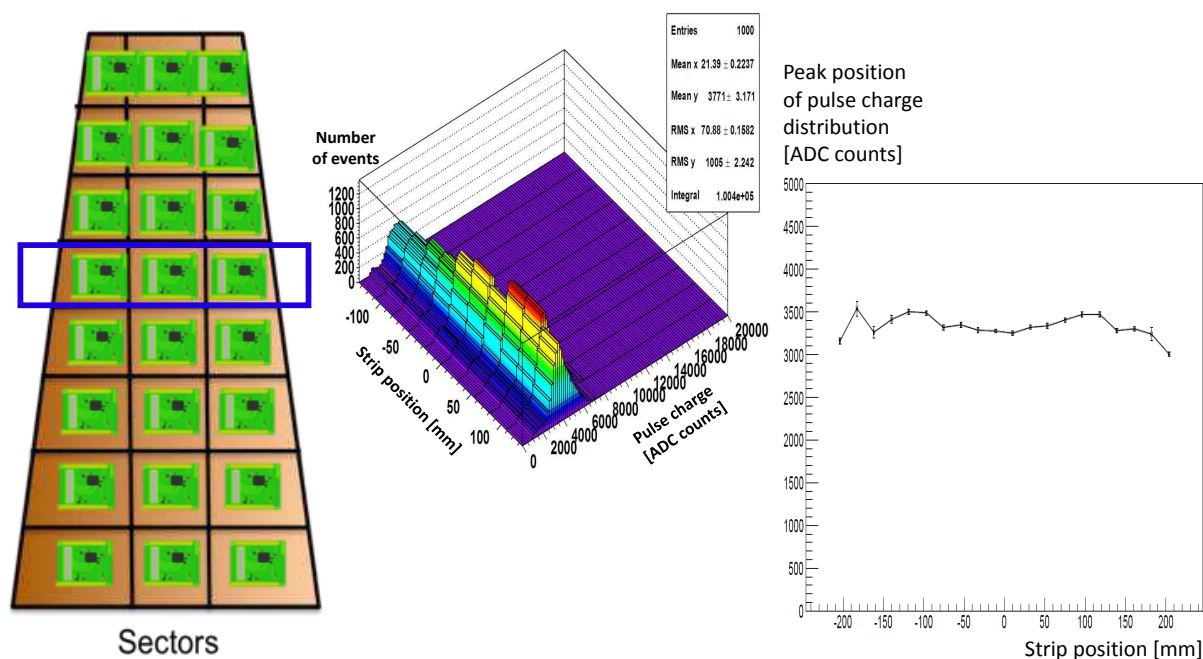


Figure 2.9: Results from a response scan across three sectors (left) of a GE1/1-III with an X-ray generator. The pulse charges measured on several adjacent strips are grouped together and histogrammed (center). The peak position of the pulse charge distributions for these strip groups are plotted vs. their positions across the chamber (right).

602 2.2.2.2 Measurements of detection efficiency, angular resolution, and timing resolution

603 Detection efficiency:

604 Figure 2.10 shows GE1/1 efficiency measurements for charged particles from two separate
 605 beam tests at CERN and Fermilab. A GE1/1-IV prototype reaches a plateau efficiency of 98%
 606 for pions when operated with Ar/CO₂/CF₄ 45:15:40 and read out with VFAT2 chips. When a
 607 GE1/1-III is operated with Ar/CO₂ 70:30 and offline cuts are placed on the strip charge mea-
 608 sured by the APV to emulate VFAT2 thresholds, the plateau efficiency is 97%. When full APV
 609 pulse height information is used, the hit threshold can alternatively be set individually for
 610 each strip as a multiple of the pedestal width. For example, with a 5 σ pedestal width cut the
 611 efficiency is measured slightly higher at 97.8%[18].

612 Angular resolution:

Results from independent GE1/1 angular resolution measurements obtained in two test beam campaigns are shown in Figs. 2.11-2.13. In the 2012 CERN beam test conducted with Ar/CO₂/CF₄ 45:15:40 counting gas and binary-output VFAT2 chips, the distribution of the residuals, i.e. the differences between the measured hit positions and the points where the fitted track impacts the chamber, in the azimuthal $\hat{\phi}$ directions shows a width of $268 \pm 2 \mu\text{m}$ when the GE1/1 is excluded from the track fit, which we refer to as an “exclusive residual” (Figure 2.11 (top)). This width represents an upper limit on the intrinsic chamber resolution because the exclusive residual width overestimates the intrinsic resolution as the residual width is due to a convolution of intrinsic hit resolution and uncertainty in extrapolated track position. This result is obtained from sector 6 of the chamber at radius $r \approx 1.95 \text{ m}$, where the strip pitch in azimuthal direction is 0.88 mm. Consequently, this residual in the $\hat{\phi}$ direction corresponds to an exclusive angular residual of $137 \pm 1 \mu\text{rad}$. This measured upper limit on the angular resolution in ϕ is

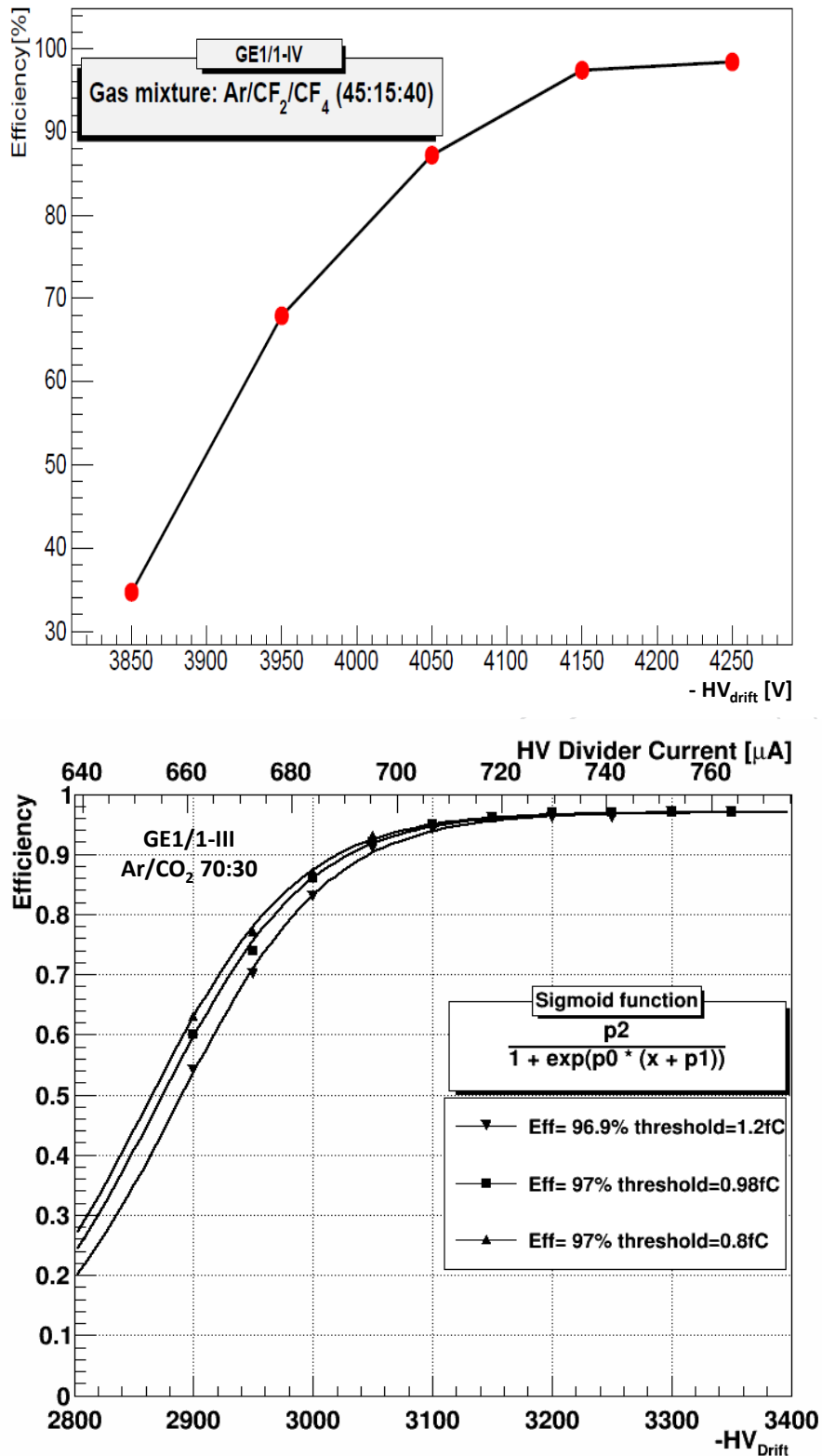


Figure 2.10: Measured detection efficiencies of GE1/1 prototypes for charged particles. *Top:* Eff. vs. HV applied to drift electrode when GE1/1-IV is operated with Ar/CO₂/CF₄ 45:15:40 and read out with VFAT2 chips configured with 0.8 - 1.2 fC strip-hit thresholds. *Bottom:* Eff. vs. HV applied to the drift electrode measured in central sector 5 of a GE1/1-III operated with Ar/CO₂ 70:30 and read out with APV chips. Three different cuts are applied offline to the strip charges to simulate VFAT2 threshold behavior and the resulting efficiency curves are fitted to sigmoid functions.

close to the expected intrinsic resolution for a binary readout, which is given by:

$$\text{angular strip pitch}/\sqrt{12} = 455 \mu\text{rad}/\sqrt{12} = 131 \mu\text{rad}. \quad (2.1)$$

613 This performance exceeds the minimum requirement of 300 μrad with a comfortable perfor-
614 mance margin.

For the 2013 Fermilab beam test data obtained with Ar/CO₂ 70:30 counting gas and analog-output APV chips, the measured strip charges can be used to determine the hit position in the GE1/1 from the barycenter of the strip charges (centroid). For these data, exclusive residuals and “inclusive” residuals were calculated. For the latter, the GE1/1 hit is included in the track fit. Measurement of both residual types are shown at the center and bottom of Figure 2.11. The inclusive residual underestimates the intrinsic resolution of the chamber because including the hit of the probed chamber biases the track towards that hit. However, the intrinsic resolution can be obtained to good approximation from the geometric mean of the widths of the inclusive and exclusive residuals[22, 23]. At a radius $r \approx 1.85$ m (sector 5), we then find an angular resolution

$$\sigma_{\text{resolution}} = \sqrt{\sigma_{\text{incl.residual}} \times \sigma_{\text{excl.residual}}} = 132 \mu\text{rad}, \quad (2.2)$$

615 which is similar to the upper limit on the resolution obtained above with VFAT2 chips and
616 Ar/CO₂/CF₄ 45:15:40 at a similar radial position. We note that this result is still a slight over-
617 estimate for the resolution because multiple scattering of the tracked particles in the material
618 of the ten chambers ($\approx 14\%$ of a rad. length) placed in the beam is not taken into account,
619 yet. Corresponding residuals and angular resolutions measured for other η -sectors using the
620 centroid method are shown in Figure 2.12 (left). The measured angular resolution varies over
621 a range of 100 - 160 μrad in sectors 2-7. The resolution could not be measured for the outer
622 sectors 1 and 8 of the prototype due to geometric constraints in the test beam setup. Figure 2.12
623 (right) shows residual widths and angular resolution as a function of drift voltage. As expected,
624 the resolution improves with increasing drift voltage, i.e. gas gain, reaching $\approx 125 \mu\text{rad}$ on the
625 efficiency plateau.

626 The number of strips in a strip cluster is observed to increase with high voltage (Figure 2.13
627 left) because the lateral size of the electron avalanche in the triple-GEM increases as the gain
628 increases. At the start of the efficiency plateau around 3200 V in Ar/CO₂ 70:30, two-strip clus-
629 ters dominate; these also produce the best angular resolutions of $\approx 115 \mu\text{rad}$ (Figure 2.13 right)
630 when the centroid method is used for calculating the hit position.

631 **Timing resolution:**

632 The timing performance measured with a 10 cm \times 10 cm triple-GEM equipped with standard
633 double-mask GEM foils is shown in Figure 2.14. The timing resolution for Ar/CO₂ 70:30 and
634 a 3/2/2/2 mm gap configuration is compared with the timing resolution for Ar/CO₂/CF₄
635 45:15:40 and a 3/1/2/1 mm gap configuration. With the faster gas and the shorter drift dis-
636 tances, the timing resolution improves by a factor of two from 8 ns to 4 ns.

637 The timing performance of an actual GE1/1-III prototype operated with Ar/CO₂/CF₄ 45:15:40
638 and read out with VFAT2 chips in the 2012 test beam at CERN[17] is shown in Figure 2.15.
639 Dedicated timing hardware selects events within a 2 ns time window from the asynchronous
640 SPS beam. Rather than performing direct TDC measurements, here the relative fraction of GEM
641 hits in adjacent 25 ns time bins is measured (Figure 2.15 left). For the configuration used, 97%
642 of all hits occur within the correct 25 ns clock cycle.

643 One can then ask what value of a Gaussian width σ would produce that plot when a close to
644 perfect ($\delta(t)$ -like) input time distribution is smeared with that Gaussian and binned in 25 ns

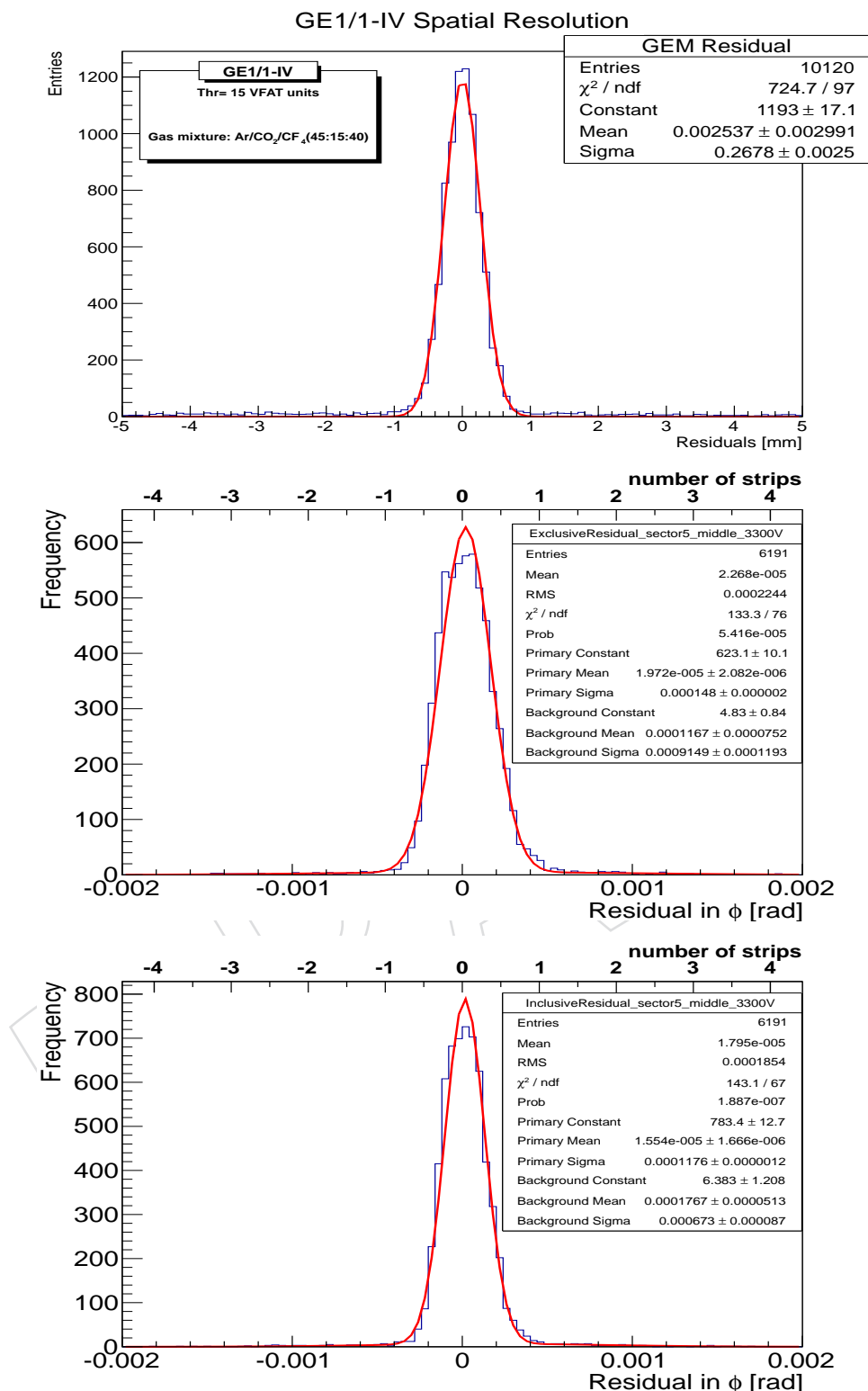


Figure 2.11: Track-hit residuals measured in central sectors of GE1/1 prototypes at $r \approx 1.9$ m. *Top*: Exclusive residuals in azimuthal $\hat{\phi}$ -direction measured with a pion beam at CERN when a GE1/1-IV is operated with Ar/CO₂/CF₄ 45:15:40 and read out with binary-output VFAT2 chips. *Center*: Exclusive angular residuals measured with a mixed pion and kaon beam at Fermilab when a GE1/1-III is operated with Ar/CO₂ 70:30 at 3300 V and read out with APV chips. Here the barycenter of the strip cluster charge (centroid) is used to determine the hit position. The residuals are fitted with a double Gaussian function. *Bottom*: Corresponding inclusive angular residuals for same measurement as center plot.

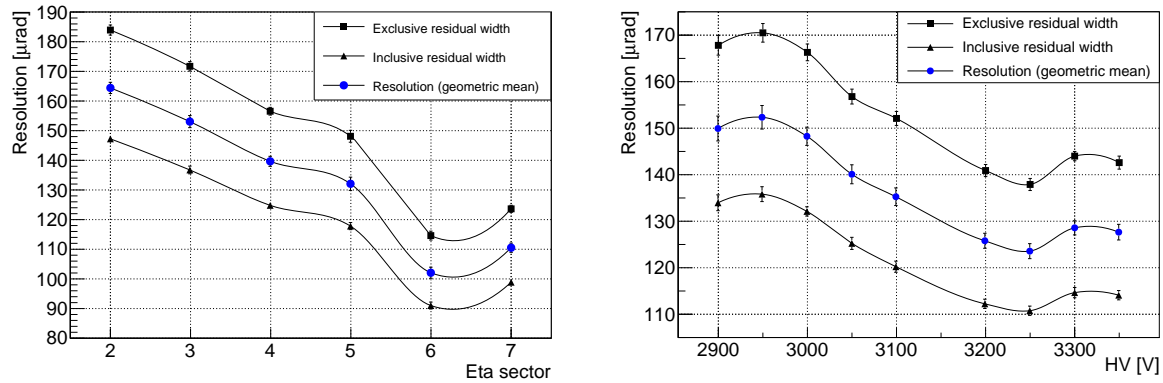


Figure 2.12: Measured exclusive and inclusive residual widths and angular resolutions (blue) of a GE1/1-III operated with Ar/CO₂ 70:30 and read out with APV chips. *Left*: As a function of η -sector for six of the eight η -sectors at $V_{\text{drift}} = 3300$ V. Sector numbers increase with increasing radius and decreasing η . *Right*: As a function of voltage V_{drift} applied to the drift electrode in central sector 5.

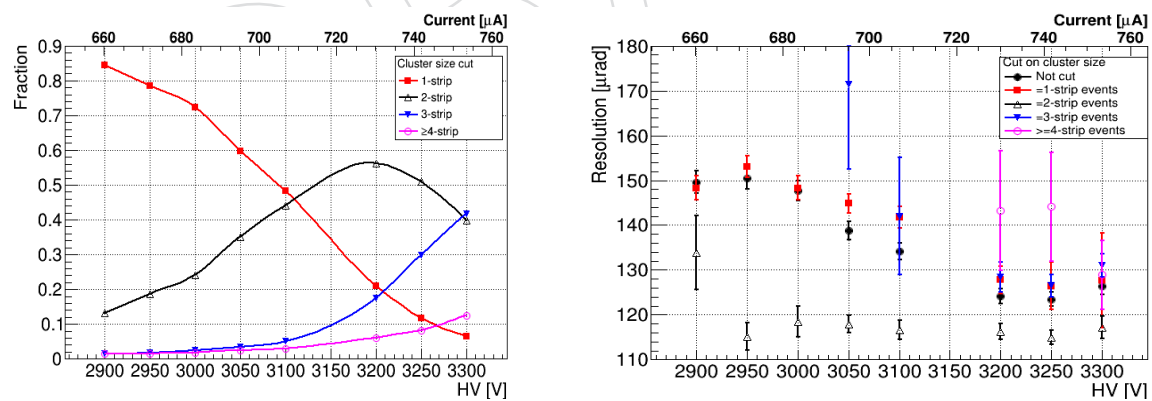


Figure 2.13: *Left*: Relative fractions of strip multiplicities observed for strip clusters in sector 5 of a GE1/1-III operated with Ar/CO₂ 70:30 and read out with APV chips as a function of high voltage applied to drift electrode. *Right*: Corresponding measured angular resolutions for different strip multiplicities of strip clusters vs. high voltage.

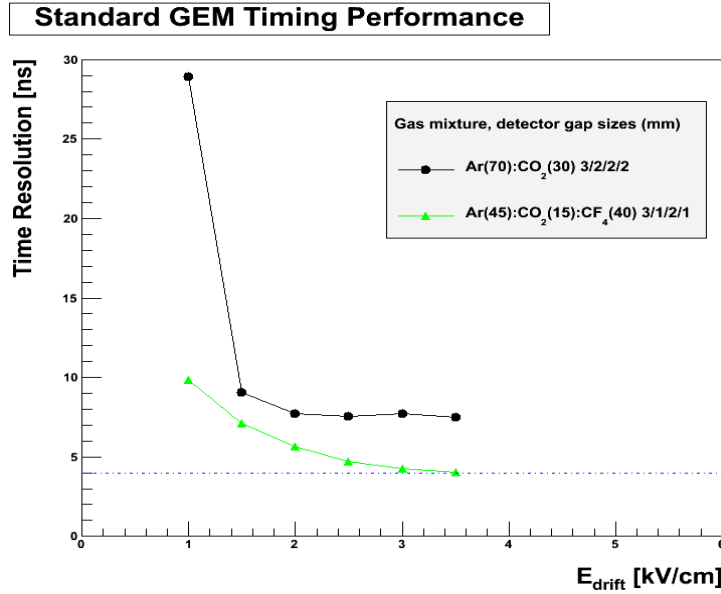


Figure 2.14: Timing resolutions measured with a TDC for a small triple-GEM detector equipped with GEM foils produced with the standard double-mask technique as a function of drift field for the counting gases under consideration.

645 bins. We take the width σ of the Gaussian that best reproduces the timing fraction histogram
 646 of Figure 2.15 (left) as our measurement of the GE1/1 timing resolution. The GE1/1 time res-
 647 olution measured with this method is shown as a function of current in the HV divider in
 648 Figure 2.15 (right). On the efficiency plateau, the GE1/1-III has a timing resolution of 6 ns. For
 649 two GE1/1 chambers in one superchamber operated with Ar/CO₂/CF₄ 45:15:40, we would ex-
 650 pect a timing resolution of $6 \text{ ns} / \sqrt{2} = 4 \text{ ns}$. Based on the results in Figure 2.14, we then expect
 651 an overall timing resolution of 8 ns for a superchamber operated with Ar/CO₂ 70:30.

652 2.2.2.3 Rate capability measurement

653 In order to confirm the high-rate capability of the GE1/1 that is expected of such a triple-
 654 GEM detector, we measure the gain vs. incident rate using a medium-intensity 22 keV Ag
 655 X-ray source and a high-intensity 8 keV Cu X-ray source. A GE1/1-III detector, operated with
 656 Ar/CO₂ 70:30, was illuminated with the Cu source and the gas gain was measured via the
 657 anode current produced in the chamber during this irradiation. The same measurement was
 658 also done with a more recent GE1/1-IV prototype, but operated with an Ar/CO₂/CF₄ 45:15:40
 659 gas mixture and illuminated with the Ag X-ray source. The gain G can be calculated with the
 660 formula $G = \frac{I}{eNR}$, where I is the measured anode current in the GE1/1 chamber, N is the
 661 total number of electrons produced in each X-ray conversion, e is the electron charge, and R is
 662 the measured rate of incident particles. The results in Figures 2.16 and 2.17 show that the gas
 663 gain is observed to be constant over four orders of magnitude of incident particle rate up to
 664 100 MHz/cm². The gain begins to drop only above that value. This result confirms that the
 665 GE1/1 chambers will easily operate in the $1.6 < |\eta| < 2.2$ forward muon region of CMS, where
 666 a maximum rate on the order of 10 kHz/cm² is expected, i.e. four orders of magnitude lower
 667 than the rate that the GE1/1 detector can operate at while maintaining constant gain.

668 2.2.2.4 Performance in magnetic field

669 Figure 2.18 shows a map of the magnetic field expected in the CMS muon endcap region during
 670 LHC Phase 2. In the location of the GE1/1, we expect a magnetic field strength of about 3T and

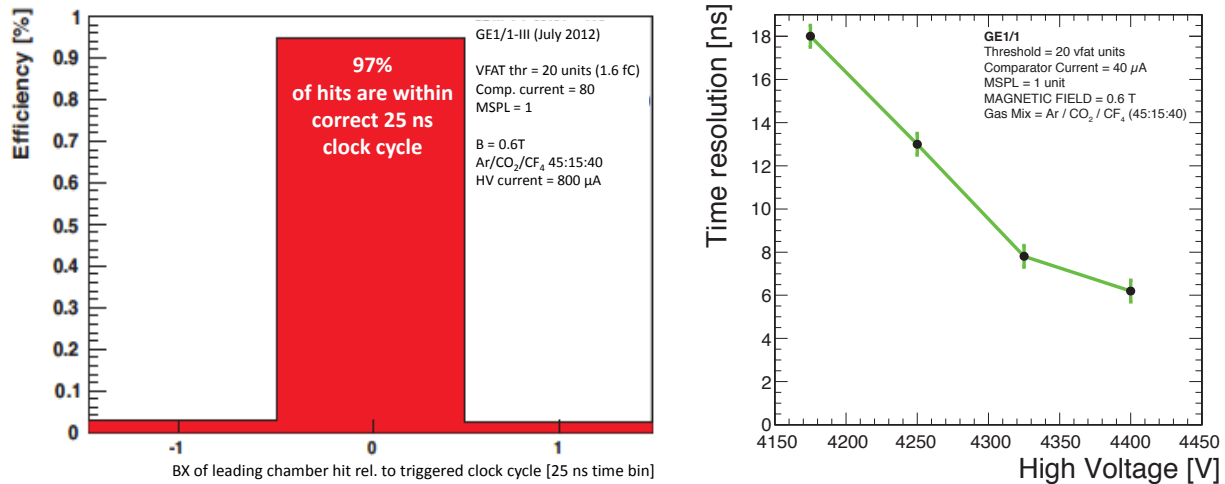


Figure 2.15: Timing measurements for a GE1/1-III prototype with VFAT2 readout in a beam with 25 ns bunch crossing time. *Left*: Fraction of hits measured in bunch crossings relative to the trigger clock cycle. *Right*: Timing resolution vs. drift voltage derived from plots as shown on the left assuming a Gaussian time resolution.

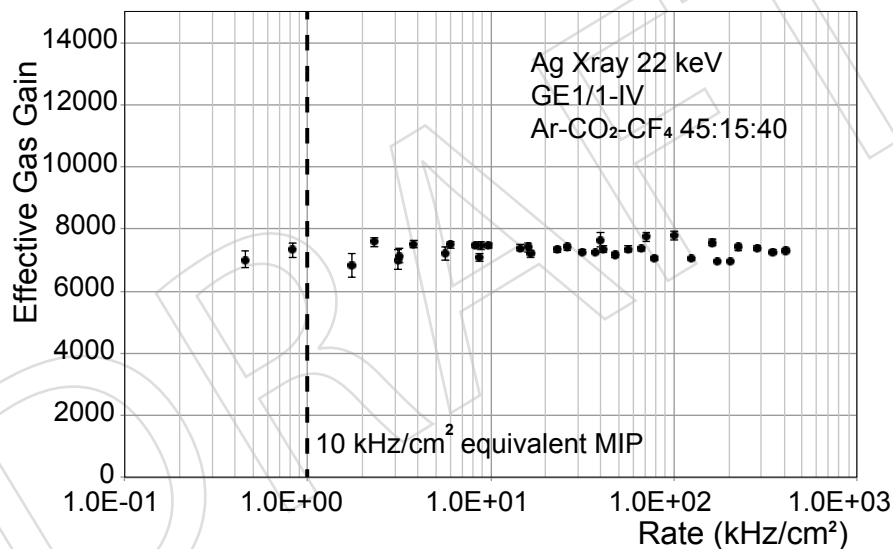


Figure 2.16: Effective gas gain as a function of the incident photon rate measured in a GE1/1-IV detector operated with Ar/CO₂/CF₄ 45:15:40 and irradiated with a 22 keV X-ray source with Ag anode.

671 a maximum polar angle of 8-9° between the magnetic field lines and the CMS z-coordinate,
 672 which is also the direction of the internal electric field lines in the drift region of the GE1/1. This
 673 demonstrates that the GE1/1 will be operated in a substantial magnetic field. Consequently,
 674 we have tested the performance of GE1/1 prototypes also in magnetic fields.

675 During a test with 150 GeV muon and pion beams in the SPS H2 beam line at CERN, a GE1/1-II
 676 prototype was operated in a magnetic field up to 1.5 T provided by the CMS M1 superconducting
 677 magnet[16, 24]. The GE1/1-II was placed between the two magnet coils to validate the
 678 detector performance in a magnetic environment similar to that in the high- η region of the
 679 CMS muon endcap. For example, the Lorentz angle for the drifting electrons at 1.5 T and

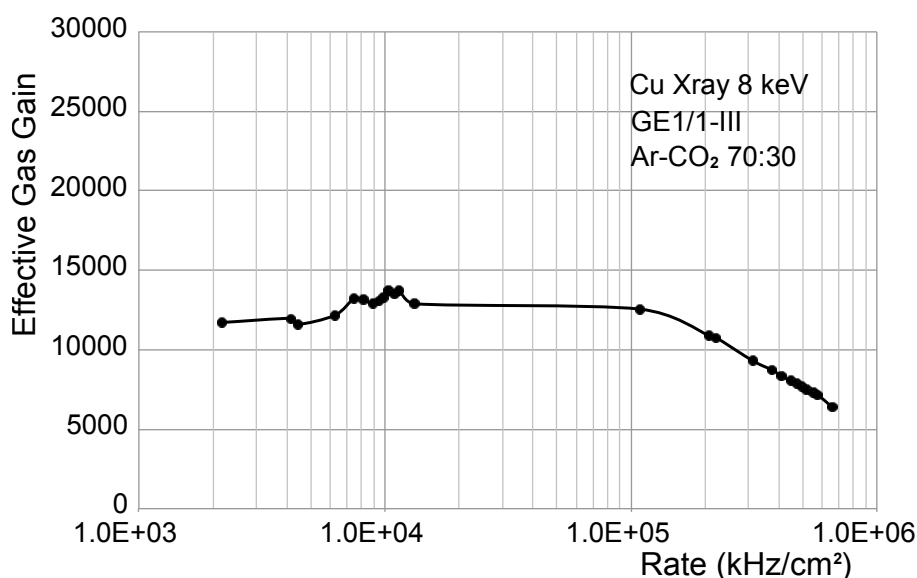


Figure 2.17: Effective gas gain as a function of the incident photon rate measured in a GE1/1-III detector operated with Ar/CO₂ 70:30 and irradiated with an 8 keV X-ray source with Cu anode.

680 $\angle(\vec{E}, \vec{B}) = 90^\circ$ is comparable to the Lorentz angle at 3.8 T and $\angle(\vec{E}, \vec{B}) = 8^\circ$ that will be encountered by the GE1/1 in CMS (Figure 2.18).

682 Figure 2.19 gives the measured strip multiplicity distribution for strip clusters in presence of
 683 a 0.6T magnetic field. Figure 2.20 shows the mean strip multiplicity of strip clusters and the
 684 cluster displacements as a function of magnetic field up to 1.5 T. The cluster size does not
 685 appear to be affected much by the magnetic field while the cluster position is displaced due to
 686 the presence of the magnetic field. The measurement of this displacement is in good agreement
 687 with simulations performed with GARFIELD. The timing performance was also measured with
 688 and without magnetic field as shown in Figure 2.21. The overall conclusion from these tests is
 689 that the magnetic field does not influence the performance of the GE1/1 detector in any way
 690 that would invalidate the conclusions from the measurements without field.

691 2.2.2.5 GEM performance simulations

692 The simulation comprises basic single-GEM simulations and a full triple-GEM simulation that
 693 includes signal generation and electronics. To simulate the detector response, one first has to
 694 calculate the electric field map, then simulate the electron transport in the gas, the avalanche
 695 production, and signal formation and induction. A simulation flowchart is presented in Figure
 696 2.22.

697 For the electric field simulation, the physical detector geometry (Figure 2.23) is implemented in
 698 ANSYS, a simulation package for computational fluid dynamics applications[25]. Appropriate
 699 electrical potentials are assigned to each electrode. The field map is then generated in both 2D
 700 and 3D formats and loaded as an input to the GARFIELD++ suite[26], which simulates and
 701 computes electron transport in the gas medium, avalanche production (Figure 2.24), and signal
 702 formation. Each simulation point consists of at least 5,000 electrons randomly distributed in
 703 X and Y and generated at a fixed 0.25 mm on the Z-axis (Figure 2.24), i.e. just below the drift
 704 cathode. The gain uniformity as a function of the readout strip pitch, signal formation, and
 705 timing resolution are studied with this simulation.

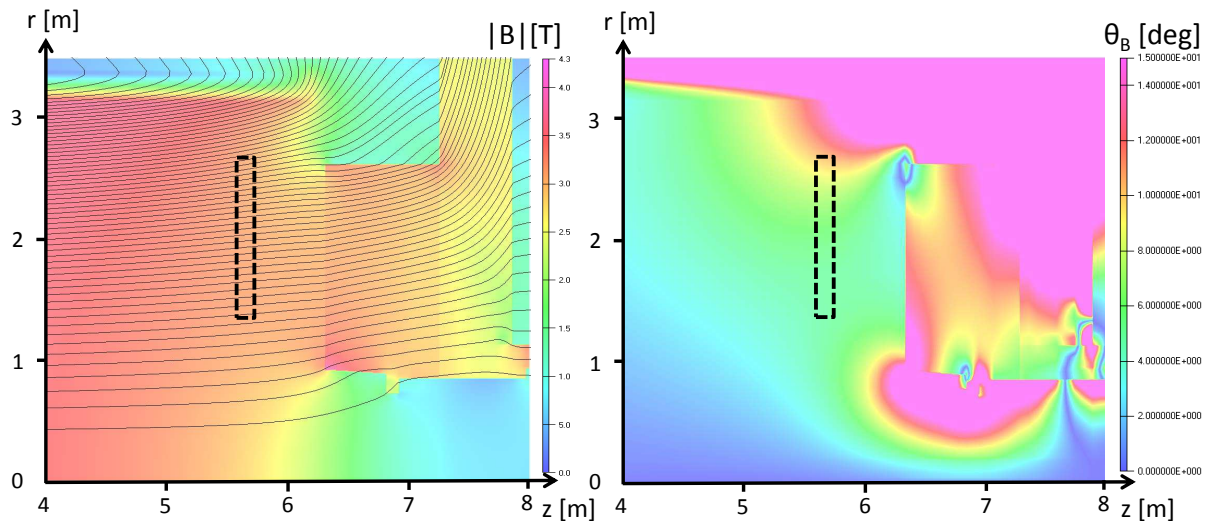


Figure 2.18: Map of the magnetic field expected in the CMS muon endcap region near the solenoid in LHC Phase 2 produced by OPERA simulation. Shown are field strength and field lines (left) and polar angle θ_B of the magnetic field vector (right), i.e. the angle between magnetic field and the z -axis of CMS. The dashed rectangles indicate the location of the GE1/1. Note that regions with $\theta_B \geq 15^\circ$ are colored pink.

706 **Uniformity:** An important GE1/1 performance parameter is the uniformity of the gain across
 707 the strips. Due to the trapezoidal shape, it is important to check the gain variations across the
 708 active area of the chamber. Figure 2.25 shows the effective gain as a function of the readout
 709 pitch in Ar/CO₂/CF₄ 45:15:40 for different values of the Penning effect parameterized by r_p .
 710 The simulated readout pitches 0.6 mm, 0.8 mm, 1.0 mm, and 1.2 mm represent the strip pitch
 711 variation in the GE1/1 going from higher to lower pseudorapidity. We observe some increase
 712 of the effective gain with pitch size, but the range of gains due to that effect does not exceed
 713 the maximum of 15% gain variation across the chamber that we require.

714 **Timing resolution:** In a triple-GEM detector, the signal on the readout strips is induced by the
 715 electrons amplified in the last of the three stages of multiplication. All electron production,
 716 transport, and amplification processes have statistical fluctuations which lead to fluctuations
 717 in the shape of the induced signal. The most important fluctuation occurs in the primary ion-
 718 ization process in the drift gap due to the clustering of the primary ionization; it dominates
 719 because of the small number of primary electrons. In the Ar/CO₂/CF₄ 45:15:40 gas mixture,
 720 the drift velocity is about 80 $\mu\text{m}/\text{ns}$ (Figure 2.6), so for a charged particle with perpendicular
 721 incidence, the primary electrons need up to 38 ns to completely clear the 3 mm drift gap. These
 722 effects are reflected in the duration and structure of the charge signals induced in the readout
 723 strips as demonstrated by the simulation results (Figure 2.26).

724 In order to fully estimate the performance of the triple-GEM detector such as time resolution,
 725 efficiency, etc., one has to include the response of the VFAT3 front-end electronics (see Ch.3) to
 726 the induced signals in the simulation. We convolute the induced signal given by the GARFIELD
 727 simulation, with the VFAT3 transfer function given by: $F(t) = \left(\frac{t}{\tau}\right)^n \exp(-n\frac{t}{\tau})$, where t is the
 728 time, τ is the peaking time (25 ns, 50 ns, 75 ns, 100 ns, 200 ns or 400 ns) and n is the filter order
 729 ($n = 3$ for VFAT3). In the VFAT3 electronics, the output signal of the shaper is sent to a Constant
 730 Fraction Discriminator (CFD), which identifies the arrival time of the signal. We apply the CFD
 731 method with 5 different peaking times (25 ns, 50 ns, 75 ns, 100 ns and 200 ns). For each peaking
 732 time, we use 500 events simulated with GARFIELD. The time resolution as a function of the

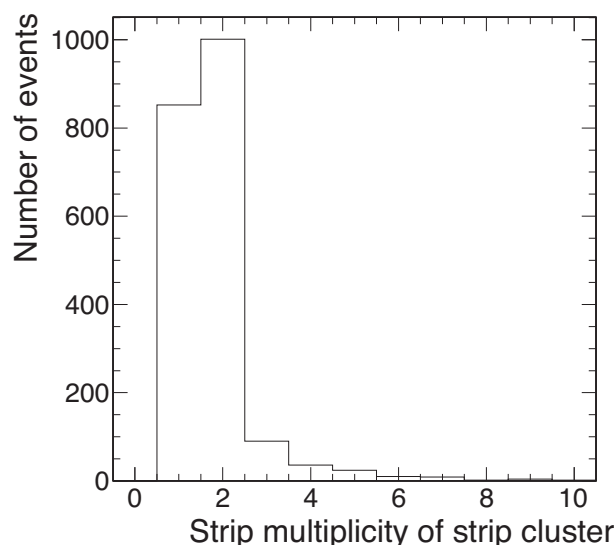


Figure 2.19: Strip multiplicity distribution for strip clusters at $B=0.6$ T when operating GE1/1-II chamber on the efficiency plateau.

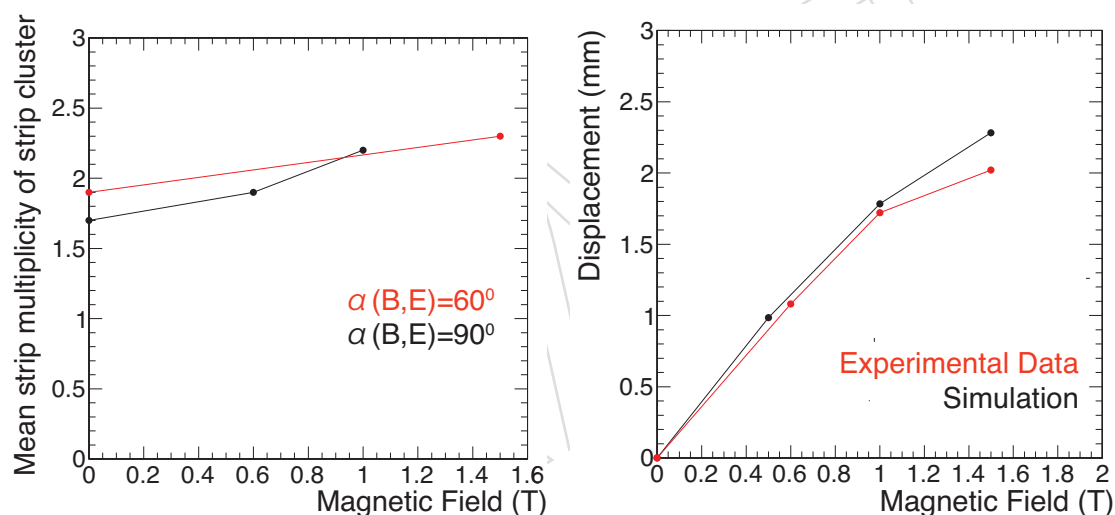


Figure 2.20: GE1/1-II performance inside a strong magnetic field. *Left*: Mean strip multiplicity of strip cluster. *Right*: Strip cluster displacement due to the magnetic field.

733 VFAT3 peaking time is better than 5 ns for peaking times longer than 50 ns (Figure 2.27). This
 734 result makes sense since it takes at least 30 ns for the fully amplified electrons from the drift gap
 735 to induce a signal; it is also consistent with the good time resolution of the CMS triple-GEM
 736 detector with Ar/CO₂/CF₄ 45:15:40 measured in the test beam experiments.

737 2.2.3 Considerations for environmentally-friendly counting gas mixtures

738 Recently, a general discussion started within the gaseous detector community about the high
 739 environmental impact of several gases used during detector operation. Many gas mixtures
 740 commonly use gas components with extremely high Global Warming Potential (GWP). For
 741 example, GEM detectors often use gas mixture with CF₄ that has a GWP of 6500 (over 100
 742 yrs) which makes this gas one of the most aggressive in terms of green house effects, the GWP
 743 of CO₂ being 1. The environmental policy (280/2004/EC) of the EU dictates that gases with

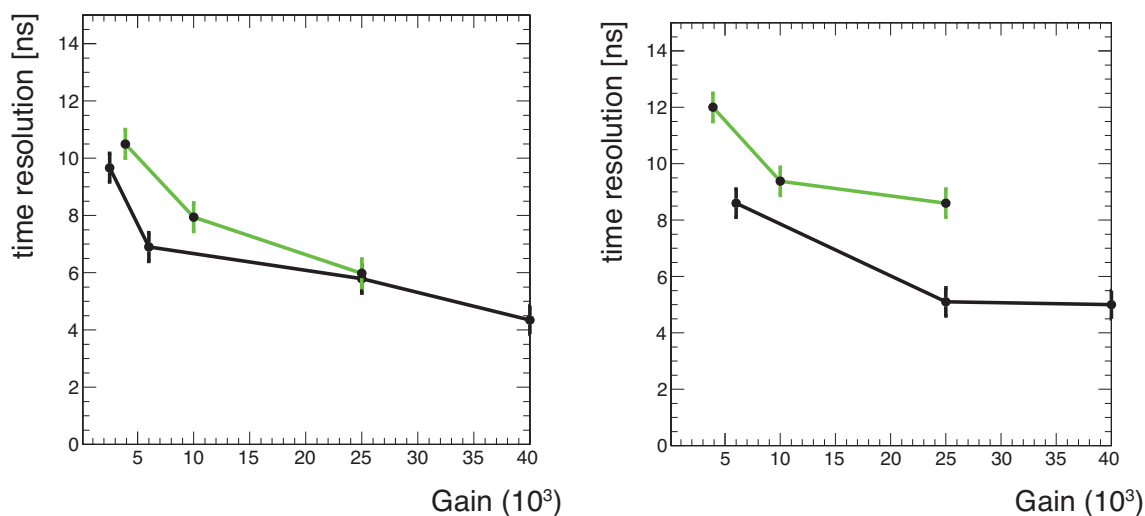


Figure 2.21: Detector time resolution as a function of gas gain without (left) and with (right) magnetic field equal to 1.5 T. The green curves are for the GE1/1-II while the black curves are for a small-size GEM prototype.

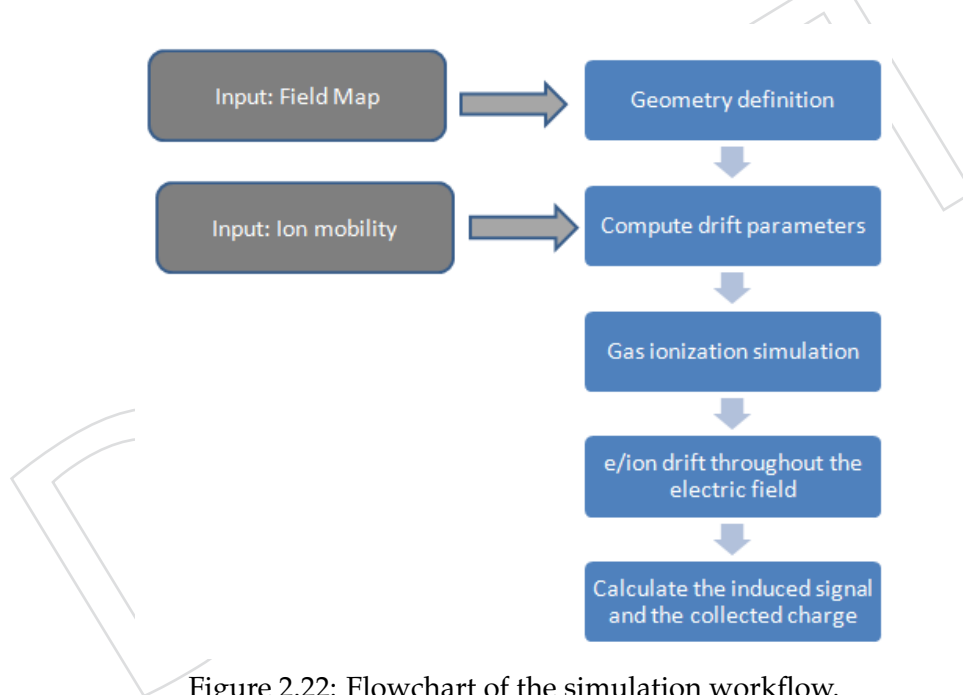


Figure 2.22: Flowchart of the simulation workflow.

744 high GWP must be phased out over the next several years. Moreover, and importantly, high
 745 GWP gases will not be produced anymore, with consequently expected rise of the gas price
 746 and difficulties with stock supplies.

747 The CMS GEM collaboration has started a campaign of studies to find potential alternatives to
 748 CF_4 . As described above, the addition of CF_4 to the counting gas mixture improves the time
 749 response of the detector while maintaining a high detection efficiency. Obviously, the alter-
 750 native to CF_4 must ensure similar performance in terms of time response, detection efficiency,
 751 and aging resistance. INFN Frascati, INFN Bari, INFN Bologna, and University of Ghent are
 752 collaborating in this search for a replacement gas. Results are expected by the end of 2015.
 753 While the tests on alternative gases are ongoing, it must be stressed that Ar/ CO_2 70:30 is a

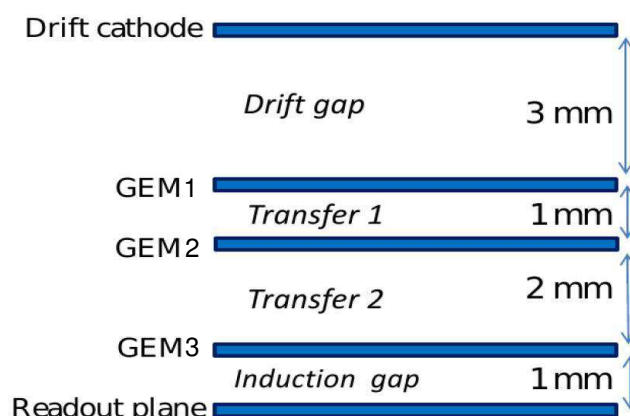


Figure 2.23: Cross section of the triple-GEM detector geometry as implemented in the simulation.

754 reasonably eco-friendly gas mixture that provides time and efficiency performances within the
 755 CMS requirements and is considered the current baseline gas for operation. This ensures that,
 756 even if a CF_4 candidate will not be found, the GE1/1 detector will be able to reach the expected
 757 performances.

758 So far, three potential candidate gases are being considered and a campaign of measuring gas
 759 characteristics and chamber performance with different gas mixtures based on these gases is
 760 ongoing. Table 2.2 summarises their main characteristics in terms of GWP. Results from these
 761 studies are expected by the end of 2015.

Chemical name (IUPAC)	Formula	CAS number	Type	GWP (100 yrs)
Tetrafluoromethane	CF_4	75-73-0	R14	6500
3,3,3-tetrafluoropropene	$\text{C}_3\text{H}_2\text{F}_4$	754-12-1	HFO-1234YF	4
1,3,3,3-tetrafluoropropene	$\text{C}_3\text{H}_2\text{F}_4$	29118-24-9	HFO-1234ZE	6
Trifluoroiodomethane	CF_3I	2314-97-8	R13I1	0.4

Table 2.2: Summary of the Global Warming Potential (GWP) over 100 yrs for different gases under study as possible CF_4 replacement candidates. CF_4 is also listed as reference.

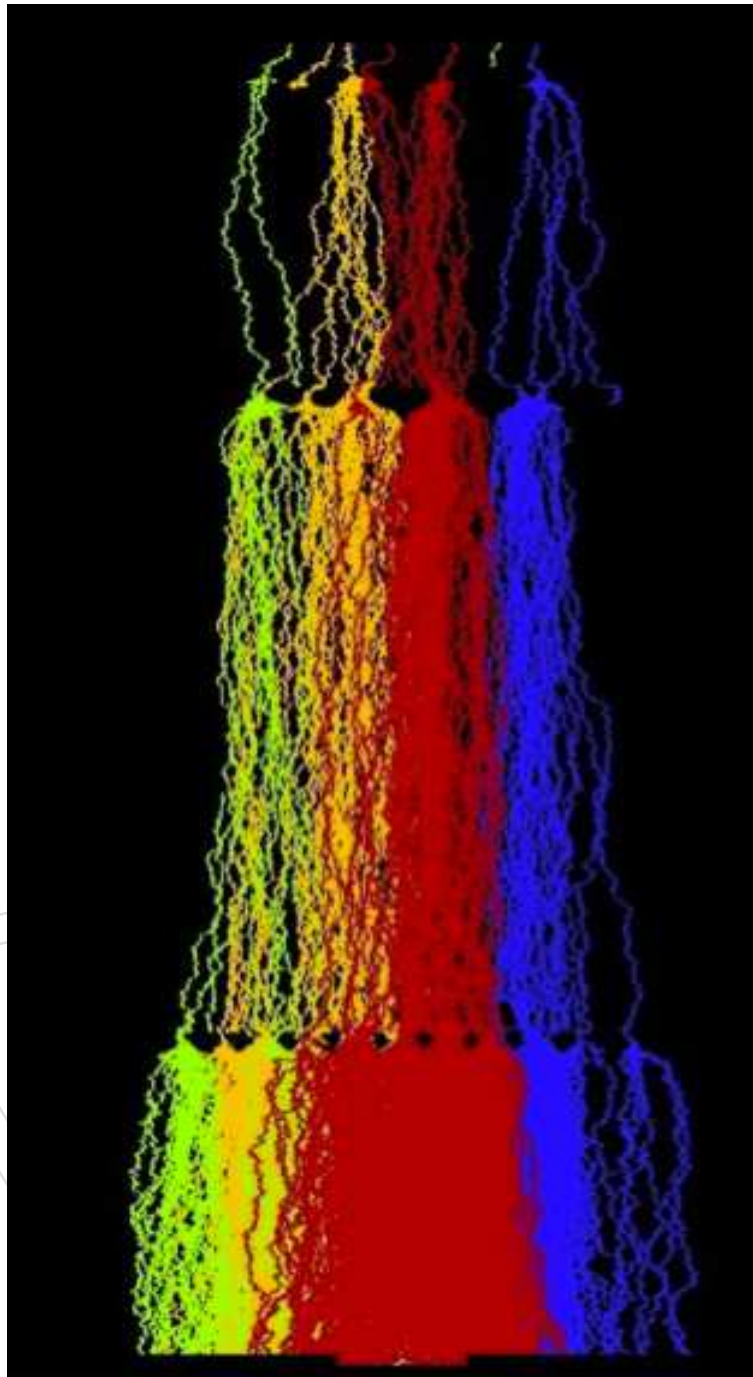


Figure 2.24: Visualization of the simulated avalanche development for seven primary electrons in a triple-GEM chamber starting from the drift volume.

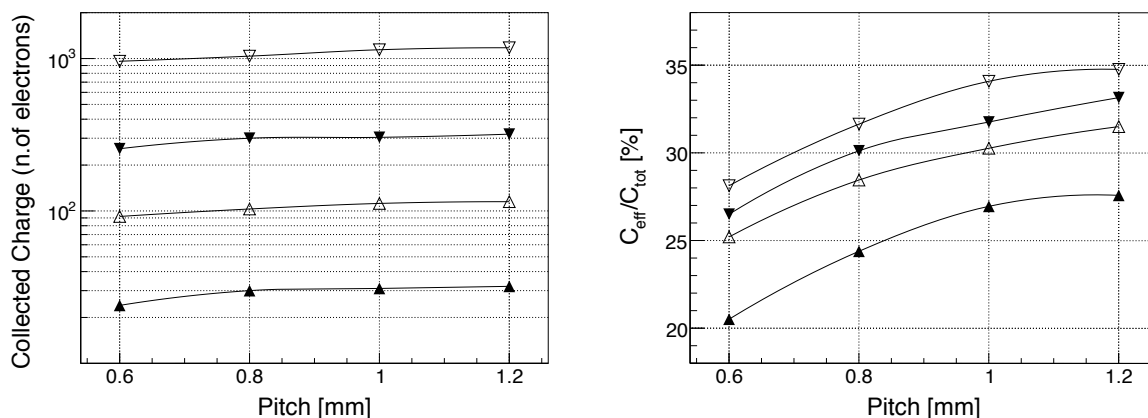


Figure 2.25: Simulation results for number of electrons collected on the anode strips (left) and ratio of effective and total charge collected (right) in Ar/CO₂/CF₄ 45:15:40 for 3650, 3850, 4050 and 4250 V (from bottom to top) as a function of readout strip pitch for $V_{\text{drift}} = 4050$ V and $r_p = 0.4$.

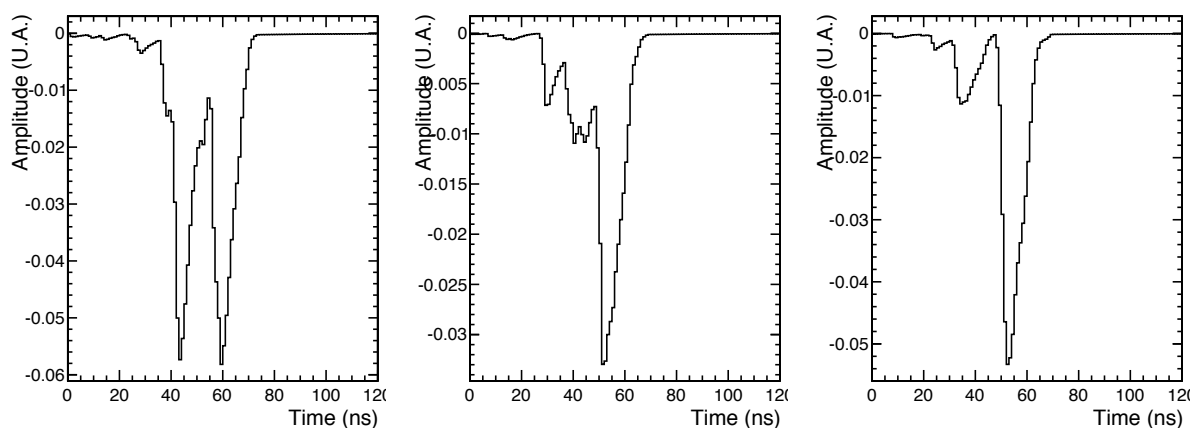


Figure 2.26: Examples for simulated signals that are induced in the readout electrodes.

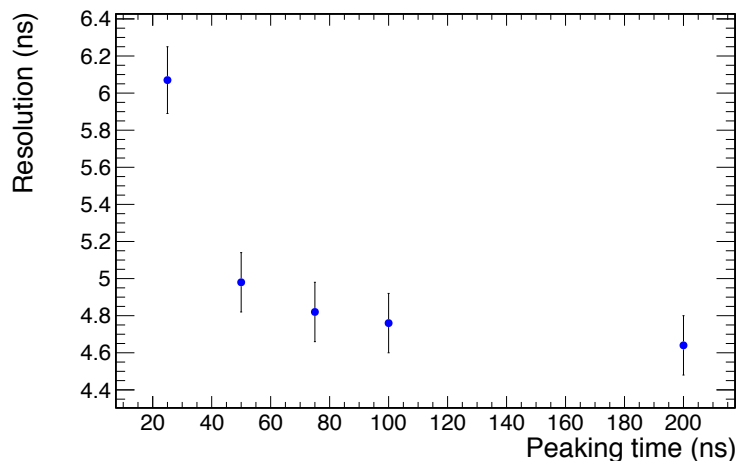


Figure 2.27: Simulated GE1/1 time resolution as a function of the VFAT3 peaking time.

2.3 Technical design of GE1/1 chambers for CMS

2.3.1 GEM foil design and production technology

The three trapezoidal GEM foils used in one GE1/1 triple-GEM detector are basically identical. However, two different foil versions need to be designed, one for the short chamber type GE1/1-S and one for the long chamber type GE1/1-L. Shape and dimensions of the active foil areas are shown in Figure 2.28. The GEM foil surfaces oriented towards the readout board are a single contiguous conductor whereas the GEM foil surfaces oriented towards the drift board are segmented into 40 strips for the short chamber and 47 strips for the long chamber. The strips run across the width of the trapezoid (Figure 2.29). Their width narrows when going from the short end of the trapezoid to the wide end so that each strip has an approximately equal area of about 100 cm^2 . This segmentation restricts the amount of charge that can flow from one foil during a discharge to roughly 100 nC and, consequently, limits the total energy of a discharge. This protects the GEM foil against destruction due to discharges, which are inevitable even if they occur at very low rates under standard operating conditions. In the worst case, if a destructive discharge were to occur in an HV segment, it would only destroy that one HV segment instead of rendering the entire chamber unusable.

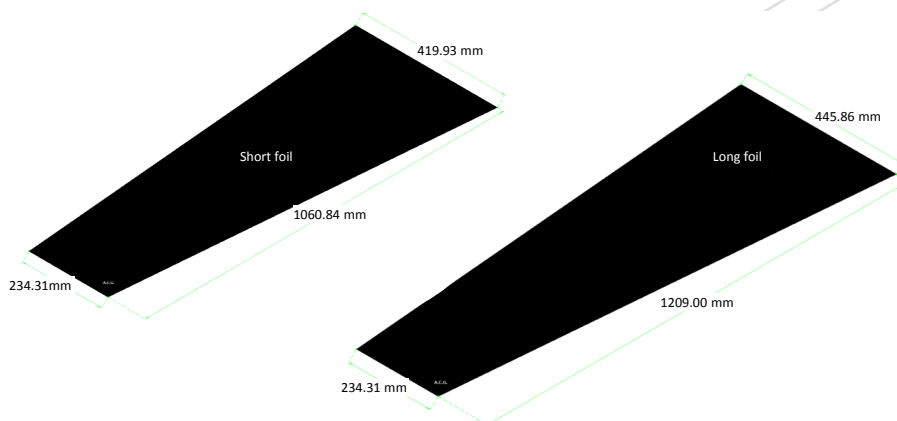


Figure 2.28: Shapes and dimensions of the active areas of short (left) and long (right) trapezoidal GEM foils for GE1/1. The trapezoids subtend an opening angle of 10° .

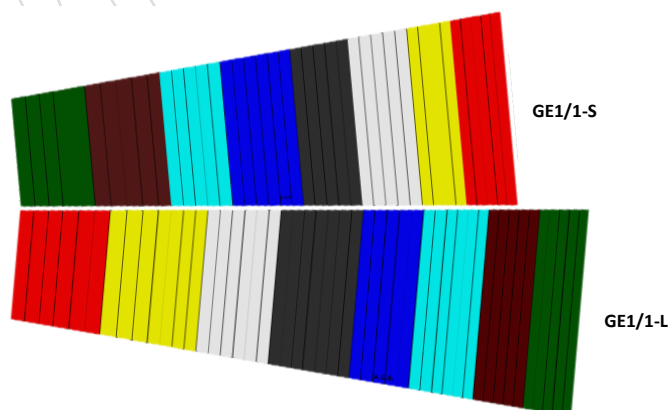


Figure 2.29: Schematic HV segmentation of short (top) and long (bottom) GE1/1 GEM foils into 40 and 47 strips, respectively, on the foil side oriented towards the drift board. The color scheme indicates which HV segments correspond to the eight η -sectors of the detector.

The design requires that each of the HV segments is supplied individually with HV. This is done by routing a trace around the edge of the GEM foil from a common connection point

780 where the external HV potential is applied to the foil (Figure 2.30). The HV trace is connected
 781 through $10\text{ M}\Omega$ surface-mounted protection resistors to each HV segment (Figure 2.30). The
 782 potential of the other side of the foil is provided by a single connection point. The common con-
 783 nection points are located at the wide end of the foil (Figure 2.30). An additional trace is routed
 784 from HV segments to dedicated test points that facilitate fast continuity and leakage current
 785 tests during chamber assembly. Both long and short chambers have eight η -sectors, which are
 786 physically implemented on the readout board. The color scheme in Figure 2.29 indicates which
 787 HV segments correspond to which of the eight η -sectors of the detector.

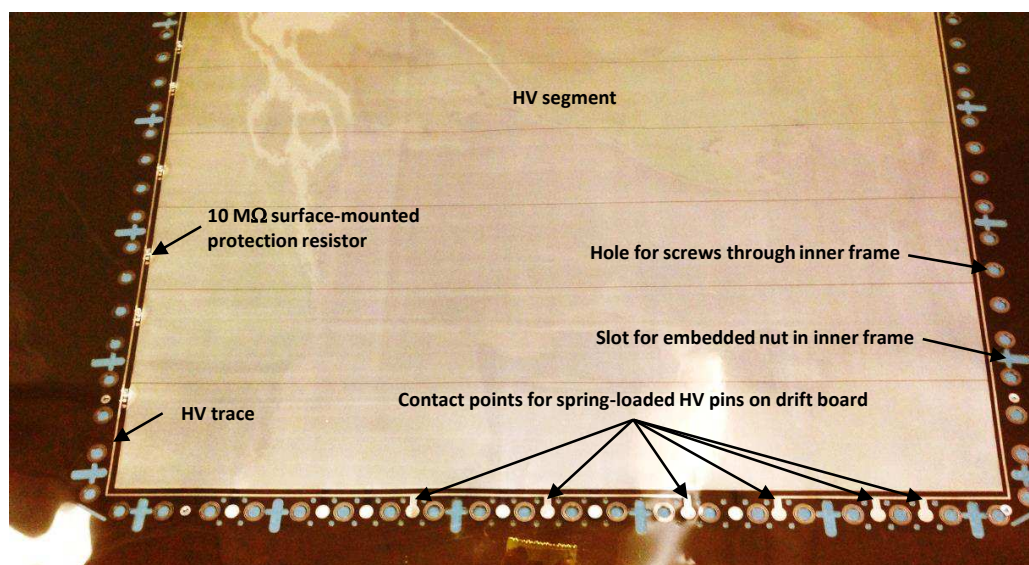


Figure 2.30: GE1/1 GEM foil with traces along the active area that route HV to the HV segments via $10\text{ M}\Omega$ protection resistors.

788 The production of GEM foils is based on photolithographic techniques commonly used by the
 789 printed circuit industry. The copper-clad polyimide substrate (kapton or apical brands) gets
 790 coated on both sides with solid photoresist of $15\ \mu\text{m}$ thickness that the GEM hole pattern is
 791 transferred onto by UV exposure through flexible masks. In order to get good homogeneity
 792 of the hole geometry across the foil, it is very important to keep the alignment error between
 793 the masks on the two GEM foil sides within $10\ \mu\text{m}$. However, since both the raw material
 794 and the two masks are made from flexible material, the manual alignment procedure becomes
 795 extremely cumbersome when the linear dimensions of the GEM exceed 40 cm.

796 A way of overcoming this alignment problem for larger foils is the use of single-mask pho-
 797 tolithography. In this technique, the GEM pattern is transferred only to one side of the raw
 798 material, thus removing any need for alignment. The exposed photoresist is developed and
 799 the hole pattern is used as a mask to chemically etch holes in the top copper electrode of the
 800 GEM foil. After stripping the photoresist, the holes in the top copper electrode are in turn used
 801 as a mask to etch the polyimide (Figure 2.31). This technique has been proven to be a valid
 802 manufacturing technique for making GEMs. It was initially used to build a prototype detector
 803 for a possible upgrade of the TOTEM T1 detector. More recently, the production process has
 804 been further refined, giving greater control over the dimensions of the GEM holes and the size
 805 of the hole rims during the production process. All GE1/1 prototypes mentioned above com-
 806 prise GEM foils produced with this technique at CERN. Effects of the hole shape are also being
 807 explored in simulation studies (see below). Production issues have been studied and single-
 808 mask GEMs are compatible with industrial production using roll-to-roll equipment, which is
 809 a very important aspect of this technique. Consequently, a price reduction for GEM foils is

810 expected from large-scale industrial production.

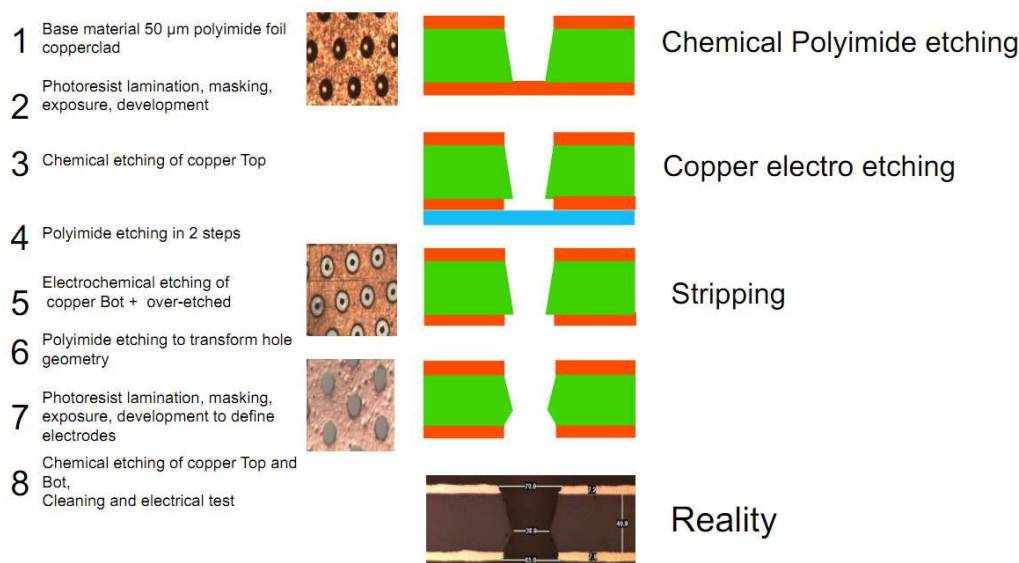


Figure 2.31: Overview of steps in the single-mask etching process for GEM foils.

811 2.3.2 Validation of chamber materials

812 Even though GEM detectors have been proven to perform well in high-rate environments and
 813 to intrinsically resist typical aging phenomena that can occur in gaseous detectors[27], it is still
 814 of paramount importance to carefully validate all materials actually used in the construction
 815 of the GE1/1 detectors. Specifically, materials used in GE1/1 construction need to be tested
 816 for potentially harmful outgassing and radiation hardness. Other system properties that could
 817 affect GE1/1 performance over long time periods, such as interactions with the gas mixture and
 818 gas system components and fluids need similar scrutiny. In addition, standard procedures for
 819 proper quality control of all materials and assembly procedure are needed to ensure uniform
 820 system performance.

821 We have adressed three aspects of material and system validation: 1) impact of water absorp-
 822 tion and desorption on the tensile properties of GEM foils, 2) outgassing of chamber compo-
 823 nents, and 3) a long-term aging test of full-size GE1/1 prototypes.

824 **Impact of water absorption on GEM tensile properties:** The materials studied were pure kap-
 825 ton foils and GEM foils. Unused samples of kapton and GEM foils were analyzed to provide
 826 reference data for subsequent comparison with samples irradiated at the GIF. The state of the
 827 reference samples was determined by means of FTIR (Fourier Transform Infra-Red) analysis,
 828 optical microscopy, and SEM-EDS (Scanning Electron Microscopy - Energy Dispersive Spec-
 829 trometry) characterization (Figure 2.32).

GEM foils interact with humidity both before assembly because of cleaning procedures with deionized water and during operation via atmospheric air intake due to leaks in gas piping. It is important to characterize the GEM foil behaviour as a function of humidity as the amount of water contained in the chambers during the activity of detector can vary. Water content is expected to affect both electrical and mechanical GEM foil properties. Diffusion of water in the GEM foil as a function of time was parameterized according to this formula

$$\frac{M(t)}{M(\infty)} = 1 - \frac{8}{\pi^2} e^{-\frac{D\pi^2 t}{4l^2}} \quad (2.3)$$

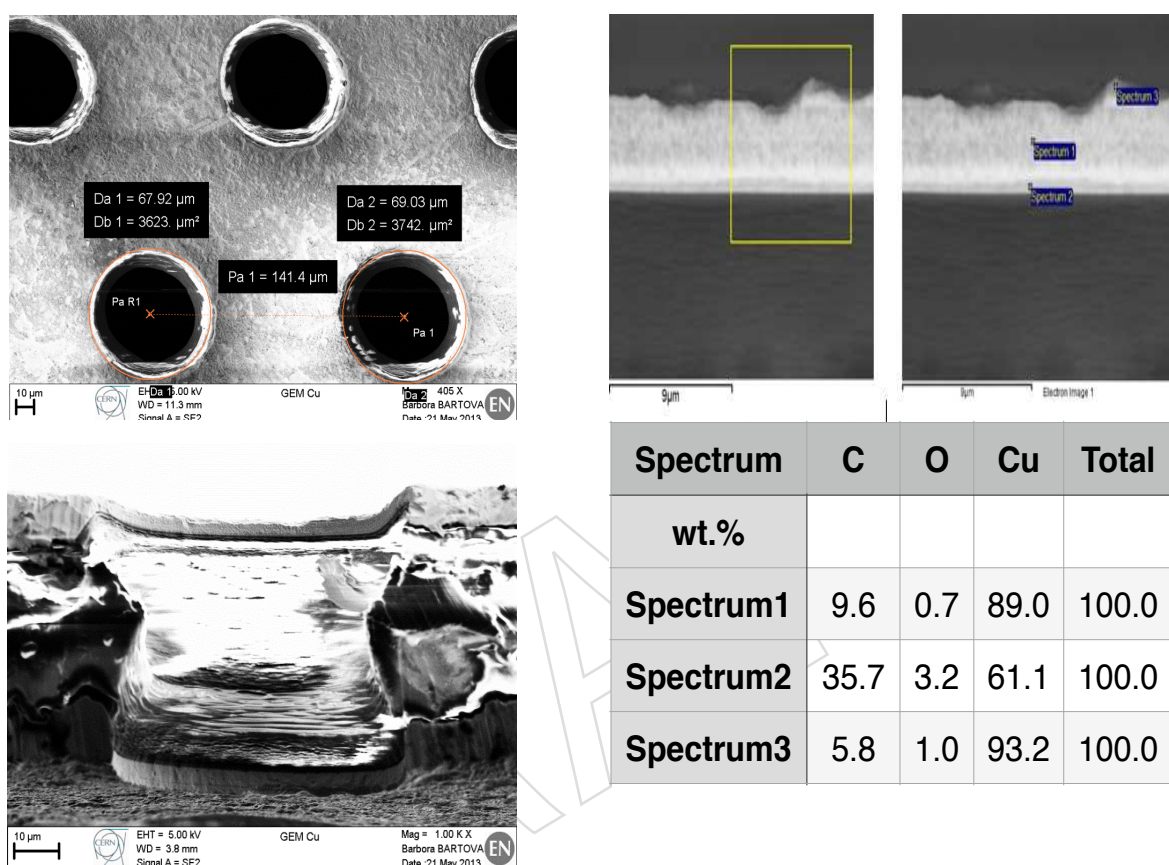


Figure 2.32: Reference microscopy images of the actual geometry of GEM holes to validate shapes and to confirm the absence of anomalous deposits (top left); cross-sectional view of GEM holes showing biconical shape (bottom left). Cross-sectional SEM-EDS analysis of GEM (top right). The table (bottom right) shows SEM-EDS analysis results for an unused sample in the cross-section spots shown in the top right picture. Such analyses provide information on composition of material, thickness and shape of copper coating, which are relevant factors for characterisation and detection of possible aging effects of the GEM foil.

830 where $M(t)$ is the mass of water adsorbed on the polyimide surface and diffusing at time t ,
831 $M(\infty)$ is the mass of water at equilibrium (saturation), D is the diffusion coefficient and ℓ
832 is the half-thickness of the polyimide layer. Two GEM samples with dimensions $10 \text{ mm} \times$
833 15 mm and approximate weight 1080 mg were dried out in an oven at 110°C for 36 hours.
834 Samples were then placed into a vessel with controlled humidity obtained using potassium
835 carbonate saturated solution (45% RH) along with a standard hygrometer to monitor internal
836 conditions. The test was conducted in this controlled environment at $T = (20 - 22)^\circ\text{C}$ and
837 $RH = (45 - 50)\%$. The constant of diffusion of water in the GEM foils D_{GEM} was determined
838 by a best fit of Eq.2.3 to the data. Preliminary results yield $D_{GEM} = (3.3 \pm 0.1) \times 10^{-10} \text{ cm}^2\text{s}^{-1}$,
839 corresponding to an 8.5 hours saturation time.

840 The mechanical response of materials was analysed by uniaxial tensile tests [28–30] for samples
841 of kapton and GEM foils in both dry and wet conditions. Four samples of GEM foils [$10 \text{ mm} \times$
842 $110 \text{ mm} \times 60 \mu\text{m}$ (50 kapton + 5 Cu + 5 Cu)] and four samples of kapton ($10 \text{ mm} \times 100 \text{ mm} \times 50$
843 μm) were dried at 100°C for 36 hours and tested using standard industrial procedures [31, 32].
844 For the test in humidity, the samples were humidified at 99.5% RH at room temperature for
845 7 days prior to measurement. Figure 2.33 shows preliminary results of the tensile tests. As
846 expected, the GEM foil shows a slight increase of its Young's modulus compared to the kapton
847 foil, due to the presence of Cu coating. However, the holes for the electronic multiplication
848 affect the mechanical resistance of the structure, behaving as defects and amplifying local stress.
849 Humidity has a larger effect on kapton foils than on GEM foils. The tensile properties of GEM
850 foils also depend on the extrusion direction. The tension typically applied to a GEM foil in
851 a GE1/1 is on the order of 5 N/cm , which is well within the elastic regime of the GEM foil
852 material. Ongoing characterization of mechanical properties of GEM foils before and after
853 irradiation will provide specific guidelines for proper tensioning of GEM foils in the GE1/1
854 chambers and information on their long-term mechanical stability.

855 **Results from outgassing studies:** Outgassing tests at room temperature and at 50°C are be-
856 ing performed on all chamber materials in contact with the counting gas. The setup for the
857 outgassing test consists of an outgassing box of $1,500 \text{ cm}^3$ equipped with a heating layer and
858 temperature sensors. The gas flows through the box that contains the materials to be tested
859 and is then sent to a Single-Wire Proportional Counter (SWPC) and a $10 \times 10 \text{ cm}^2$ triple-GEM
860 detector. A gas chromatograph can be connected to the input or the output of the gas line to
861 identify possible impurities. The test procedure has two steps. Each material is first flushed
862 with the standard gas mixture Ar/ CO_2 / CF_4 45:15:40 at room temperature for two weeks and
863 then for two more weeks at 50°C to enhance any outgassing. During this period, the relative
864 gain of both SWPC and triple-GEM detector are monitored every ten minutes using a ^{109}Cd
865 energy spectrum. Once a gas gain drop of 5% is observed, the test ends and the material is
866 rejected.

867 So far, two different polyurethane (PU) varnishes used for coating the inner and outer GE1/1
868 frames and the Viton o-ring material have been tested (Figure 2.34). While the Cellpack PU fails
869 the test due to strong outgassing at 50°C , the other PU (Nuvoverne) and the Viton material
870 pass the test and are validated for use in GE1/1 construction. Further outgassing tests will
871 be conducted with the kapton material of the washers used for sealing the drift and readout
872 board screws, pcb material used for drift and readout boards, glass-epoxy frame material, SM
873 resistors mounted directly on GEM foils, and solder used to mount the resistors.

874 **Aging test of GE1/1-IV prototype:** A long-term aging test is performed at the Gamma Irra-
875 diation Facility (GIF) at CERN (Figure 2.35). The GIF bunker contains a ^{137}Cs source of 566
876 GBq that emits gamma rays of 662 keV. A GE1/1-IV prototype detector is placed 30 cm from

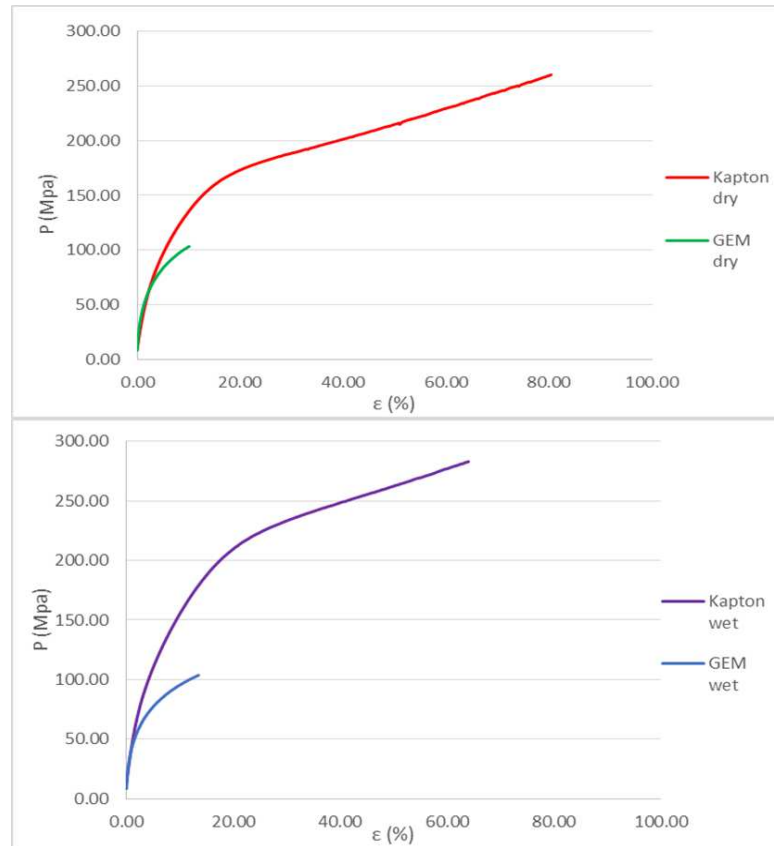


Figure 2.33: Behavior of dry (top) and “wet” (bottom) kapton and GEM foils during tensile stress test.

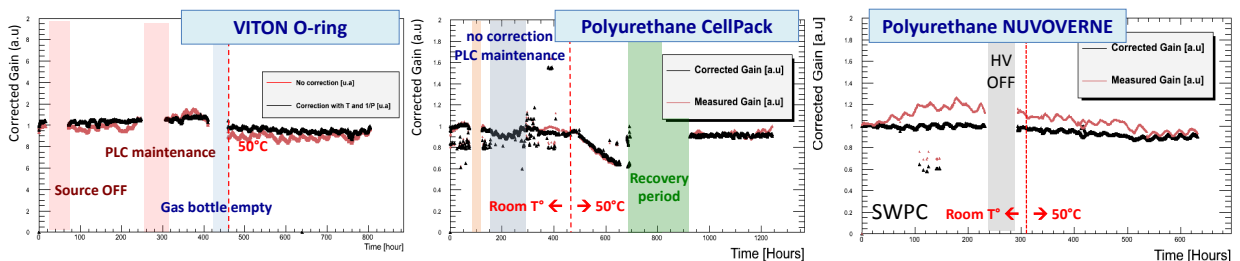


Figure 2.34: Results of outgassing studies of three GE1/1 candidate chamber materials: O-ring material Viton (left); polyurethane varnishes for inner and outer frames - Cellpack (center) and Nuvovern (right).

877 the source, where it receives an incident gamma rate on the order of 100 kHz/cm^2 with an
 878 observed pulse rate from gammas interacting in the detector of a few kHz/cm^2 . Two sectors
 879 of the GEM chamber are irradiated by the ^{137}Cs source while two other sectors are shielded by
 880 lead blocks to provide a reference. Due to scattering and fluorescence effects, it is still possible
 881 to see a signal in these sectors; however, the rate is 15 times lower than in the irradiated parts.
 882 The detector is operated at a gas gain of 2×10^4 and is flushed with the standard $\text{Ar}/\text{CO}_2/\text{CF}_4$
 883 45:15:40 gas mixture at 0.5 liters/hr. The gas system for the test provides a dedicated gas line
 884 into the GIF irradiation bunker. The system is equipped with two SWPCs, one upstream and
 885 one downstream of the GE1/1 chamber. The SWPCs are particularly sensitive to the gas qual-
 886 ity and can quickly indicate the presence of pollutants coming from the gas input (SWPC 1) or
 887 from the GE1/1 detector (SWPC 2). These counters monitor the cleanliness of the gas system.

888 By continuously monitoring the readout current of the GE1/1-IV detector, we can identify possi-
 889 ble aging of the detector. A polymer deposit would affect the gas gain and the discharge
 890 probability. After corrections for fluctuations of the environmental parameters (T,P) are ap-
 891 plied, the normalized gain of the irradiated sectors of the GE1/1-IV prototype shows no drop
 892 after accumulating about 10 mC/cm^2 of charge (Figure 2.36). This charge is accumulated over
 893 a run period of 12 months and corresponds to about two years of GE1/1 operation at the HL-
 894 LHC (see also app. B). As the GIF has been shut down by now, the test setup is being moved
 895 to the new higher-intensity Gamma Irradiation Facility (GIF++) at CERN, where the aging test
 896 will continue with a goal of reaching $\geq 100 \text{ mC/cm}^2$.

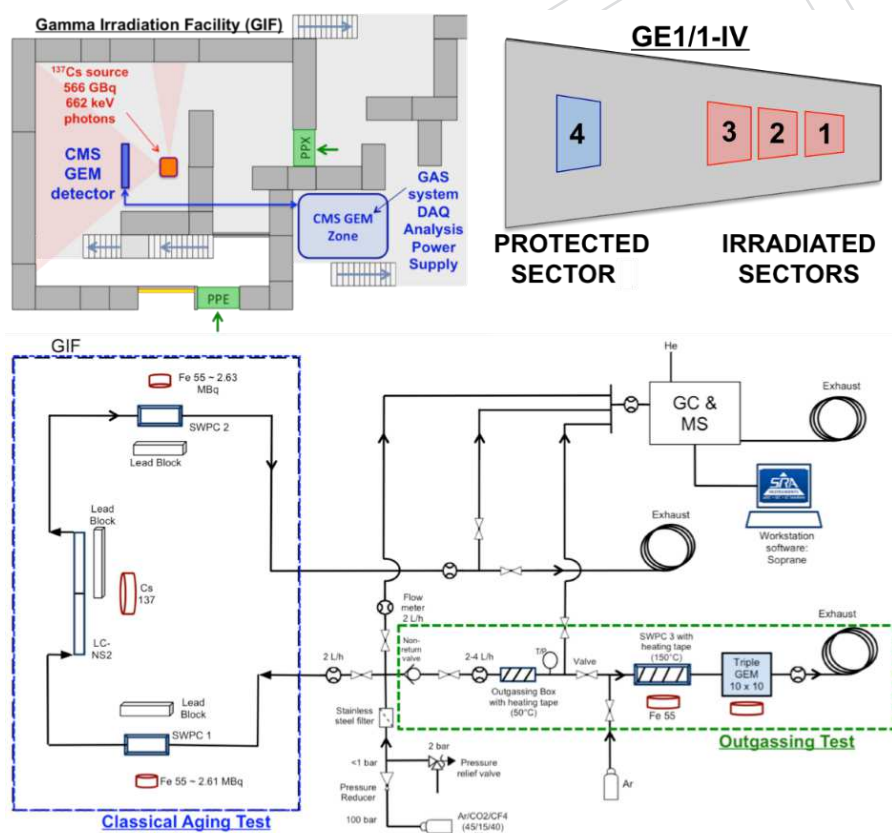


Figure 2.35: Schematic view of the aging test setup at the Gamma Irradiation Facility (GIF) at CERN and of the irradiated and shielded sections of the GE1/1 detector under test (top). Overview of the gas system for the classical aging test in blue and the outgassing studies in green (bottom).

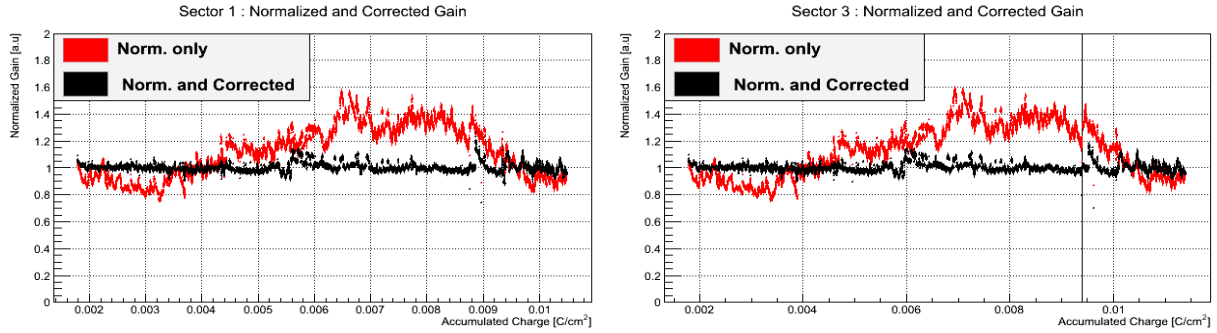


Figure 2.36: Corrected and normalized gain in irradiated GE1/1-IV sectors 1 (left) and 3 (right) as a function of the total charge accumulated in the detector during the GIF aging test. Note that the result for sector 2 (not shown) looks very similar. No aging effects have been observed after a total accumulated charge of about 10 mC/cm^2 .

Table 2.3: Summary of layer structure and materials of a single GE1/1 chamber.

Layer	Material	Thickness (mm)
Protective cover	Al	1.0
Cooling pipe	Cu (filled with H ₂ O)	8 external \varnothing , 6 inner \varnothing
Cooling pads	Cu	1.0
GEB board	Cu/FR4	0.140/0.856
Readout board	Cu/FR4/Cu	0.035/3.2/0.035
Induction gap	Ar/CO ₂ (/CF ₄)	1.0
GEM 3	Cu/polyimide/Cu	0.005/0.050/0.005
Transfer gap 2	Ar/CO ₂ (/CF ₄)	2.0
GEM 2	Cu/polyimide/Cu	0.005/0.050/0.005
Transfer gap 1	Ar/CO ₂ (/CF ₄)	1.0
GEM 1	Cu/polyimide/Cu	0.005/0.050/0.005
Drift gap	Ar/CO ₂ (/CF ₄)	3.0
Drift board	Cu/FR4/Cu	0.035/3.2/0.035

897 2.3.3 Mechanical design

898 This section describes the mechanical design of the GE1/1 chambers in full detail.

899 2.3.3.1 Design Overview

900 An overview of the mechanical design of a single trapezoidal GE1/1 chamber is shown in
 901 Figs. 2.37 and 2.38. The main components and materials of a single GE1/1 chamber are listed in
 902 Table 2.3. The assembly and sealing of the detector are entirely mechanical. No glue is applied
 903 during assembly, which makes it possible to open a detector again for repairs if needed. It also
 904 speeds up the assembly of the chamber since there are no wait times due to curing of glue.

905 The three GEM foils are sandwiched at their edges between four layers of a thin frame made
 906 from halogen-free glass epoxy (ISOLA DE156) that is composed of 8 individual pieces per layer
 907 (Figs. 2.39). The thicknesses of the different frame layers define the spacings between GEM
 908 foils as well as between GEM foils and drift/readout boards as follows: Drift gap / GEM1-
 909 GEM2 transfer gap / GEM2-GEM3 transfer gap / induction gap : 3/1/2/1 mm. The stack
 910 is held together by numerous small M2×6 stainless steel screws. They penetrate all frame

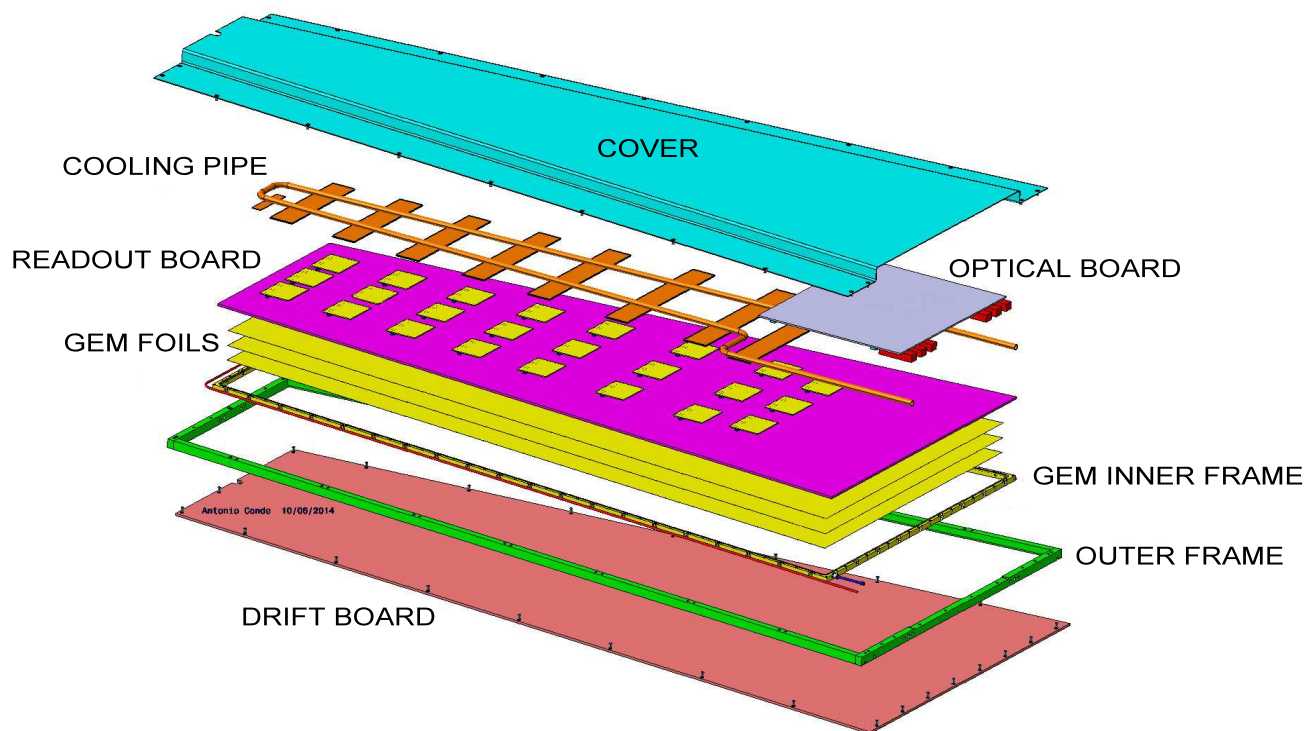


Figure 2.37: Exploded view of the mechanical design of a single GE1/1 chamber.

911 layers and foils about every centimeter and are tightened against small threaded M2 brass
 912 inserts (Figure 2.39). Using inserts to counter the screws avoids loosening macroscopic and
 913 microscopic glass epoxy particulates from the frames as was observed in earlier prototypes
 914 where screws were threaded directly into the frame material. Frame pieces are coated with
 915 Nuvovern polyurethane varnish before assembly. Both those measures ensure that no glass
 916 epoxy particulates detach from the frames during assembly, fall onto GEM foils, and potentially
 917 produce electrical shorts in the GEM holes. The screw heads are conical with flat outer surfaces
 918 and are sunk into counterbores in the frames that surround the through-holes during tightening
 919 (Figure 2.39 left). Similarly, the nuts are sunk into counterbores on the frames (Figure 2.39
 920 center), so that the screws and nuts are flush with the top and bottom surfaces of the inner
 921 frame after the stack is assembled.

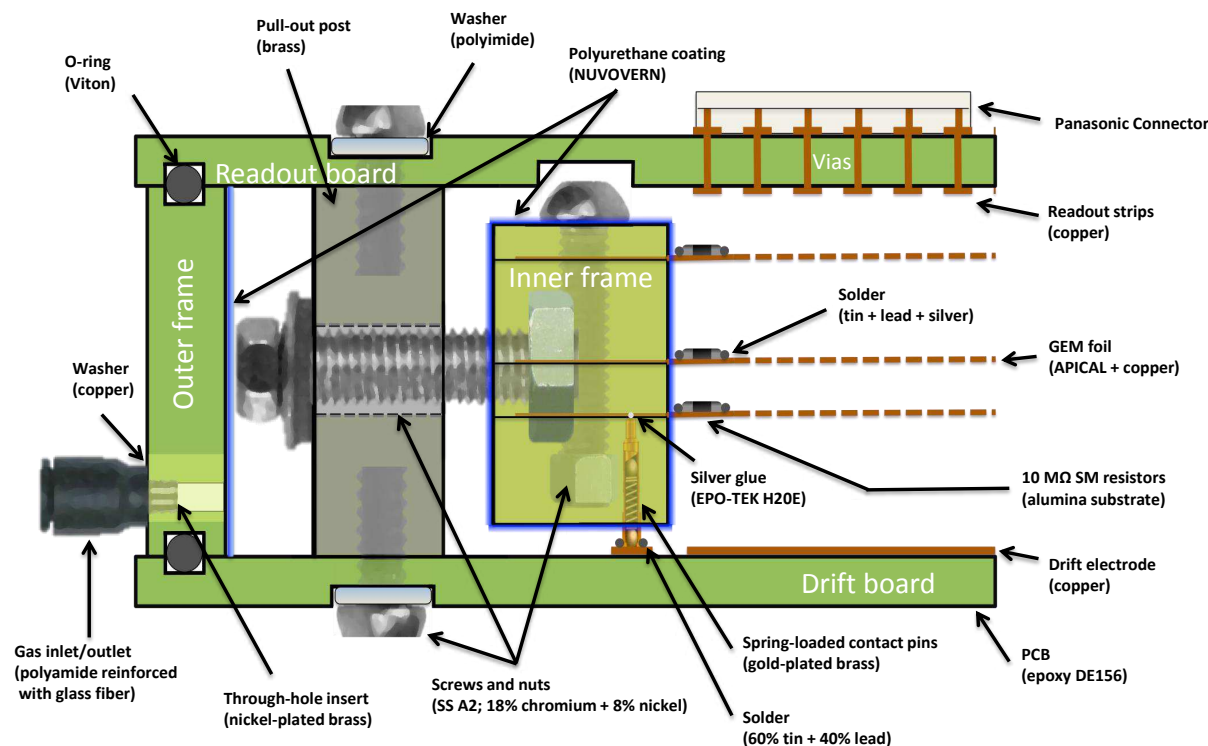


Figure 2.38: Cross section through inner and outer chamber frames and GEM foils that shows how the GEM foils are mounted within the GE1/1 chamber so that they can be mechanically tensioned against the brass pull-out posts without deforming the drift or readout boards. The materials of all chamber components are specified.

922 Additional square stainless steel nuts are embedded into the frames every few centimeters
 923 with the axes of their threaded holes oriented perpendicular to the inner frame and GEM foil
 924 surfaces (Figs. 2.38, 2.39 right). These nuts counter M2.5 × 10/× 8 stainless steel screws that are
 925 inserted into small brass posts, so-called “pull-outs”, which are located within the gas volume.
 926 When the pull-out screws are tightened manually, the GEM foils in the stack are tensioned as
 927 the inner frame is being pulled outwards towards the pull-outs. Due to the large number of
 928 screws, the GE1/1 can be assembled with good manual control over the GEM tension so that
 929 the foils can be tensioned as uniformly as possible. The relative large size of the square nuts

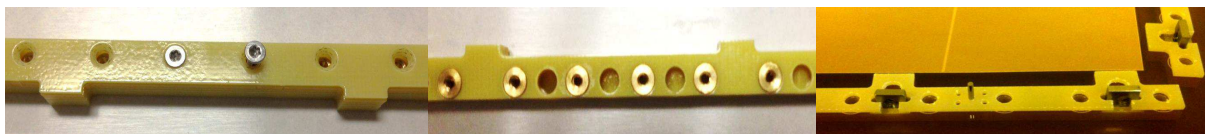


Figure 2.39: Section of the inner frame of a GEM stack with stainless steel screws and counterbores on one side (left) and embedded counteracting brass nuts on the other (center). The tabs on the frame are where vertically embedded square nuts (right) are located that are used for tensioning the GEM stack against brass pull-outs. The shiny frame surface (left) is due to its coating with Nuvovern polyurethane varnish.

930 and their large number ensure that the force on the frame at each pull-out is kept as low as
 931 possible to avoid any long-term local deformations of the frame due to the stress. The pull-
 932 outs are in turn bolted down onto the pcb that provides the drift cathode with two A2 stainless
 933 steel $M2.5 \times 4/\times 8$ screws that are sealed with polyamide washers against the drift board. With
 934 these nuts and screws, the GEM stack is attached to the drift pcb.

935 A large outer glass-epoxy frame machined from a single piece and placed around the tensioned
 936 GEM stack and the brass pull-outs provides the border of the gas volume (Figure 2.40). The
 937 frame has numerous wide notches to accomodate the brass pull-outs. It is also coated with
 938 Nuvovern polyurethane varnish before assembly to seal in particulates. On both sides of the
 939 outer frame, a Viton O-ring is placed into a groove that runs around the entire outer frame to
 940 seal it. The anode readout board is placed on top of this outer frame and attached to the brass
 941 pull-outs with A2 stainless steel $M2.5 \times 4/\times 8$ screws which are sealed with polyamide washers
 942 against the readout board in the same way as the drift board screws. This sandwiches the outer
 943 frame tightly between the drift board and readout board and holds it in place essentially by
 944 friction. It provides a solid gas barrier that is only penetrated by two small holes in diagonally
 945 opposed corners to provide the gas inlet and outlet for the chamber.

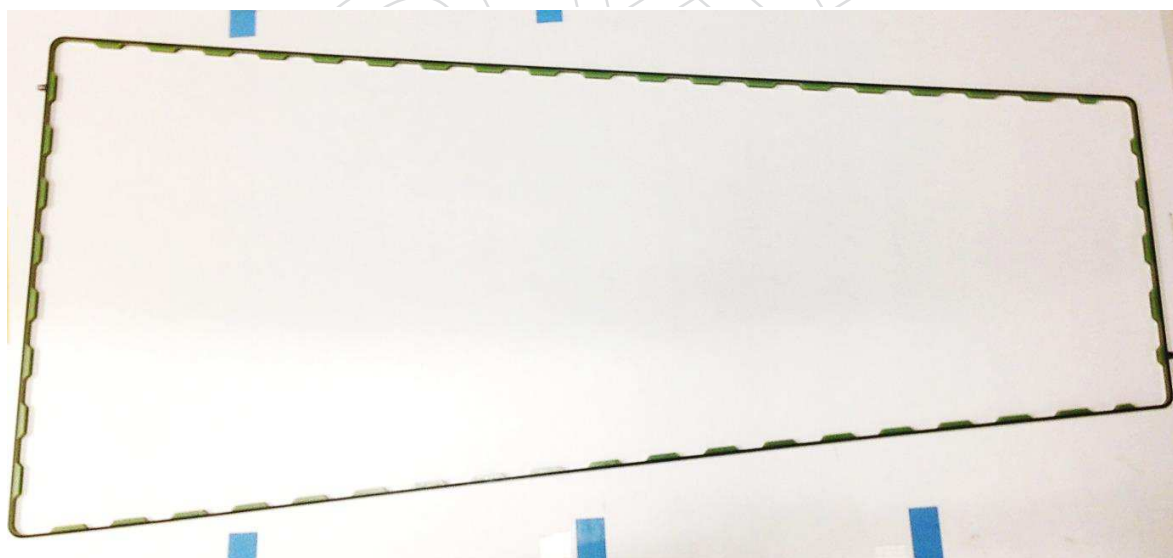


Figure 2.40: Outer gas frame of GE1/1-V with O-ring inserted. The frame is made from a single solid piece of halogen-free glass epoxy (ISOLA DE156). Gas inlet and outlet are visible in the top left and bottom right corners.

946 The drift board features a single drift cathode on its inner side and a solid ground plane on
 947 the outside of the chamber for rf shielding purposes. It provides connections to external high

948 voltage supply lines via HV noise filtering circuitry. The drift board routes a total of seven
949 different potentials to the various GEM electrodes and to the drift cathode.

950 The readout board has 24 high-density header connectors (Panasonic part no. AXK6SA3677YGJ)
951 with 130-pins on its outside to interface the radial readout strips on the inside to the VFAT2 hy-
952brids that plug into the readout board from the outside. The connection is made with vias in
953the readout board that need to be sealed. A kapton coverlay attached with pure epoxy glue
954or alternatively prepreg material are being investigated by the CERN pcb workshop for that
955purpose. A third sealing method is to fill the vias with metal, which is the most expensive
956solution. The VFAT2 hybrids also plug into a second full-size pcb, the GEM Electronics Board
957(GEB), that is attached directly on top of the readout pcb. The GEB carries the digital output
958signals from all VFAT2 hybrids to the wide end of the chamber for processing and transporting
959to the Trigger/DAQ as described in detail in the chapter on electronics and DAQ. The GEB
960has cut-outs that allow the 130-pin connectors on the readout board to reach through. Copper
961pipes are routed on top of the GEB to provide coolant to the VFAT hybrids.

962 Finally, an aluminium frame is mounted on the drift board all around the outer edge (Fig-
963ure 2.37). An aluminium sheet with a thin central chimney along the long axis of the chamber
964is attached to that aluminium frame to cover the entire assembly from the readout side. To-
965gether, frame and cover provide solid protection for the on-chamber electronics and utilities.

966 2.3.3.2 Drift board design

967 Figure 2.41 shows the mechanical design and dimensions of the short and long drift boards of
968 GE1/1-VI-L. A close-up view (Figure 2.42) of the wide end of the drift board side that faces
969the chamber interior shows details of the on-board HV circuit traces for the HV noise filtering
970section, pads for a HV divider, and pads for the spring-loaded pins that make the electrical
971connections to the GEM foils. This design can be easily modified to allow for multi-channel HV
972supply lines instead of the HV divider. The design is asymmetric because the central section of
973the chamber needs to accommodate the on-chamber readout electronics.

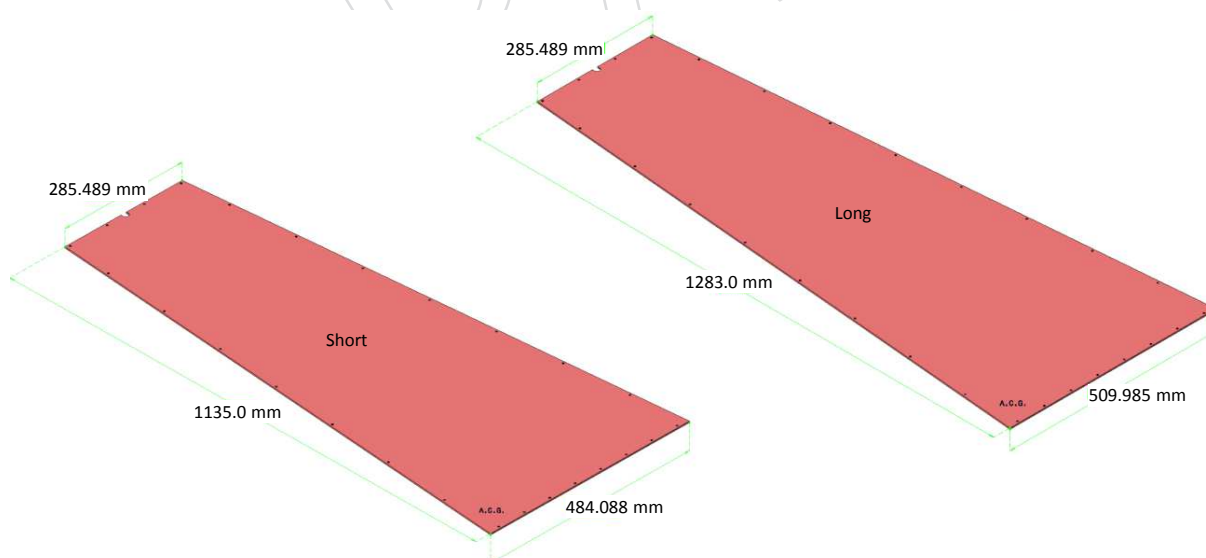


Figure 2.41: Design and dimensions of the drift boards for short (left) and long (right) GE1/1 chambers.

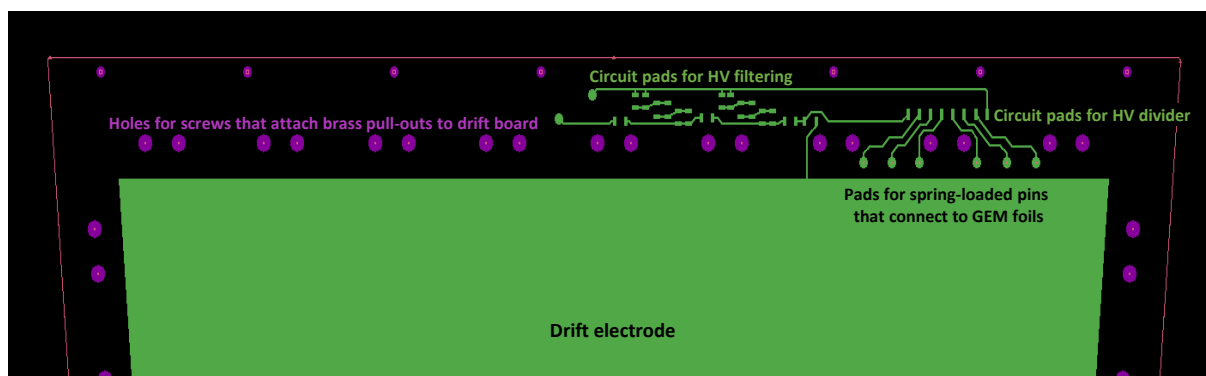


Figure 2.42: Close-up of the wide end of the GE1/1-VI-L drift board design with HV circuit traces.

974 2.3.3.3 Readout board design

975 The inner side of the readout board, i.e. the side that faces GEM3, features 3,072 truly radial
 976 readout strips arranged in eight η -sectors. The vertex of the strips coincides with the beam
 977 line. The active area covered by the strips subtends an angle of 10.15° , which allows for an
 978 overlap of 1.3 mrad (equivalent to 2.8 strips) between the active areas of adjacent chambers.
 979 The strips have a width of $230 \mu\text{rad}$ and are arranged with a pitch of $463 \mu\text{rad}$. Each η -sector
 980 comprises 384 strips that in case of the long chamber vary in lengths from 11 cm at the short
 981 end (η -sector 1) to 19 cm at the wide end (η -sector 8). In addition, a couple of ground strips of
 982 the same dimensions are placed along the outer edges of the active area to prevent distortion
 983 of the electric field in the induction gap as the GEM foils cover a slightly larger area than the
 984 readout strips. The baseline design for the strip material is gold-plated copper produced in
 985 an electroless nickel / immersion gold (ENIG) process that is standard for pcb's. Figure 2.43
 986 shows a close-up of the design of the short end of the readout board on that side. The smallest
 987 sector, i.e. η -sector 1, and a portion of η -sector 2 are shown. The view on the right of Figure 2.43
 988 zooms in on the center of the strips in sector 1, where the vias are located that connect the
 989 strips to the outside of the readout board. On that outer side, traces are routed from the vias to
 990 24 130-pin Panasonic connectors that the front-end VFAT3 hybrids plug into (Figure 2.44). A
 991 set of three connectors serves each η -sector. Two of the pins on each Panasonic connector are
 992 connected to chamber common while the other 128 pins are connected to readout strips. The
 993 six tabs on the edges of the two long sides of the board allow attaching the GEB to the readout
 994 board (Figure 2.45) after the chamber has been closed without compromising the active gas
 995 volume of the detector.

996 2.3.4 Foil stretching

997 The foils in the GEM stack are tensioned and made taut by uniformly pulling the stack outward
 998 against the brass pull-outs. This is achieved by manually tightening the screws that go through
 999 the holes in the brass pull-outs (Figure 2.46) and that are countered by the nuts embedded in
 1000 the inner frame that surrounds the GEM stack (Figure 2.38). The screws are tightened to a
 1001 torque of about 0.1 Nm. The end result are tautly stretched GEM foils closely surrounded by
 1002 the outer gas frame (Figure 2.47).

1003 Tolerances inherent in this method for stretching GEM foils and their relative positioning have
 1004 an impact on the uniformity of gas gain and timing response. Previous studies on small GEM
 1005 foils (by the LHCb experiment [33]) specify the required mechanical tolerances of gap dimen-
 1006 sions and uniformity to $\pm 10\%$, e.g. $\pm 100 \mu\text{m}$ for the 1 mm transfer and induction gaps, which

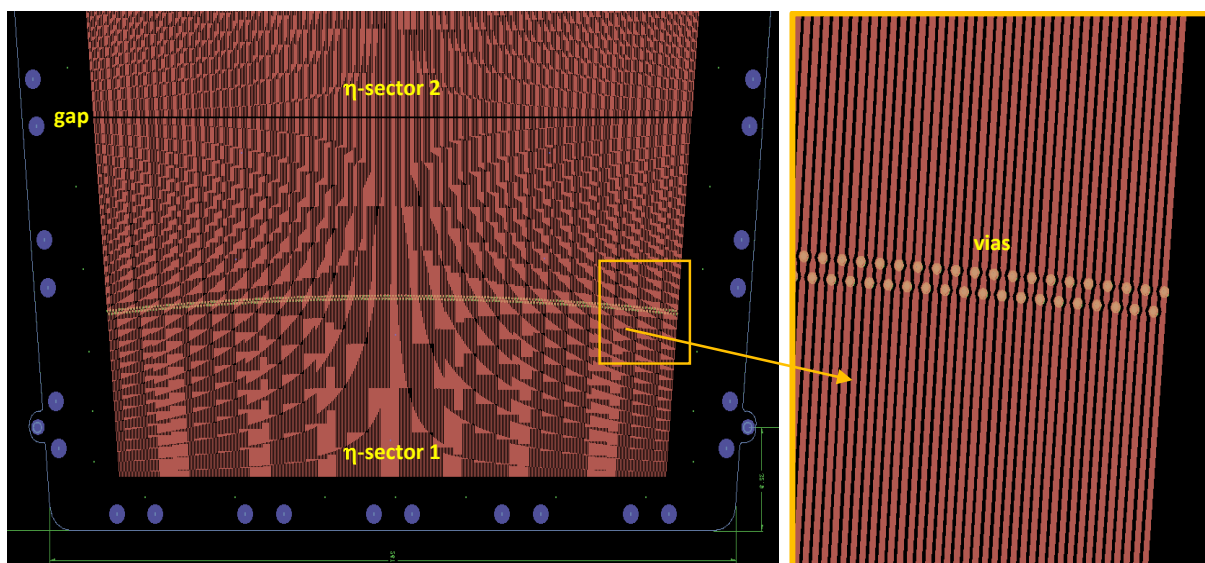


Figure 2.43: Design of the readout board for the long chamber GE1/1-VI-L (left). Shown is the inner side that faces into the gas volume opposite GEM3 at the short end of the board. Due to the high density of strips (384 readout strips in each sector), individual strips are not visible at this resolution. Note that the “hyperbolic” geometric pattern is an artifact of the display on a screen. Strips are visible when zooming in (right). The circular structures on each strip are vias that connect the strips to the outside of the board. The blue circles around the edge indicate positions of holes for screws that attach the readout board to the brass pull-outs.

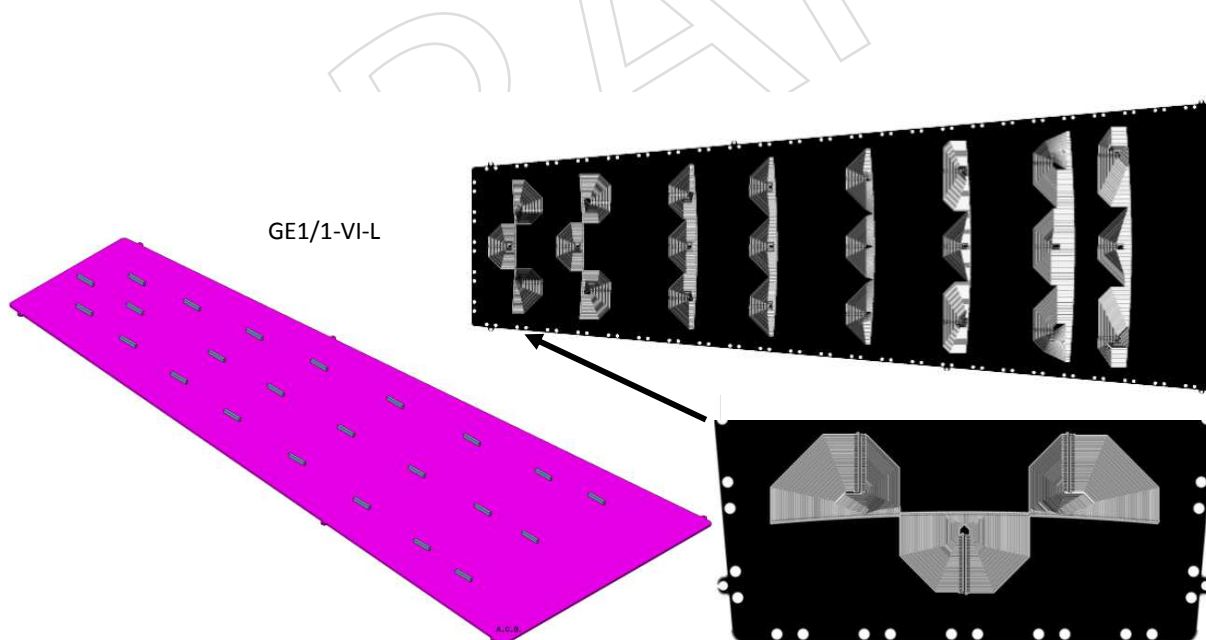


Figure 2.44: Design of the outer side of the readout board for the long chamber GE1/1-VI-L showing Panasonic connectors for VFAT2 hybrids (left) and traces from vias to Panasonic connectors (right).

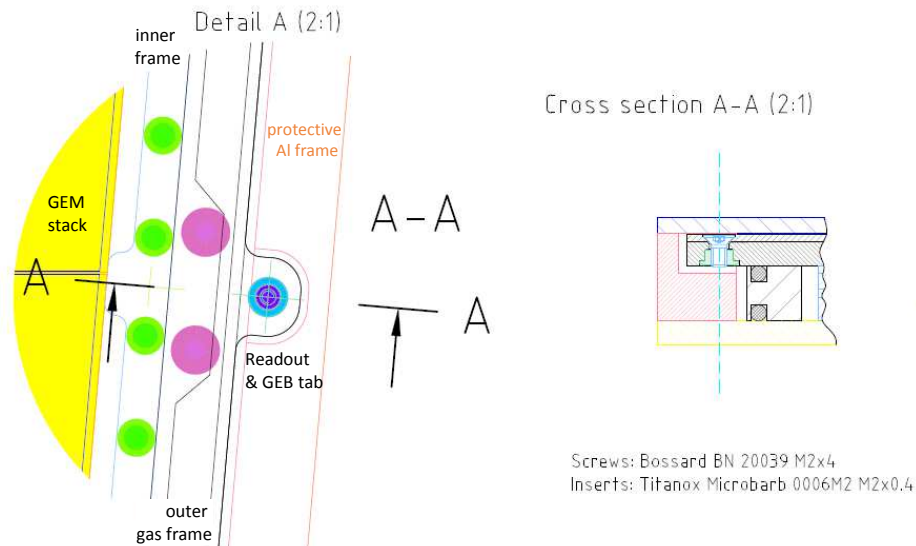


Figure 2.45: Design of tab for single screw (blue) that attaches GEB to readout board in top view (left) and cross section (right). The protective outer aluminium frame is notched to allow space for the tabs.

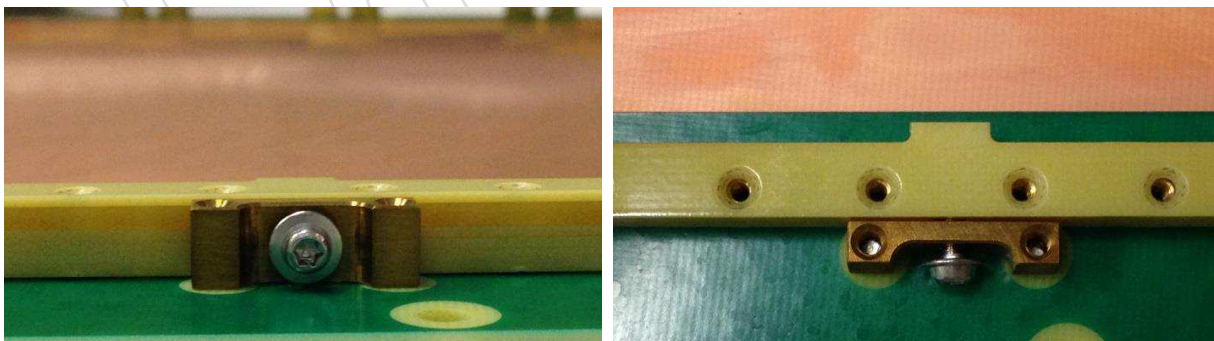


Figure 2.46: Brass pull-out with screw inserted into inner frame for tensioning the GEM foils in the stack in side view (left) and top view (right).

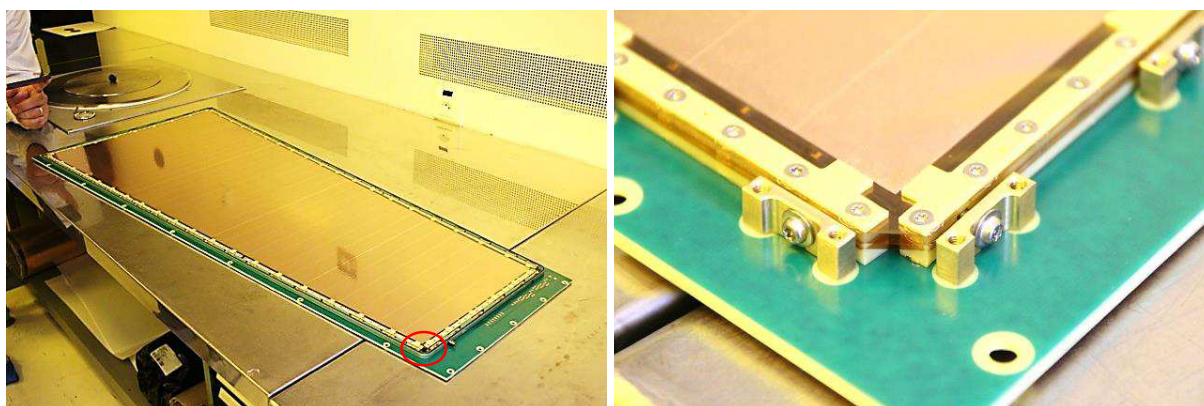


Figure 2.47: GE1/1-V prototype with GEM foil stack tensioned against brass pull-outs, mounted onto drift board, and surrounded by outer frame (left). The clear optical reflections in the top foil indicate that the stack is uniformly taut. The active chamber volume is now ready to be closed with the readout board. To help with scale reference, one of the editors (LB) of this chapter is lending a hand. A detail (red circle) of the stack is given that shows the gap between inner frame sections in one corner and the pull-outs (right).

1007 corresponds to a 6% gain variation. In case of Ar/CO₂/CF₄ gas mixture, there is a slight depen-
 1008 dence of the electron drift velocity on the electric field which translates into a small dependence
 1009 of the timing performance on both mechanical precision and tension stability of the GEM foil
 1010 stack.

1011 Consequently, it is crucial to ensure precision during assembly, to determine reliable quality
 1012 control (QC) procedures for mechanical tension, and to study the long-term stability of the
 1013 mechanical foil tension. The assembly precision will be ensured by setting specifications on
 1014 the torques applied to the pull-out screws during assembly. The specifications will be derived
 1015 with a reference chamber for which the foil flatness will be monitored by Moirè interferometry
 1016 (see below). We expect that interference patterns will assure flatness and uniformity to about
 1017 30 μ m in the plane orthogonal to the foil. Long-term stability will be guaranteed by optical
 1018 strain gauges. The technique has been applied to several detectors in HEP for strain and de-
 1019 formations, temperature and humidity measurements, with a great deal of experience in the
 1020 collaboration [34–36].

1021 2.3.5 Gas distribution within chamber

1022 The gas distribution inside the detector should not give rise to areas with very low gas flow that
 1023 could result in pockets or regions where potentially harmful gas contaminants can accumulate.
 1024 We evaluate the velocity field inside a GE1/1 detector design with a finite-element simulation
 1025 using ANSYS, an engineering simulation software package for computer-aided engineering.
 1026 A 3D CAD model of a (somewhat enlarged) GE1/1 detector geometry was developed and
 1027 meshed by means of standard tetrahedrons using the ANSYS mesher package. The presence
 1028 of the GEM foil stack is ignored in this basic model. The mesh is refined accurately in highly
 1029 curved and sharp parts in order to control rounding errors arising from the discretized domain
 1030 equations. Ultimately, the model is tuned with more than 500k elements.

1031 The analysis is performed in a steady-state laminar regime with the ANSYS CFX module to
 1032 solve the discretized Navier-Stokes equations [37–39] within the domain. The choice of laminar
 1033 flow is based on the fact that the Reynolds number (Re) is very low in this case, $Re = \frac{\rho|\vec{v}|L}{\mu} \simeq$

1034 150, where L is the characteristic linear dimension (length traveled by fluid), μ the dynamic
 1035 viscosity of the fluid. Boundary conditions in terms of mass flow are applied to the inlets and
 1036 outlets; the walls are considered as having no-slip flow.

1037 We simulate the gas flow behaviour inside this (enlarged) GE1/1 chamber geometry with a sin-
 1038 gle inlet and a single outlet on diagonally opposed corners (Figure 2.48). The gas flows broadly
 1039 diagonally and creates two areas with lower velocity fields near the corners without inlet or
 1040 outlet. However, we still find laminar flow in those areas and we expect that the presence of
 1041 the GEM stack will redirect more gas flow towards those corners. This justifies adopting this
 1042 simplest possible internal gas distribution for the GE1/1 design.

1043 The gas volumes inside the GEM stack, i.e. between GEM foils, are directly accessible to gas
 1044 flow and gas diffusion via the gaps between the eight sections of the inner gas frame and
 1045 through the GEM holes. Gas flow through GEM holes was verified experimentally with a
 1046 simple test. The two halves of a $10 \times 10 \times 1 \text{ cm}^3$ volume are separated by a septum made from
 1047 a GEM foil (Figure 2.49). The gas inlets are organised in such a way that it is possible to flush
 1048 two different gases into the two halves. The gas outlets also collect the gases of the two halves
 1049 separately. The two outgoing gases are sent to a gas chromatograph (GC) for analysis. With
 1050 this arrangement, it is impossible that the two gases mix unless they flow or diffuse through
 1051 the GEM holes. In the test Argon and CO_2 flowed into the chamber with a flow rate such that
 1052 the volume had an overpressure of about 5 mbar, similar to the one expected in the GE1/1
 1053 chambers. The result of the GC gas analysis shows that the output gases in both halves are
 1054 basically a perfect Ar/ CO_2 50:50 gas mixture. This mixture is found right from the start of
 1055 flushing, which indicates that the mixing is mainly due to flow and not due to diffusion. This
 1056 demonstrates that the gas mixture can freely flush the whole GE1/1 gas volume with the GEM
 1057 foils presenting no significant obstacle to the flow.

1058 2.3.6 On-chamber HV distribution to GEM foils and drift electrode

1059 The electrical HV connections to the GEM foils are made via spring-loaded pins (Figure 2.50)
 1060 that are soldered onto the drift board (Figure 2.42) and that push against corresponding con-

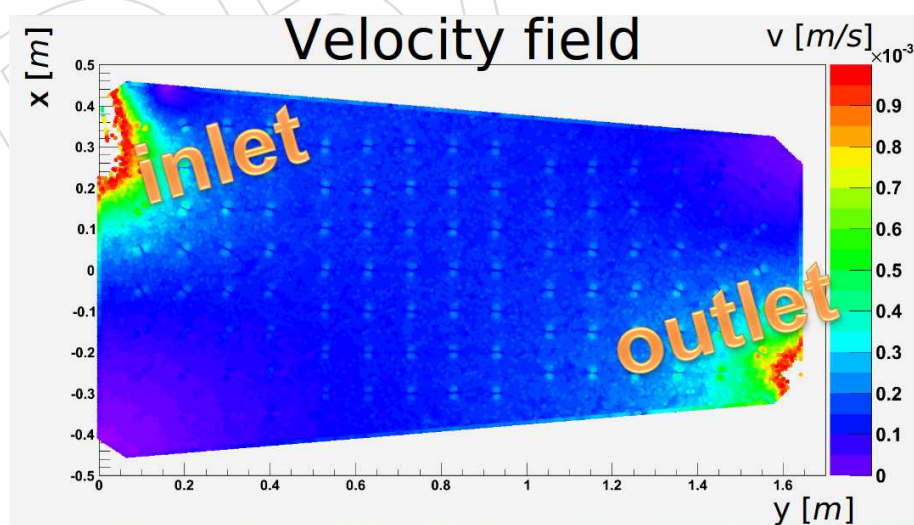


Figure 2.48: Gas flow distribution inside a (somewhat enlarged) GE1/1 detector volume with one inlet and one outlet according to ANSYS simulation. The effect of the GEM foil stack is ignored here. The butterfly-shaped regions of higher flow are an artifact in the simulation due to the overall very low gas flow velocity.

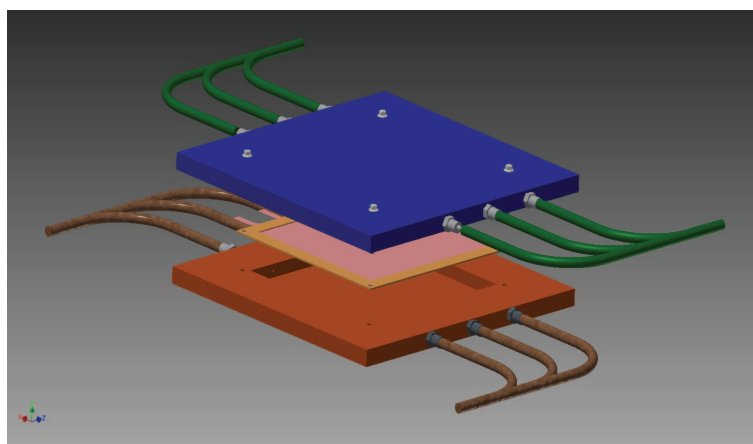


Figure 2.49: Setup for measuring the gas flow through the GEM holes.

1061 nection pads on the GEM foils (Figure 2.30). For the HV pins to reach GEM foils 2 and 3, the
 1062 corresponding connection pads are cut out of GEM foil(s) 1 and 2 during assembly. The drift
 1063 electrode is powered directly off of the HV line that enters the drift board (Figure 2.42). Below
 1064 we discuss two basic schemes for powering all seven electrodes (drift electrode plus two sides
 1065 of each of the three GEM foils) of the GE1/1 with HV.

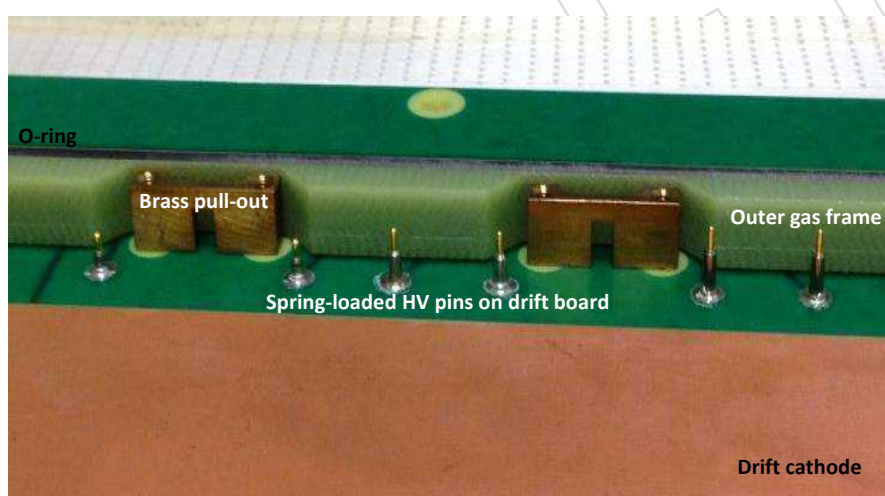


Figure 2.50: Six spring-loaded pins are soldered to the drift board for making electrical HV connections to corresponding contact pads on the GEM foils. Note that the three pairs of pins have different heights so they can properly reach the three GEM foils. Shown here is the arrangement for the GE1/1-V prototype.

1066 2.3.6.1 Single-line HV input plus voltage divider

1067 A simple voltage divider has been used very successfully during the R&D phase of the project
 1068 to produce the seven needed potentials directly on the chamber (Figure 2.51). The voltage is
 1069 divided down from one HV input line that provides the drift potential, i.e. the most negative
 1070 potential. The design of the voltage divider evolved from a large board with discrete resistors to
 1071 a small ceramic device with single-inline pin (SIP) configuration that is soldered onto the drift
 1072 board (Figure 2.52). The current through the divider chain produces a voltage drop across every

1073 resistor which creates the electric potentials needed to power the elements of the detector. The
 1074 electric fields produced with the HV divider in the various inter-electrode gaps of the triple-
 1075 GEM detector can be easily calculated from $E_{gap} = \frac{I_{div} R}{x}$, where I_{div} is the divider current, R is
 1076 the resistance across the gap in question, and x is the corresponding gap distance.

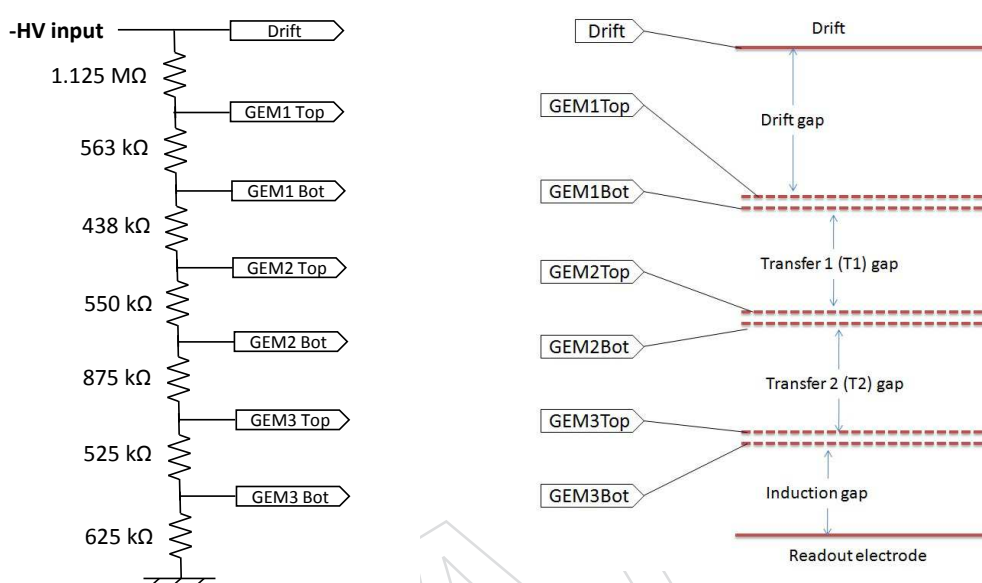


Figure 2.51: HV divider circuit diagram (left) for the 3/1/2/1 mm gap configuration and corresponding connections to GE1/1 chamber electrodes (right). Note that additional 10 MΩ protection resistors are located on the segmented sides of all GEM foils.

1077 The advantage of this design is its simplicity. Only one channel of an HV power supply is
 1078 needed to power the entire chamber via a single cable. The power supply has to supply about
 1079 $800 \mu A$ of bias current I_{div} that flows through the HV divider. The strong disadvantage is that
 1080 if a single HV segment on one of the GEM foils develops a short, e.g. due to a discharge, then
 1081 the corresponding resistor on the HV divider and consequently the entire GEM foil is shorted
 1082 out since all HV segments are connected to one pin on the HV divider. This kills the gain on
 1083 that GEM foil and renders the entire chamber unusable. When such an incident occurred during
 1084 the R&D phase and the short on a GEM foil could not be fixed, then typically the protection
 1085 resistor on the offending HV segment was removed to isolate that segment so that the rest of
 1086 the chamber could still be operated. Obviously, this kind of a remedy is not practical for the
 1087 full GE1/1 system as it required opening the chamber. Instead, the HV powering system must
 1088 be designed so that it is robust enough to inherently tolerate single-segment HV shorts so that
 1089 it can keep operating without any intervention. This can be achieved with multiple-line HV
 1090 input to the chamber.

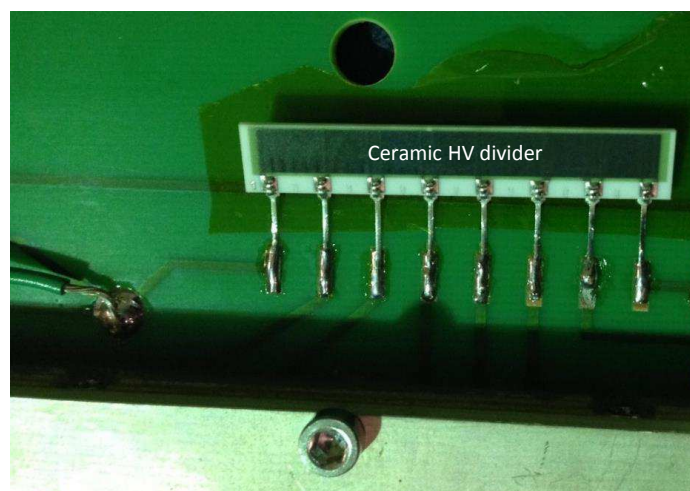


Figure 2.52: Miniaturized implementation of the HV divider on a ceramic substrate with single-inline pin configuration soldered onto the drift board of a GE1/1-III prototype.

1091 **2.3.6.2 Multiple-line HV input for production chambers**

1092 In this case, the seven required potentials are brought on individual HV lines to the drift board
1093 and routed on-board to the drift electrode and GEM foils (Figure 2.53). This requires installation
1094 of an additional multi-pin HV connector on the drift board. Seven HV cables must be routed
1095 from each chamber to a HV distribution board.

1096 This power configuration imposes two important requirements on the HV supply system. In
1097 case of a short in one HV segment of a GEM foil, the HV supply system must be able to sustain
1098 the voltage across that foil and simultaneously provide the current that is then flowing through
1099 the 10 M Ω protection resistor on the shorted HV segment. This will allow continued operation
1100 of the chamber despite the presence of a short in one (or more) segments. The second require-
1101 ment is that the ramping (up or down) of the potentials on the two sides of all GEM foils that
1102 are now provided independently by different HV channels is very well synchronized, moni-
1103 tored, and safe-guarded so that the voltages across the GEM foils can never exceed a maximum
1104 given value (about 500V) – even for a very short time. Otherwise, even a brief temporary over-
1105 voltage could lead to sparking across the GEM foils that could destroy it. Designs of the HV
1106 supply and distribution system that address these concerns are discussed below in the section
1107 on power systems in Ch. 7.

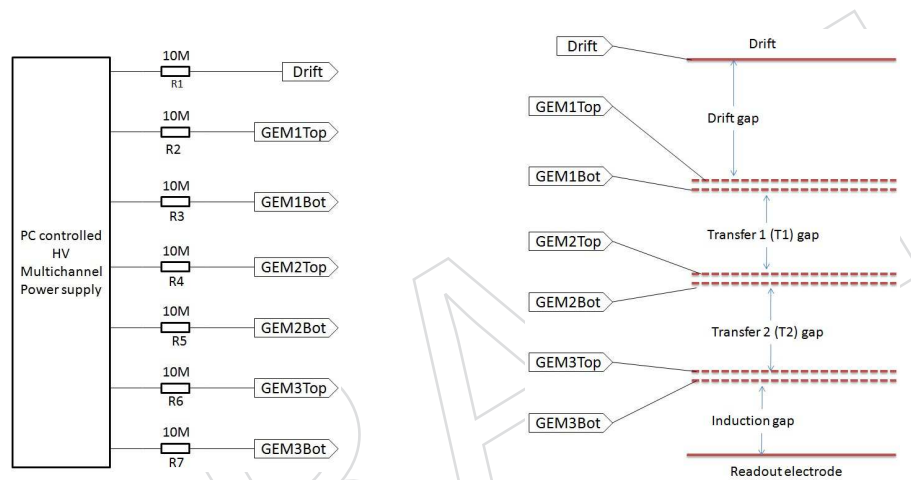


Figure 2.53: Multi-channel HV supply (left) and corresponding connections to chamber electrodes (right). Note that the 10 M Ω protection resistors are located directly on the GEM foils.

DRAFT

1108 **Chapter 3**

1109 **Electronics**

1110 **Editors:** P. Aspell, G. De Lentdecker

1111 **Contributors:** P. Aspell, G. De Lentdecker, G. De Robertis, M. Dabrowski, F. Loddo, J. Talvitie

1112 **3.1 Electronics system overview**

1113 This chapter focuses on the hardware used for the treatment and readout of the detector signal
1114 from this starting point through the data acquisition system (DAQ) to the interface with CMS.

1115 A block diagram of the main system components in the signal/control path is shown in Fig-
1116 ure 3.1.

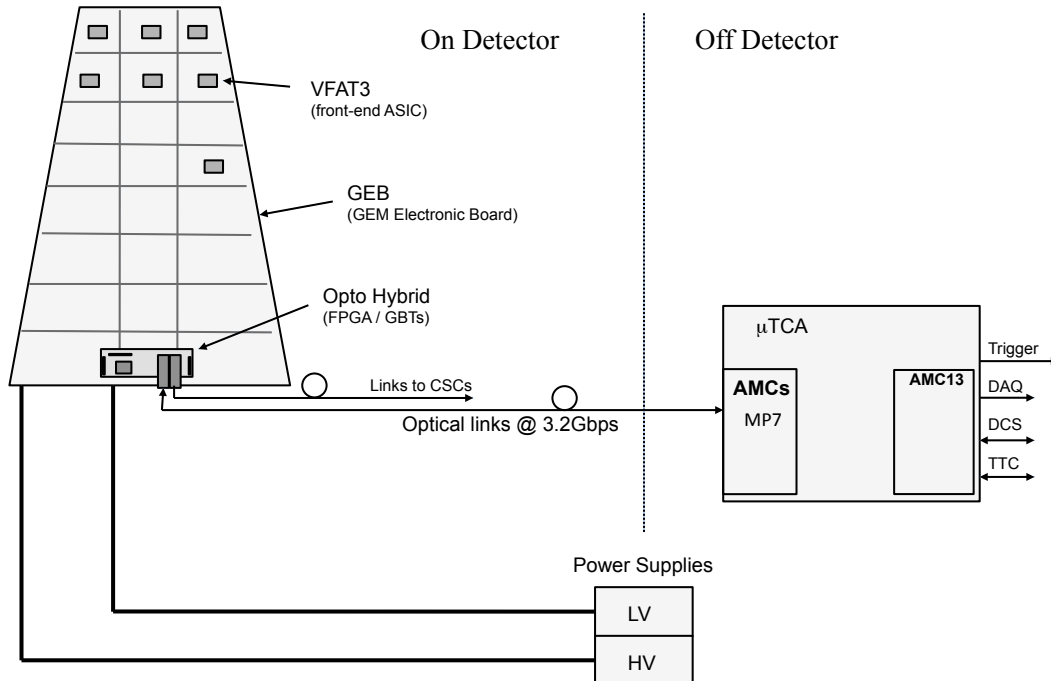


Figure 3.1: The GEM electronics readout system.

1117 The block diagram illustrates the main system components for the readout of a single GEM
 1118 chamber and is divided into 2 main regions, namely On-Detector and Off-Detector. Visible in
 1119 the On-Detector part is the division of the GEM chamber into 24 sectors. The 128 strips from
 1120 each sector are connected to the inputs of the front-end ASIC (VFAT3) via a connector on a
 1121 board known as the GEM readout board. The VFAT itself is mounted on a hybrid which plugs
 1122 into the GEM Readout Board connector. The control, readout and power to/from the VFAT
 1123 hybrid is delivered via electrical signals (E-links) running through a large flat PCB known as
 1124 the GEM Electronic Board (GEB). An opto-hybrid board also plugs into the GEB which contains
 1125 the GigaBit Transceiver (GBT) chip set, an Field Programmable Gate Array (FPGA), as well as
 1126 optical receivers and transmitters to provide the link to the Off-Detector region.

1127 There are two optical paths to the opto-hybrid. The first is bidirectional and runs between
 1128 the micro-TCA crates located in the counting room and the opto-hybrid. This path is used
 1129 for sending set-up and control signals to the front-end chips. The return path is used for the
 1130 VFAT3 tracking and trigger data packets as well as to return slow control data. The second
 1131 path is unidirectional and takes the VFAT3 fixed latency trigger data from the GEM system to
 1132 the Cathode Strip Chamber (CSC) system.

1133 The two data paths are illustrated in Figure 3.2.

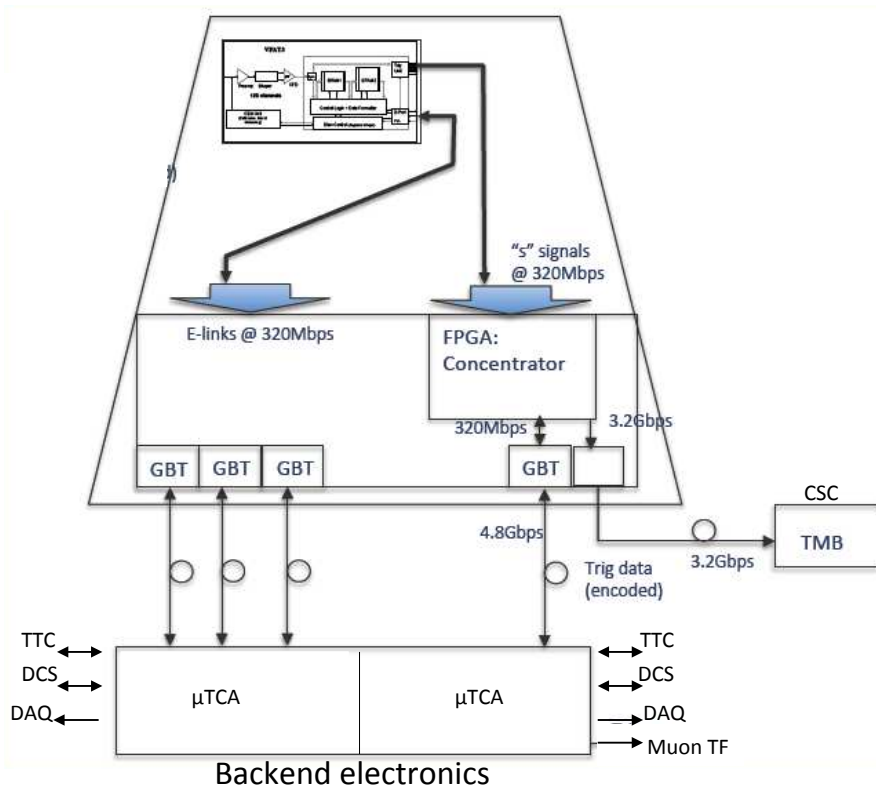


Figure 3.2: Block diagram of the system showing the tracking and trigger paths (detail of inset is given in the figure 3.3).

3.2 The VFAT3 front-end ASIC

The GEM detectors will be used to provide information relevant to triggering and tracking. The VFAT2 chip was used within the TOTEM experiment for the readout of GEM detectors. The requirements within TOTEM also necessitated tracking and triggering functionalities within the front-end chip. The VFAT2 architecture consisted of 128 channels continuously sampling the GEM strips. Its outputs provided "fast OR" fixed latency trigger information grouping together 16 channels at a time and also full granularity tracking information after the receipt of a level 1 trigger. The requirements of GE1/1 are similar, but there are some important differences that necessitate a new ASIC design. The most fundamental changes are the following:

- **Charge readout:** The signal charge delivered from a GEM detector on the passage of an ionising particle has a duration of \approx tens of ns depending on the exact gas mixture used. The VFAT2 has a fixed shaping time of 25 ns which is much shorter than the duration of the signal. This results in a ballistic deficit. The VFAT3 is being designed with a programmable shaping time to be able to integrate all the signal charge. The result will be an increased signal to noise ratio compared to the VFAT2.
- **Timing resolution:** The timing resolution is dominated by the properties of the GEM detector. Since this is a very important parameter for optimal trigger performance; the electronics must process the charge delivered without degrading the intrinsic detector timing resolution. The VFAT2 achieves this by acting on the rising edge of the GEM charge signal with a short (25 ns) shaping time. The VFAT3 will have the option to operate in this mode or extend the shaping to integrate all of the charge and therefore boosting the signal to noise ratio. In this later case the timing resolution would normally be degraded due to time walk of a comparator. The VFAT3 is being designed to compensate for this effect and maintain the timing resolution at the level given by the detector itself.
- **Trigger granularity:** The VFAT2 had a trigger granularity of 16 channels. The specification for GE1/1 is a trigger granularity of 2 channels. The VFAT3 will hence be designed for this increased granularity specification.
- **Level 1 Latency:** The level 1 trigger latency within CMS will be increased. The VFAT2 was designed for a L1A latency of $3.2 \mu\text{s}$ (with a maximum programmable latency up to $6.4 \mu\text{s}$). The VFAT3 will increase the latency capability to beyond $12.5 \mu\text{s}$. This complies with the requirements from the CMS trigger upgrades.
- **Level 1 trigger rate:** The trigger rate within CMS will be increased. The requirement being asked is possible L1A rates to a maximum of 1 MHz. The VFAT2 can cope with L1A rates up to 200 kHz. The important parameter here is the length of time needed for the readout of a data packet and the depth of the buffer for trigger data. The VFAT3 interface will run at 320 Mbps, which is a factor 8 faster than the VFAT2. In addition, the VFAT3 will have many programmable options to significantly reduce payload. This will result in a much increased data throughput going well beyond the CMS specification.
- VFAT3 is also being designed to be compatible with other system components foreseen for the CMS upgrades. Of particular importance is the GBT which communicates directly with the front-end chip. VFAT3 will have direct compatibility with the GBT interface.

The most basic requirements for the front-end ASIC are summarized here:

- 128 channel chip

- 1180 • Read positive and negative charges from the sensor
- 1181 • Provide tracking and trigger information
- 1182 • Trigger information: Minimum fixed latency with granularity of 2 channels
- 1183 • Tracking information: Full granularity after L1A.
- 1184 • L1A capability: L1A latency beyond $12.5 \mu\text{s}$
- 1185 • Time resolution of less than 7.5 ns (with detector).
- 1186 • Integrated calibration and monitoring functions
- 1187 • Interface to and from the GBT at 320 Mbps
- 1188 • Radiation resistant up to 100 MRads (radiation hardness of up to 1 MRad is sufficient
- 1189 for the GE1/1 application through Phase-II)
- 1190 • Robust against single event effects

1191 The block diagram for VFAT3 is shown in Figure 3.3.

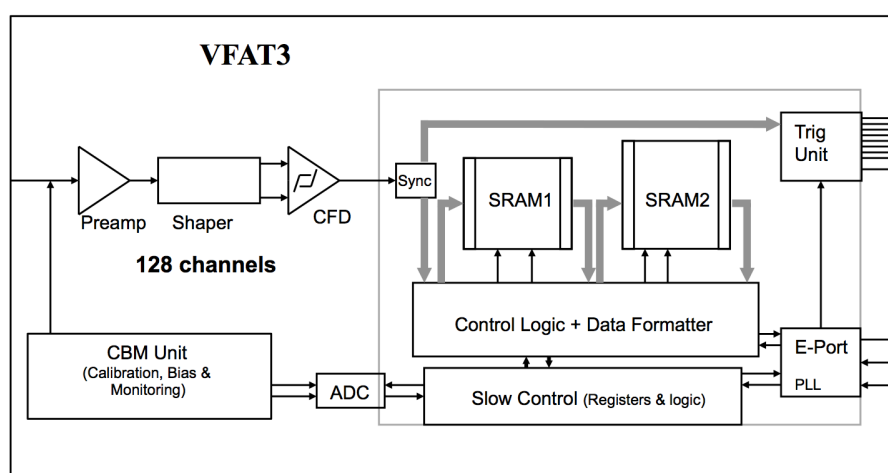


Figure 3.3: VFAT3 block diagram

1192 The VFAT3 architecture is composed of 128 channels, each comprising a charge sensitive preamplifier and shaper. This is followed by a constant fraction discriminator per channel. Following
 1193 the discriminator is a synchronization unit which synchronises the comparator result with the
 1194 the 40 MHz clock. The data then splits into two paths, one with a fixed latency for trigger signals,
 1195 and the second for tracking data which is non-synchronous. All communication with VFAT3
 1196 occurs through the E-port. This includes synchronisation to the LHC clock, slow control com-
 1197 mands as well as fast trigger commands, data packets, calibration and monitoring. The chip
 1198 is highly programmable to offer maximum flexibility. The sections below highlight the main
 1199 characteristics and options.
 1200

1201 3.2.1 The analog front-end

1202 The analog front-end is optimized for the readout of gaseous detectors (and in particular GEM)
 1203 but could also be used to read out silicon detectors. The front-end preamplifier and shaper are
 1204 programmable to offer flexibility when connecting to detectors of different capacitances and
 1205 charge characteristics. Each channel contains internal input protection to offer robustness to
 1206 charge (discharge) spikes. The front-end specification is shown in table 3.1 including a list of
 1207 the programmable options.

1208 Signal charge from GEM detectors can last for approximately 60 ns or so depending on the

Table 3.1: Main specifications of the analog front-end.

Key parameter	Comment
Detector charge polarity	Positive and Negative
Detector capacitance range	5 - 80 pF
Peaking times (T_p)	25, 50, 75, 100, 200 ns
Programmable gain	1.25 to 50 mV/fC
Max dynamic range (DR)	Up to 200 fC
Linearity	< 1% of DR
Power consumption	2 mW/ch
Power supply	1.5 V
ENC	$\approx 1100e$ (with $T_p=100$ ns, $C_d = 30$ pF)
Technology	IBM 130 nm

1209 gas mixture (see Figure 2.26). The shaping time of the front-end can be adjusted to fully inte-
 1210 grate this charge and hence maximize the signal to noise ratio. Optimum timing resolution is
 1211 maintained by the use of a CFD. Simulations show that the overall timing resolution can reach
 1212 around 7 ns with shaping times of 50 ns or more.

1213 The calibration system provides internal charge pulses to the input of the front-end preampli-
 1214 fier. The magnitude, phase and polarity of the charge pulses are programmable. The channel to
 1215 which the charge is injected is also programmable. This feature helps significantly in the pro-
 1216 duction test and characterisation stage as well as the detector setup and commissioning stage.
 1217 The functionality has two modes, one that injects a quick charge pulse (similar to a delta pulse)
 1218 and another that injects charge via a constant current for a programmable length of time.

1219 3.2.2 Variable latency data path

1220 The block diagram for the variable latency data path is shown in Figure 3.4.

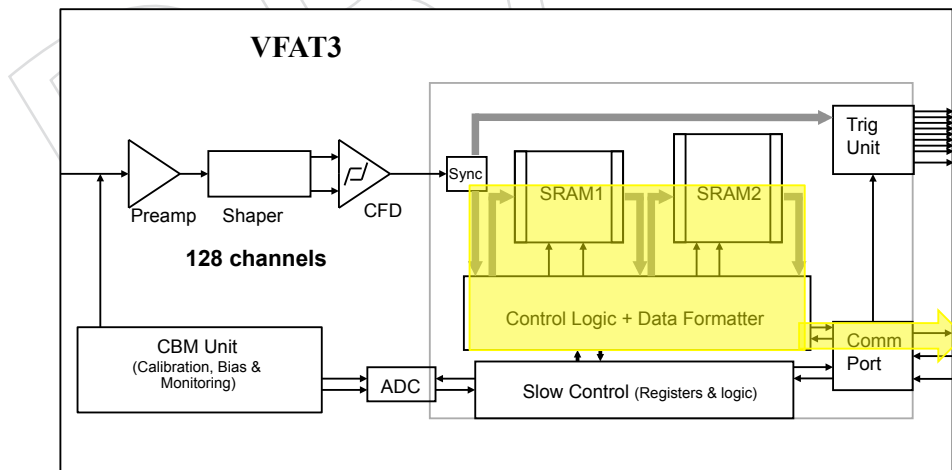


Figure 3.4: The VFAT3 block diagram with the variable data path highlighted.

1221 This path is used for transmitting full granularity information via the E-port. The data rate is
 1222 reduced by the application of a trigger arriving with a fixed latency. For operation in LHC for
 1223 tracking data, this trigger is the L1A. The data transmitted therefore have to be accompanied via
 1224 a time-stamp to identify the bunch crossing (bx) associated with the data. The SRAM memories
 1225 are sized to satisfy the L1A maximum latency and rate specifications.

1226 3.2.2.1 Data formats

1227 For the variable latency path there are two data types. The first is lossless and it is used to
1228 transmit full granularity information. The second is SPZS (sequential partition zero suppression)
1229 which has a reduced size.

1230 An important concept for the data packet description is the use of control characters (CC) as
1231 headers. Encoding in the E-Port allows the use of unique CC that can act as data packet headers
1232 and inform the receiving DAQ system what type of data it is receiving.

1233 3.2.2.2 Data type: lossless

1234 The lossless data packet style is derived from the VFAT2 data packet, but is optimized in terms
1235 of content.

Table 3.2: The VFAT3 lossless data packet.

Data packet	No. Bits
Header I/ Header IW	8
EC+BC/EC/BC	8-48
Data	128
CRC	16

1236 The lossless data packet structure is shown in table 3.2. A unique CC acts as a header identifying
1237 the start of the packet. The time-stamp is next in the form of an event counter (EC) and
1238 bunch counter (BC) numbers. This is followed by a data field which has 128 bits for the 128
1239 channels. A logic 1 represents a hit in that channel. If 1 or more channels are hit, there is no further
1240 attempt to zero suppress the data. The final piece of information is the cyclic redundancy
1241 check (CRC) to confirm the integrity of the data packet.

1242 The data packet size and content are programmable. Options exist to vary the number of bits
1243 in the time tags EC and BC. It is also possible to suppress the entire data field if no channels
1244 are hit. Indeed a further possibility is to suppress the entire data packet if no hits are registered
1245 and transmit only the header to acknowledge receipt of the trigger.

1246 This data packet structure allows all VFAT3s to operate synchronously sending data packets
1247 regardless of their content or to have a data driven operation where data packets are sent only
1248 when registering hits. Since most of the chips will record nothing in any given bunch crossing,
1249 the latter option optimizes bandwidth enormously. Each chip, however, even in the minimum
1250 setting, will respond to an L1A trigger by sending at least a CC to acknowledge receipt of the
1251 trigger signal and also report that no hits corresponding to this trigger are present.

1252 3.2.2.3 Data type: SPZS

1253 The SPZS style incorporates zero suppression and is a variant on the CMS RPC data format. In
1254 this case the size of the data packet is a function of the number of hits in the chip. This enables
1255 very small data packets and hence the highest possible data transmission rate. This is very
1256 good for operation at high trigger rates.

1257 The principle is as follows: The 128 channels are divided into 16 partitions, each containing
1258 eight channels. For each event, only the partitions containing data will be transmitted. If the
1259 overall occupancy is low, there will be a bandwidth saving on the payload transmitted per
1260 event.

Table 3.3: The SPZS Data Packet

Data packet	No. Bits
Header I/ Header IW	8
EC+BC/EC/BC	8-48
Data	16-144
CRC	16

1261 The SPZS data packet is shown in table 3.3. It is the same form as the lossless data packet
 1262 with the same programmable options relating to the time tags and the full suppression of the
 1263 data field in the case of no hits. However, the data field follows the SPZS sequence. The SPZS
 1264 sequence is shown in figure 3.5. It starts with a partition list of 16 bits, each bit representing
 1265 a partition. A 1 represents a hit in that partition. The partition list is then followed by the
 1266 channel list. If 1 partition is hit then the channel list is 8 bits long, if 2 partitions are hit then it
 1267 is 16 bits long, etc. The order of the sequence is always MSB first for both the partition list and
 1268 the channel list.

1269 The maximum number of partitions allowed is a programmable parameter.

Partition List	Channel Correspondence
p15	<127:120>
p14	<119:112>
p13	<111:104>
p12	<103:96>
p11	<95:88>
p10	<87:80>
p9	<79:72>
p8	<71:64>
p7	<63:56>
p6	<55:48>
p5	<47:40>
p4	<39:32>
p3	<31:24>
p2	<23:16>
p1	<15:8>
p0	<7:0>
Channel List of 1st partition in the partition list. 8b <msb:lsb>	
Channel List of 2nd partition in the partition list. 8b <msb:lsb>	

etc

Figure 3.5: The SPZS data field sequence.

1270 3.2.3 Fixed latency trigger path

1271 The fixed latency path is highlighted in Figure 3.6. The purpose is to provide fast hit informa-
 1272 tion that is synchronous with the LHC 40 MHz clock. The hit information can then be put in
 1273 coincidence with other detectors (such as the CSCs) to build CMS muon triggers. There are 8

1274 SLVS (scalable low-voltage signaling) pairs, which are used to transmit 64 bits/bx . The for-
 1275 mat can be programmable to have trigger information based on a fast OR of channels or using
 1276 the SPZS format. A bandwidth of 64 bits/bx allows the transmission of the fast OR signals
 1277 of 2 channels or the full granularity information for up to 6 hit partitions with the SPZS data
 1278 format.

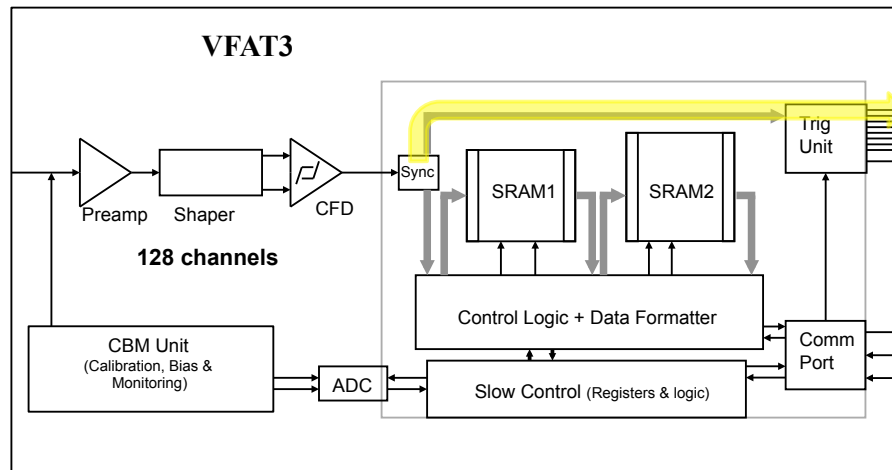


Figure 3.6: The VFAT3 block diagram with the fixed latency trigger path highlighted.

1279 3.2.4 Slow control

1280 Slow control defines configuration of operational parameters permitting the writing and read-
 1281 ing of internal registers which in turn provides the functions of programmability and monitor-
 1282 ing.

1283 VFAT3 uses the E-port for all data communication including the slow control. The use of CC in
 1284 the E-port allows slow control commands and data to be distinct from all other commands and
 1285 data fields. This is achieved by having two slow control CCs, one for communicating a slow
 1286 control 0 and the other for writing a slow control 1.

1287 The slow control protocol adopts the IPbus protocol [40] (standard within CMS upgrades) and
 1288 wraps this within the HDLC protocol. This ensures correct chip addressing and error checking
 1289 of slow control packets. Reception and transmission of slow control commands/data must take
 1290 *low* priority when compared to real data traffic. It is therefore possible to start and stop the
 1291 slow control communication in mid-flow and resume when the E-port is free. The maximum
 1292 allowable slow control communication rate is 40 Mbps.

1293 3.3 The GEM electronic board (GEB)

1294 The GEM chamber (complete with readout electronics) fits into a very narrow slot where the
 1295 mechanical constraints are very tight. The limited space means that running individual flat
 1296 cables to each VFAT3 hybrid is not possible. As a result, the GEB was designed to provide the
 1297 electrical link between VFAT3 hybrids and the opto-hybrid within the limited space available.

1298 Fabricated as a single large multilayer PCB, the GEB is a crucial element in the design of the
 1299 GEM detector readout system. There are three main functions: (1) to carry electrical signals
 1300 between the front-end chips and the opto-hybrid board; (2) distribute power; and (3) provide
 1301 electrical shielding to the detector. The GEB is placed on top of the GEM readout board as
 1302 shown in Figure 3.7.

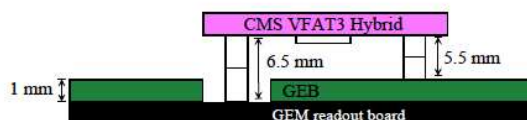


Figure 3.7: Schematic cross-section of the GEB placed on top of the GEM readout board. One VFAT3 hybrid and its connections to the GEB and the GEM readout board is also shown.

1303 The GEB board is a 1 mm thick 6-layer PCB. The lowest layer is grounded and acts a shield
 1304 preventing the EMI created by the switching of the digital electronics from interfering with the
 1305 analog low-level signals on the GEM readout board. The top layer hosts the connectors and the
 1306 SMD components. The other layers are used for the signal routing and powering.

1307 A first version of the GEB board has been manufactured and tested. The prototype has the size
 1308 of a long GE1/1 detector. Manufacturing with 6 layers was found to be feasible and cost ef-
 1309 fective. Electrical measurements have been done to characterize the signal integrity at 40 MHz
 1310 and the functionality of the GEB board with the VFAT2 hybrids has been tested successfully.
 1311 Figure 3.8 (Left) shows the layout of the second version of the GEB board. For clarity only a
 1312 few signal lines are shown. The first version-2 GEB boards have been delivered to CERN in
 1313 January 2015. Figure 3.8 (Right) shows a picture of the first version of the GEB board with a
 1314 couple VFAT2 hybrids mounted on it.

1315 3.4 The opto-hybrid and optical links

1316 The opto-hybrid consists of a mezzanine board mounted along the large side of the GEB board,
 1317 with typical dimensions of 10.0 cm × 20.0 cm × 1.1 cm. The tasks of the opto-hybrid board
 1318 are to synchronize the data sent by the VFAT3 chips, zero-suppress the trigger data, encode the
 1319 data and send them via optical links to the trigger electronics. The opto-hybrid, of which the
 1320 schematic of a prototype is shown in Figure 3.9, is composed of an FPGA, 3 GBT chipsets and
 1321 2 optical connectors of type SFP+ (small form factor pluggable) or a Quad-SFP (QSFP).

1322 3.4.1 The gigabit transceiver (GBT) and the versatile link

1323 The CMS GEM readout system includes the use of the GBT and Versatile Link technologies
 1324 under development at CERN [41]. These technologies are tolerant to radiation up to 200 Mrad,
 1325 which is several order of magnitude greater than the expected GE1/1 exposure levels. The GBT
 1326 is an optical data link technology providing bidirectional 4.8 Gb/s serial communication with
 1327 the capability to receive parallel data with an arbitrary phase at the 40 MHz LHC frequency,
 1328 or at multiples of 2, 4, 8. Additionally, the GBT can recover the frame clock, reduce the jitter
 1329 from an input clock, and distribute phase-controlled clock signals. The data rate (bandwidth)
 1330 available is lower than the 4.8 Gb/s line rate, and depends on how the GBT is configured. For
 1331 the CMS GEM project the data bandwidth will reach 3.2 Gbps.

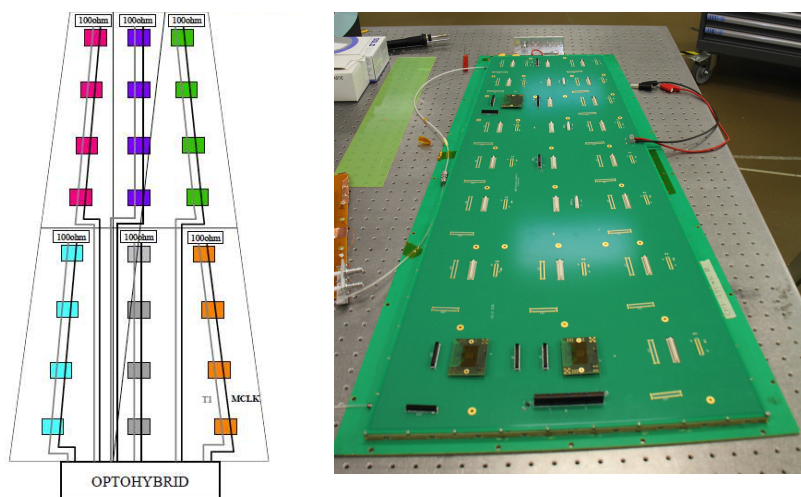


Figure 3.8: Layout of the GEB board version 2 (Left). First boards have been delivered to CERN in January 2015. A picture of the GEB board version 1 (Right).

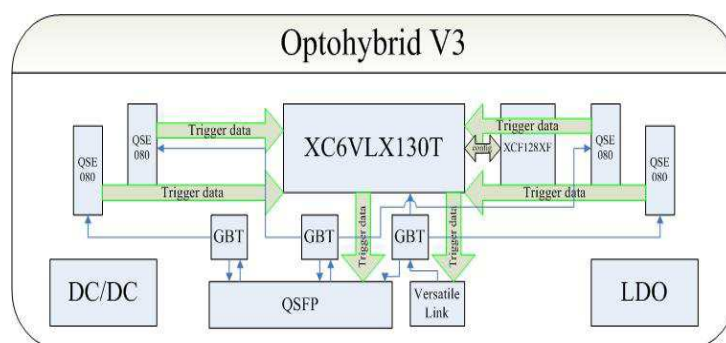


Figure 3.9: Schematic drawing of the opto-hybrid board. For the prototype the XC6VLX130T FPGA has been chosen.

1332 The GBT Transceiver (GBTX) will work as a full link transceiver with bidirectional data communication with the front-ends and the counting room. The GBTX delivers the global system clock reference, which comes from the counting room, to all front-ends. The communication with the VFAT3 chips is made through sets of local Electrical Links (E-Links). Depending on 1333 1334 1335 1336 the data rate and transmission media, the E-links connections can extend up to a few meters. 1337 E-Links use SLVS, with signal amplitudes that are programmable to suit different requirements in terms of transmission distances, bit rate, and power consumption. The E-links are driven by 1338 1339 the E-Ports that are integrated into the front-end chips.

1340 The optical link will simultaneously carry readout data, trigger data, timing information, trigger and control signals, and experimental control data that must be transferred with very high 1341 1342 1343 reliability. To ensure error free data transmission at high data rates in a harsh radiation environments, the GBT adopts a robust line coding and correction scheme that can correct bursts of 1344 bit errors caused by single event upsets (SEU).

1345 This is important because a single bit error in the control path can affect many readout channels for many clock cycles. In this mode, the GBT system can be configured over the GBT link itself. 1346 1347 The counting room electronics will use the LHC clock to transmit commands to the VFAT3 chips and the opto-hybrid; the GBTX will recover the LHC clock and provide it as a system 1348 1349 clock for the entire front-end electronics.

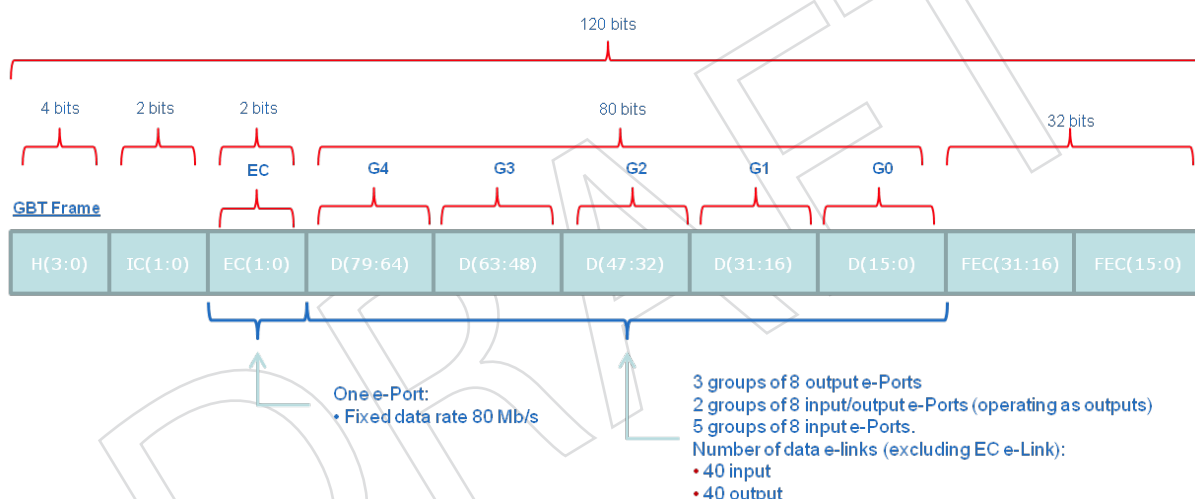


Figure 3.10: The GBT frame format.

1350 Figure 3.10 represents the GBT frame format consisting of 120 bits transmitted during a single 1351 LHC bunch crossing interval (25 ns) resulting in a line rate of 4.8 Gbps. Four bits are used 1352 for the frame Header (H) and 32 are used for Forward Error Correction (FEC). This leaves a 1353 total of 84 bits for data transmission corresponding to a user bandwidth of 3.36 Gb/s. Of the 1354 84 bits, 4 are always reserved for Slow Control information (Internal Control (IC) and External 1355 Control (EC) fields), leaving 80 bits for user Data (D) transmission. The D and EC fields are 1356 not assigned, and can be used for DAQ, Timing Trigger Control (TTC), or Experiment Control 1357 (EC) applications. DC-balance of the data being transmitted over the optical fiber is ensured 1358 by scrambling the data contained in the SC and D fields. For FEC, the scrambled data and the 1359 header are Reed-Solomon encoded before serialization. The 4-bit frame header is chosen to be 1360 DC-balanced.

3.4.2 Trigger path to the CSC

1361

1362 The trigger data will be sent in parallel to the CSC trigger mother board (TMB) and combined
 1363 with the CSC data to improve the Level-1 trigger efficiency of the CSC system. To send the
 1364 trigger data to the CSC TMB we will use the existing optical fibers currently used by the CSC
 1365 detectors inside CMS. However, these fibers cannot sustain the GBT protocol so, the 8B/10B
 1366 protocol will be used instead. The GEM-CSC data flow is described in section 4.3.

3.5 The back-end electronics

1367

1368 The back-end Electronics provides the interfaces from the detector (and front-end electronics)
 1369 to the CMS DAQ, TTC and Trigger systems. The design foreseen for the CMS GEM off-detector
 1370 electronics is based on FPGAs and Multi-GBit/s links that adhere to the micro-TCA (μ TCA)
 1371 standard. Micro-TCA is a recent standard that has been introduced for the Telecom industry
 1372 and aims at high data throughput (2 Tbit/s) and high availability (with very low probability
 1373 of interruption at $\approx 10^{-5}$). It is compact, hot swappable and has a high speed serial backplane.
 1374 The μ TCA is now a common standard for all the CMS upgrades and will replace the VME
 1375 electronics.

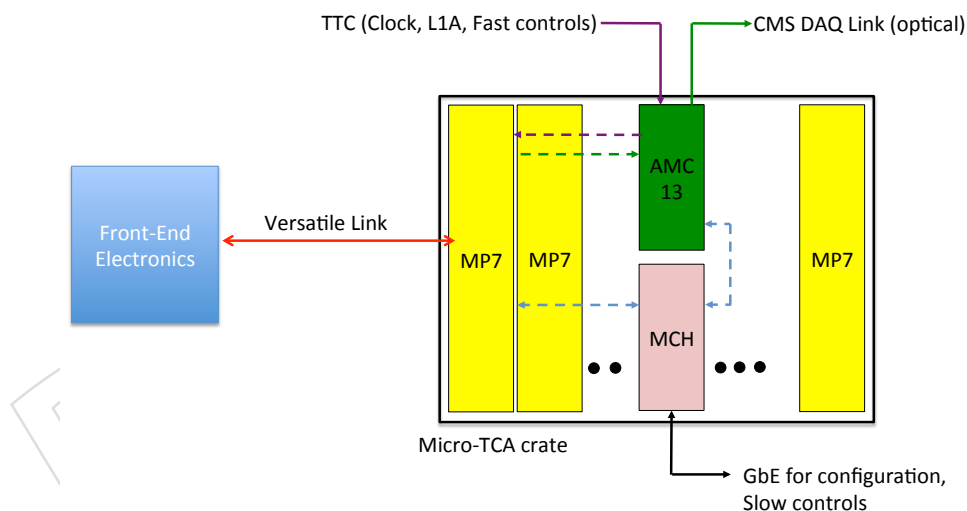


Figure 3.11: Layout of the back-end electronics μ TCA crates.

1376

1377 The CMS GEM off-detector electronics, shown in Figure 3.11, consists of the preferred CMS
 1378 μ TCA crate, the VadaTech VT892, which supports 12 double-width, full-height AMC cards
 1379 and two μ TCA Carrier Hub (MCH) slots. The MCH1 slot houses a commercial MCH module,
 1380 which provides gigabit Ethernet (GbE) communication and control using the IPMI protocol.
 1381 The MCH2 slot houses a custom MCH developed by Boston University and called AMC13.
 1382 The AMC13 is the standard module within CMS to interface the μ TCA crates to the CMS data
 1383 acquisition system and to provide the CMS Trigger Timing and Control (TTC) signals down-
 link.

1384

1385 The AMC cards that will equip the μ TCA crates will be the MP7 (Master Processor) card de-
 veloped by Imperial College, London. The MP7, based on the Xilinx Virtex-7 FPGA and Avago

1386 MiniPOD optical modules, can provide 72 optical transceivers and 72 optical receivers, capable
1387 of operating above 10 Gbps. Eight MP7 boards, which are hosted within one micro-TCA crate,
1388 are needed to readout the entire GE1/1 system.

1389 For the optical link between the opto-hybrid and the MP7 boards, the GBT protocol will be
1390 used for data transmission over (48 way) Mutlifiber Termination Push-On (MTP) cables.

DRAFT

DRAFT

Chapter 4

Data Acquisition and Trigger

Editors: G. De Lentdecker, J. Hauser, A. Safonov

Contributors: P. Aspell, G. De Lentdecker, J. Gilmore, Th. Lenzi, Y. Yang

4.1 Introduction

This chapter focuses on the trigger and tracking data flow from the front-end electronics to the muon trigger and the CMS DAQ system. This chapter also presents the expected data rate and latency on the different data paths. We also describe the firmware and software environment as well as the interface between the GEM readout system and the CMS DAQ.

4.2 Tracking data flow

Upon a Level-1 accept (L1A) signal, the full granularity data stored in the VFAT3 SRAM2 memories will be formatted by the Data Formatter and sent out by the chip through the E-port towards the GBT chipset. One GBT chipset will read out 8 VFAT3 chips. The format and content of the data packets has multiple options and are described in section 3.2.2.1. In the case of the basic lossless data format, the data rate per optical link will amount to less than 200 Mbps at an L1A rate of 100 kHz (see section 4.4).

Note that the GBT is fully transparent to the user data being transferred. In the GBT chip, after phase alignment, the data coming from the VFAT3 chips through the E-ports is first processed by the scrambler, a 4-bit header is then added, the Reed-Solomon (RS) encoding and interleaving takes place and finally the data are serialized. While the scrambler maintains the word size, the RS encoder adds the 32-bit Forward Error Correction (FEC) field adding up to a total frame length of 120 bits. This leads to an overall line code efficiency of $84/120 = 70\%$. At the receiver end the inverse operations are repeated in the reverse order. There the tasks will be performed by the AMCs located in the μ TCA crates (see section 3.5).

As described in section 3.4.1, each GBT data link will carry 80 bits of user data for every LHC bunch crossing. Each GBT link will handle the data of 8 VFAT3 as shown in table 4.1. The Control Character indicates which data format is being sent. The possible data formats are described in section 3.2.2.1. BC0 indicates that this sample is from the bunch with number zero in the orbit. This bit is used for latency/alignment of the data links. The packet number indicates the sample number.

Figure 4.1 shows the mapping of the optical links from the GEM detectors to the back-end electronics. Each MP7 can receive up to 72 high speed optical links, that is 24 GE1/1 chambers or 12 superchambers tracking data. In total, one GE1/1 endcap require 3 MP7 boards to read-

Table 4.1: GEM data format for the GBT. The control character indicates which data format is being sent. BC0 indicates that this sample is from the bunch with number zero in the orbit (used for latency/alignment of the data links). Packet Nbr indicates the sample number.

Byte	7	6	5	4	3	2	1	0
0	Control Character							
1	Packet Nbr [6:0]							BC0
2	VFAT 0							
3	VFAT 1							
4	VFAT 2							
5	VFAT 3							
6	VFAT 4							
7	VFAT 5							
8	VFAT 6							
9	VFAT 7							

1424 out the tracking data and 1 MP7 for the trigger data. The full GE1/1 data can be hosted by one
1425 μ TCA crate.

1426 The rate of the incoming GEM data per MP7 card will be ≈ 12 (120) Gbps at 100 (1000) kHz
1427 for the lossless data format. After data reduction, the DAQ data will be sent through the μ TCA
1428 backplane from each MP7 board to the AMC13 board which will then transmit the data frag-
1429 ments to the CMS DAQ system. The DAQ capacity of the AMC13 amounts to three 10 Gbps
1430 links. Data reduction on the MP7 boards can be easily achieved by requiring the matching of
1431 hits in the two GEM detectors making one superchamber.

1432 4.3 Trigger data flow

1433 Each VFAT3 chip will send the fixed latency data (see section 3.2.3), also called trigger data, to
1434 the frontend FPGA on the opto-hybrid board through 8 SLVS pairs resulting in the transmission
1435 of 64 bits per LHC bunch crossing per VFAT3, where each bit represents the logical 'OR' of two
1436 adjacent strips, also called a GEM pad. At an average particle rate of 10 kHz/cm², we expect 1.2
1437 hit/bx per GEM chamber, which means that most of the bits will be '0'. On the front-end FPGA
1438 a finite state machine will look for non-'0' bits and encode the pad position in the following
1439 way: 6 bits (padId) + 2 bits (ϕ column) + 3 bits (η -partition) = 11 bits.

1440 These trigger data will be sent by the frontend FPGA, through the GBT chipset, to a dedicated
1441 MP7 board host in the μ TCA crate. On this board coincidences will be searched for using the
1442 trigger data coming from the superchambers. This will allow the rejection of noise hits and
1443 reduce the data volume. Indeed, simulations (see chapter 6) show that the photon and neutron
1444 backgrounds hit the two GEM detectors of a superchamber only in a couple of % of the cases.
1445 The local GEM trigger algorithm will therefore search for pairs of hits in coincidence in space
1446 and time within each superchamber using a LUT. The data will then be sent to the upgraded
1447 Muon Track Finder board (MTF7) [42].

1448 A copy of this trigger data will be sent from the frontend FPGA to the CSC Optical Trigger
1449 Mother Board (OTMB) over two optical fibers, where it will be combined with the CSC data to
1450 improve the Level-1 trigger efficiency of the CSC system (see section 6.2.1). The fibers needed

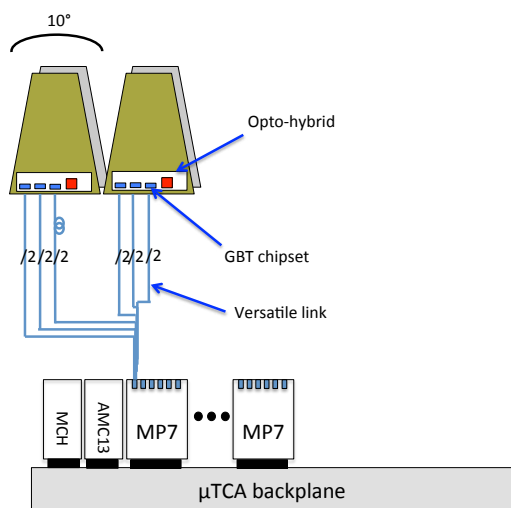


Figure 4.1: Mapping of the optical links for the tracking data. One MP7 can receive the data from 12 superchambers.

1451 for the transmission of data to the OTMB already exist as part of the current CSC installation
 1452 and are located along the CSC detectors inside CMS. Since the CSC OTMBs do not support the
 1453 GBT protocol, the 8b/10b protocol will be used instead, providing 48 bits/bx per fiber for data.
 1454 Consequently up to 8 trigger hits per GEM detector can be sent to the CSC OTMB at each LHC
 1455 bunch crossing (bx).

1456 The GEM trigger data should arrive at the CSC OTMB within a latency of 17-18 bx. Table 4.2
 shows the breakdown of the latency of the GEM-CSC trigger data path.

Table 4.2: Latency in bx of the GEM-CSC trigger data path.

Component	Latency (bx)
TOF	1 – 2
VFAT3	5
GEB	1
FPGA	2
SFP	5
Fiber (15 m)	3
Total	17 – 18

1457

1458 All Level 1 trigger primitives built in OTMB using GEM and CSC data will follow the usual
 1459 CSC trigger path: from OTMB to the Muon Port Card (MPC) and further to CSC Track Finder
 1460 (CSC TF).

4.4 Data rate simulations

In this section we present the estimation by simulation of the output trigger and tracking data rates of the opto-hybrid concentrator for several data formatting options and for LV1A rates of 100 kHz and 1 MHz. Those simulations are of importance to minimize data losses and compute the probability to reach the bandwidth limit of the optical links.

By design, the opto-hybrid is equipped with 3 tracking optical links, 1 trigger optical link, and 1 optical link which is connected to the CSCs OTMBs to communicate trigger information. Each link uses the GBT protocol with a maximum data bandwidth of 3.2 Gbps, except the link towards the CSC OTMBs, which has a maximum data bandwidth of 1.92 Gbps.

Using the averaged hit rate in the η -regions covered by GE1/1, dominated by the neutron and photon background (see chapter 6), we simulate a number of hits, following a Poisson distribution, in the detectors and compute the size of the generated packet. For the trigger data packets, each hit pad (Fast OR of two neighboring strips) generates 11 bits of data (5 bits for the address of the VFAT3 on the GEB and 6 bits for padId in the VFAT3). For the tracking data packets, the VFAT3 flexibility allows the use of the lossless algorithm or the SPZS algorithm (see section 3.2.2.1).

Table 4.3: Opto-hybrid output data rates in GE1/1 for L1A rates of 100 kHz and 1 MHz.

Algorithm	Data rate (Gbps)	Probability of overcapacity
Trigger Fast OR	0.05	$6 \times 10^{-5} \%$
LV1A at 100 kHz		
Tracking Lossless	0.48	$< 10^{-7} \%$
Tracking SPZS	0.17	$< 10^{-7} \%$
LV1A at 1 MHz		
Tracking Lossless	4.8	$< 10^{-7} \%$
Tracking SPZS	1.73	$< 10^{-7} \%$

Table 4.3 lists the average data rates for GE1/1 for L1A rates of 100 kHz and 1 MHz. The probability that the links are used in overcapacity is defined as the fraction of L1A during which the transferred amount of data is larger than the allocated bandwidth, as calculated using the number of links described in the previous paragraphs.

The results show that in all cases the available bandwidth is sufficient to cope with the tracking data rates, while data losses on the trigger data might occur with a probability of $6 \times 10^{-5} \%$. To recover those events, one could use the GBT in dual transmitter mode, thus doubling the bandwidth, or use a slightly more complex encoder.

To reduce the data losses, a modified trigger data encoder is also proposed where 1 bit is added to each packet to indicate the cluster size. With the unmodified algorithm, when two neighboring pads are hit, two packets are created. With the new encoder only one is formed. Using this new algorithm, the probability of overcapacity for the trigger links is lowered to $< 10^{-7} \%$ for GE1/1.

1490 4.5 DAQ firmware and software

1491 4.5.1 MP7 and μ TCA control

1492 The μ TCA standard does not specify any details of the communication between a control PC
1493 and an AMC beyond the low-level transport specification of gigabit Ethernet. The CMS Up-
1494 grade Working Group has adopted a standard protocol called IPBus [40] to provide a uniform
1495 solution for communication across all CMS upgrades which will use μ TCA. The protocol de-
1496 fines a virtual A32/D32 bus on each Ethernet target and allows the programmer to pack multi-
1497 ple read, write, bit-set, and bit-clear operations into a single Ethernet packet. The base protocol
1498 uses the User Datagram Protocol (UDP) over the Internet Protocol (IP). The use of UDP rather
1499 than bare Ethernet allows development of control code with no specialized drivers or enhanced
1500 machine access, i.e. standard user accounts and interfaces can be used for all purposes. The
1501 use of UDP/IP instead of TCP/IP greatly reduces the complexity of the implementation in the
1502 FPGA firmware of the AMC. Reliable delivery is ensured by a software server layer which
1503 manages multiple parallel requests for the same resources across multiple clients. The IPBus
1504 protocol and firmware module are supported by the Bristol University group.

1505 4.5.2 Firmware

1506 On each chamber, the front FPGA located on the opto-hybrid is responsible for synchronizing
1507 the trigger data from the 24 VFAT3, applying zero-suppression and transmitting the data to the
1508 CSC OTMB (see section 6.2.1) and to the μ TCA MP7 board. Once a Level 1 decision is issued
1509 the VFAT3 chips transmits the full granularity data associated to the event to the MP7 board
1510 through the GBT protocol. The FPGA of the MP7 boards will synchronize the data, apply the
1511 matching of pairs of hits in each superchamber for the trigger data, then transmit the trigger
1512 data to the Muon Track Finder or the full granularity data to the AMC13 through the μ TCA
1513 backplane.

1514 To handle the communication between the Detector Control System computer (DCS, see chap-
1515 ter 8) and the μ TCA electronics, a dedicated IPBus slave will be implemented on the MP7 to
1516 translate the IPBus requests to a custom data format. The addresses used by IPBus to execute
1517 read/write operations will be mapped to the physical registers in the VFAT3 chips. Each IPBus
1518 slave will be connected to one optical link controller. The existence of firmware for the inter-
1519 face to the AMC13 as well as for the GBT core will allow the GEM developpers to focus on the
1520 GEM-specific firmware.

1521 For the front FPGA located inside the CMS detector and therefore exposed to radiation, the
1522 firmware will require Single Event Upset (SEU) mitigation logic. We will follow the recommen-
1523 dation of the CSC group which uses the same FPGA on the ME1/1 CSC chamber and which
1524 has tested the radiation hardness of many commercial components, including the FPGA, up
1525 to several tens of krad [43]. The SEU mitigation in the FPGA will be provided by the use of
1526 triple-voting and with the embedded Virtex-6 Error Correction Checking (ECC) feature for the
1527 FPGA Block RAM.

1528 4.5.3 Overview of the online software

1529 The online software of the GEM readout system is designed according to the general scheme
1530 of the CMS online software. The implementation is based on the generic solutions provided by
1531 the CMS software framework: XDAQ, Trigger Supervisor, etc.

1532 The direct steering of the hardware is performed on the computers controlling the μ TCA crates.
1533 The central control over the hardware is split in two:

- 1534 • the XDAQ applications providing access to the AMC boards receiving the GEM
1535 tracking data and the AMC13 are managed by the GEM node of the Function Man-
1536 ager,
- 1537 • the XDAQ applications providing access to the AMC boards receiving the GEM trig-
1538 ger data and the opto-hybrid boards are managed by the GEM cell of the Trigger
1539 Supervisor.

1540 The software is abstracted into several layers. The Hardware Access XDAQ application is a
1541 custom class derived from the *Application* class provided by the XDAQ package. At the low-
1542 est level are the interfaces to the IPBus protocol. Above this layer is the standard CMS μ HAL
1543 layer which defines the access functions (Write, Read, ...). The next layer above becomes board
1544 dependent. However since the boards receiving the GEM trigger or the tracking data are the
1545 same, the C++ classes will be essentially identical. Functions like Reset, Configue, Start, Fin-
1546 ished, etc. are defined at this level.

1547 4.5.4 Testing and integration

1548 In 2014, a first GEM DAQ system has been developed to read-out VFAT2 chips, while the
1549 VFAT3 chip is being designed. The system is composed of new CMS VFAT2 hybrids mounted
1550 on the first version of the full size GEB board on which the first version of the opto-hybrid is
1551 placed. The layout of this first version of the opto-hybrid is shown in Fig. 4.2. This version
of the opto-hybrid can read-out a sub-set of 6 VFAT2 chips. The opto-hybrid is read-out by

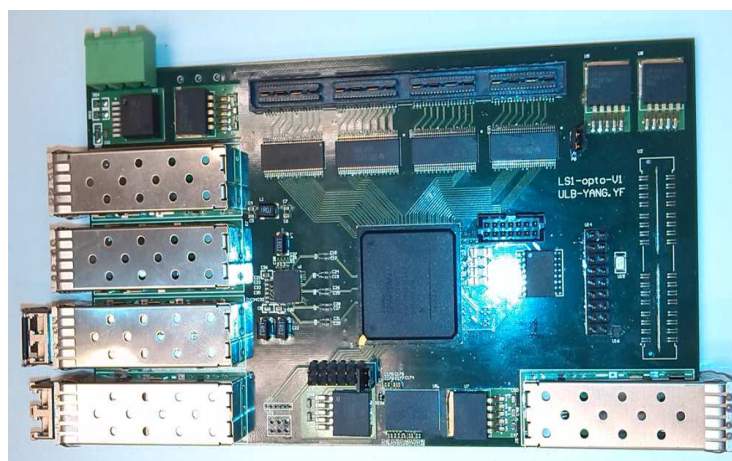


Figure 4.2: Layout of the opto-hybrid v1. It is equipped with a Spartan 6 FPGA.

1552 a GLIB board [44] installed in a μ TCA crate, controlled through IPBus. Since the Spartan 6
1553 FPGA does not have high-speed transceivers that run faster than 3.2 Gbps, the GBT protocol
1554 can not be implemented, but a simpler 8b/10b encoding is possible. However, the GBT
1555 protocol has been successfully tested between a GLIB board and a Virtex 6 development board.
1556 This prototype is a proof of concept of the full GEM read-out chain that allows the test of the
1557 signal integrity in the GEB PCB as well as in the connection between the GEB and the opto-
1558 hybrid, and provides first measurements about the power consumption. The full read-out
1559

1560 chain has been successfully tested in the lab as well as during a test beam at CERN in December
1561 2014. During this test beam many of the functionalities needed for the final system have been
1562 tested, implying the implementation of the corresponding firmware and software: control of
1563 the VFAT2 chips and data readout through the bi-directional optical link, data integrity over
1564 the optical link, control from the DAQ PC through IPBus, etc.

1565 Although the DAQ prototype differs from the final design in multiple ways, the firmware and
1566 software for the first version of the opto-hybrid and the GLIB are developed taking care to make
1567 them compatible with the later versions of the opto-hybrid with minimal changes. The current
1568 version of the system focuses on the control of the VFAT2 hybrids through I²C which allows
1569 the software developers to test several functionalities of the chip as well as the communication
1570 between all the components of the DAQ chain.

1571 In addition a GEM-CSC integration teststand is being built at CERN to test the full system. This
1572 facility is now composed of a GE1/1 prototype equipped with the first version of the GEB and
1573 of the opto-hybrid. The GE1/1 prototype is mounted on top of a ME1/1 CSC chamber and it
1574 is read-out by a GLIB and an AMC13 hosted in a μ TCA crate controlled by a DAQ PC running
1575 XDAQ. The opto-hybrid also transmits the trigger data to the CSC OTMB. While this facility is
1576 being commissioned the synchronization of both electronics systems has already been achieved
1577 and data sent from the GEM detector to the CSC OTMB.

1578 The second version of the GEB board are already available and the design of the second version
1579 of the opto-hybrid will be finalized by the end of January 2015. These components will then
1580 be thoroughly tested by 5 laboratories in Europe and in the US, as well as in the GEM-CSC
1581 integration facility at CERN.

1582 By the end of 2015, the design of the final versions of the GEB and opto-hybrid, compatible
1583 with the VFAT3 chip will start.

DRAFT

1584 Chapter 5

1585 Chamber production, quality control and 1586 quality assurance

1587 **Editors:** L. Benussi, O. Bouhali, P. Karchin, A. Sharma, M. Tytgat

1588 **Contributors:** L. Benussi, O. Bouhali, S. Colafranceschi, B. Dorney, A. Marinov, J. Merlin, P.
1589 Karchin, A. Sharma, M. Tytgat

1590 5.1 GE1/1 component production and assembly overview

1591 In the last four years, the design of the full-size GE1/1 detectors has been optimized and now
1592 chambers are being prepared following the final production design. This has been possible
1593 given the excellent collaboration with various institutions with previous experience in building
1594 CMS muon detectors. A full length movie of the assembly of a GE1/1 detector can be seen here:

1595 <https://www.youtube.com/watch?v=Ssuqh5GAVZ4&feature=youtu.be>

1596 The philosophy of production is based on the experience gained during the construction phase
1597 of the CMS muon detector. Quality control (QC) and quality assurance (QA) are key factors to
1598 ensure the delivery of fully efficient detectors yielding their best performance when installed in
1599 CMS. The final chamber quality and performance depend on the production quality and on the
1600 accuracy of the chamber assembly operation, tracking, and documentation. In this chapter the
1601 QA and QC procedures of the complete cycle of the construction project of chambers for the
1602 GE1/1 station are described. Throughout the component procurement and production, and
1603 chamber assembly procedure, systematic inspections are also needed including verification of
1604 the QA and QC results. This will be done exploiting an extensive database that is used for
1605 reference throughout the life of the detector, from the moment of its assembly to its installation
1606 and operation inside CMS. Standardized procedures have been established that are identical as
1607 far as possible for all assembly sites which are described in Section 5.3.

1608 The assembly and production workflow is presented in the process chart in Figure 5.1. The
1609 overall process is divided into three major parts:

- 1610 • component production and quality control
- 1611 • assembly and commissioning of single GE1/1 chambers at production sites
- 1612 • assembly and commissioning of superchambers at CERN before delivery for instal-
1613 lation at CMS P5.

1614 The corresponding timeline is presented in Table 5.1. The tasks for QA, and QC procedures for
1615 components and chambers are described below. For each task, the average time is expressed.
1616 These numbers are generally estimated and additional delays may happen.

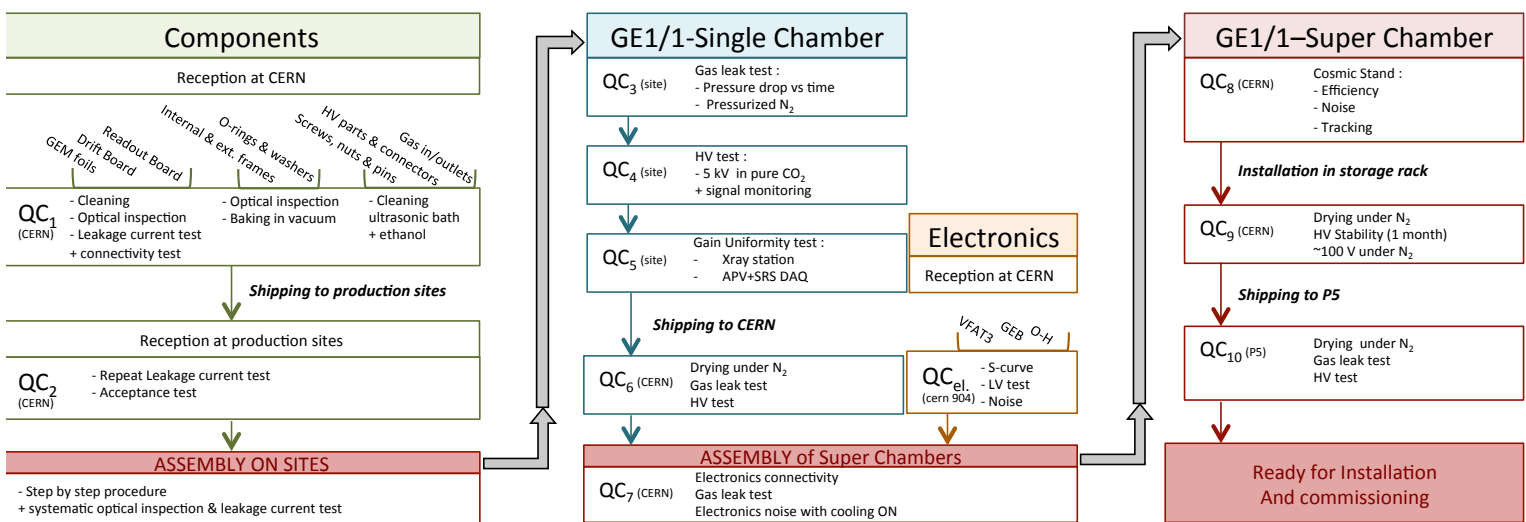


Figure 5.1: Process of GE1/1 chamber and superchamber assembly and construction from component production to final chamber commissioning.

QC	Expected time
QC ₁	2 days (all components)
QC ₂ + <i>assembly</i>	2 days
QC ₃	1 day
QC ₄	1 day
QC ₅	1-2 days
QC ₆	Until needed to assemble Superchamber
QC ₇	2 days
QC ₈	5 days
QC ₉	Waiting for installation
QC ₁₀	Quick test after transport

Table 5.1: Timeline for the GE1/1 superchamber assembly.

5.2 Component production and quality control

Components produced by industrial companies will be delivered to CERN where they will be visually inspected for defects and tested. Components passing this quality control, denoted QC₁, will be shipped to the assembly sites. Some of the specific inspections and tests are described below.

Quality Control of HV divider. The HV divider is a chain of resistors used to deliver appropriate voltages to the drift plane and the three GEM foils (see Figure 2.1). A HV test is applied to the divider and the I-V curve is used to check the resistor value at each stage of the chain.

Drift PCB. An optical inspection is performed in a cleanroom to identify possible scratches and defects. A nitrogen gun is used to clean the drift plane for possible dust. The drift plane is then connected to HV and progressive HV ramping is used to check for possible sparks and/or changes in impedance.

PCB Readout. The PCB readout is inspected for possible shorts between strips or open strip-readout connections. A special connector is used to simultaneously check all the strips in one PCB readout.

GEM foil. The GEM foil must be handled and tested in a clean room. An optical inspection is first performed to identify defects, scratches, irregular hole sizes, and contact between top and bottom metalized surfaces. A leakage current test is part of the quality control of the GEM foils. Before and after the test, the GEM foils are stored in a safe and clean container with a maximum humidity of 35% and an ambient temperature between 10 and 40 °C. High pressure nitrogen is used to remove possible dust. A microscope is also used when necessary to further investigate defects. The quality of the foil (leakage current and impedance) is checked using a picoammeter. With an applied potential difference of 500 V between the GEM metal sides, the GEM foil should draw a current of no more than 30 nA.

Other components needed for chamber assembly include O-rings, frames, gas in/outlets, and connectors. Once the acceptance criteria are fulfilled, complete assembly sets are shipped to the production sites after recording all QC and QA results in the database, as described in Section 5.5.

5.3 Chamber assembly at production sites

5.3.1 Assembly site requirements

The GE1/1 chamber assembly will take place at several sites. There is a minimum set of requirements for hardware and expertise for a site to be qualified. The site must have established a good track record of GEM chamber production and testing, including quality control checks (QC₃ to QC₅ of Figure 5.1), gain measurements, successful operation in test beam campaigns of chambers produced from the center, and sufficiently skilled personnel. The following is a list of requirements for the production sites.

- Qualified personnel who are well trained in the assembly of GE1/1 chambers. The training will be done at CERN using dedicated final prototypes. The CERN group has already organized two weeks of intensive training with a total of 30 participants from 10 institutions. Personnel must be trained to work in a cleanroom and must understand the details of each step in the production process.
- Sufficient and appropriate space with dedicated areas for testing, assembly, storage, and logistics (reception and shipping of equipment).
- A certified cleanroom, rated at least at class 1000, equipped with at least one large bench to assemble full GE1/1 chambers. Auxiliary benches for assembly tools and spares are also required. Moreover, the cleanroom must be equipped with clean and dry nitrogen gas lines used to blow chamber parts during assembly. Storage cabinets are also required.
- A gas system, implemented with stainless steel pipes and leak proof. All components, such as valves, unions, and manometers, must be cleaned well to remove any oil residue from their production. The gas system must be capable of operation with CF₄-based gas mixtures, hence requiring components to be tolerant of fluorine. There must be filters to remove possible water contamination from the pipes. The use of oil bubblers or any oil-based devices is forbidden. Bubblers must be substituted with rotameters.
- Leakage current measurement station. There must be a nitrogen-flushed box of large enough size to comfortably house GE1/1 foils. A power supply must be available to provide 500 V at sufficient current for a single GEM foil. The nitrogen gas used for flushing in the leakage current box must be sufficiently dry and clean.
- X-ray setup to check the uniformity of the detector gain across the chamber surface.
- Gas leak measurement station. In this area the assembled chamber will be tested for gas leaks. The station must be equipped with a dry and clean nitrogen gas line and with a manometer to measure a pressure drop of the order of a few tens of a millibar per hour. The proposed method employs a U-shaped tube with millimeter scale. The U tube must be filled with water. No vaseline oil or other oil is allowed. Since the gas leak measurement will be done with dry and clean nitrogen, the piping can be done with clean plastic tubing.

5.3.2 Assembly site readiness present status

The GE1/1 collaboration has identified six possible assembly sites so far. The selection criteria are based on past experience at assembly sites in detector construction and on the support from their home institute given to the GE1/1 project. In the end, the final selection of assembly sites will be done after an assesment of their readiness for the final production six months before it starts. The site readiness will be judged following the criteria described in the previous section.

1690 Following is a brief description of the six candidate sites and their present status.

- 1691 • **Bhabha Atomic Research Center (BARC) Mumbai - India** BARC has actively par-
1692 ticipated in the RPC RE4 production, both in detector assembly (50 certified cham-
1693 bers) and in the chamber quality control using a cosmic-ray stand (see Figure 5.2(a))
1694 instrumented with a gas system suitable also for GE1/1 chambers. The facility has a
1695 large area for GE1/1 chamber storage and the present cleanroom (class 100) is being
1696 enlarged. The x-ray box for the gain uniformity test is under final design and will
1697 be completed by the end of 2014. BARC has successfully assembled and tested one
1698 GE1/1 full-size prototype demonstrating their full capability to participate to the
1699 final production.
- 1700 • **INFN Sezione di Bari - Italy** INFN Bari participated to the RPC barrel chamber mass
1701 production and had a major role during the detector installation in CMS P5. The site
1702 has a wide cleanroom ($\sim 40m^2$) of class 10000 equipped with one optical table and
1703 one large marble table. The cleanroom contains a clean compressed-air line and a
1704 clean dry-nitrogen line. Assembly of an x-ray box and gas distribution system is
1705 complete. INFN Bari has already successfully assembled a GE1/1 prototype, which
1706 is presently under test in their x-ray facility (see Figure 5.2(b)).
- 1707 • **CERN - Switzerland** The CERN site has the major responsibility for GE1/1 chamber
1708 construction and final validation. Assembly of GE1/1 chambers will take place in
1709 the Building 102 cleanroom. The chambers will then be moved to the tracker inte-
1710 gration facility (TIF) cleanroom (see Figure 5.2(c)), where they will be assembled into
1711 superchambers and tested on the cosmic stand, which is currently under construc-
1712 tion. At the TIF, all GE1/1 chambers assembled and validated from the different
1713 assembly sites will be delivered. The TIF has an operational x-ray setup for the gain
1714 uniformity QC of the chambers assembled at CERN. The GE1/1 superchambers will
1715 be placed in a storage area at the TIF before dispatch to CMS P5 for installation.
- 1716 • **Ghent University (UGent) - Belgium** Ghent University previously produced 50 cer-
1717 tified RPC RE4 chambers. It will take advantage of its present RPC lab (see Fig-
1718 ure 5.2(d)), which has an operational cosmic stand. An x-ray station is assembled
1719 and ready with a movable gas mixing unit. A box for leakage current measure-
1720 ments on GEM foils is also ready. Options for installing a cleanroom near the Ghent
1721 GEM lab are being investigated. Using the Engineering Department cleanroom, one
1722 GE1/1 full-size prototype was successfully assembled.
- 1723 • **Florida Institute of Technology (FIT) - USA** The FIT cleanroom (class 1000) is fully
1724 commissioned. It has a workspace for assembling up to two GE1/1 chambers in
1725 parallel (see Figure 5.2(e)). It is equipped with a clean gas line (nitrogen) and optical
1726 and marble tables for the GE1/1 assembly. A leakage current station and gas system
1727 are ready. A lead shielding box to accommodate GE1/1 detectors for x-ray tests was
1728 recently completed. FIT has successfully assembled and tested two GE1/1 full size
1729 prototypes.
- 1730 • **INFN Laboratori Nazionali di Frascati (LNF) - Italy** The Frascati site already par-
1731 ticipated in “mass production” and will profit from the infrastructure and logistical
1732 capacity of the Frascati laboratory. The Frascati assembly site candidate has a large
1733 cleanroom (class 100) of about $20 m^2$ with an adjacent large cleanroom (class 10000)
1734 of $42 m^2$. The GE1/1 assembly will be done in the class 100 cleanroom, which is
1735 already equipped with marble and optical tables and cabinets, and was used to suc-
1736 cessfully assemble two GE1/1 full-size prototypes. The cleanroom (see Figure 5.2(f))
1737 is equipped with clean gas lines (nitrogen and air). The x-ray facility is under con-

1738 construction and will be completed at the beginning of 2015. The site has an operational
 1739 gas system with three (clean) gas lines for ternary gas mixtures instrumented with a
 1740 gas chromatograph station for gas mixture quality control and monitoring.

1741 Table 5.2 gives a list of production sites and the status in fulfilling the required characteristics
 1742 described in the text.

	BARC	INFN - Bari	CERN	FIT	INFN - LNF	UGent
Cleanroom		X	X	X	X	
Leakage current setup		X	X	X	X	X
Gas system	X	X	X	X	X	X
X-ray setup	X	X	X	X	assembling	X
Shipping logistics	X	X	X	X	X	X
GE1/1 prototypes assembled	X	X	X	X	X	X
Past experience	X	X	X	X	X	X

Table 5.2: List of candidate production sites and current status of required characteristics.

1743 5.3.3 Single GE1/1 chamber assembly

1744 Upon receipt of the different components, the production site will start the QC₂ quality check
 1745 procedure to identify possible damage that might have been incurred in transport.

1746 As described before, visual inspection and leakage current measurements are the basis of the
 1747 QC₂ process required to validate the components for assembly. The GEM foils will be tested
 1748 for leakage current and the readout boards will be checked with a dedicated tool capable of
 1749 identifying any possible bending damage.

1750 The assembly procedure is well demonstrated in the video file:
 1751 <https://www.youtube.com/watch?v=Ssuqh5GAVZ4&feature=youtu.be>

1752 The main steps are summarized below, as shown in Figure 5.3.

1753 Step 1: preparation of the drift board

- 1754 • The PCB is equipped with metallic inserts and HV contact probes.
- 1755 • The outer frame is fixed to the PCB thanks to guiding pins.

1756 Step 2: preparation of the GEM stack

- 1757 • The first frame is placed on a rigid support.
- 1758 • The first GEM and the second frame are then placed on top.
- 1759 • The stretching nuts are inserted into the frames.
- 1760 • The third GEM is installed and the last frame then close the stack.

1761 Step 3: installation and stretching

- 1762 • After removing the guiding pins the full stack is placed on the drift plane.
- 1763 • The electrical contacts are checked for every GEM foil and the HV-divider.
- 1764 • The chamber is closed with the readout PCB.
- 1765 • Gas in/outlets are inserted in the outer frame.

1766 The detector is now ready for the Quality Control.

5.3.4 Flatness and planarity check and monitoring

One of the critical steps in the assembly is to certify the tensile properties of GEM foils. This is accomplished using a Moiré interferometric system and a monitoring system that uses fiber Bragg grating (FBG) optical sensors. The required precision is $30\ \mu\text{m}$ in order to measure the $100\ \mu\text{m}$ maximum accepted deviation from planarity [45]. Long-term stability will be monitored by FBG optical strain gauges. This technique has been applied to several detectors in HEP for strain and deformations, temperature and humidity measurements, with a great deal of experience in the collaboration [34–36]. The Moiré system under development in Frascati (see Figure 5.4) is composed of a projector equipped with an optical grating, a photographic camera equipped with an identical grating, the GEM foil mounted on optical slides, and a Laser Displacement System (LDS) to calibrate the Moiré fringes. The sensitivity of the LDS is $1\ \mu\text{m}$.

The systematic error of the LDS connected to the optical slits system was measured by performing back and forth scans on a flat reference surface. The residuals are limited to less than $5\ \mu\text{m}$ (see Figure 5.6).

Preliminary results on a circular target scanned with the LDS (Figure 5.7a) have shown well separated fringes for a $100\ \mu\text{m}$ displacement (see Figure 5.7b). A $30\ \mu\text{m}$ resolution is expected with finer gratings and the implementation of a phase-shift algorithm.

A network of FBG sensors (see Figure 5.5) is used to validate the stretching procedure, to intercalibrate the Moiré interferometry, and to provide a continuous monitoring of stretching planarity. The stretching procedure is validated once by comparing uniformity response of FBG sensors installed in the active area of each GEM foil. A uniform stretching of three foils will be certified by identical response of the three FBG sensors. Intercalibration for Moiré interferometry and continuous monitoring will be provided by FBG sensors located on the edges of the upper GEM plane, in non-active areas.

Preliminary results have shown reliable gluing of FBG sensors on GEM and Apical films (see Figure 5.8), as well as excellent correlation between LDS and FBG displacement measurements (see Figure 5.9).

In Fig.5.10 are shown very preliminary results on how the response of FBG sensors installed on each GEM film, both parallel and perpendicular to the film bases as described in in Fig5.5, provide extremely similar strain pattern when subjected to a tensioning cycle. Once tensioned, the difference in their strain is less than 0.05 mstrain. This preliminary result is a strong and solid indication that the three GEM foils are subject to the same tensile load during the assembly procedure.

5.3.5 Single GE1/1 chamber commissioning

Upon completion of the assembly, the chamber is tested for gas leaks with pure, dry, filtered nitrogen. A chamber is then pressurised up to 20 mbar (maybe even more) and kept under such pressure for some hours. Chambers not leaking will be flushed with Ar/CO₂ and turned on after 12 hours by applying a moderate HV. Thus they would have completed QC_{3–4}.

The next step is QC₅: the gas gain is the most important parameter to characterize GEM detectors. It reflects the good behavior of the GEM foils, the purity of the gas and in general the accuracy of the electric field configuration. The gain is also considered to be a basic measurement and a reference value associated with various properties of a GEM detector. It is therefore extremely important to perform the gain calibration with the greatest care and to fol-

1811 low common techniques at all chamber production sites to facilitate the comparison with other
1812 detectors or results from the literature.

1813 The gain can be reliably measured from the pulse height spectrum of a radioactive source based
1814 on the amplitude of the collected signal compared to the electronic noise, the energy of the
1815 particles emitted by a radioactive source, and the way they interact with the detector.

1816 **5.4 superchamber assembly and production at CERN**

1817 A superchamber (SC) is fabricated by coupling together two GE1/1 GEM single chambers. The
1818 mechanical assembly of a superchamber is shown in Figure 5.11 where one long and two short
1819 superchambers have been prototyped for integration studies purposes.

1820 After gain calibration, at QC₅ a HV voltage scan is performed on the GE1/1 chambers and
1821 relevant parameters (gain, noise, and cluster size are measured) with final electronics, validated
1822 via QC_{el}. These measurements are performed with a cosmic stand and documented as QC₈

1823 **5.4.1 Cosmic ray tests (QC₈)**

1824 The goal of the cosmic ray test is to validate the performance of a chamber and its electronics.
1825 Figure 5.12 shows the cosmic stand setup built at CERN for this purpose. The setup allows
1826 several chambers (up to 10 superchambers) to be tested at the same time. The experimental
1827 setup includes the following features.

- 1828 • Fully automatic HV scan, to allow measurement of the efficiency and spatial resolu-
1829 tion.
- 1830 • Measurement of cosmic muon tracks over a large area of the chamber.
- 1831 • A DAQ system comparable to the one used in the CMS experiment, to test the on-
1832 chamber electronics.
- 1833 • Data Storage and analysis. Raw data will be stored on disk for further offline pro-
1834 cessing. A central software will be developed to allow fast online data analysis.

1835 Once this stage is completed, the superchamber is declared ready for final installation after
1836 documenting QC₉₋₁₀ in the database.

1837 **5.5 Database**

1838 All QA and QC aspects of the assembly procedure and components are stored in a common
1839 database. The DB is based on Oracle and contains the following information.

- 1840 • Main detector components: the chip FrontEnd, GEB board, GEM frames, and cool-
1841 ing. For each component the validation results will be recorded.
- 1842 • Detector assembly: information about the assembly and quality check procedures of
1843 the chamber. It also includes preliminary validation tests: gas leak, channel connec-
1844 tivity, and electrical tests.
- 1845 • Detector performance: includes results from x-ray and cosmic ray tests. It will con-
1846 tain plots from a full HV scan of cluster size, noise, and detector conditions including
1847 threshold, gain, environmental conditions, assembly site, date, location, and opera-
1848 tor.



(a) BARC



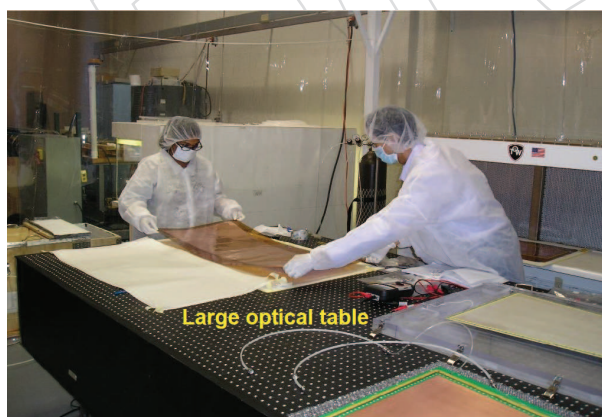
(b) INFN-Bari



(c) CERN



(d) UGent



(e) FIT



(f) INFN-LNF

Figure 5.2: Pictures from different assembly site candidates.

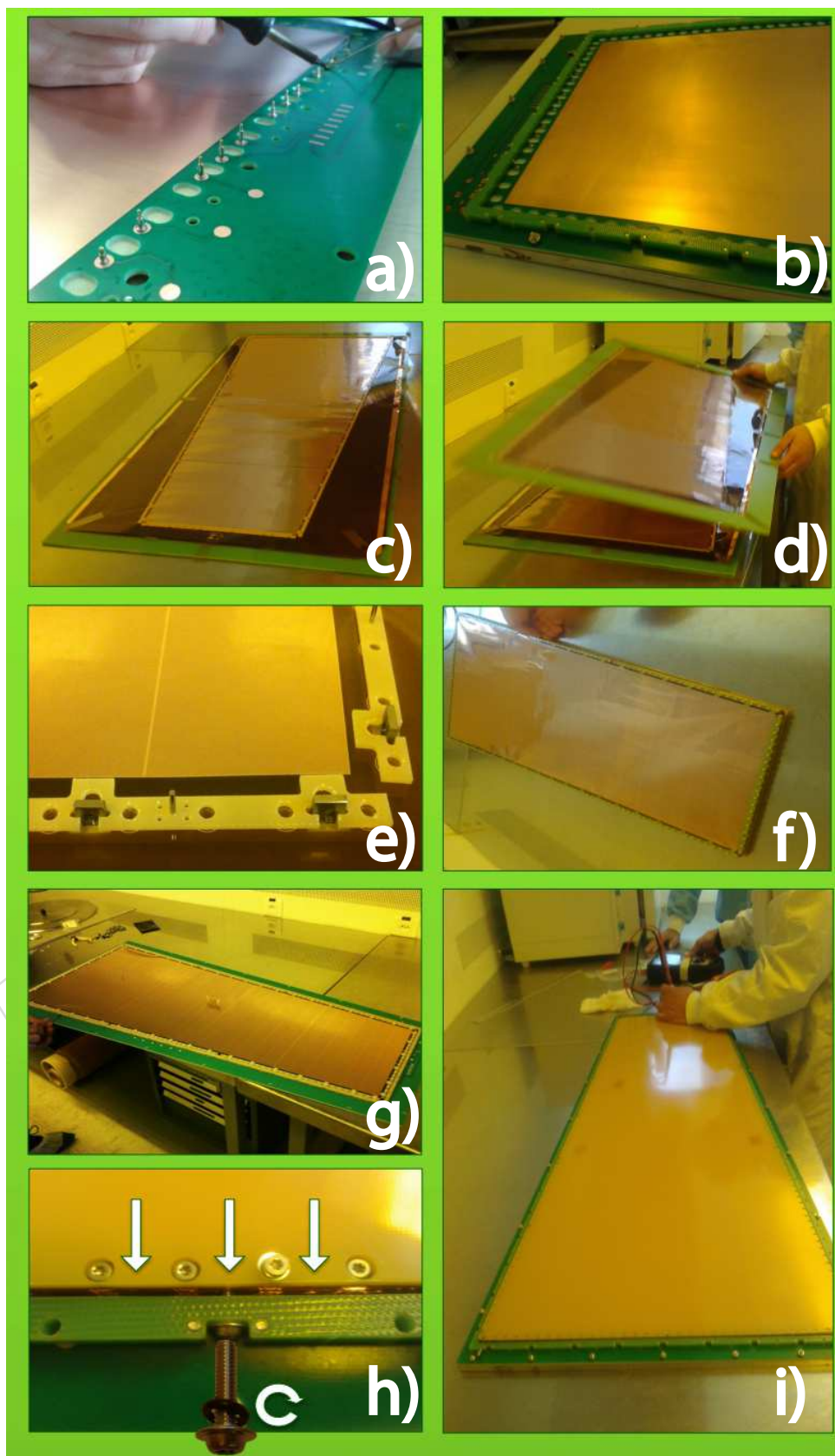


Figure 5.3: Main steps of the GE1/1 chamber construction. a Preparation of the drift board by soldering of the HV spring contacts and deep cleaning of the copper plane, b screwing of the brass pullouts needed for the foil stretching, c-d assembly of the of the GEM foil stack on a separated bench, e insertion of the pulling nuts into the stack frame, f-g the GEM foil stack is moved on the drift board, h the GEM foils are stretched with the dedicated screws, i The GE1/1 chamber is ready to be closed with the readout board

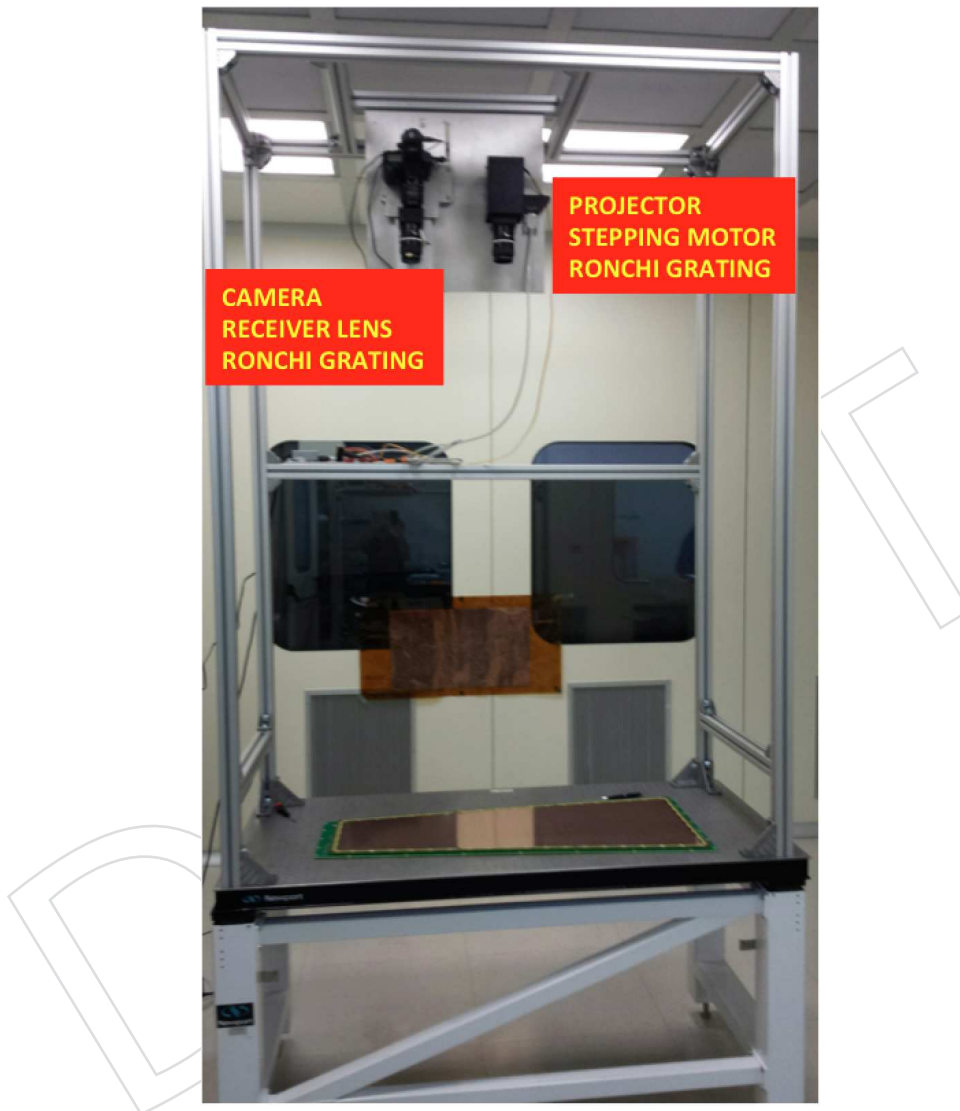


Figure 5.4: Moirè setup in Frascati clean room projecting fringes on a whole GE1/1 GEM chamber. The projector (mounted on a translational stage for phase-shift algorithm) illuminates the GE1/1 with a pattern generated via a Ronchi grating. The receiver lens is equipped with the same Ronchi grating. Moirè fringes are generated on the lens focal plane proportional to the GE1/1 non-planarity.

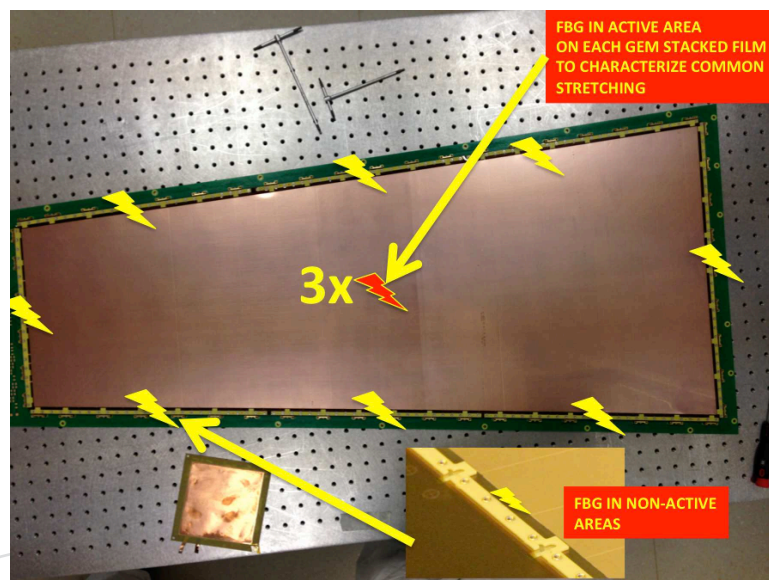


Figure 5.5: FBG sensors on GEM films in a GE1/1 chamber. The sensors in the middle of GEM planes are used once to certify the uniformity of stretching procedure over the three GEM planes. Sensors installed on the upper GEM plane only, provide intercalibration with Moirè and LDS systems, and deformation monitoring.

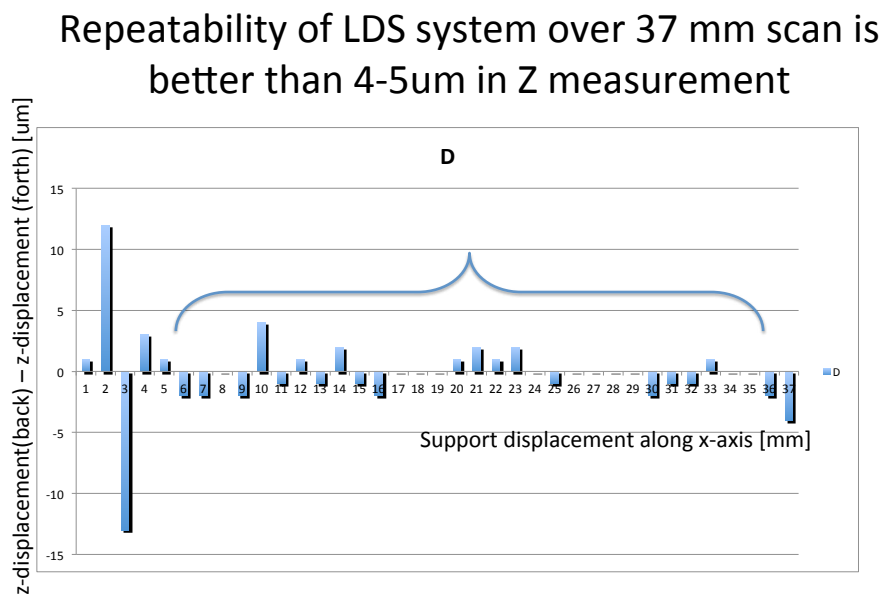
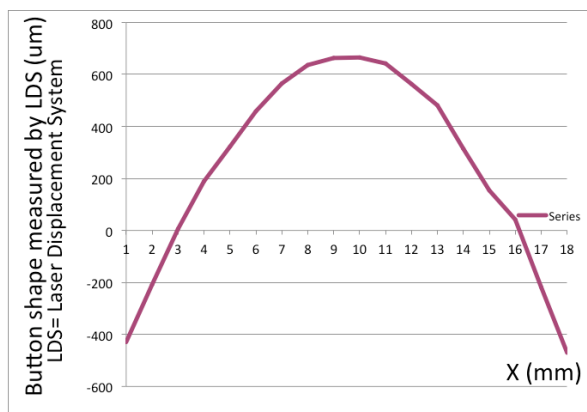
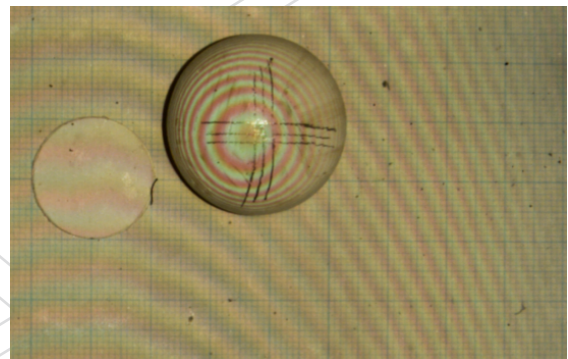


Figure 5.6: Residuals for a back-forth scanning of reference surface with the Laser Displacement System used to calibrate the Moirè fringes. Repeatability of LDS system over a 37-mm scan is better than about 4 μ m in the measurement of z direction (transversal to scan) displacement.



(a)



(b)

Figure 5.7: Fringes on a circular object as scanned by LDS (a); Moiré fringes (b). One-fourth of period is easily visible, hence the estimate on resolution is $100 \mu\text{m}$. Finer grating and phase-shift algorithm will improve resolution to better than $30 \mu\text{m}$.



Figure 5.8: Gluing of a FBG sensor on GEM sample. Glues tested include UHU PWS 24h, 2011 ARALDITE HUNTSMAN, PATTEX PLASTIC HENKEL, UV-RAY WELLOMER UV4028. Glue selected was 2011 ARALDITE whose mechanical properties and radiation hardness are well known. A suitable set of tools and procedures was developed to assure reliable mechanical strength, while still retaining the requirement of minimal glue deposition.

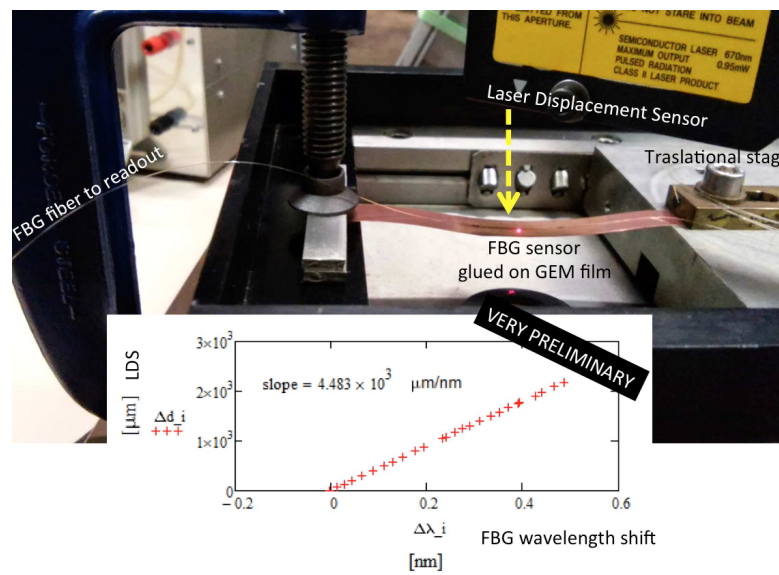


Figure 5.9: Test of gluing a FBG sensor on a GEM film strip. The FBG response is very well correlated with the gravitational sag as measured by LDS. Illustration shows the experimental setup with LDS (top), translational stage pulling the GEM film strip (right), FBG sensor glued on GEM film strip (centre) and optical fiber funnelling the laser light to interrogation system (left).

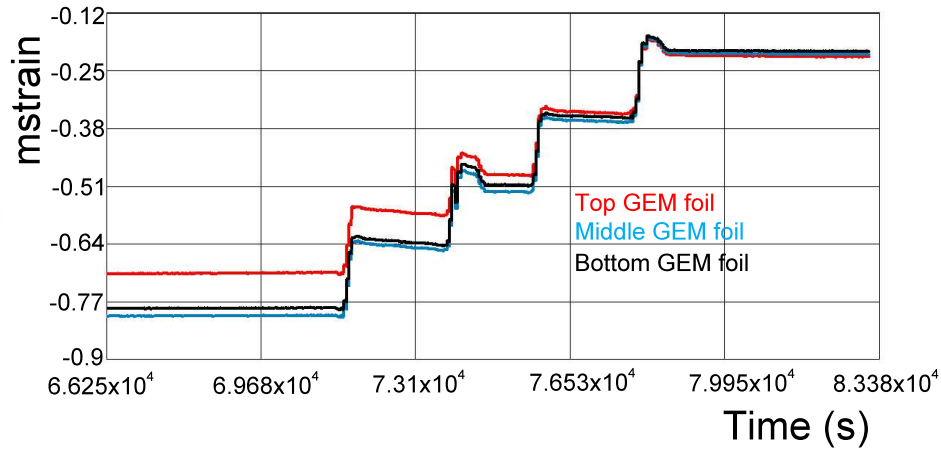


Figure 5.10: Preliminary data on the FBG sensors output during a tensioning cycle. The mechanical tension of the GEM film was varied over time from a non-tensioned state to a tensioned state. The sagitta as measured by LDS relative to the final (tensioned) state is shown (black curve). Two sets of sensors are used, i.e. perpendicular of parallel to the GEM film bases. Each set is composed of three sensors each glued on a GEM film. The sensors output (shown in strain units) is very consistent and uniform during the film tensioning, and, in the tensioned final state, is equal to better than 0.05mstrain.

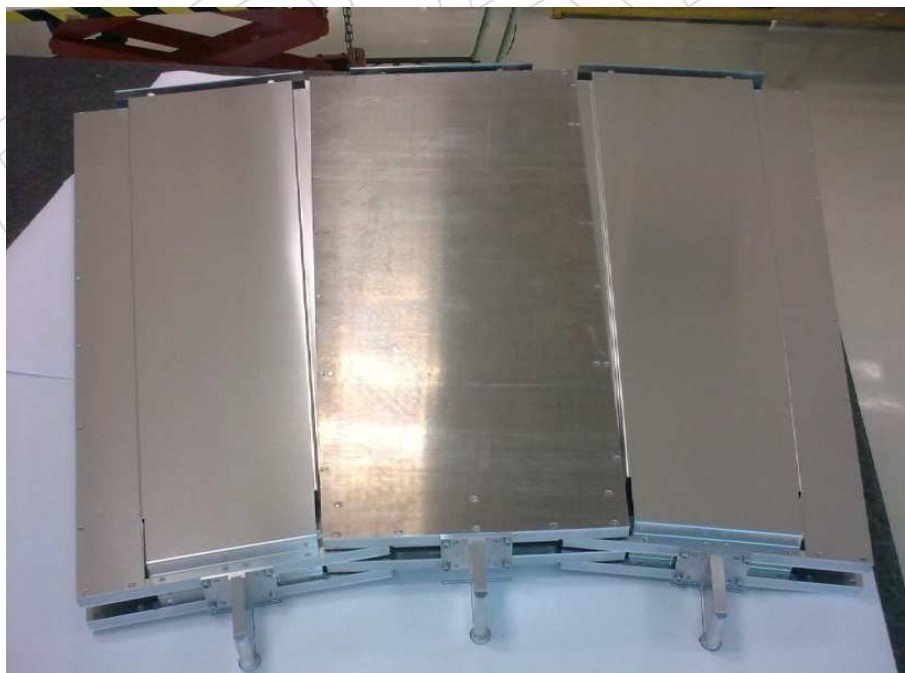


Figure 5.11: GEM dummy superchambers.



Figure 5.12: Schematic view of the Cosmic Stand at CERN. In the picture are visible the two mock-up of a GE1/1 superchamber. The cosmic stand can accommodate up to 15 superchambers

1849 Chapter 6

1850 System Performance

1851 **Editors:** A. Colaleo, A. Safonov

1852 **Contributors:** C. Calabria, A. Castaneda, F. Cavallo, A. Colaleo, S. Dildick, P. Giacomelli, T.
1853 Huang, A.K.Kalsi, V. Krutelyov, J. Lee, R. M.Hadjiiska, K. Hoepfner, M. Hohlmann, A. Mag-
1854 nani, A. Mohapatra, R. Radogna, C. Riccardi, A. Safonov, A. Sharma, R. Venditti, F. Zenoni.

1855 The overarching goal of the proposed upgrade is to avert a potential significant deterioration
1856 of the CMS muon triggering capabilities in the range $1.6 < |\eta| < 2.2$ once the instantaneous
1857 luminosity approaches and exceeds $1.7 \times 10^{34} \text{ cm}^{-2}\text{s}^{-1}$. As the affected range represents well
1858 over a quarter of the overall CMS muon coverage, such deterioration could significantly affect
1859 the CMS physics reach.

1860 The very forward region is the most challenging for muon triggering and reconstruction due
1861 to exceptionally high background rates and a much reduced magnetic field. These effects com-
1862 plicate pattern recognition and reduce momentum resolution. Despite being operated in the
1863 harshest environment, the very forward part of the muon detector currently has the least red-
1864 undancy in the entire muon system. While in the range $|\eta| < 1.6$ muon hits are reconstructed
1865 by at least two muon detector systems (either DT+RPC, or CSC+RPC), the region of $|\eta| > 1.6$
1866 relies on the CSC system alone, as at the time of the CMS construction the available RPC tech-
1867 nology did not meet the requirements for operating at such high rates. Fig. 6.1(Left) illustrates
1868 these observations by showing the average number of muon layers with hits for a typical muon
1869 as a function of muon η overlaid with the flux of background particles.

1870 Maintaining efficient muon triggering in the forward region at increased luminosity represents
1871 a particular challenge. With the current system, the inclusive muon trigger rate features a rapid
1872 growth with the increasing η , as illustrated in Fig 6.1(right). Already at $\mathcal{L} = 1.7 \times 10^{34} \text{ cm}^{-2}\text{s}^{-1}$,
1873 maintaining the Level-1 trigger threshold of $p_T > 15 \text{ GeV}$, at which the efficiency for muons
1874 with $p_T > 20 \text{ GeV}$ reaches the plateau, would generate a trigger rate of 10 kHz from this region
1875 alone. This is comparable to the single muon trigger rate for the entire muon trigger in Run
1876 1 and is one tenth of the entire CMS Level-1 bandwidth of 100 kHz, which will not increase
1877 until after LS3. The upgrade of the CMS Level-1 trigger electronics capabilities [42] planned
1878 in anticipation of instantaneous luminosity increases following the LS2, muon track finders
1879 will simultaneously use hits from all available detector systems (DT, CSC, RPC) to reconstruct
1880 candidate tracks and measure their momenta. Efficient use of the available redundancy im-
1881 proves muon trigger efficiency and reduce rate driven by p_T mismeasurements in the region of
1882 $|\eta| < 1.6$, but not in the range $|\eta| > 1.6$ where no redundancy is available. Trigger threshold
1883 studies in [42] show that achieving an acceptable trigger rate for muons with $p_T > 22 - 25 \text{ GeV}$
1884 is not possible without substantial additional efficiency losses in the endcap half of the overall
1885 CMS muon coverage.

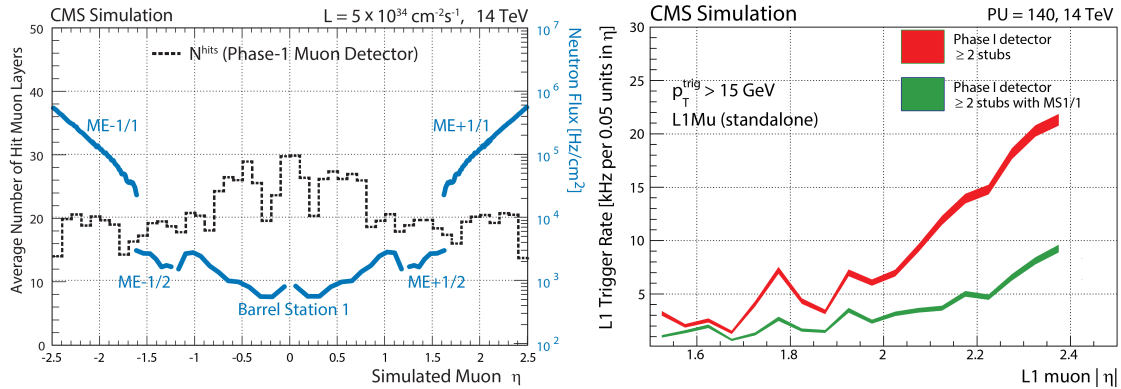


Figure 6.1: (Left): The average number of muon layers with reconstructed hits for a simulated muon as a function of η . It is compared to the flux of neutrons in Hz/cm² shown as colored curves (note the log scale on the right), which are the dominant cause of background hits, for the muon station first crossed by a muon with a given η . Forward region is exposed to the highest rates in the system, yet has the fewest muon layers needed for offline and trigger reconstruction and momentum measurement. Depending on the detector type the conversion factor can vary somewhat, but typically the hit rate is of the order of 0.2% of the neutron flux. (Right): Trigger rate as a function of η shows a large increase towards high η due to the increased particle rates and weakening magnetic field.

1886 The proposed GE1/1 upgrade addresses these concerns, both for the period between LS2 and
 1887 LS3 and beyond into the HL-LHC era. First, it will allow maintaining a robust muon trigger
 1888 in essentially the full range of current muon coverage by reducing the contribution from
 1889 $1.6 < |\eta| < 2.2$ by an order of magnitude. Second, strengthened redundancy of the system in
 1890 the forward region will add to the robustness of the trigger and offline performance by provid-
 1891 ing means to reduce performance losses if parts of or entire CSC chambers become inoperable;
 1892 these situations are unavoidable in real life operations and will become increasingly difficult to
 1893 anticipate with the system aging. Third, the design of the GE1/1 system allows a seamless in-
 1894 tegration into the CMS muon offline reconstruction and identification adding to its robustness
 1895 and performance. Maintaining reasonably low muon thresholds has an important impact on
 1896 a broad range of physics scenarios relevant for the period of Phase-I LHC operation following
 1897 the LS2, when large amounts of data are to be collected. Some of the examples of physics pro-
 1898 cesses for which the sensitivity is dependent on low muon trigger thresholds include scenarios
 1899 with “compressed” SUSY scenarios yielding low momenta leptons, SM Higgs measurements
 1900 in $h \rightarrow \tau\tau \rightarrow \mu + X$, or resonant production of higgs boson pairs via $H \rightarrow hh \rightarrow \tau\tau bb$ predicted
 1901 in models with extended Higgs sectors[46] relevant in many contexts including studies related
 1902 to electroweak baryogenesis [47]. These considerations are not limited to the case of the inclu-
 1903 sive muon trigger, as the reduction of the Level-1 rate in the most difficult region allows lower
 1904 Level-1 thresholds across the board for inclusive muon trigger, di-muon trigger, and all of the
 1905 muon+X triggers without increasing their rate.

1906 The improvements in muon trigger and reconstruction brought by the GE1/1 upgrade will
 1907 continue playing a critical role in maximizing the CMS physics reach in the post-LS3 HL-LHC
 1908 environment. The GE1/1 detector has been designed in anticipation of future integration with
 1909 other planned Phase-II CMS upgrades, of which the most notable for muon performance is
 1910 the addition of the tracking trigger with its excellent momentum resolution. Preserving the
 1911 high performance of the standalone muon trigger is essential in designing the ultra-high pu-
 1912 rity muon trigger, based on matching tracks from the tracking trigger with standalone muon

1913 candidates, and ensuring its stable performance. The latter is true not only for Level-1, but also
1914 for the High Level Trigger, which uses a variant of the offline standalone muon reconstruction.
1915 The redundancy provided with the deployment of GE1/1 improves the quality of standalone
1916 muon reconstruction and can avert a deterioration in standalone muon momentum resolution
1917 if the performance of the aging ME1/1 system degrades. Incidentally, standalone muon trig-
1918 gering and reconstruction capabilities will also remain of critical importance on its own due
1919 to its unique role in enabling sensitivity to new physics scenarios predicting new long living
1920 particles via their decays to pairs of muons.

1921 In this Chapter, we discuss the impact of the new GE1/1 detector in improving the capabil-
1922 ities of the muon system and present a detailed evaluation of the projected performance of
1923 the upgraded detector. We also describe the tools and methods developed to perform these
1924 studies, trigger and reconstruction algorithms, and provide details of important intermediate
1925 measurements that our conclusions rely on.

1926 **6.1 Background evaluation and modeling the high luminosity en-** 1927 **vironment**

1928 The high collision rates at the new energy and luminosity regime of the LHC gives rise to an ex-
1929 treme radiation environment. High background particle rates complicate signal identification
1930 and can have a significant impact on the performance of the detectors themselves, in extreme
1931 cases making them inoperable. These considerations place high emphasis on the accurate eval-
1932 uation of the expected background rates in the region where a new detector will be installed;
1933 this is particularly true for the very forward region where these background are especially high.

1934 The cavern background consists of a gas of neutrons, photons, electrons and positrons in a
1935 wide energy spectrum filling the CMS cavern during LHC operation. The neutron induced
1936 background is the most significant contribution, which determines the hit rate and occupancy
1937 in the muon detectors. This background has a long lifetime as neutrons can propagate for
1938 seconds without interacting. Neutrons are produced in interactions of hadrons produced in
1939 primary pp collisions with the material of the beam pipe and the structures positioned in the
1940 very forward region (very forward calorimeter (HF), beam collimator and shielding). The spec-
1941 trum of these long-lived neutrons ranges between the thermal region and a few GeV. The slow
1942 neutron capture by nuclei with subsequent photon emission in the detector material yields
1943 photons and consequently electrons capable of producing detectable amounts of ionization in
1944 gas detectors.

1945 The radiation environment is a key consideration in selecting detector technology and the sub-
1946 sequent detector design. The high occupancy and hit rate can lead to inefficiencies in detector
1947 response, degraded resolutions and momentum mismeasurements, or can render the detector
1948 inoperable. It can also yield an unacceptably high rate of track misreconstructions and con-
1949 tributes to the trigger rate. Moreover, the high flux of incident particles can lead to radiation
1950 damage of the electronics as interactions leading to anomalous local deposits of radiation can
1951 disrupt electronic signals (single event upsets), or destroy the components (single event dam-
1952 age). Therefore, evaluation of the background flux is an important prerequisite for correctly
1953 ascertaining its effects on the detector and trigger performance, aging of the detectors and elec-
1954 tronics.

1955 Evaluation of the improvements in the overall CMS detector performance with the addition of
1956 the GE1/1 system relies on detailed simulation developed and integrated with the standard
1957 for CMS GEANT-based CMSSW framework. CMSSW includes GEANT-based propagation of

1958 particles through the detector material, digitization packages used for emulating detector and
 1959 electronics response, trigger simulation and event reconstruction. The standard CMSSW sim-
 1960 ulation workflow does not allow simulating the long-lived backgrounds in one go with the
 1961 particles arriving immediately following the beam crossing. This is because of a cut-off imple-
 1962 mented in CMSSW on the time GEANT is allowed to propagate particles in order to optimize
 1963 the time required to generate the events. Therefore, inclusion of the long-lived background
 1964 contributions in CMSSW is performed by first evaluating the rate and the properties of the
 1965 “hits” due to long-lived backgrounds followed by embedding hits emulating the contribution
 1966 of the long-lived backgrounds into the CMSSW simulated data events. We use the CMS adap-
 1967 tation of the FLUKA package to calculate particle fluxes, which are then convoluted with the
 1968 parameterization of the GE1/1 detector response obtained using a dedicated GEANT simula-
 1969 tion study.

1970 6.1.1 Evaluation of the backgrounds due to long-lived neutrons

1971 The study of the long-lived component of the cavern background is performed using the FLUKA
 1972 simulation tool. FLUKA allows the evaluation of the fluxes of long-lived neutrons and sec-
 1973 ondary particles produced in interactions of neutrons with the material of the detector (sec-
 1974 ondary particles capable of reaching GE1/1 chambers are typically produced at the edges of
 1975 the volumes surrounding the enclosures where chambers are positioned). These fluxes are then
 1976 convoluted with the chamber sensitivities in order to obtain the hit rates.

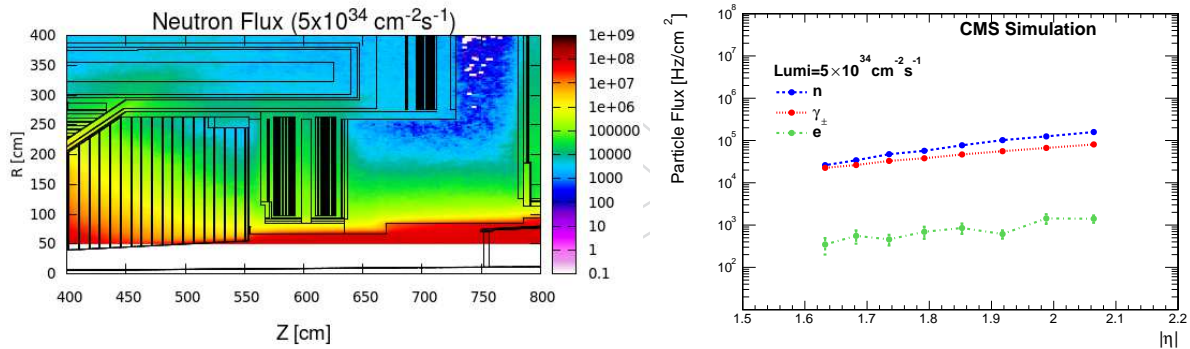


Figure 6.2: (Left) The 2D flux map for neutrons normalized to an instantaneous luminosity of $5 \times 10^{34} \text{ cm}^{-2} \text{ s}^{-1}$ and overlaid on the diagram showing the detector elements. (Right) Particle flux for GE1/1 region as a function of the pseudorapidity range assuming an instantaneous luminosity of $5 \times 10^{34} \text{ cm}^{-2} \text{ s}^{-1}$.

1977 The CMS adaptation of the FLUKA package contains a detailed description of the dimensions
 1978 and material composition of each of the detector subsystems, i.e. tracking, calorimetry, muon
 1979 system, etc. The validity of FLUKA predictions in the CMS environment has been extensively
 1980 studied using Run 1 data and the comparison shows a good agreement. To estimate the par-
 1981 ticle flux, we use the geometry corresponding to the Run 2 configuration of the CMS detector,
 1982 which accounts for the planned improvements to the central beampipe and muon chamber
 1983 shielding description in comparison with the version used for Run 1. FLUKA simulation has
 1984 been setup with the beam energy of 7 TeV. The energy cut-off, below which the particles are
 1985 no longer tracked, for neutrons has been set as 10^{-14} GeV. The corresponding cut-offs values
 1986 for photons, electrons and positrons vary between 10^{-5} and 10^{-3} GeV depending on the de-
 1987 tector region. The results of the simulation are saved as a set of flux maps for each particle
 1988 specie, as illustrated in Fig. 6.2(Left) showing the neutron flux map for the region surrounding

1989 the location of the future GE1/1 detector. Fig. 6.2(Right) shows the predicted flux of neutrons
 1990 through the volume corresponding to the location of the GE1/1 chambers as a function of
 1991 pseudorapidity η . The same figure shows the simulation prediction for the flux of photons and
 1992 electrons arising from neutron interactions in the material surrounding the enclosure that the
 1993 GE1/1 chambers will be installed in. Table 6.1 provides the numeric estimates of the particle
 1994 flux through the top, middle and the bottom parts of the GE1/1 chambers for $\mathcal{L} = 1 \times 10^{34}$
 1995 $\text{cm}^{-2} \text{s}^{-1}$ and $\mathcal{L} = 5 \times 10^{34} \text{cm}^{-2} \text{s}^{-1}$.

Table 6.1: FLUKA predictions for the particle fluxes through the volume where the GE1/1 chambers are to be installed. Flux values are provided for each particle type and four points in the (R,z) coordinates corresponding to the bottom, lower middle, super middle, and the top parts of the chamber.

Particle type	R (cm)	z (cm)	Flux (Hz/cm ²) for $\mathcal{L} = 10^{34} \text{cm}^{-2} \text{s}^{-1}$	Flux (Hz/cm ²) for $\mathcal{L} = 5 \times 10^{34} \text{cm}^{-2} \text{s}^{-1}$	Flux uncertainty (%)
Neutrons	150	560	2.9×10^4	1.5×10^5	1.5%
	170	560	2.0×10^4	1.0×10^5	1.7%
	190	560	1.3×10^4	0.6×10^5	1.9%
	210	560	0.9×10^4	0.4×10^5	2.3%
Photons	150	560	1.5×10^4	7.6×10^4	1.8%
	170	560	1.1×10^4	5.6×10^4	2.0%
	190	560	0.8×10^4	4.1×10^4	2.1%
	210	560	0.6×10^4	3.0×10^4	2.3%
Charged	150	560	2.8×10^2	1.4×10^3	16.4%
	170	560	2.0×10^2	9.8×10^2	21.4%
	190	560	1.2×10^2	6.2×10^2	24.0%
	210	560	1.0×10^2	5.2×10^2	26.0%

1996 Evaluation of the rate of the hits generated in the chambers by the backgrounds induced by the
 1997 long-lived neutrons requires knowledge of the flux for each particle type and the probability
 1998 for a given type of particle to generate a spurious signal in the detector. The latter probability,
 1999 referred to as the detector sensitivity, depends on the particle energy and the direction it crosses
 2000 the outer surface of the chamber. When neutrons or photons enter a GEM chamber, their inter-
 2001 actions with the material of the detector gives rise to secondary particles which can reach the
 2002 gas gaps and generate signal. Electrons and positrons can generate signal directly by penetrat-
 2003 ing the chamber and ionizing the gas or can cause electromagnetic showers by interacting with
 2004 the walls or the inner structures of the chamber, in which case the signal can be generated by
 2005 secondary particles.

2006 The sensitivity of the GE1/1 chambers to neutrons, photons, electrons and positrons is evalu-
 2007 ated with a standalone simulation using Geant4.9.6.p02 and the FTTP_BERT_HP physics list [48]
 2008 known to provide an accurate description of neutron interactions with matter down to thermal
 2009 energies). The detector being modeled is the GE1/1 superchamber (two trapezoids with the
 2010 height of 1283 mm and the lengths of the large and the small bases of 510 mm and 279 mm,
 2011 respectively, stacked one on top of the other and separated by 3.7 mm) complete with a full
 2012 material description, see Table 6.2. In the simulation, particles of fixed energy and given type
 2013 cross the outer surfaces of the superchamber with uniform density over the outer surface of the
 2014 chamber frame and with the incident angles distributed according to the angular distribution

Table 6.2: Layer structure of a single GE1/1 chamber as implemented in Geant4

Layer	Material	Thickness (mm)
Aluminum frame	Al	1.0
Cooling pipe	Cu (filled with H ₂ O)	8 external \varnothing , 6 inner \varnothing
Cooling pads	Cu	1.0
GEB board	Cu/FR4	0.140/0.856
Readout board	Cu/FR4/Cu	0.035/3.2/0.035
Induction gap	Ar:CO ₂ :CF ₄ (45:15:40)	1.0
GEM 3	Cu/Kapton/Cu	0.005/0.050/0.005
Transfer gap 2	Ar:CO ₂ :CF ₄ (45:15:40)	2.0
GEM 2	Cu/Kapton/Cu	0.005/0.050/0.005
Transfer gap 1	Ar:CO ₂ :CF ₄ (45:15:40)	1.0
GEM 1	Cu/Kapton/Cu	0.005/0.050/0.005
Drift gap	Ar:CO ₂ :CF ₄ (45:15:40)	3.0
Drift board	Cu/FR4/Cu	0.035/3.2/0.035

2015 obtained in the FLUKA simulation study described earlier. The simulation is repeated for each
 2016 particle type scanning over a range of particle energies. Events, in which at least one charged
 2017 particle tracked by GEANT reaches the drift volume or the first transfer gas gap of either of the
 2018 two stacked GEM chambers, are assumed to yield a valid signal in that chamber. The minimum
 2019 energy thresholds for secondary particles production in GEANT has been set to about 1 keV
 2020 for all types of particles except protons and nuclei, for which the threshold has been completely
 2021 removed.

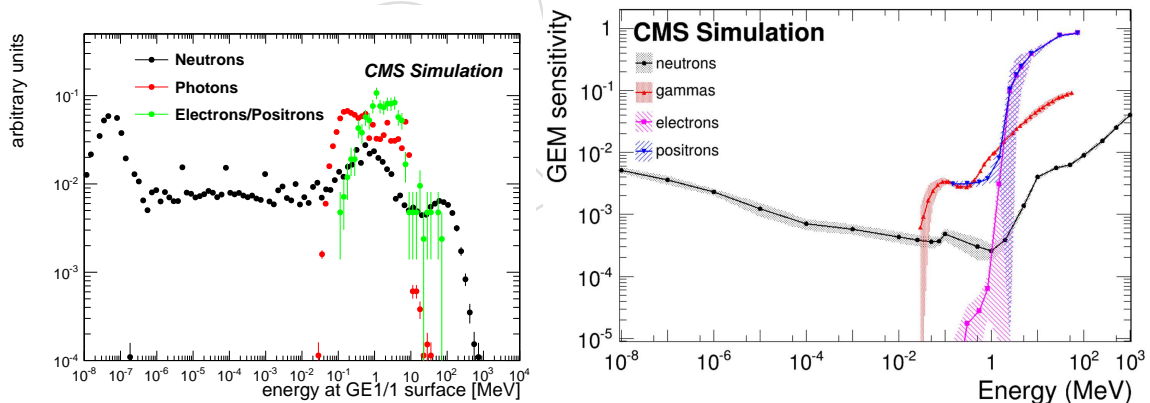


Figure 6.3: (Left) The energy spectrum of incident particles crossing the GE-1/1 chambers predicted using FLUKA. (Right) Energy-dependent sensitivity, defined as the probability to produce a measured hit in the chamber, of the GE-1/1 chamber to neutrons, photons, electrons, and positrons, as a function of the incident particle energy.

2022 The final detector sensitivities we seek to obtain require averaging over both the angular and
 2023 energy spectra of the background particles. While the averaging over particle directions is
 2024 included at the generation stage, proper inclusion of the energy dependence is very important
 2025 as particle energy spectra are changing by orders of magnitude in the range of interest, as
 2026 illustrated in Fig. 6.3(Left). Just as for angular distributions, the energy spectra are extracted
 2027 from the FLUKA simulation. The sensitivity at a given particle energy is computed as the

2028 fraction of all generated events, in which a signal is observed, for each of the two detectors
 2029 in the superchamber. The sensitivity for the two chambers in a superchamber are found to be
 2030 very similar and the difference is taken as the systematic uncertainty. The latter is combined in
 2031 quadrature with the statistical error for the total uncertainty. Thus obtained energy dependent
 2032 sensitivities are shown in Fig. 6.3(Right) with the bands indicating the total uncertainty. The
 2033 final average sensitivities are computed as a convolution of the energy spectra with the energy
 2034 dependent sensitivities for each particle type and are shown in Table 6.3. In the neutron case,
 2035 the error includes an additional systematic uncertainty related to the Geant4 model used to
 2036 simulate low energy neutron interactions.

Table 6.3: Sensitivity results for GE1/1. The errors include both the statistic and the systematic uncertainty related to the different response of the two layers of chambers installed in an even and the odd configuration. In the neutron case, also a source of systematic uncertainty related to the Geant4 model used to simulate low energy neutron interactions is included.

	Sensitivity (%)
neutrons	0.24 ± 0.07
photons	0.99 ± 0.04
electrons	8 ± 3
positrons	8 ± 3

2037 Final computation of the detector hit rates induced by long-lived neutrons is performed by
 2038 summing up the contributions from neutrons, photons and charged particles. Each contribu-
 2039 tion is calculated as the particle flux (Fig. 6.2(Right)) weighted by the corresponding average
 2040 sensitivity (Table 6.3). The combined hit rate as a function of η is shown in Fig. 6.4 along with
 2041 the individual contributions from neutrons, photons and charged particles.

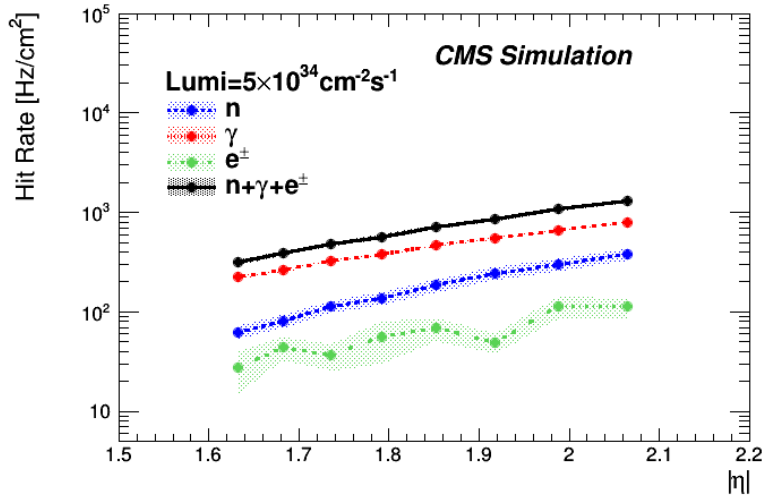


Figure 6.4: The expected contribution to the GE1/1 detector per-chamber hit rate associated with the backgrounds induced by long-lived neutrons for instantaneous luminosity of $5 \times 10^{34} \text{cm}^{-2} \text{s}^{-1}$ as a function of pseudorapidity.

6.1.2 Implementation of the GE1/1 system in the CMSSW framework

The integration of the GE1/1 detector into the full GEANT-based CMSSW framework has been a necessary step for the design of the algorithms and performance studies related to trigger, reconstruction and identification. The geometry and the material description the GE1/1 detectors has been integrated into the common CMS detector description used by GEANT. A second required step is the digitization, which uses the ionization energy deposits generated by GEANT to emulate signals measured in detector electronics according to an appropriate model. As standard CMSSW does not include simulation of the long living particles, we use the digitization step to embed the hits due to the long-living backgrounds using the measurements described earlier. In the following, we describe the details of modeling implemented in the digitization procedure.

Similar to the implementation of the simulation of other CMS sub-detectors, GE1/1 digitization uses a parametric model derived using a combination of test beam data analysis results and specialized simulation studies of the detector response. In the digitization process, energy deposits generated by GEANT for all particles crossing the detector are first individually converted into detector signals, i.e. signals induced on the detector readout strips or groups of strips. The digitization model takes into account the type of particle depositing energy as well as the time of the particle arrival, which is additionally smeared for the detector timing resolution. Next, the electronics noise is added, which in GE1/1 case is also used to embed detector signals associated with the long-living backgrounds that are not simulated in standard CMSSW. Next, the overlapping signals are merged, pruned as necessary and assigned to the corresponding 25 ns clock windows, which associate signals with the LHC bunch crossings. In the following, we describe the default parameters used in the GE1/1 digitization model.

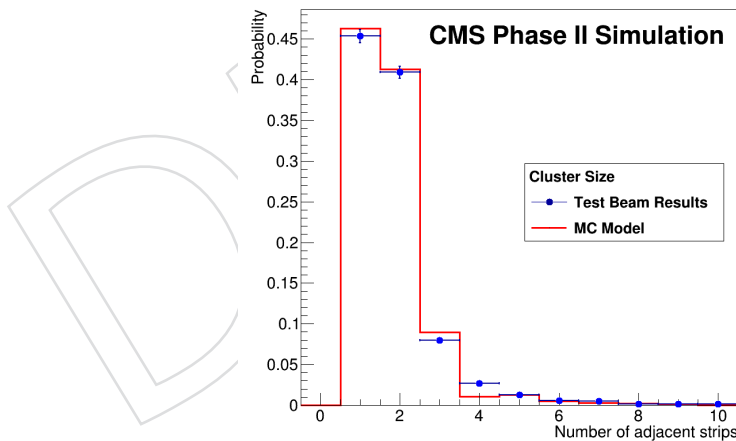


Figure 6.5: Comparison of the cluster size distribution obtained with the CMSSW simulation (line) compared with the test-beam measurements, which have been used to model the detector response in CMSSW.

- Efficiency:** The registration efficiency is set to 98% for true muons crossing an individual chamber, which follows the results of the test beam studies [17]. The efficiency for all other particles crossing the chamber, e.g. photons from muon showering, follow the results of the sensitivity studies presented in the previous section.
- Timing:** The true time at which the particle crosses the chamber is first adjusted by subtracting the time of flight for a muon from the nominal interaction point to the

2071 centre of the chamber to emulate future t_0 calibration of the detector readout. Next,
2072 it is smeared according to the timing resolution set to $\sigma = 5$ ns following a Gaussian
2073 distribution. Finally, the time is corrected for the signal propagation time along the
2074 strip and the resultant time is used in assigning signal to the corresponding time
2075 window (bunch crossing).

- 2076 • **Cluster size:** The readout strips are set “on” (GE1/1 electronics readout is binary)
2077 according to the geometrical location of the hit and according to the signal shape
2078 measured in the test beam data for charged pions. The latter is implemented by
2079 setting additional adjacent strips “on” based on the probability function extracted
2080 from the test beam data. The mean value of the measured and simulated cluster size
2081 has been found to be ~ 1.8 . A validation of the procedure is illustrated in Fig. 6.5
2082 comparing the cluster size in the simulation using the digitization model with the
2083 test beam data.
- 2084 • **Neutron-induced background and intrinsic noise:** modeling of the long-living back-
2085 ground is implemented following the results of the simulation-based hit rate mea-
2086 surement described in the previous section. The embedding of spurious signals
2087 due to photons, neutrons and charged particles follows parameterized η -dependent
2088 functions extracted from the results illustrated in Fig. 6.4. Signals shapes follow
2089 the same cluster model as for muons and pions and the time assignment follows a
2090 flat distribution. The intrinsic noise rate has been estimated as ~ 0.01 Hz/cm² and
2091 deemed negligible.

2092 The implementation of the GE1/1 digitization model with a realistic detector response and the
2093 inclusion of the neutron-induced backgrounds in the CMSSW framework allows the evaluation
2094 of the impact of GE1/1 upgrade on the overall performance of the CMS experiment. Simulation
2095 studies of muon trigger and offline reconstruction performance presented in the remainder of
2096 this chapter are carried out in the context of the common CMSSW framework.

2097 6.1.3 Summary of the GE1/1 detector hit rates

2098 The fully inclusive detector hit rate for the GE1/1 system is a sum of the hit rates due to the
2099 prompt and long-living backgrounds. Figure 6.6 shows the contributions of each of these two
2100 components obtained using the simulation in the context of CMSSW for the instantaneous lu-
2101 minosity $\mathcal{L} = 5 \times 10^{34}$ cm⁻²s⁻¹. Note that Fig. 6.6(left) compares the hit rate using a sam-
2102 ple simulated in CMSSW with the FLUKA-based predictions used as input to the digitization
2103 model, which is essentially a closure test. The majority of the prompt component of the hit rate
2104 is due to the secondary electrons and positrons arising from Compton scattering, secondary
2105 ionization, conversions, and e^+e^- pair production. Secondary muon contributions arise from
2106 nuclear interactions of hadrons in the calorimeter and the absorber, heavy flavor, and decays in
2107 flight. The energy spectrum of secondary particles is dominated by very low energy particles.
2108 The prompt particle rates are evaluated using sample with minimum bias events simulated
2109 with CMSSW. The integrated number of hits in a given η partition is normalized to the sen-
2110 sitive area of the partition and the full simulated time. The time of flight of the particles has
2111 been counted with respect to the primary interaction and the time cut-off has been set to 500
2112 ns. However it is important to note that about 70% of the particles cross the GE1/1 detection
2113 planes within the first 50 ns. The right plot on the Fig. 6.6 shows the obtained rates as a function
2114 of the distance from the center of the partition to the beam pipe.

2115 It is important to note that the estimated GE1/1 detector hit rate of up to a few kHz is much
2116 lower than the rates existing GEM detectors have been exposed in other working experiments.

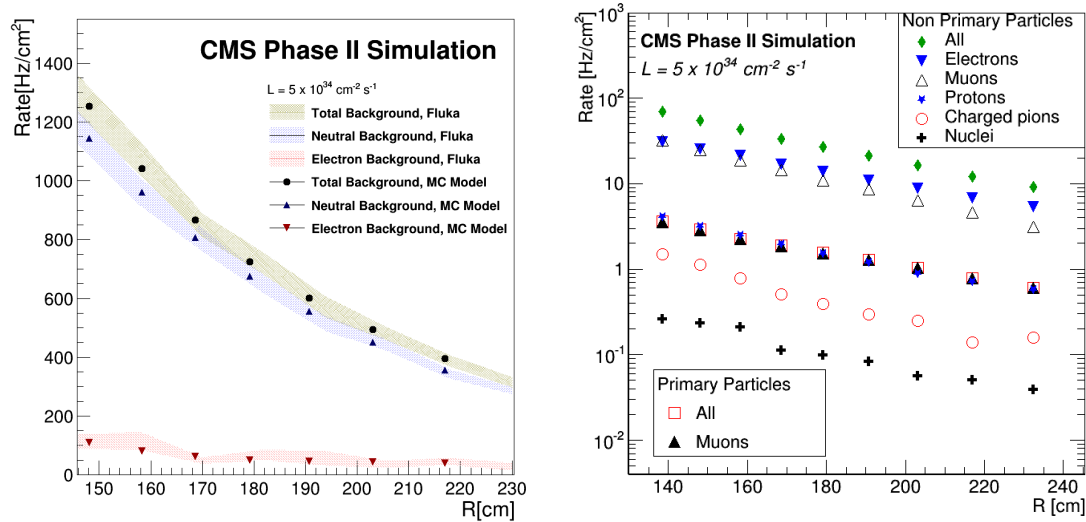


Figure 6.6: (Left): The GE1/1 hit rate due to neutron-induced backgrounds obtained with the CMSSW simulation (data points) compared with the FLUKA prediction used to model these backgrounds in CMSSW (the width of the band indicates the uncertainty). (Right): Rates of prompt particles reaching GEM detector planes in the first endcap station as a function of the radial distance to the beam pipe.

2117 Results of the simulations can be used to calculate the total neutron fluence and the total irradiation dose accumulated by the GE1/1 chambers. After accumulating 3000 fb⁻¹ of integrated
 2118 luminosity, the total dose amounts to 1kGy (100 kRad) at the highest eta region of GE1/1 chambers. We therefore conclude that the background environment of the future GE1/1 detector is
 2119 adequate for a safe and reliable long-term operation of a GEM-based detector (Sec. 2.2.2.3).
 2120
 2121

2122 6.2 Muon trigger performance

2123 Maintaining efficient Level-1 muon triggering in the forward region $|\eta| > 1.6$ becomes progressively more difficult as the instantaneous luminosity increases. The very forward region is
 2124 inherently challenging due to low magnetic field and high background rates, which is further
 2125 exacerbated by the lack of redundancy as the region is only instrumented by the CSC detector.
 2126 As a result, the trigger rate shows a fast growth towards higher η illustrated in Fig 6.1(right).
 2127 The lack of redundancy in the region $|\eta| > 1.6$ will become even more pronounced with the
 2128 deployment of the upgraded muon trigger in 2016, capable of including hits from all available
 2129 detectors in the track momentum fit. That essentially doubles the number of “guaranteed”
 2130 points on tracks within ensuring a good muon momentum measurement and reducing the
 2131 trigger rate, which is driven by soft muons with mismeasured momentum, but only in the
 2132 region of $|\eta| < 1.6$ where such redundancy is available.
 2133

2134 The GE1/1 upgrade provides an effective solution to the trigger rate problem and allows CMS
 2135 to preserve its excellent muon triggering capabilities in the range $|\eta| < 2.2$ until the LS3 and
 2136 beyond. Low muon trigger thresholds have an important impact on Higgs physics, searches
 2137 for new physics with extended Higgs sectors, and a broad range of SUSY scenarios. Among
 2138 the latter, both conventional and the difficult for the LHC split [49, 50] and anomaly mediated
 2139 [51, 52] SUSY, which require targeting lower rate electroweak production of gauginos, are

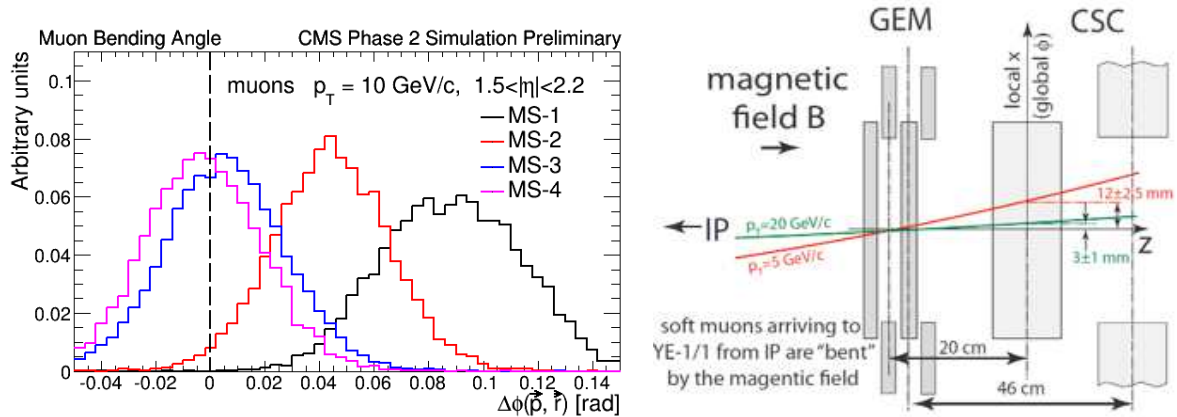


Figure 6.7: (Left) Azimuthal bending angle of a simulated 10 GeV muon with respect to a normal vector to a CSC chamber, comparing the distributions for the four stations. (Right) Sketch of a measurement of the bending angle with a pair of a CSC and a GEM chamber, illustrating discrimination between lower and higher momentum muons.

2140 relevant, particularly in scenarios with “compressed” mass spectra. With the deployment of
 2141 the Level-1 tracking trigger in LS3, standalone muon trigger candidates will be matched to the
 2142 inner tracks allowing for ultra-high purity muon triggering. Throughout the HL-LHC, high
 2143 quality standalone muon trigger will remain important in maintaining efficiency for signatures
 2144 with displaced muons, which the tracking trigger will be inefficient for. Some of the scenarios
 2145 predicting displaced signatures arise in models with hidden sectors [53], GMSB and R-parity
 2146 violating SUSY [54]. GE1/1 will also add to the stability of the system as GE1/1 can partially
 2147 offset the effects of possible decreased performance of the aging ME1/1 chambers.

2148 6.2.1 Integrated local CSC-GEM L1 trigger

2149 The challenge for triggering in the forward region, with $|\eta| \gtrsim 1.6$ arises from decreasing ca-
 2150 pabilities to discriminate low momentum muons from the high momentum ones. The rate is
 2151 driven by muon momentum mis-measurements associated with the tails in the p_T resolution of
 2152 the muon trigger. The CSC trigger measures muon p_T using the positions of stubs reconstructed
 2153 in muon stations that the track crosses: if a soft muon undergoes a substantial scattering in the
 2154 material of the absorber, it can be reconstructed as a high- p_T candidate.

2155 Of the four muon stations in the CSC system, the first one (ME1/1) is of special importance for
 2156 triggering. This is because muon lateral displacement (along the direction of a change of the
 2157 azimuthal angle), the main observable used by the CSC track finder for measuring the muon
 2158 momentum, is the largest in the first station. As a result, presence of a reconstructed segment
 2159 in the first station plays a key role in the CSC track finder momentum measurement. Inversely,
 2160 any inefficiency in reconstructing segments in station ME1/1 reduces momentum resolution.
 2161 The turning angle from the magnetic field also reaches the maximum in the first station ME1/1,
 2162 as shown in Figure 6.7 (left). However, muon direction measurement cannot be utilized in the
 2163 trigger because of low accuracy of a measurement within the ME1/1. It is limited by the low
 2164 magnetic field in the forward region and, with the thickness of the CSC chambers of only about
 2165 11 cm, the lever arm is too small to compensate for it.

2166 The strong improvement in trigger performance with the addition of GE1/1 is because the
 2167 proposed upgrade allows addressing both of the aforementioned points simultaneously. First,
 2168 it creates a large enough lever arm between GE1/1 and ME1/1 chambers to enable a good

2169 measurement of the muon direction (the “bending angle”) within the first station, as illustrated
 2170 in Figure 6.7 (right). Second, the added redundancy allows reducing the fraction of muons
 2171 with unreconstructed segments in the first station, which in turn reduces the fraction of poorly
 2172 measured muon candidates.

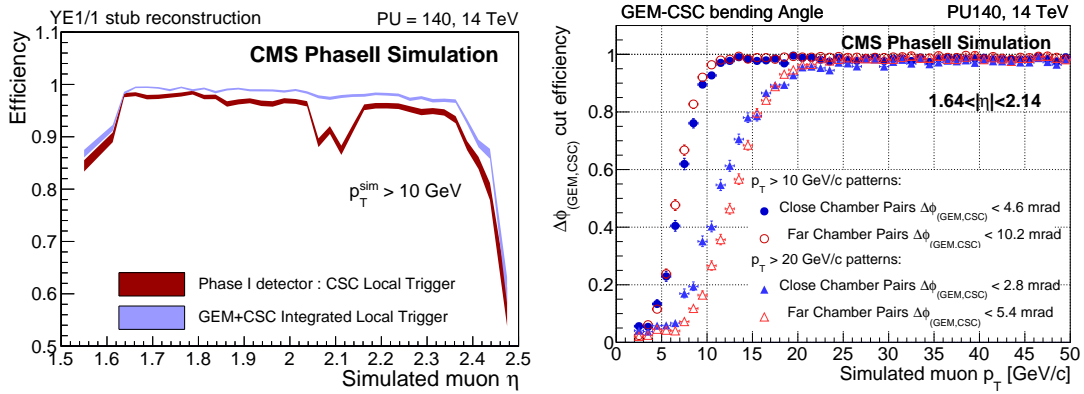


Figure 6.8: (Left): Muon track segment (LCT) reconstruction efficiency of the integrated GEM-CSC trigger as a function of the simulated muon $|\eta|$, compared to the same for the Phase-I CSC-only algorithm. The upgrade allows for a large reduction in the number of muon candidates without a reconstructed segment in the first station, which have a reduced momentum resolution and make a disproportionately large contribution to the Level-1 trigger rate. (Right): Simulated muon efficiency to pass a predetermined threshold high-efficiency pattern flag for even (“close”) and odd (“far”) GEM-CSC chamber pairs. The thresholds on the bending angle are selected to deliver a 98% efficiency for p_T values of 10 and 20 GeV. The bending angle selection effectively provides a second independent measurement of muon p_T , which is mostly uncorrelated with the measurement based on deflections of trajectory utilized in the current endcap Level-1 muon trigger.

2173 The integrated CSC-GEM local trigger has been designed for implementation in the ME1/1
 2174 Level-1 trigger board (OTMB) [2]. The OTMB reconstructs local charged track segments (LCT
 2175 stubs) based on the inputs received from the CSC and GEM detectors. The CSC information
 2176 is combined from the anode wire-group measurements in the polar angle (or radial position)
 2177 change direction and from the cathode strip measurements in the azimuthal angle change di-
 2178 rection. The anode measurements are combined in anode LCT stub component (ALCT) by the
 2179 on-chamber electronics processor. The cathode LCT stub component (CLCT) is reconstructed
 2180 by the OTMB based on data from on-chamber comparators which deliver per-layer strip infor-
 2181 mation as binary hits with half a strip granularity achieved by using charge-sharing informa-
 2182 tion in three neighboring strips. The wire-groups run at an angle along the length of an ME1/1
 2183 chamber. The strips are cut at a distance from a nominal beam line of 150 cm at $|\eta| \approx 2.1$, corre-
 2184 sponding to ME1/1a and ME1/1b parts in the lower (higher $|\eta|$) and upper parts, respectively.
 2185 A GE1/1 super-chamber covers ME1/1b part in full and the lowest partition covers approxi-
 2186 mately 1/3 of the ME1/1a. The GEM trigger pad information (a hit from two strips combined)
 2187 arrives separately from each chamber in a super-chamber. A coincidence of pads between two
 2188 chambers with some tolerance to allow non-normal incidence is treated as a co-pad bit.

2189 An LCT is built by the integrated CSC-GEM algorithm for the following input cases in addition
 2190 to the presence of an ALCT:

- 2191 • There is a CLCT with at least four layers.
- 2192 • There is a CLCT with only three layers and at least one matching GEM pad is found

2193 in the region of coverage by GEM; a three layer CLCT is used in ME1/1a region not
 2194 covered by GEM.

- 2195 • No CLCT is found and there is a GEM co-pad.

2196 Except for the last case, the LCT data is built from the ALCT and CLCT. In the last case, an LCT
 2197 is built from ALCT and GEM co-pad. Since an ALCT reconstruction efficiency is higher than
 2198 99% in the full range of ME1/1, an ALCT is always required to build an LCT.

2199 The efficiency to reconstruct an LCT by the integrated CSC-GEM trigger, compared to the re-
 2200 construction based on the CSC chamber data alone is shown in Figure 6.8 (left). Additional
 2201 redundancy provided by GE1/1 results in an increase in efficiency in the entire η range of the
 2202 chamber. Additionally, a large drop in efficiency in the ME1/1a-ME1/1b transition region is
 2203 recovered with help from GEM information. The bending angle is computed whenever both
 2204 a GEM pad and a CLCT are available. The value of the bending angle is used to define high-
 2205 efficiency angle pattern bits (98% used here), which are encoded in the modified LCT hardware
 2206 data format. A modified track finder algorithm will use the bending angle in the definition of
 2207 its track finding patterns. A simpler alternative is to use it to reject muons if the momentum
 2208 measured by the track finder is not compatible with the bending angle measurement, but at the
 2209 cost of a small inefficiency. Results of this selection are illustrated in Figure 6.8 (right) where 10
 2210 and 20 GeV thresholds are used.

2211 6.2.2 Muon trigger performance in Phase 1

2212 Installation of the GE1/1 station in LS2 will allow for a reliable and efficient muon triggering
 2213 with low thresholds in the entire range of $|\eta| < 2.2$ in the period of highest instantaneous
 2214 luminosity of Phase 1 operations. Figure 6.9 shows the large reduction in the muon trigger
 2215 rate in the region of $1.6 < |\eta| < 2.2$ achievable with the deployment of the GE1/1 detector.
 2216 The new trigger also provides for a non-negligible improvement in efficiency with the plateau
 2217 efficiency of 96%. An important operational feature of the new trigger is that it eliminates the
 2218 flatness seen in the curve for the CSC-only trigger, making reductions in the rate of the trigger
 2219 achievable with only small increases in the threshold values.

2220 Improved performance of the Level-1 muon trigger allows for lower thresholds at a given rate
 2221 not only for the inclusive Level-1 muon trigger, but also for the multi-object triggers involving
 2222 muons in their selections. Lower trigger thresholds increase acceptance and enhance the CMS
 2223 physics reach for a broad range of scenarios featuring relatively soft muons. In the SM Higgs
 2224 sector, even a modest reduction in muon trigger thresholds leads to a significant increase in the
 2225 acceptance for $h \rightarrow \tau\tau \rightarrow \mu\tau_{had} + X$, which has the highest sensitivity among all $\tau\tau$ final states
 2226 and in which muons, arising from the three body decays of tau leptons, are inherently soft,
 2227 as illustrated in Figure 6.9 (right). Processes with associated Higgs production where Higgs
 2228 decays into a pair of taus provide another example. Other interesting scenarios include mod-
 2229 els with the extended Higgs sector which can have an appreciable cross section, e.g. signal
 2230 acceptance for the heavier Higgs production followed by a decay $H \rightarrow hh \rightarrow \tau\tau bb$ strongly
 2231 depends on muon trigger thresholds for $m(H)$ up to a few hundred GeV. Some striking exam-
 2232 ples include “compressed” SUSY scenarios, such as stop pair production where stop decays
 2233 via $\tilde{t} \rightarrow \mu\chi^0 + X$ and the mass difference $m(\tilde{t}) - m(\chi_1^0)$ is small. Sensitivity to such signatures
 2234 will critically depend on the muon trigger threshold, as illustrated in Figure 6.10 (left) showing
 2235 the distribution of muon p_T . Other examples dependent on muon or muon+X triggers include
 2236 challenging SUSY scenarios with heavy squarks and gluinos and small mass splittings among
 2237 the lighter gauginos yielding soft leptons, e.g. $\chi^+ \rightarrow \mu\chi^0 + X$.

2238 A number of trigger paths targeting a range of physics signatures in Higgs, SUSY and “exotic”

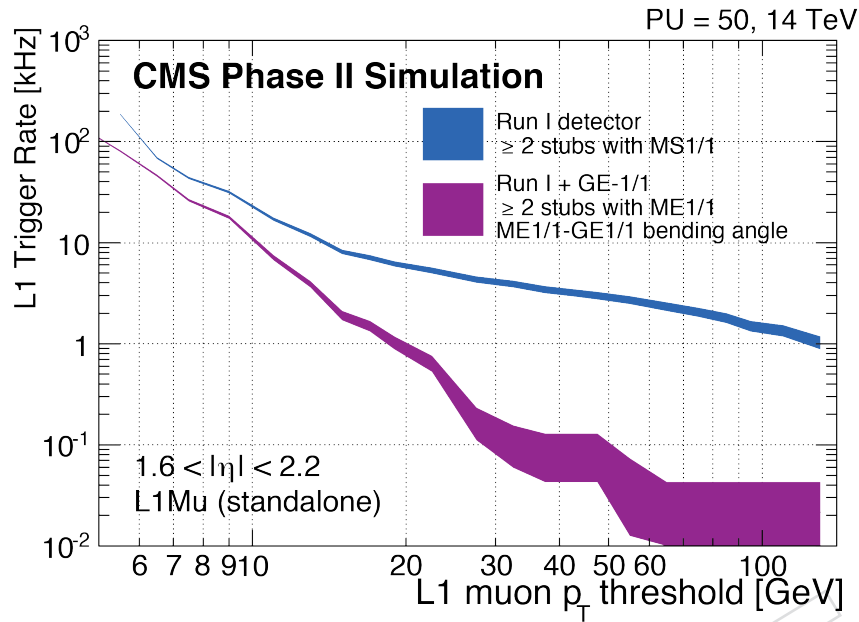


Figure 6.9: (Left): L1 muon trigger rate at a luminosity of $2 \times 10^{34} \text{cm}^{-2} \text{s}^{-1}$ as a function of p_T threshold. For the Phase-I system, 2 or more stubs, one of which is in the ME1/1 station are required. With the addition of GE1/1, the bending angle between the two stations can be used and the trigger rate is greatly reduced. (Right): Distribution of muon p_T for several illustrative physics processes, for which acceptance strongly depends on low trigger thresholds for the single muon trigger: production of a SM-like higgs decaying via $\tau\tau \rightarrow \mu + X$, 2HDM type heavy higgs production $pp \rightarrow H \rightarrow hh \rightarrow \tau\tau bb$ with $m(H) = 350 \text{ GeV}$, and SUSY stop production in a challenging for the LHC scenario with the “compressed” mass spectra (in this case $m(\tilde{t}) - m(\chi_1^0) = 40 \text{ GeV}$).

2239 realms rely on muon selections at Level 1. Examples of such triggers include di-muon, tri-
 2240 muon, muon+hadronic tau and muon+jet triggers, in which more exclusive selections allow
 2241 lower thresholds and thus an increased acceptance for the targeted processes. Improvements
 2242 in Level 1 muon trigger performance associated with the deployment of GE1/1 will reduce
 2243 the rates of these triggers allowing lower thresholds on muon p_T or momenta of other objects.
 2244 As an illustration, Figure 6.10 () shows the fast decrease in the acceptance for $H \rightarrow \tau\tau \rightarrow \mu\mu$
 2245 events with tightened thresholds on the momenta of the two muon candidates. This general
 2246 illustration is relevant for a number of other processes, e.g. the SUSY dilepton searches in
 2247 scenarios with light \tilde{t} and gauginos featuring very soft muons as the mass difference $m(t\tilde{a}u) -$
 2248 $m(\chi_1^0)$ becomes smaller.

2249 General considerations on the importance of maintaining lower muon triggering thresholds
 2250 arising from signal kinematics at generator level remain valid in the environment with a sub-
 2251 stantially increased density of particles. We illustrate that using a sample of simulated $H \rightarrow$
 2252 $2\tau \rightarrow \mu\tau_h$ events, in which Higgs boson is produced via Vector Boson Fusion (VBF). The chan-
 2253 nel with one tau decaying to a muon and the other decaying hadronically is special in that it
 2254 makes a very large contribution to the overall sensitivity of the $H \rightarrow \tau\tau$ measurement [55] due
 2255 to low backgrounds, with respect to the other decay channels, and a large branching fraction.
 2256 The events are generated at $\sqrt{s} = 14 \text{ TeV}$ and overlaid with an average of 50 additional min-
 2257 imum bias events to emulate the high pile-up environment using standard CMS simulation
 2258 tools.

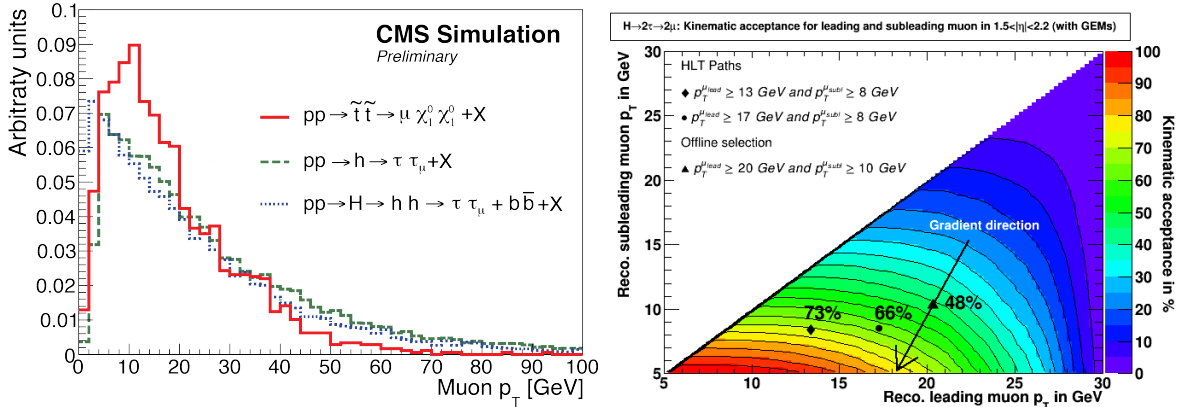


Figure 6.10: (Left): Distribution of muon p_T for several illustrative physics processes, for which acceptance strongly depends on low trigger thresholds for the single muon trigger: production of a SM-like higgs decaying via $\tau\tau \rightarrow \mu + X$, 2HDM type heavy higgs production $pp \rightarrow H \rightarrow hh \rightarrow \tau\tau bb$ with $m(H) = 350$ GeV, and SUSY stop production in a challenging for the LHC scenario with the “compressed” mass spectra (in this case $m(\tilde{t}) - m(\chi_1^0) = 40$ GeV). (Right): Acceptance for the simulated $H \rightarrow \tau\tau \rightarrow \mu\mu$ events as a function of the p_T thresholds applied in selecting the two muon candidates. The low momenta of muons produced in the three-body decays of tau leptons leads to a fast decrease in the acceptance with the increase in the thresholds emphasizing importance of low thresholds for the di-muon trigger.

2259 Events are reconstructed with the common CMS techniques using the Particle Flow framework,
 2260 followed by kinematic and particle identification selections closely resembling requirements in
 2261 the CMS Run 1 $H \rightarrow 2\tau$ observation paper [55]. Selections include the same requirement of two
 2262 jets separated by a large rapidity gap as in the original analysis, which greatly improves the
 2263 ratio of signal to background dominated by $Z(\rightarrow \tau\tau) + \text{jets}$. Isolation selections used in muon
 2264 and hadronic tau identification have been adjusted to loosen the requirements on the isolation
 2265 energy deposited by neutral particles, as their contributions cannot be associated to vertices
 2266 and the selection becomes too restrictive at high luminosity.

2267 We evaluate the effect on the signal acceptance by varying the muon p_T threshold used in
 2268 analysis selections in the range $5 < p_T^\mu < 60$ GeV. Figure 6.11(Left) shows the distribution for
 2269 the reconstructed visible mass of the $\mu + \tau_h + \text{MET}$ system for p_T^μ thresholds of 15, 20, and 25
 2270 GeV along with the total number of reconstructed events passing all selections (in 23% of these
 2271 events, muon candidate falls into the GE1/1, with this fraction being nearly independent of
 2272 the p_T^μ threshold). Note that even with $L = 300 \text{ fb}^{-1}$ of data, the final sample remains fairly
 2273 limited in statistics, emphasizing the importance of maximizing the acceptance. These results
 2274 shows that, on average, reducing muon threshold by 5 GeV yields a 35% increase in the number
 2275 of signal events passing all analysis selections. Figure 6.11(Right) summarizes the gain in the
 2276 acceptance as a function of p_T^μ threshold.

2277 6.2.3 HL-LHC trigger performance

2278 Deployment of the tracking trigger by CMS in LS3 will allow an ultra-high purity and low-rate
 2279 trigger targeting prompt muons by matching standalone muon candidates with the Tracker
 2280 tracks. The excellent momentum resolution of the Tracker eliminates the flattening of trigger-
 2281 rate curve owing to mismeasured low- p_T muons and yields a very sharp turn-on of the trigger
 2282 efficiency. Using tracking isolation, which is less sensitive to PU than calorimeter isolation, and
 2283 combining objects targeting exclusive final states allows very high purity and low trigger rates.

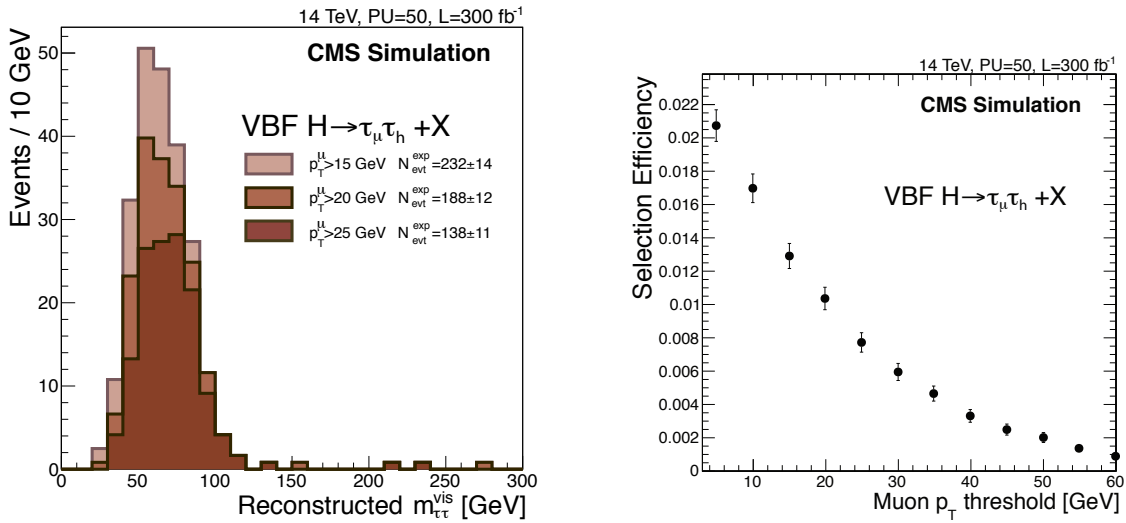


Figure 6.11: Left: The distribution of the visible mass of the μ, τ_h, met system for events surviving all analysis selections for the $H \rightarrow \tau\tau$ search in the VBF category in the $\mu\tau_h$ final state. The three distributions correspond to a sample with 300 fb^{-1} and the offline muon p_T threshold set to 15, 20, and 25 GeV, illustrating importance of maintaining low muon thresholds in the trigger and in the offline. Right: Full $h \rightarrow \tau\tau$ analysis selection efficiency for the $\mu\tau_h$ VBF category as a function of the chosen offline muon p_T threshold.

2284 The new combined trigger objects, referred to as L1TkMu, use track-trigger tracks extrapolated
 2285 to the muon stations and matched with L1 standalone muon candidates. The GE1/1 infor-
 2286 mation can contribute in resolution of ambiguities. More details about the Tracker part of the
 2287 trigger can be found in [2].

2288 Preserving the standalone muon triggering capabilities will continue being important in HL-
 2289 LHC era. One particularly critical aspect is preserving the sensitivity to scenarios of new
 2290 physics predicting displaced muons arising from decays of new particles with finite lifetime.
 2291 Such models are motivated by a range of considerations spanning from the electroweak baryo-
 2292 genesis requiring additional singlet fields, models with hidden sectors, a number of SUSY sce-
 2293 narios etc. As the tracking trigger efficiency vanishes for tracks produced away from the beam
 2294 spot, standalone muon triggering is the only viable option to trigger on such events, as trig-
 2295 gering on displaced electrons or pions with energies at the electroweak scales is hardly conceivable
 2296 in the high occupancy environment of the HL-LHC.

2297 To illustrate the sensitivity of the standalone muon trigger to signatures with displaced leptons,
 2298 we picked two benchmark scenarios suitable for exploring a broad phase space of possible
 2299 models predicting displaced muons. Both are implemented in the context of a SUSY scenario
 2300 with hidden sectors, in which new bosons are produced in the decays of a SM-like Higgs boson
 2301 h with a mass of 125 GeV into pairs of neutralinos n_1 , which are no longer stable and can
 2302 decay into the stable dark sector neutralino n_d and a dark photon via $H \rightarrow 2n_1 \rightarrow 2n_d 2\gamma_d$.
 2303 A similar scenario $H \rightarrow 2n_1 \rightarrow 2n_d 2z_d$ differs only in the “dark” Z boson z_d having a higher
 2304 mass. The new dark bosons are allowed to decay to pair of muons and the two scenarios
 2305 shown in Figure 6.12(Left) and (Right) correspond to γ_d and z_d each having a lifetime of $c\tau =$
 2306 50 mm. The two scenarios are selected to yield two very different topologies. The light γ_d
 2307 decays into a collimated pair of muons with the decay taking place predominantly far away
 2308 from the beamline and approximately pointing back to the beamspot thus with a typically
 2309 small transverse impact parameter d_{xy} and a large transverse decay length L_{xy} . In the case of

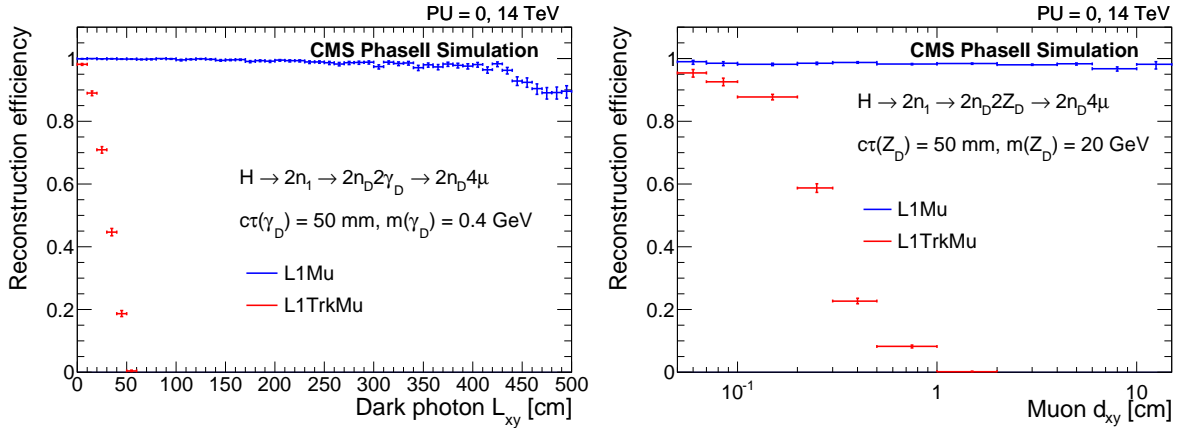


Figure 6.12: Trigger efficiency for non-prompt muon signatures where muon momentum at the muon production vertex points back to the beamline as a function of a distance of the production vertex to the beamline in the transverse plane (left). A scenario with long-lived dark photon production of mass 0.4 GeV with a mass of $n_1=10$ GeV and $c\tau = 50$ mm is used as a benchmark. Trigger efficiency as a function of muon transverse impact parameter for non-prompt muon signatures where muon momentum at the production vertex doesn't necessarily point to the beamline (right). A scenario of dark Z bosons production of 20 GeV mass with $n_1=50$ GeV is used as a benchmark. Events are triggered either by a stand-alone single muon trigger (blue) or a L1 track trigger (red).

2310 the heavier Z_d , muons typically have small L_{xy} and large d_{xy} . For these two topologies, we
 2311 compare the performance of the L1TkMu and the standalone muon trigger in reconstructing
 2312 at least one of the two muons, as shown in Figure 6.12, with no p_T thresholds required. As
 2313 expected, the standalone muon trigger has high efficiency up to very high L_{xy} , essentially until
 2314 the point where the decay vertex is far into the muon system, while L1TkMu shows efficiency
 2315 falling and completely vanishing at around $L_{xy} = 50$ cm. In the d_{xy} case, the standalone muon
 2316 trigger has a high efficiency for muons with a fairly substantial d_{xy} , while L1TkMu efficiency
 2317 quickly deteriorates past $d_{xy} \sim 2 - 3$ mm. These observations suggest a muon trigger based
 2318 on two complementary flavors: the L1TkMu featuring low thresholds and targeting prompt
 2319 muons and the standalone muon version targeting muons reconstructed with high quality in
 2320 the muon spectrometer in either a pointing topology with no matching track or in the explicitly
 2321 not pointing topology. In the latter case, muon candidates will feature muon chamber stubs
 2322 aligned along a straight line non-pointing to the beamspot. Cosmic and beam halo muons also
 2323 featuring this unusual topology would be easy to remove already at the trigger level.

2324 Another important consideration for Phase 2 detector operations is the possibility that the ag-
 2325 ing of the CSC system can increase the rate of hardware failures and/or degrade the perfor-
 2326 mance of the chambers. Figure 6.13 shows the fast deterioration of the standalone muon trig-
 2327 ger efficiency with even a moderate fraction of non-triggering CSC chambers. In this scenario,
 2328 presence of GE1/1 allows to offset the losses in trigger performance. Details of the simulation
 2329 are as follows: in the Phase-II case, the trigger requires hits in two or more stations includ-
 2330 ing hits in ME1/1, in which case a bending angle cut is applied. If hits are not reconstructed
 2331 in ME1/1 and the bending angle becomes unmeasurable, the trigger requires hits in three or
 2332 more stations including GE1/1.

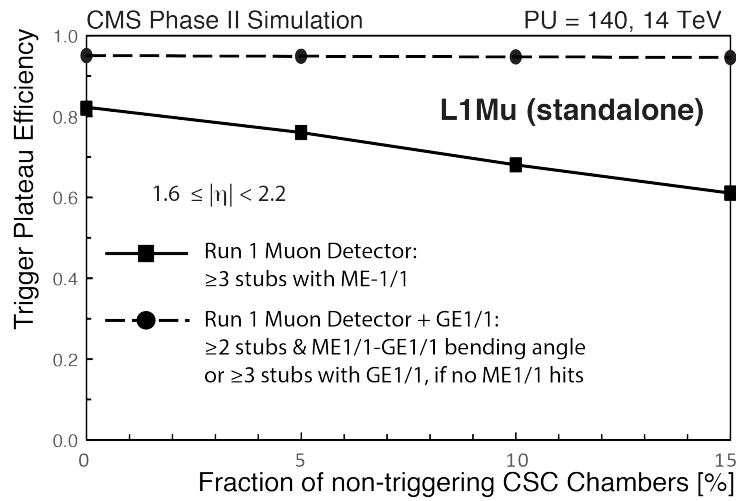


Figure 6.13: Single-muon trigger efficiency at the plateau in p_T as a function of the fraction of non-triggering CSC chambers, in Phase-I and Phase-II.

6.3 Muon reconstruction performance

2333

2334 Maintaining the high reconstruction efficiency and low misidentification rate of muon recon-
 2335 struction at high luminosity is a high priority for CMS. Physics reach of the CMS experiment
 2336 is dependent on the excellent performance of muon reconstruction, as evidenced by the role
 2337 of the final states with muons in the recent Higgs discovery and abundance of searches for
 2338 new physics relying on channels with muons. With the luminosity increases, the relative im-
 2339 portance of muons will grow as the muon system is all but immune to the effects related to
 2340 random overlaps of particle energy deposits or combinatorics induced by high occupancy due
 2341 to the shielding provided by the massive absorber and significant redundancy.

2342 The high luminosity environment and the aging of the existing detector brings several chal-
 2343 lenges. The standard CMS muon reconstruction relies on matching the inner tracks propagated
 2344 into the muon system with standalone muon tracks reconstructed in the muon spectrometer.
 2345 The small size of the matching windows, thanks to the accurate position measurement and
 2346 good momentum resolution of standalone muons, prevents degradation in performance even
 2347 with large increases in the multiplicity of the inner tracks. However, aging of the elements of
 2348 the existing muon detector can accelerate the rate of detector failures and degrade the spatial
 2349 and momentum resolution of standalone muon reconstruction. The increase in combinatorics
 2350 with the use of larger matching windows can in degrade the efficiency and increase the rate of
 2351 misidentifications. Failures in the first muon station, where the multiple scattering is the low-
 2352 est and the bending of the tracks in the magnetic field is the largest, have a particularly strong
 2353 impact on the quality of standalone muon reconstruction. Chambers in the first station of the
 2354 very forward muon region are the ones that will accumulate the highest doses of radiation.

2355 Similar to the standalone muon trigger case, standalone muon reconstruction has another im-
 2356 portant role in physics scenarios predicting long-living particles. If the lifetime of these new
 2357 particles is significant, the bulk of the CMS acceptance to such signatures would be hinging
 2358 on the quality of standalone muon reconstruction. In this case, the high performance of recon-
 2359 struction in first muon station is especially critical as it drives the momentum resolution.

2360 In the following, we demonstrate that the new GE1/1 system can be seamlessly integrated into
 2361 the CMS muon reconstruction paradigm. We show that the addition of a new precision muon

2362 detector in the strategically important first station adds to the robustness of the muon recon-
 2363 struction by minimizing the degradation in performance if parts of the existing system become
 2364 inoperable due to aging. The impact on the standalone muon reconstruction is particularly sig-
 2365 nificant. The following results do not include effects such as miscalibration or alignment, but
 2366 those are not expected to have a significant impact on our conclusions.

2367 6.3.1 Integration of the GE1/1 detector into the common CMS muon reconstruc- 2368 tion

2369 The design of the GE1/1 detector facilitates its seamless integration into the common CMS
 2370 muon reconstruction framework. In the following, we describe the details of how the new
 2371 detector information is used in the reconstruction with the upgraded CMS detector.

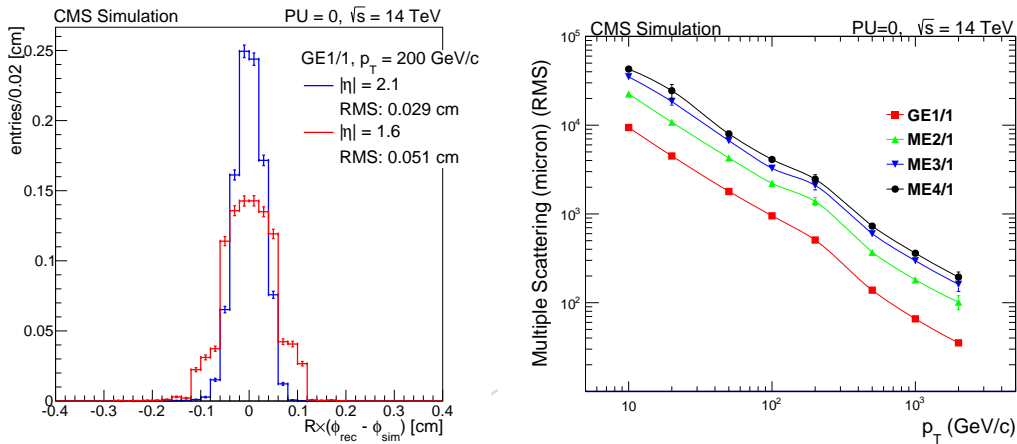


Figure 6.14: Left: The distributions of the differences between the reconstructed hit x -position and the true hit position in GE1/1 in the top and bottom parts of the chamber. The RMS of the distributions is the single hit resolution in the x -coordinate in the corresponding parts of the chamber, which is not constant as the GE1/1 strips are pointing radially. The distribution corresponds to a sample of muons with $p_T = 200$ GeV/c and is averaged. Right: The RMS of the multiple scattering displacement as a function of muon p_T , for GE1/1 and all the other forward muon stations, evaluated at $\eta = 2$. All of the electromagnetic processes such as bremsstrahlung and magnetic field effect are included in the simulation.

2372 The local reconstruction of the GE1/1 system uses the digital readout data to combine the
 2373 nearby signal strips to form clusters. The position of the clusters is determined as an average
 2374 of the x -positions of the strips assigned to the cluster (GEM digital readout does not provide the
 2375 information on the signal amplitude for the strips, so each strip is assigned the same weight).
 2376 The uncertainty is calculated as the $N_{st} \times \delta x_p / \sqrt{12}$, where N_{st} is the number of strips in the
 2377 cluster, $\delta x_p = 450 \mu\text{rad} \times R$ is the pitch size in local x direction at the radius R correspond-
 2378 ing to the center of the partition, which the cluster belongs to (counted from the beam line).
 2379 The reconstructed clusters become GE1/1 RecHits used in the standalone and global muon
 2380 reconstruction. Figure 6.14(Left) shows the single hit resolution in the $R\phi$ -coordinate, which
 2381 runs in the plane of the chamber along a circumference centered at the beam position) and
 2382 which determines momentum resolution. The spatial resolution at two different η positions
 2383 on the chamber are shown. The RMS ranges from 0.029 cm at higher η to 0.051 cm at lower
 2384 η . The single hit resolutions can be compared to the RMS of the multiple scattering shown in
 2385 Figure 6.14(Right) as a function of momentum. For muons with momenta $p_T \simeq 200$ GeV the
 2386 uncertainty in the momentum fit due to the multiple scattering is $\simeq 0.05$ cm.

2387 It is worth noting that the studies of muon reconstruction performance do not include effects
 2388 related to possible misalignment of the detectors, instead assuming a perfect alignment of the
 2389 GE1/1 chambers. While this can never be true, effects of the misalignments are expected to
 2390 become negligible after just a short period of operations with the upgraded detector. For com-
 2391 parison, alignment of muon chambers in station ME1/1 to the accuracy of $300\ \mu\text{m}$, compa-
 2392 rable with the GE1/1 single hit spatial resolution, requires only about $20\text{-}30\ \text{pb}^{-1}$ of collision
 2393 data with the algorithm that extrapolates inner tracks to the plane of the ME1/1 chambers.
 2394 GE1/1 and ME1/1 chambers are very comparable in the precision of the relative positioning of
 2395 the readout strips, chamber size and even the multiple scattering that muons undergo before
 2396 reaching ME1/1 or GE1/1 is exactly the same. The only significant difference is a noticeably
 2397 better single hit resolution of the ME1/1 chambers. However, for muons with $p_T > 20\ \text{GeV}$
 2398 used for alignment, multiple scattering is about $4\ \text{mm}$ for both ME1/1 and GE1/1, which is
 2399 much larger than the single hit resolution of either chamber, and so the alignment precision is
 2400 proportional to $(4\ \text{mm})/\sqrt{L}$ in both cases down to the point where the systematic effects can
 2401 become significant.

2402 6.3.2 GE1/1 impact on muon performance

2403 The GE1/1 RecHits are used in the trajectory and momentum fits in both global and standalone
 2404 muon reconstruction algorithms. In the following, we evaluate the degree to which the perfor-
 2405 mance of muon reconstruction can be affected by degradation in the performance of the CSC
 2406 chambers in the region $|\eta| > 1.6$. The specific figures of merit used are the standalone recon-
 2407 struction efficiency and the transverse momentum resolution. The choice of standalone muon
 2408 reconstruction is driven by its impact on a broad range of physics scenarios through the HLT
 2409 performance and the unique access the standalone muons provide for models with new parti-
 2410 cles decaying meters away from the interaction point. We show that the redundancy provided
 2411 with the installation of the GE1/1 detector significantly adds to the stability of the system and
 2412 allows recovering of a significant fraction of the inefficiency even in very pessimistic scenarios.
 2413 Figure 6.15(left) shows the standalone muon reconstruction efficiency at $\mathcal{L} = 5 \times 10^{34}\ \text{cm}^{-2}\text{s}^{-1}$
 2414 as a function of pseudorapidity η of the simulated muon when the percentage of reconstructed
 2415 hits matches the simulated ones for more than 50%. The recovery of the reduction in recon-
 2416 struction efficiency with the addition of GE1/1 is evident across the board and particularly in
 2417 the higher η region. The improvement is applicable to both the standalone muon reconstruc-
 2418 tion and the global muon reconstruction, which is seeded by standalone muons. Note that
 2419 efficiency recovery does not reduce the purity of standalone muon candidates as illustrated in
 2420 Figure 6.15(right) showing the corresponding rate of reconstructing fake muons per event. Ef-
 2421 ficiency recovery shown should be considered as the low bound on the potential improvement
 2422 as the current implementation does not reconstruct GE1/1 segments, and therefore GE1/1 is
 2423 not used in seeding the standalone reconstruction. While the directional accuracy of GE1/1
 2424 segments is more coarse compared to that of ME1/1, the probability of reconstructing both hits
 2425 in each of the two chambers in the super chamber is high and such segments could be used to
 2426 seed standalone muon reconstruction. In particular, seeding with GE1/1 segments would re-
 2427 cover efficiency in the highest η bin in Figure 6.15(left) where the CSC segment reconstruction
 2428 is affected near the border of the high and low η parts of the CSC ME1/1 chambers.

2429 The lack of redundancy of the system in the forward region $|\eta| > 1.6$, which relies solely on
 2430 the CSC chambers that are seeing the highest radiation exposure in the entire muon system, is
 2431 a concern that is not limited to the performance of the Level-1 trigger. The standalone muon
 2432 reconstruction is not only used in the offline, where alternative algorithms such as the tracker
 2433 muon reconstruction can be used to partially mitigate the reduction in performance. The very

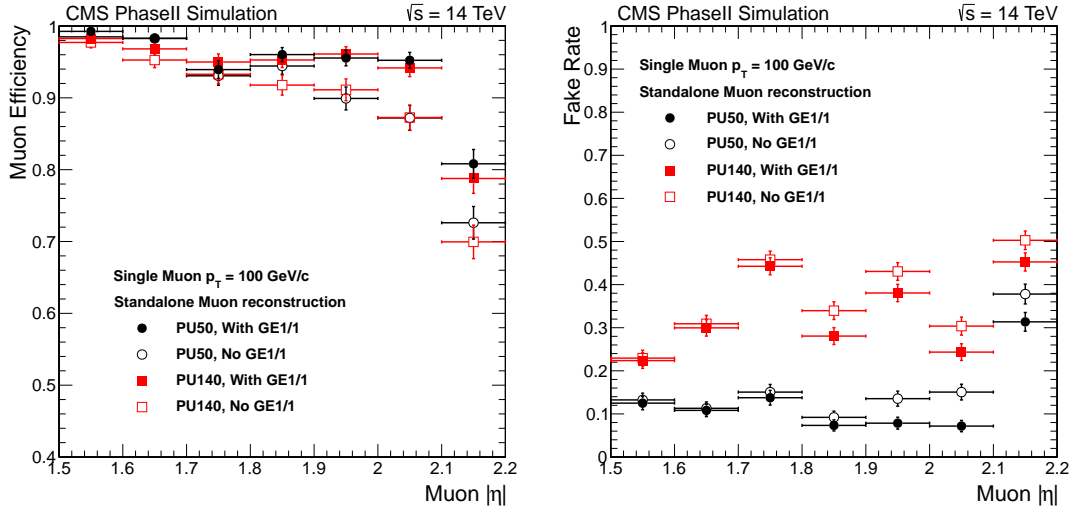


Figure 6.15: Standalone muon efficiency (left) and average number of fake muons per event (right) as a function of η for “2019” scenarios using $\langle PU \rangle = 50$ and 140 samples. Gain in standalone muon efficiency is found adding new detectors GE1/1 when the percentage of reconstructed hits matches the simulated one for more than 50% without any increase in the number of fake muons. A cut of 10 GeV/c is applied on the reconstructed p_T is applied to reduce the number of fakes coming from pile-up.

2434 same standalone muon reconstruction and the global muon reconstruction, which directly re-
 2435 lies on standalone muons, are also used in the HLT. Aging of the CSC chambers can not only
 2436 reduce its performance, but lead to parts of entire chambers becoming inoperable for extended
 2437 periods of time as repairs of the chambers and the onboard electronics can only be done dur-
 2438 ing major shutdowns. Such scenarios can result in reduced momentum and spatial resolutions
 2439 leading to degraded efficiency and increase in misidentification rates, and ultimately affecting
 2440 the sensitivity of physics analyses and causing irreversible losses in data selection by the High
 2441 Level Trigger.

2442 Figure 6.16 shows what happens to the standalone muon efficiency when ME1/1 is completely
 2443 broken with and without the help provided by the installation of GE1/1. As already discussed,
 2444 the upgraded system shows a visible increase in the efficiency and reduction in the rate of
 2445 misidentifications. However, the most important observation is that the additional redundancy
 2446 associated with the GE1/1 system allows recovering most of the efficiency losses even in the
 2447 most pessimistic scenario where the entire ME1/1 becomes inoperable. We consider different
 2448 detector configurations at $\langle PU \rangle = 50$, which corresponds to the period between the LS2 and
 2449 LS3.

To quantify the impact of the CSC detector degradation on standalone muon momentum res-
 olution and charge misidentification, we study the relative resolution of the muon curvature
 measurement. The specific figure of merit chosen is the residual distribution q/p_T defined as:

$$\frac{\delta\left(\frac{q}{p_T}\right)}{\frac{q}{p_T}} = \frac{q^{Rec}/p_T^{Rec} - q^{Sim}/p_T^{Sim}}{q^{Sim}/p_T^{Sim}}, \quad (6.1)$$

2450 where q is the charge and p_T^{Sim} and p_T^{Rec} are the simulated and reconstructed transverse mo-
 2451 menta. Sigma of the q/p_T residual distribution is obtained by fitting the distribution to the
 2452 mean \pm RMS.

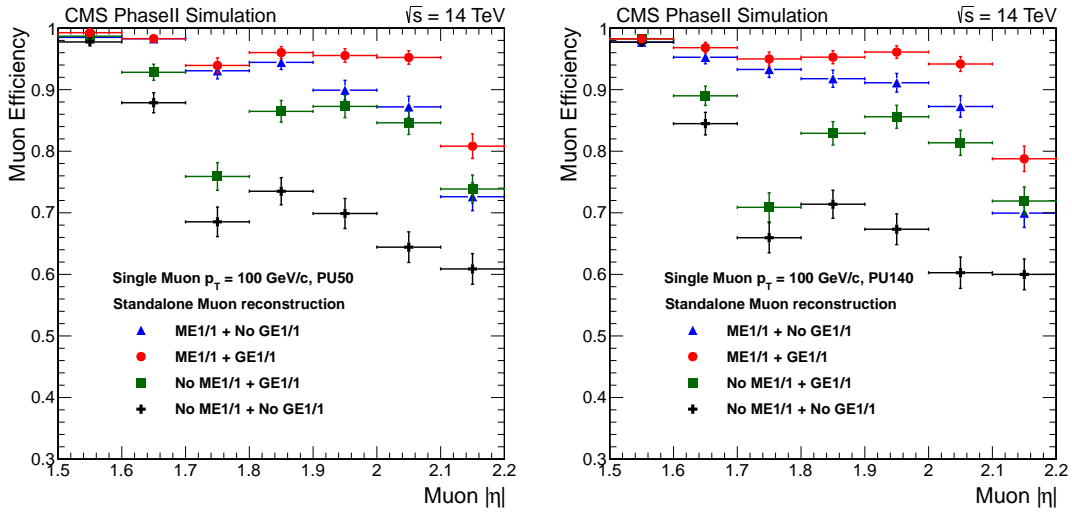


Figure 6.16: Standalone muon efficiency for high quality muons as a function of η in case of ME1/1 failure in the 2019 scenario at PU = 50 (left) and 140 (right). In both the scenarios the reconstruction efficiency is recovered by adding GE1/1.

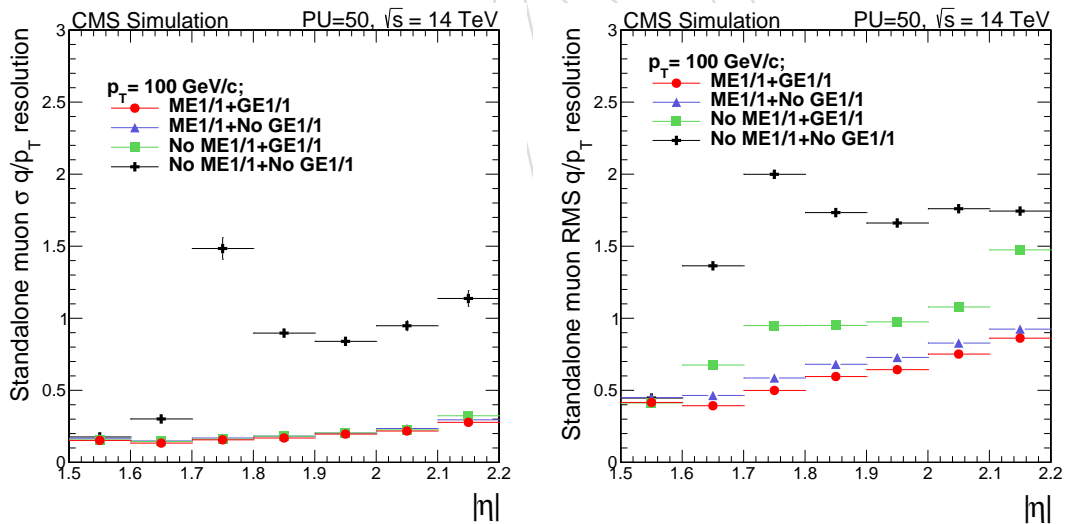


Figure 6.17: The dependency of the Sigma (left) and relative RMS (right) of the $\delta(q/p_T)/(q/p_T)$ distribution as a function of the simulated muon pseudorapidity for several scenarios, illustrating the recovery of momentum resolution for standalone muons using hits in GE1/1 in the scenario where parts of the ME1/1 system become non-operational due to aging or other effects. The distributions are shown for muons with $p_T = 100$ GeV reconstructed using the standalone muon algorithm at PU= 50.

2453 While the addition of GE1/1 does not change substantially the core resolution of the distribu-
2454 tion, the presence of GE1/1 allows a significant reduction of otherwise unavoidable dramatic
2455 deterioration of momentum resolution in the scenario where ME1/1 becomes inoperable. Fig-
2456 ure 6.17 makes this observation abundantly clear by showing the Sigma (left) and RMS (right)
2457 distributions for several scenarios as a function of the simulated muon pseudorapidity.

DRAFT

DRAFT

2458 **Chapter 7**

2459 **Integration and Installation in CMS**

2460 **Editors:** A. Marinov, M. Tytgat

2461 **Contributors:** A. Gaddi, S. Bally, G. Bencze, N. Beni, I. Crotty, A. Conde, A. Lanaro, A. Madorsky,
2462 A. Marinov, G. Mitselmakher, P. Paolucci, M. Saleh, Z. Szillasi, M. Tytgat

2463 **7.1 Introduction**

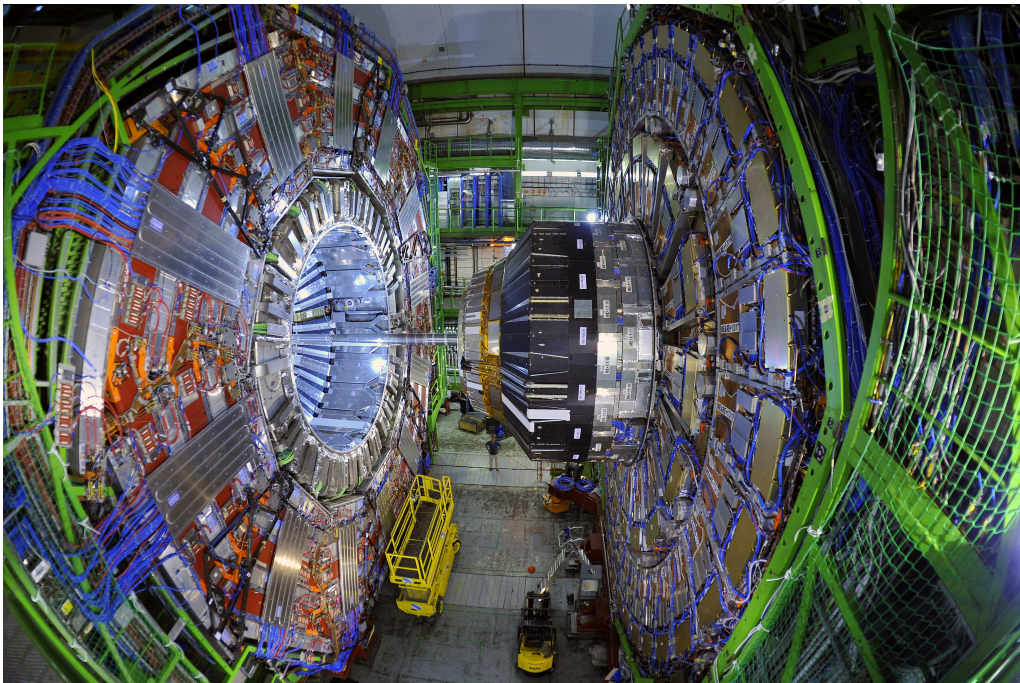


Figure 7.1: General view of the YE-1 endcap on the right.

2464 The high- η part of the CMS detector can be seen in Figure 7.1 with a picture of one of the
2465 YE1 endcap disks on the right. The dark part (the black covers) of the endcap is the nose,
2466 which is physically the region of interest to install the new muon GE1/1 detectors covering
2467 the $1.6 < |\eta| < 2.2$ region. At present, this zone is partially vacant, with the CSC-ME1 station
2468 located there as only muon detector.

2469 Services to be integrated for the GE1/1 system are the high and low voltage power system in
2470 the underground service cavern (USC55) and corresponding power lines to the chambers in the
2471 experimental cavern (UXC55), the gas mixing system in the gas building on the surface, the gas

2472 and cooling circuit to the chambers in UXC55, and the optical fibers connecting the chambers
 2473 to the off-detector electronics in UXC55.

2474 7.2 Mechanical aspects and alignment

2475 7.2.1 Description of the GE1/1 location

2476 Figure 7.2 shows a quarter cut of the CMS detector. There, more details are shown of the
 2477 GE1/1 zone, which is located just in front of the ME1/1 detectors. The GE1/1 are mounted
 2478 using guide rails attached to the HE back-flange (see Figure 7.3) which is located 5674 mm
 2479 away from the CMS interaction point. Mechanically, the GE1/1 chambers are not attached
 2480 in any way to the CSC chambers. The back-flange is made of non-magnetic stainless steel,
 2481 transparent to magnetic forces. This puts the GE1/1 chambers in a favorable location where
 2482 the displacement of the chambers due to the CMS magnetic field is expected to be only a few
 2483 millimeters along the Z direction (beam axis).

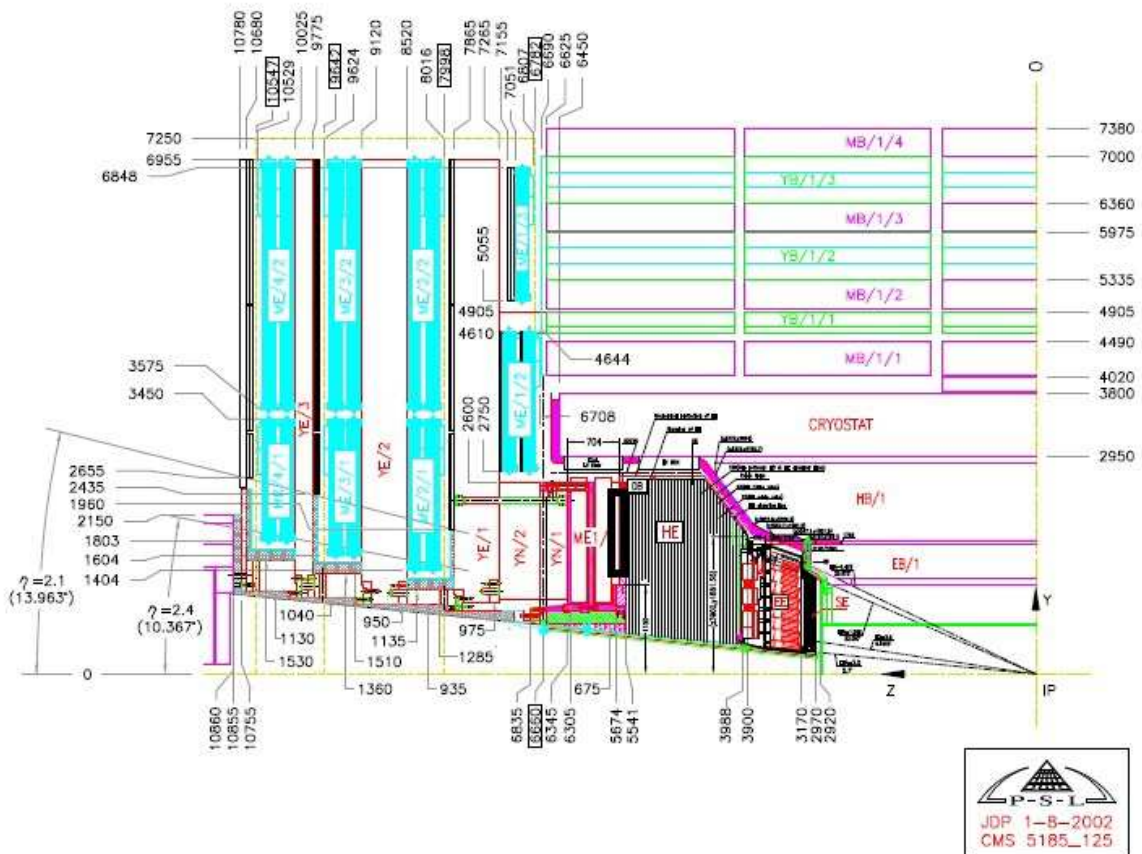


Figure 7.2: Quarter cut of the CMS detector. The GE1/1 superchambers will be installed on the HE back-flange, 5674 mm away from the interaction point, as indicated by the black box.

2484 A general view of the GE1/1 installation slots is shown in Figure 7.4. In the figure one can see
 2485 the ME1/1 detectors in position as well as their blue LV cables. The small pockets between
 2486 the black covers of the nose and the ME1/1s are the actual installation slots for the GE1/1
 2487 superchambers. As is shown in the figure, the only accessible part of the GEM detectors after
 2488 their installation will be their patch panel.



Figure 7.3: CMS HE back-flange showing GE1/1 chamber support rails.



Figure 7.4: General view of the GE1/1 installation slots (as indicated by the red box).

2489 7.2.2 Position monitoring and alignment

2490 7.2.2.1 Introduction

2491 The GE1/1 detector on both sides of CMS can be considered as a double-layer disk (GE1/1-
2492 disk) formed by 36 superchambers mounted on the back-flange of the HE calorimeter. The
2493 determination of the chamber positions in the CMS coordinate system is split into two tasks:
2494 the positions of the chambers in the coordinate system of the GE1/1-disk and the location of
2495 the entire disk in CMS. The chambers themselves can be considered as rigid bodies.

2496 The initial positions of the individual superchambers and the GE1/1-disk as a whole will
2497 change after closure: displacement of the chambers with respect to each other and their collec-
2498 tive movement cannot be excluded due to magnetic field and temperature changes (though the
2499 thermal expansion of the individual chambers can be neglected). Therefore, a position mon-
2500 itoring system is necessary to determine the absolute chamber-positions and to follow these
2501 position changes.

2502 The precision of the chamber positioning can be deduced from the physics requirements and
2503 consequently from detector design parameters. The most demanding direction is the azimuthal
2504 ($R^*\phi$) angle. The monitoring accuracy must be a fraction of the azimuthal resolution of the
2505 chambers (see Section 2.1) leading to $<50 \mu\text{rad}$ requirement. The radial (R) position of the
2506 superchambers with respect to the GE1/1-disk and the X-Y position of the GE1/1-disk in CMS
2507 require the knowledge of the position with $<100 \mu\text{m}$ precision. The position of the GE1/1-
2508 disk along CMS-Z has to be known with millimeter accuracy. The accuracy of the rest of the
2509 translations and rotations can be fulfilled by the installation accuracy for both the individual
2510 superchambers and the GE1/1-disk as a whole.

2511 7.2.2.2 Alignment concept

2512 Different methods to solve the task of alignment are applied in CMS for other subsystems [1], [56].
2513 This experience has been used to work out the concept for the GE1/1-chambers.

2514 As the readout strips that are relevant for the alignment cannot be observed after the assem-
2515 bly of the chambers, the first step is to transfer the strip positions during the construction to
2516 positioning elements to be mounted on the outside of the chamber body. These positioning
2517 elements can be used for monitoring at the installation and during the running period. Two
2518 types of elements are planned to be used: precision survey holes for removable survey targets
2519 and distance sensors permanently fixed on the chambers. The survey targets help to locate the
2520 chambers with moderate ($\sim\text{mm}$) precision during the installation.

2521 The distance sensors measure the $R^*\phi$ and the R distances between the adjacent chambers
2522 and are capable of defining the chamber positions in the GE1/1-disk coordinate system with
2523 the required precision. Following the layout of the GE1/1-disk the plan is to put distance-
2524 sensors on the long chambers: two on each ϕ -side and two in R-direction (Figure 7.5). The
2525 total number of sensors planned to be used for the full project is 432 (6 per long chamber).

2526 Finally, track-based alignment methods can define the entire GE1/1-disk in the CMS coordi-
2527 nate system, cross-check the results of the position monitoring system and further improve the
2528 precision of the alignment.

2529 This concept that is based on three different, independent and complementary methods can
2530 guarantee the precise and robust solution of the alignment task.

2531 The proposed scheme has been simulated using a simplified model of the GE1/1-disk contain-

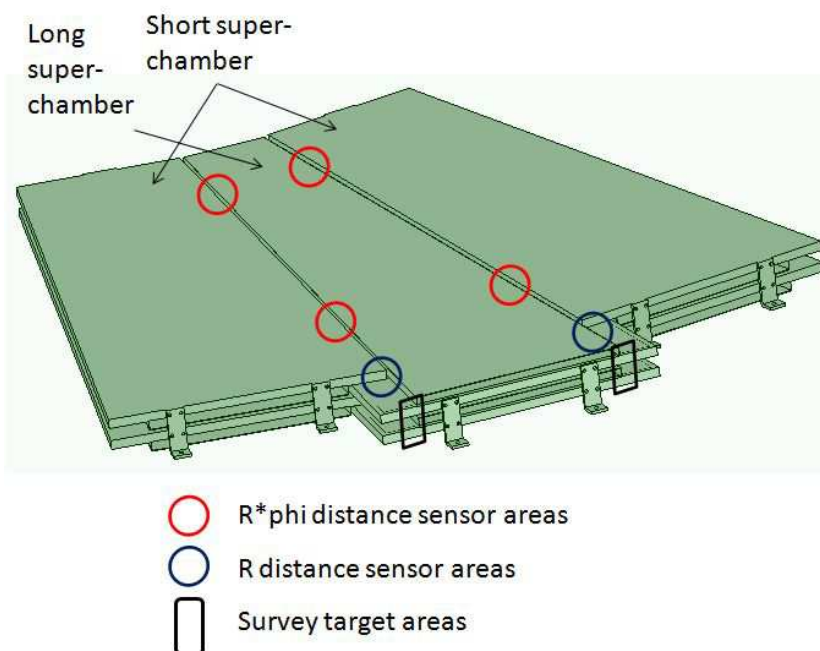


Figure 7.5: Locations of the distance sensors and survey targets.

2532 ing six superchambers of 60 degree angular size and enlarged chamber distance (to 100 mm
 2533 instead of the designed 38 mm). The larger angle and distance in the simulation could help
 2534 us to detect possible problems that might occur during the position reconstruction from the
 2535 measured data. The results have confirmed the correctness and completeness of the concept.

2536 7.2.2.3 Distance sensors and calibration

2537 Two different sensor types are studied as possible active elements of the position monitoring
 2538 system: capacitive sensors and FBG-sensors (see e.g. [57]). The design dimensions of the sensor
 2539 are $10 \times 10 \times 50 \text{ mm}^2$, independent of the final solution. The measuring range is 0-10 mm.

2540 As the task of the position monitor system is to provide the absolute positions of the chambers
 2541 and the GE1/1-disk, the dimensions and locations of all the elements have to be known with
 2542 the necessary precision. As the production cannot guarantee this accuracy these parameters
 2543 have to be measured, in other words calibrated. Careful calibration is a key element of the
 2544 accuracy that the system can obtain.

2545 The first calibration step is the transfer of the strip positions of the readout board to its outer
 2546 side using a 2D table (see Figure 7.6). This operation has to be done when the strips are still
 2547 measurable (visible), i.e. before the chamber assembly.

2548 First, the so-called sensor positioning plates are placed in the precisely machined holes of the
 2549 base plate of the scanner table (Figure 7.6A). Then, the readout board is put on the table with
 2550 the strips upwards and the sensor positioning plates are glued to the back (connector) side of
 2551 the readout board (Figure 7.6B). Then, the upper surface is scanned and the images obtained
 2552 by the camera are stored. This 2D scan -besides the alignment needs- is opening a possibility
 2553 to check the quality of the strips and also to detect and measure their possible defects.

2554 The fixations of the individually calibrated sensors are mounted on the chambers after the
 2555 assembly of the GEM part. Then, those frame sections that are used as sensor targets on the
 2556 short chambers and the survey holes have to be measured with respect to the sensors (for

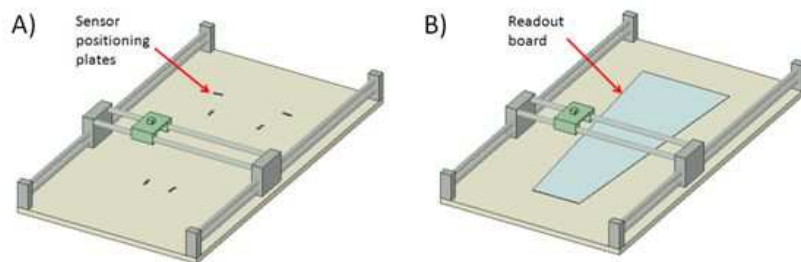


Figure 7.6: Principle of the chamber calibration: A) Measurement of the sensor positioning plates. B) Measurement of the strip positions and gluing of the plates to the connector side.

2557 the long chambers) or the sensor positioning plates (for the short chambers) by a coordinate
 2558 measuring machine (CMM).

2559 7.2.2.4 GE1/1-alignment R&D

2560 There are still areas related to the distance sensors of the GE1/1-alignment hardware system
 2561 where R&D work is required. Though both the capacitive and FBG options are based on known
 2562 and used techniques, the conditions of the present application require further studies. For the
 2563 capacitive solution the main concern is to develop a cost-effective but radiation-hard low-noise
 2564 electronic transducer. For the FBG version the main problem is to find the best inner geometry
 2565 and assembling technology of the sensor unit.

2566 Besides the sensor R&D, considerable work is still required on the pattern recognition program
 2567 for the scanning table to ensure fast, reliable and precise evaluation of the data. The simulation
 2568 of the accuracy of the proposed system based on optogeometrical modeling is still being devel-
 2569 oped. Finally, the development of the software package providing the position reconstruction
 2570 from the calibrated and measured data is still to be optimized.

2571 7.3 Power system

2572 7.3.1 HV power system

2573 During the R&D phase of this project, a single-channel HV powering scheme based on a HV re-
 2574 sistive divider circuit on the chamber was used (see Section 2.3.6.1). Unfortunately, this option
 2575 has limits. For example, it is not possible to measure the currents of the individual GEM foils.
 2576 The final system offers advanced multi-channel HV powering with the flexibility to provide
 2577 the voltage levels to the GEM foils or sectors almost individually. This permits fine granularity
 2578 in terms of HV settings for the GE1/1 detector, as well as GEM foil current measurements. Be-
 2579 low, two options for such a multi-channel system are described; an engineering review will be
 2580 organized early 2015 to determine the optimal solution.

2581 The HV working point for the GE1/1 detectors with high gain and best time resolution is
 2582 shown in Table 7.1. The potentials are shown for all detector electrodes as they are described
 2583 in Section 2.3.6.1.

2584 7.3.1.1 Multi-channel HV powering system

2585 The HV system proposed by the University of Florida (UF) - Petersburg Nuclear Physics Insti-
 2586 tute (PNPI) team is based on an already existing design currently used in CMS to power the
 2587 CSC (except ME1/1) [58]. The design has been extensively tested over a few years of operation
 2588 of these detectors. The system consists of two major components (see Figure 7.7):

Detector electrode	Voltage [V]	Dark current [nA]
Drift	900	0
GEM1	450	<35
T1	350	0
GEM2	440	<35
T2	700	0
GEM3	420	<35
Induction	500	0

Table 7.1: Expected HV working point of the GE1/1 detectors. The indicated voltage levels are actual voltage differences across the gaps or GEM foils.

- 2589 • Primary HV power supplies and master boards, located in the Underground Service
2590 Cavern (USC55)
- 2591 • HV distribution boards, located in Underground Experimental Cavern (UXC55),
2592 near the detector. These boards are designed to be radiation-hard and magnetic-
2593 field tolerant.

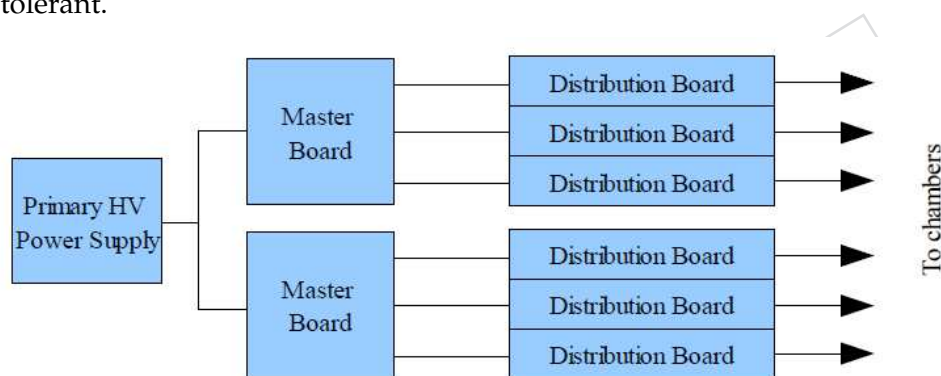


Figure 7.7: Multi-channel high voltage distribution structure.

2594 The custom-designed GE1/1 HV system proposed here offers the following features:

- 2595 • Each HV segment (or group of segments) in the GEM chamber is powered from its
2596 own HV regulator
- 2597 • Each regulator is capable of adjusting the voltage, measuring the output current, de-
2598 tecting voltage deviations and over-current conditions. This is extremely convenient
2599 for tasks such as monitoring chamber aging, adjusting the gas gain, and detecting
2600 any abnormalities in the chamber behavior.
- 2601 • In comparison to the single-line HV option, the UF/PNPI HV system does not use
2602 resistive dividers. Such dividers, consuming around 4W of power and being located
2603 in a small closed volume inside GE1/1 chamber with no air flow, lead to a significant
2604 local heat load. Also, in the presence of substantial leakage currents, passive HV
2605 dividers give rise to undesired biases in operating voltages across foils and gas gaps.

2606 The GE1/1 chambers require several different voltage levels for proper operation. The UF/PNPI
2607 HV system is designed to power each chamber from several HV regulators, with at least one
2608 regulator per voltage level. This allows for greater flexibility during operation. Each voltage
2609 level can be individually adjusted for gas gain control, and the current and voltage can be mea-
2610 sured on each output to prevent over-current conditions and voltage deviations. Additionally,
2611 complex chamber protection scenarios can be used, such as adjusting voltages on all chamber

Number of output channels in the system	144 chambers * 7 outputs = 1008 channels
Output channel organization	4 chambers per distribution board
Nominal output voltages	-3760 V Drift Catode
	-2860 V GEM1 TOP
	-2410 V GEM1 BOT
	-2060 V GEM2 TOP
	-1620 V GEM2 BOT
	-920 V GEM3 TOP
-500 V GEM3 BOT	
Absolute maximum voltage between top and bottom foil of the GEM	450 V
Absolute maximum voltage across drift, transfer and induction regions	2000 V
Voltage settings, resolution, each output	1 V
Voltage adjustment individually for each output	$V_{nominal} \pm 100$ V
Maximum output current per output, I_{max}	150 μ A
GEM current leak tolerance	Up to two shorted segments per chamber, 100 μ A leakage current
Individual output turn-off (trip) timeout	Programmable, with the step of 20 ms, up to 5 sec
Trip level software programmable	From 1 μ A to 150 μ A
Trip Level setting resolution	1 μ A
Voltage measurement individually for each output	Via software, resolution 1 V
Current measurement individually for each output	Via software, resolution 1 μ A
Rate of voltage change	2 to 100 V/s
Maximum HV ripple	20 mV p-p, bandwidth: 100 Hz to 20 MHz
Output control via software	Status: on/off, ramp, current limit/measurement, overcurrent trip, over/undervoltage trip

Table 7.2: Specifications of the UF/PNPI GE1/1 HV system (baseline option).

2612 foils in case of over-current on one of the foils. In case of current leaks or complete shorts
 2613 in some GEM segments, the individual regulators keep the voltages unchanged on all other
 2614 segments, such that the chamber can still operate normally.

2615 The GEM foils each have 47 sectors on the top side and a single common layer at the bottom. In
 2616 addition, in each GE1/1 detector there are a drift electrode and readout plane (see Section 2.3).
 2617 Powering each segment from its own HV regulator is impractical as it would require a huge HV
 2618 output count (145 outputs per chamber, and 20880 outputs in the entire system). Several seg-
 2619 ment ganging options are being considered. The baseline option assumes that all segments on
 2620 each segmented layer are ganged together. This requires only seven HV outputs per chamber,
 2621 or 1008 outputs in the entire system.

2622 Detailed specifications of the UF/PNPI GE1/1 HV system are listed in Table 7.2. A prototype of
 2623 the HV distribution board was successfully tested at CERN during November-December 2014.
 2624 The test program included the following steps:

- 2625 • Standalone parameter measurements and complete calibration of voltage measure-
 2626 ment, voltage setting, and current measurement circuitry
- 2627 • Tests with a GE1/1 chamber simulator circuit, including ramp-up, ramp-down, and

2628 behavior during simulated chamber over-current conditions and sparks

- 2629 • Tests with an actual GE1/1 generation 3 chamber prototype using x-ray irradiation
- 2630 • Tests with a tracking GEM chamber performed during beam test at the GIF facility

2631 7.3.1.2 HV Complex-Channel powering system

2632 INFN-Napoli and CAEN are designing a power system for the future RPC and GEM detec-
 2633 tors, called HV Complex Channel system, that is back compatible with the present system and
 2634 fulfills all CMS requirements. The HV power boards of the HV-CC system will be allocated
 2635 directly in the new CAEN mainframe (SY1527) in order to reduce the number of crates, con-
 2636 nections and the complexity of the present RPC system but with the caveat to be allocated in
 2637 USC.

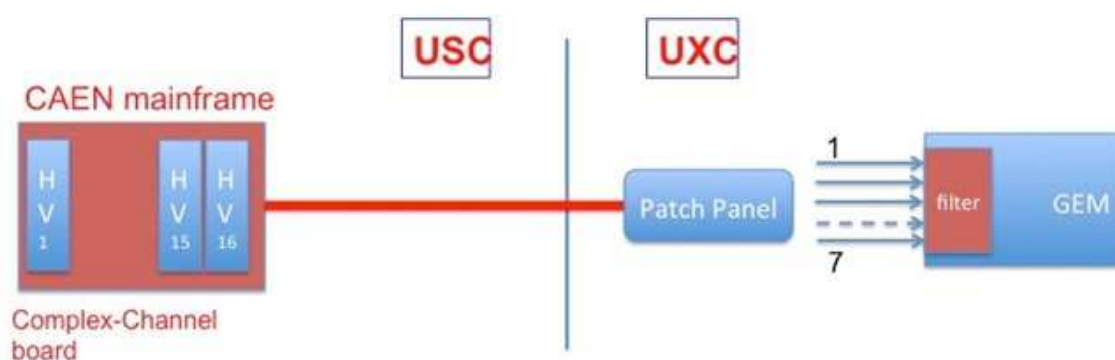


Figure 7.8: Schema of the complex-channel GEM power system. The entire power system hardware is placed in USC. A 80 meters multi-conductors cable will bring HV in UXC area.

2638 The GEM version of the HV-CC (see Figure 7.8) is based on the following ideas:

- 2639 • To power a GE1/1 chamber with 7 independent HV channels in order to be able to
 2640 regulate and to change over time if needed the working point of each foil.
- 2641 • To place the full power system in the USC area in order to have the core of the GEM
 2642 system in an accessible area.
- 2643 • To design a power system fully compatible with the hardware, firmware, DCS and
 2644 DSS presently used by CMS.

2645 The HV board for the GEM HV-CC is now under design. A first prototype will be delivered
 2646 in the first part of 2015. It is a 1U board that can be allocated directly in the back of a SY1527
 2647 CAEN mainframe and is equipped with two independent complex channels, each providing
 2648 7 voltages that can be regulated and monitored independently. The main features of the HV
 2649 board are:

- 2650 • 7 stacked (serial) HV channels (up to 1000 V)
- 2651 • Current monitor on each channel (resolution of 10 nA)
- 2652 • Voltage setting/monitor on each channel (resolution of 1 V)
- 2653 • Hardware Channel protections: maximum voltage, interlock
- 2654 • Software Channel protections: overvoltage, overcurrent, overtemperature
- 2655 • Very fast hardware feedback in case of discharge (local control)
- 2656 • Ripple lower than few volts
- 2657 • Floating at 5-10 V

- Back compatible with previous CAEN system

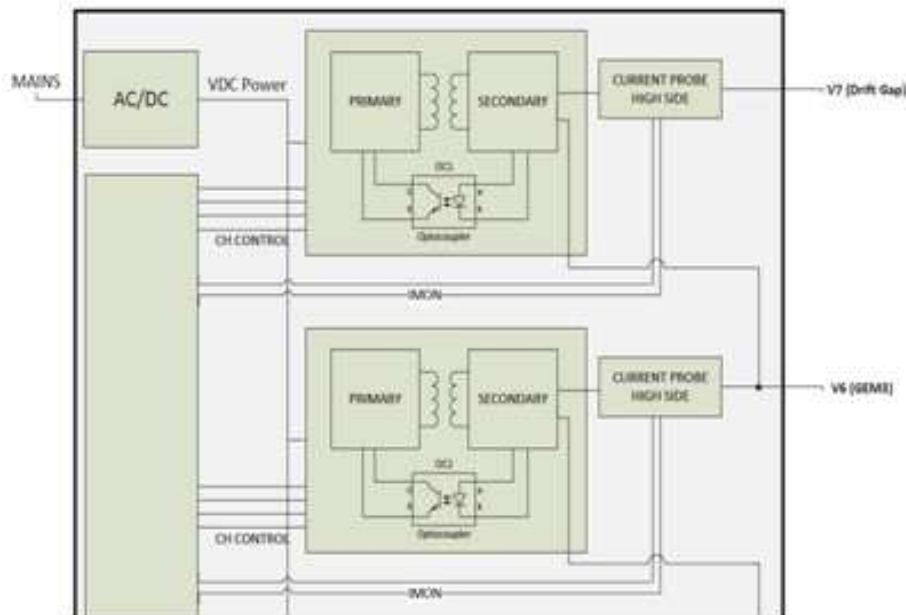


Figure 7.9: Schema of a voltage channel of the HV GEM board.

As shown in Figure 7.9, the full hardware system will be located in USC in order to reduce the number of inaccessible components and be able to access the system for maintenance and reparation anytime. This solution was strategic for the RPC project and was extremely useful to solve the problems encountered during the data taking. The USC (mainframe) and UXC (patch panel) will be connected through a multi-conductors cable (5 x 7 wires). Every set of 7 wires will be shielded and at same time one more shield will be added to the whole cable in order to protect it from external noise. The multi-conductors cable will run from the distributor in USC to the patch-panel in UXC. The USC distributor will be eventually used to join more chambers in one and reduce the number of HV boards needed but keeping the possibility to readout the absorbed current of every single chamber reading out the return line with a dedicated ADC.

7.3.2 LV power system

The LV power system will be based on CAEN EASY 3000, A3016 LV modules (see Figure 7.10).

	Voltage	Current consumption for single GE1/1 Detector	Current consumption for GE1/1 superchamber
VFAT	3.3 V	8 A	16 A
Opto-hybrid	4 V	6 A	12 A
Opto-hybrid	1.7 V	4 A	8 A

Table 7.3: LV power requirements for a single GE1/1 detector and a GE1/1 superchamber.

The LV power requirements for a GE1/1 superchamber are shown in Table 7.3. For each superchamber there are three LV channels to power the on-detector electronics.

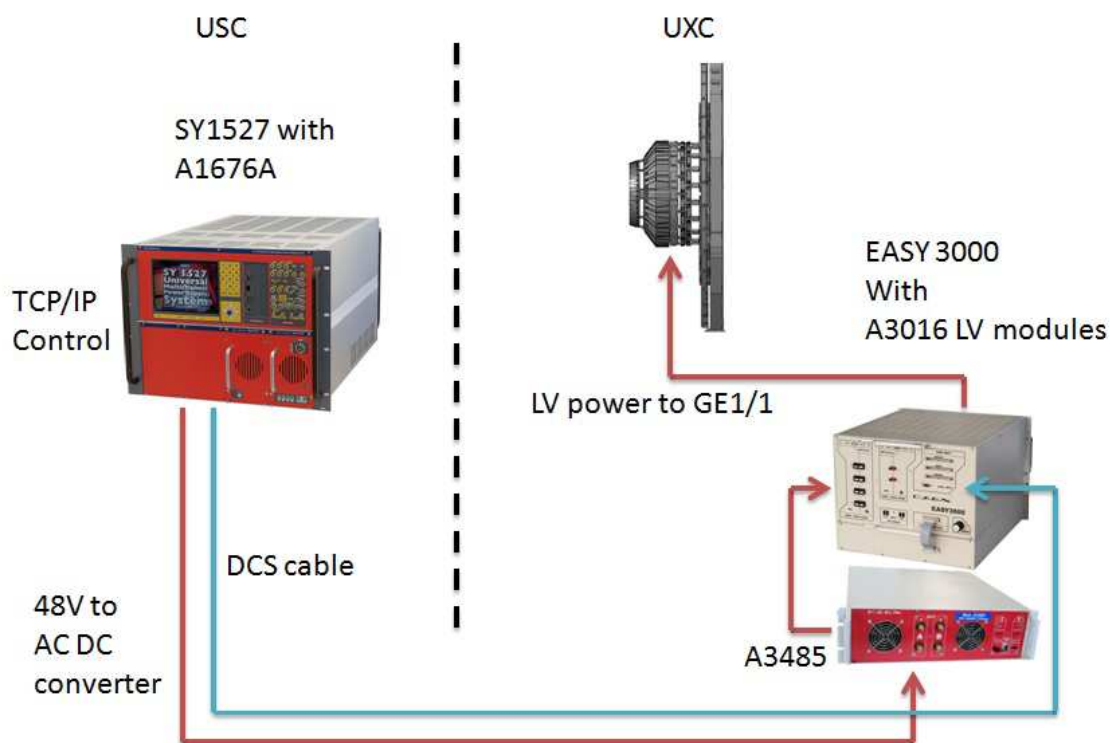


Figure 7.10: Architecture of the A3016 based LV power system.

7.4 Readout, control and power lines

7.4.1 Optical links and architecture

The GE1/1 chambers require optical fibers for the data flow and control as described in Chapter 3. For a single GE1/1 detector, 8 single fibers are needed to connect the GE1/1 Opto Hybrid (OH) with the μ TCA crates located in the service cavern (USC55). In Figure 7.11 the general plan is shown with the number of fibers indicated for each endcap. Per endcap, there will be 36 GE1/1 superchambers installed, each requiring 16 fibers, i.e. a total of 576 fibers per endcap without considering spares.

The environmental conditions of the GE1/1 installation slots require the fibers located on the YE1 endcaps to be radiation hard. Radiation hard fibers will be used only on the nose and the disk periphery. For the rest of the connections normal telecommunication fiber cables will be used from the YE1 disks to the backend crates in the service cavern. The proposed radiation hard fiber is the DrakaElite™ Super RadHard OM2 Multimode Optical Fiber, which permits lengths up to 300 m, with a bandwidth of 10 Gb/s, while the non-radhard fiber is the DrakaElite™ OM3 Multimode Optical Fiber [59]. To implement this scheme, 2 patch panels are planned for each connection: one located on the GE1/1 superchambers and another on the YE1 periphery. To accommodate 576 lines a 20U space is required for each endcap for patch panels. This space has to be equally distributed across the disk periphery to permit efficient routing of the services. As is shown in Figure 7.11, from the 20U patch panels on, the fibers are grouped into 7 telecommunication optical cables per endcap, which go to the USC μ TCA crates. To secure the connectivity of the GE1/1 superchambers, 20% of spare radhard fiber lines are foreseen to be distributed equally to every installation slot.

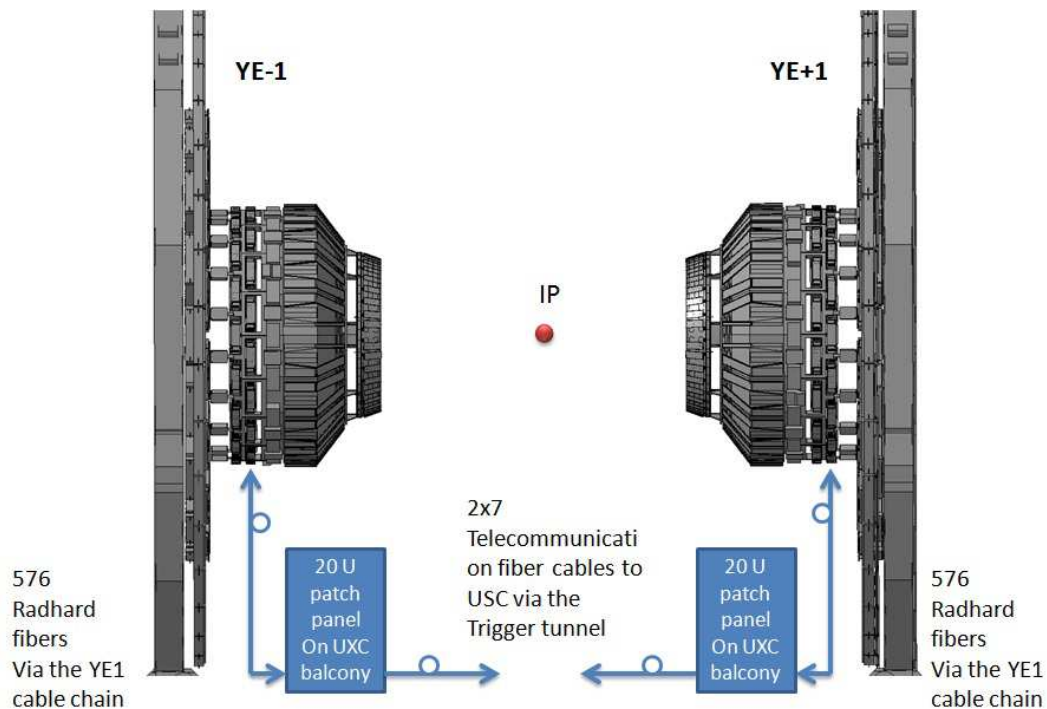


Figure 7.11: General scheme of the GE1/1 optical fibers.

7.5 Cable routing

2695

2696 The global routing plan of all cables for GE1/1 is shown in Figure 7.12. The bold red line
 2697 shows schematically the path of all cables from the GE1/1 superchambers, indicated as orange
 2698 rectangles, to the periphery of the YE1 disk. The cable routing on top of the ME1/2 and ME1/3
 2699 chambers is also shown, where dismantling of these detectors will be not necessary for the
 2700 GE1/1 installation.

2701 A complex issue to be faced in this upgrade project is the fact that all cable trays inside the
 2702 nose are already completely filled with services for other sub-detectors. Hence, a strategy to
 2703 avoid the standard paths was developed. Figure 7.13 shows the proposed routing of the cables
 2704 inside the YE1 nose structure. This scheme is valid only when all cables for LV and HV and
 2705 optical fibers are placed inside flexible ducts in order to secure and maintain the cable package
 2706 volume. The GE1/1 cables will follow the paths of the ME1/1 cooling pipes which are marked
 2707 in the figure as zig-zag blue dashed lines. In this way, the use of the nose cable trays is no
 2708 longer needed. The cables will simply be routed close to the right side of the trays as seen from
 2709 the interaction point.

2710 Figure 7.14 shows the clearance available between the top of the small cable tray, placed in the
 2711 ϕ direction and the YE1 nose covers. This represents the most critical point of the cable path
 2712 inside the nose. The picture shows this distance is about 30 mm, but for safety we are counting
 2713 it as 20 mm.

2714 Figure 7.15 shows several parts of the cable routing. The right picture shows the ME1/1 and
 2715 the copper cooling pipes starting from the detectors. Just in front, towards the interaction point,
 2716 the GE1/1 superchambers will be installed. The middle picture shows the overall path of the
 2717 cable duct which will be exact as the copper cooling pipe seen in the picture. In the left picture
 2718 one can see the breaking point which will go from the nose to the YE1 disk. On the endcap

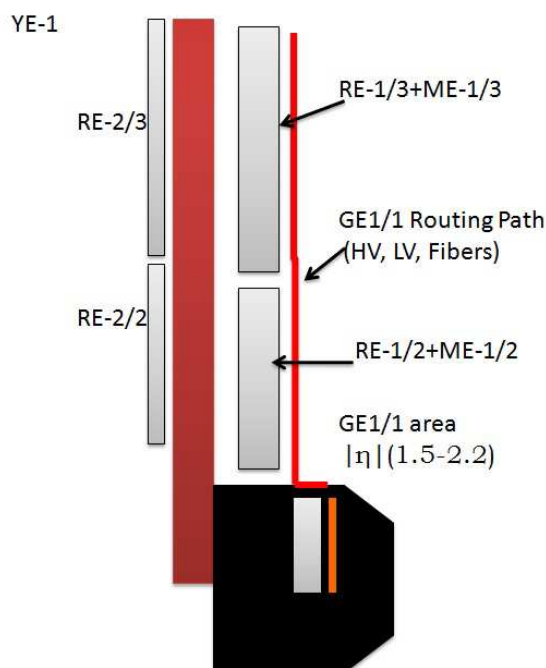


Figure 7.12: Diagram of the cable routing in the nose and on the YE1 disk.

2719 disks, the ducts will be placed on top of the ME1/2 and ME1/3 chambers, and will go all the
 2720 way to the periphery of the disks where the crate racks are located.

2721 7.6 Gas system

Detector gas volume	Volume [cm ³]	Gas flow [Volume/h]	Gas mixture [%]
Single GE1/1 detector - Long	3120	1	<i>Ar/CO₂/CF₄</i> 45 : 15 : 40
GE1/1 superchamber -Long	6240		
Endcap disk	224640		
Full installation	449280		

Table 7.4: General specifications of the GE1/1 gas system.

2722 Table 7.4 shows the basic parameters of the gas system for the GE1/1 stations in CMS. The
 2723 GE1/1 chambers are operated with a gas mixture of *Ar/CO₂/CF₄* 45 : 15 : 40%. It is similar
 2724 to the CSC mixture, but with different fractions of the main gas compositions. The tetraflu-
 2725 oromethane (*CF₄*) in the mixture demands the use of only copper and stainless steel pipes in
 2726 order to avoid water absorption and the formation of hydrofluoric acid, which is very danger-
 2727 ous for the detector electrodes. The GE1/1 gas system is partially using the existing RE1/1
 2728 gas infrastructure, in particular the previously installed copper pipes which run between the
 2729 GE1/1 installation zones and the gas distribution rack located on the YE±1 X1 towers at the
 2730 far side.

2731 Figure 7.16 shows the overview of the gas supply system for the GE1/1 stations. The main gas
 2732 mixer with the supply cylinders is placed in the gas building located on the surface. The final
 2733 *Ar/CO₂/CF₄* mixture is transported to the detector cavern through a 254 m long stainless steel

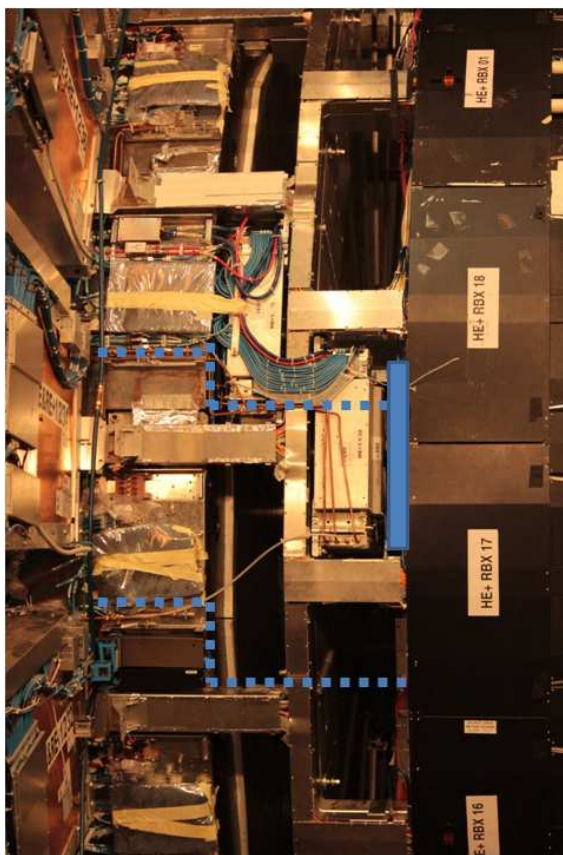


Figure 7.13: The cable routing inside the nose. The blue rectangle represents the patch panel of a GE1/1 chamber, while the blue dashed lines indicate the cable paths.

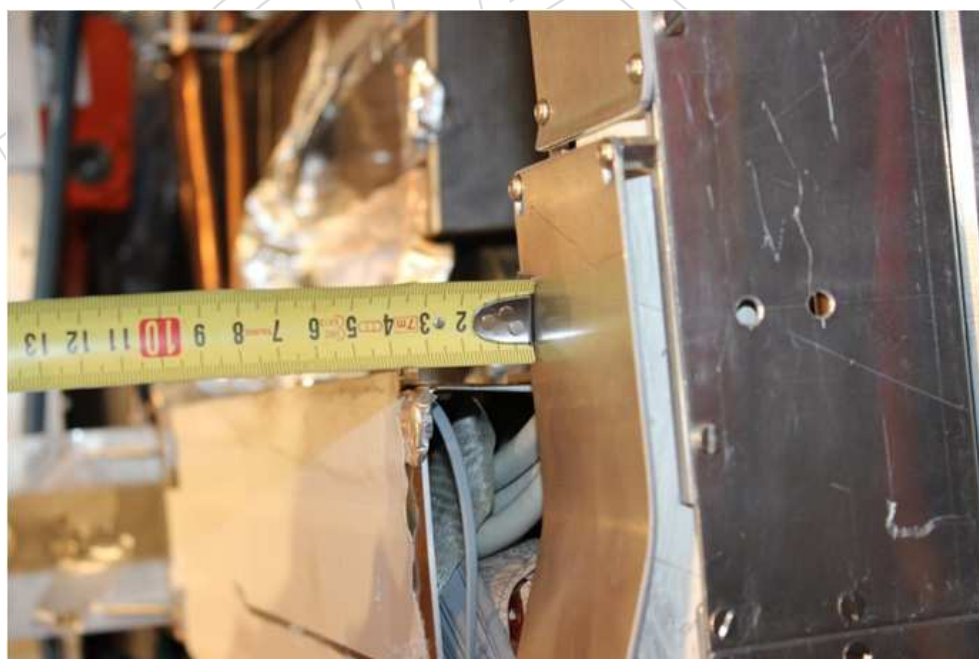


Figure 7.14: The maximum clearance available to install the cables between the CSC and the GE1/1 patch panel.

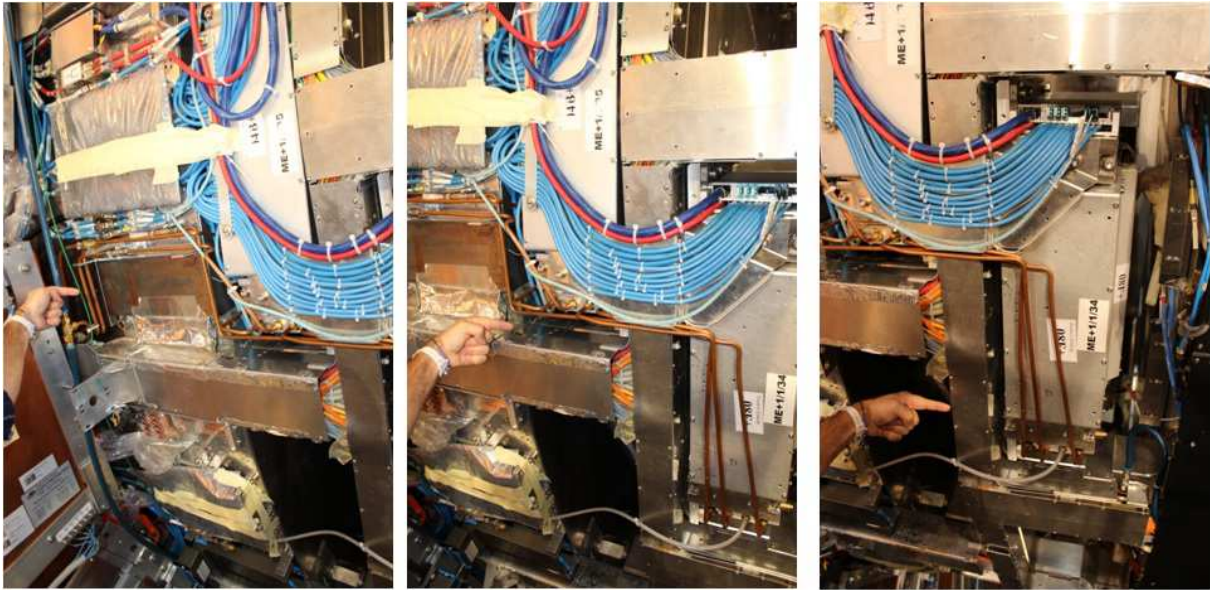


Figure 7.15: Cable routing inside the nose from GE1/1 to the YE1 disk.

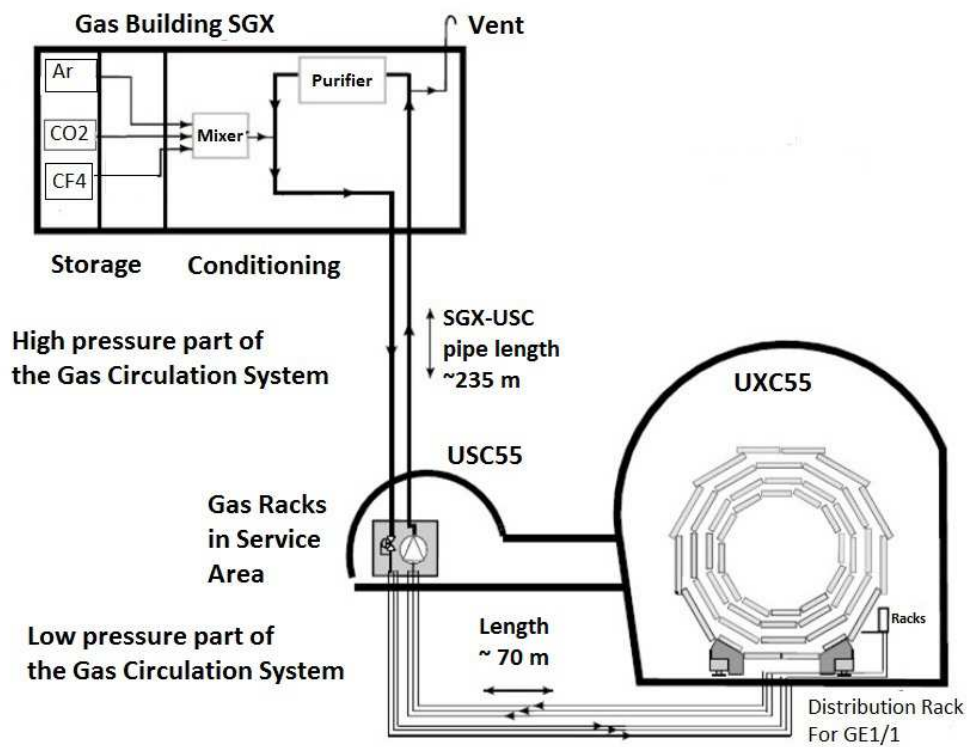


Figure 7.16: Overview of the GE1/1 gas system.

2734 transfer pipe of 30 mm in diameter which runs in the PM54 shaft and connects the surface gas
2735 building with the gas racks in USC55.

2736 The gas distribution for the GE1/1 installation slots is based on the existing pipe infrastructure
2737 foreseen initially for the RPC RE1/1 detectors. Tests are ongoing to validate the gas distribution
2738 circuit inside the YE1 nose.

2739 7.7 Cooling system

2740 The design of the GE1/1 cooling system is based on the calculations shown in Table 7.5 where
2741 the numbers are given for each heat power source on the detector side, i.e. the VFAT boards,
2742 the optical hybrid and the HV divider.

	Power consumption for GE1/1			
	Single chamber	superchamber	Endcap	Total
HV Divider	4 W	8 W	288 W	576 W
VFAT boards	24 W	48 W	1.7 kW	3.5 kW
Opto-hybrid	50 W	100 W	3.6 kW	7.2 kW
Total	78 W	156 W	5.6 kW	11.2 kW

Table 7.5: Power calculations for a single GE1/1 chamber, a superchamber, and total power consumption per endcap and both GE1/1 stations together.

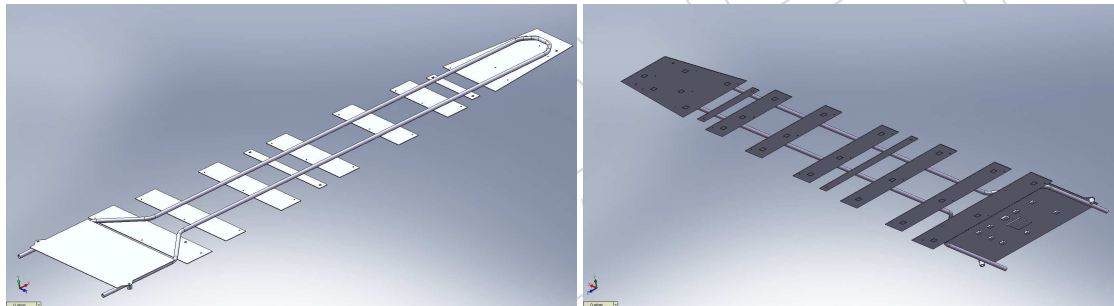


Figure 7.17: Top and bottom view of the GE1/1 cooling design.

2743 The GE1/1 on-detector cooling design is shown in Figure 7.17. The concept is based on the use
2744 of a u-shaped, 6 mm inner diameter copper pipe. The thermal contacts between the pipe and
2745 the heat sources are made with copper strip plates of 1 mm thickness.

2746 The YE1/1 cooling circuit is shown in Figure 7.18 where one can see the 12 cooling loops for
2747 ME1/1, RE1/1 and the HCAL readout box (RBX). The GE1/1 chambers will use the cooling
2748 loops that were foreseen for RE1/1.

2749 Figure 7.19 shows one of the 12 cooling loops of the YE1/1 circuit. There, the GE1/1 super-
2750 chambers are connected in series with the RBX. The amount of cooling power per supercham-
2751 ber is foreseen to be 156 W, including an extra safety margin. This will give a negligible impact
2752 on the present cooling system of the endcaps and will not lead to perturbation of the nearby
2753 subdetector systems.

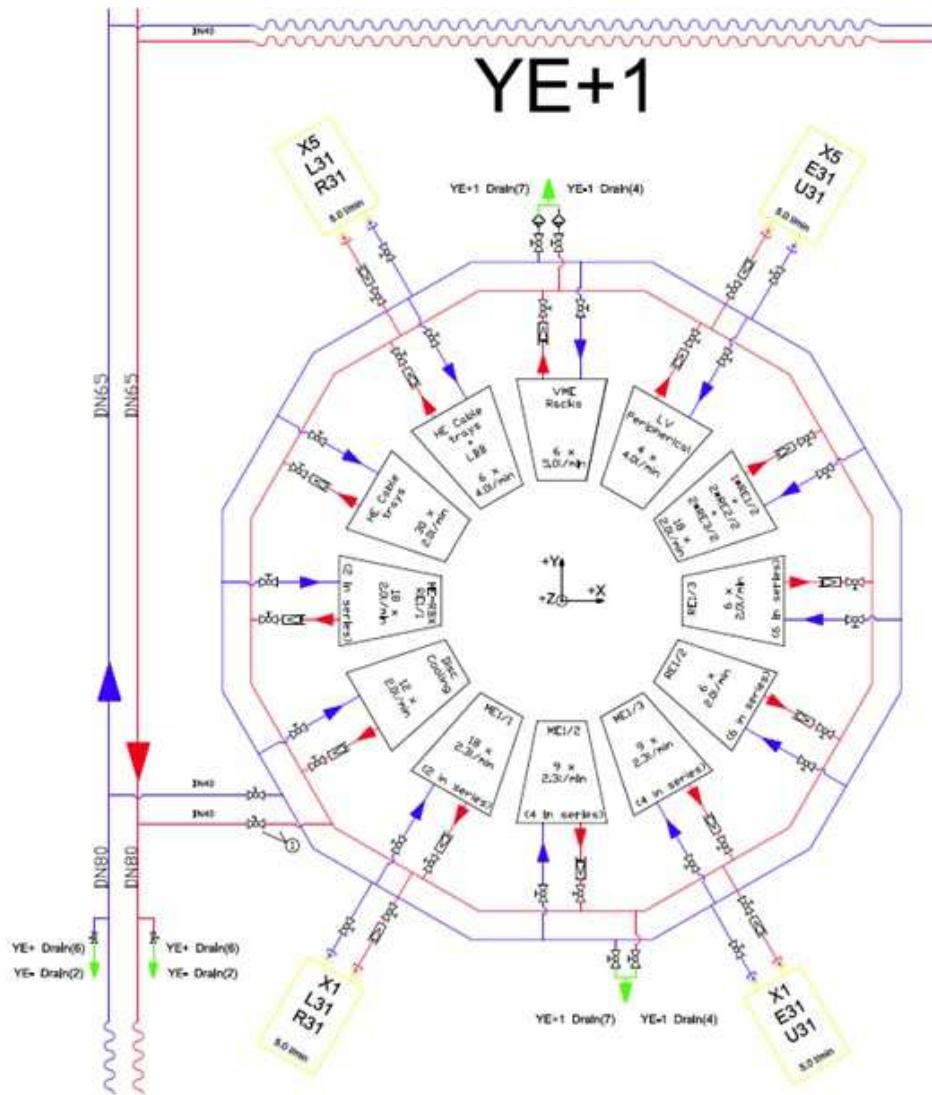


Figure 7.18: Overview of the YE1/1 cooling circuit.

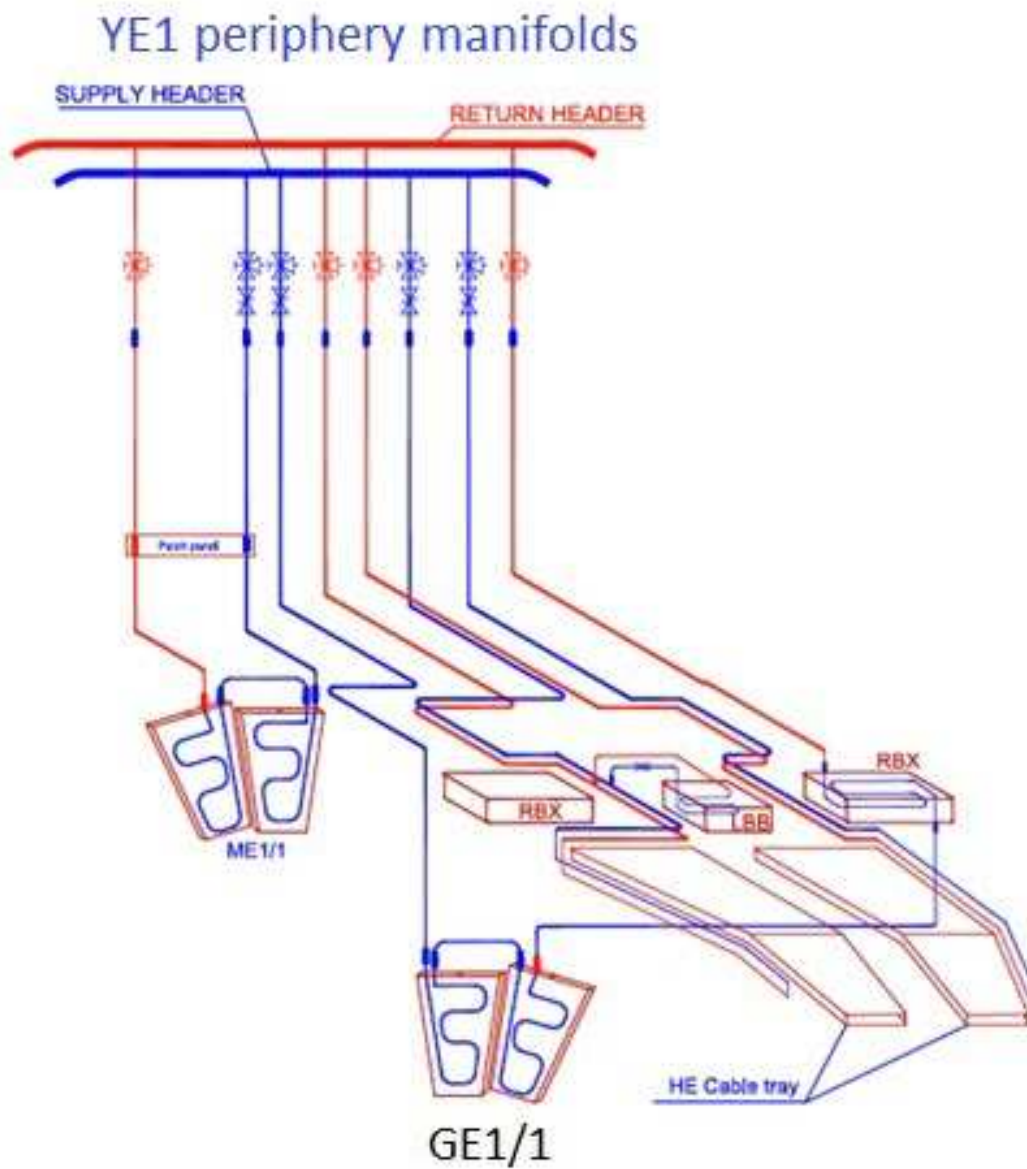


Figure 7.19: Overview of a single YE1/1 cooling loop.

2754 7.8 Proposal for radiation monitoring with RADMONs

2755 There is a proposal to monitor radiation on the GEMs with RADMONs [60]. RADMONs are
 2756 solid-state dosimeters developed at CERN that can provide a quantitative measurement of the
 2757 deposited dose and the exposed particle fluence in semiconductor devices. In one RADMON
 2758 there are four detectors mounted: two radiation-sensitive field-effect transistors (RADFETs) for
 2759 the photon dose and two p-i-n silicon diodes for the neutron and hadron dose measurement.
 2760 For the RADFETs the range of the deposited dose is 0.001 Gy to tens of kGy (depending of
 2761 required sensitivity). For p-i-n silicon diodes the range for neutrons is $10^8 - 2 \times 10^{12} \text{ cm}^{-2}$ (all
 2762 fluencies are quoted in terms of 1 MeVeq) and for fast hadrons ($E > 100 \text{ keV}$) and high en-
 2763 ergy neutrons ($E > 1 \text{ MeV}$) $2 \times 10^{12} - 4 \times 10^{14} \text{ cm}^{-2}$. The minimum setup is 12 RADMONs per
 2764 GE1/1 disk, i.e. one RADMON for three GE1/1 superchambers. The inhomogeneity across
 2765 superchambers as seen in FLUKA simulations (see Figure 7.20) justifies the number of RAD-
 2766 MONs.

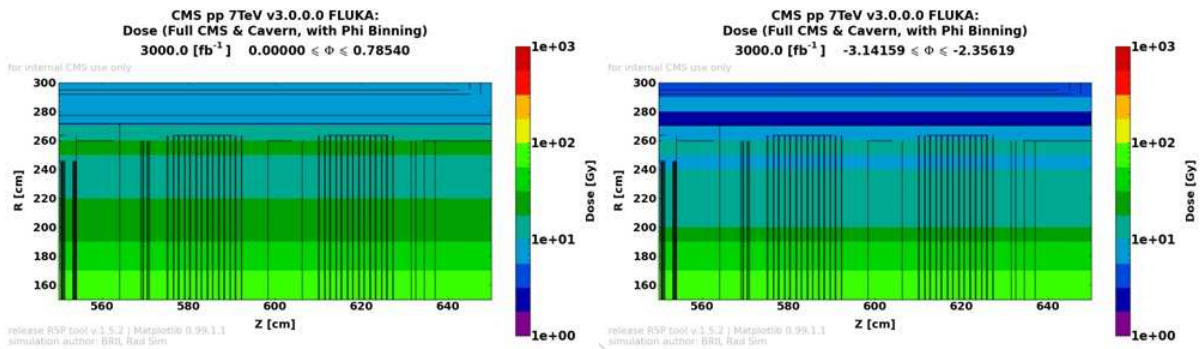


Figure 7.20: FLUKA simulation of the expected dose near the GE1/1 chambers, for $0 < \Phi < 0.78 \text{ rad}$ (left) and $-3.14 < \Phi < -2.36 \text{ rad}$ (right). Simulation performed for 3000 fb^{-1} of 7 TeV pp -collisions.

2767 The proposal made by the Sofia-INRNE group is to install and commission (at least) 2×12
 2768 RADMONs and controller boards for communication with the DCS (RS485, or CANBUS).

DRAFT

2769 Chapter 8

2770 Controls and Monitoring

2771 **Editors:** A. Cimmino, M. Maggi

2772 **Contributor:** J. Sturdy, O. Aboamer

2773 8.1 Introduction

2774 The complexity of the GEM system demands a high level of automation in operation in order to
2775 reduce human errors and optimize recovery procedures. In CMS the Detector Control System
2776 (DCS) [61] has two main tasks: the safe operation of the experiment and the monitoring of
2777 the status and performance of the detector. Data quality and certification of reconstructed
2778 data are tasks covered by the Data Quality Monitoring (DQM) system. These systems provide
2779 homogeneous environments across various subdetectors and trigger monitoring applications,
2780 allowing each subsystem to design and implement its own monitoring and control functions
2781 depending on its specific needs. Data from each subsystem are made available to central control
2782 system, which, in return, provides console hardware and software, archiving and other higher-
2783 level services.

2784 This chapter presents the design and implementation of the DCS and DQM systems for the
2785 GEM subdetector. The Database management system, being developed for the GEM project, is
2786 also briefly described.

2787 8.2 Detector control system

2788 The CMS DCS system provides control over all subdetectors, all infrastructure, services, its
2789 active elements, the electronics on and off the detector, the environment in proximity of the
2790 experiment, as well as communications with the accelerator. All of these tasks are historically
2791 referred to as “slow controls”.

2792 The architecture of each subsystem can be divided into Front-End hardware components (i.e.
2793 sensors, power supplies, etc.) located in the experimental area, and a Back-End system, com-
2794 posed of the DCS computers, network, and software applications. Because of the large vari-
2795 ety of equipment to be controlled, the standardization of the hardware and of the software
2796 interfaces is of primary importance for the homogeneous control of all different detector com-
2797 ponents. It aids the development of a uniform operator interface as well as minimizes the
2798 implementation and maintenance efforts. In accordance with CMS official guidelines, all back-
2799 end applications are developed using the commercial SIEMENS SCADA (Supervisory Control
2800 And Data Acquisition) [62] software, SIMATIC WinCC Open Architecture (WinCC OA) [63]
2801 and the Joint Control Project (JCOP) framework components [64] designed to enhance WinCC
2802 OA functionalities. JCOP includes components to control and monitor the most commonly

2803 used hardware at the LHC experiments, effectively reducing development effort and creating
 2804 a homogeneous system at the same time. It also defines guidelines for alarm handling, control
 2805 access, and partitioning to facilitate the coherent development of subdetector specific compo-
 2806 nents in view of their integration in the central system.

2807 The DCS is integrated in the CMS DAQ system [65] as an independent partition and, during
 2808 data taking, it is supervised by the Run Control and Monitoring System (RCMS) [66]. The
 2809 RCMS controls the subdetector and the central data acquisition systems. It is based on the hier-
 2810 archical control structure needed to control around $O(10^4)$ applications, which in turn control
 2811 electronics or handle event building and processing. The applications themselves are devel-
 2812 oped using the C++ based XDAQ [67] data acquisition framework, which provides hardware
 2813 access, powerful data transport protocols and services. XDAQ is a software platform. It has
 2814 been designed at CERN specifically for the development of distributed data acquisition sys-
 2815 tems.

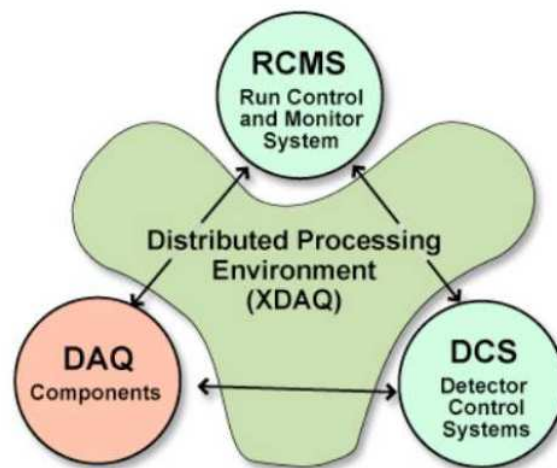


Figure 8.1: Schema of the interconnection among DCS, RCMS, DAQ, and XDAQ. [66]

2816 The interconnection among DCS, RCMS, DAQ, and XDAQ is schematically shown in Fig. 8.1.
 2817 A general set of system requirements for DCS are: partitionability, modularity, homogeneity,
 2818 scalability, automation and radiation tolerance. Furthermore, the high radiation and magnetic
 2819 field make the experimental hall inaccessible during running conditions. Therefore, the control
 2820 system must be fault-tolerant and must allow remote diagnostics. Many of its functionalities
 2821 are needed at all time. To ensure this continuity, UPS and redundant software and hardware
 2822 systems are implemented in critical areas. Besides these general requirements, each subdetector
 2823 has specific ones resulting from its unique design and implementation. Requirements specific
 2824 to the GEM subdetector are discussed in the following section.

2825 8.2.1 GEM detector control system

2826 The GEM DCS provides continuous control and monitoring of the subdetector, the trigger, and
 2827 all ancillary subsystems. It takes appropriate corrective and automatic actions when patho-
 2828 logical conditions are detected to maintain operational stability and ensure high quality data.
 2829 It monitors and controls the environment in proximity of the experiment, handling electricity
 2830 supply, cooling facilities, environmental parameters, crates, and racks. Safety related functions,
 2831 such as detector interlock, are provided by the GEM DCS in collaboration with the Detector
 2832 Safety System (DSS) [68]. The DSS, in fact, delivers uninterrupted and autonomous detector
 2833 protection in case of major hazards such as fire, gas leakage, or oxygen deficiency. The GEM

2834 DCS is not designed to be a personnel safety system.

2835 The GEM DCS is hierarchically organized in a tree-like structure and divided in subcompo-
2836 nents: high voltage (HV), low voltage (LV), environmental (humidity, temperature, and pres-
2837 sure), frontend electronics, gas, and cooling. Each component can work standalone, or in par-
2838 allel distributed over different machines. A supervisor level is required in order to gather and
2839 summarize all information, and to present it in a simplified but coherent interface to the oper-
2840 ators.

2841 All the information regarding running conditions and logging, referred to as conditions data,
2842 needs to be stored in order to monitor system behaviour over time and to perform off-line
2843 analysis. The GEM DCS stores conditions data in the CMS Online Master Data Storage, used
2844 by all the online subsystems. In its final configuration, the amount of GEM DCS data stored
2845 will be ~ 5 GBytes/year.

2846 These data are not easily searchable and viewable from outside the CMS site due to security
2847 restrictions. A natural method to convey and display this information is through a web server.
2848 Thus, a Web Based Monitoring (WBM) tool [69], which uses Apache Tomcat application con-
2849 tainer [70, 71] and Java Servlet technology, is in place and accessible via web browsers for
2850 collaborators locally and remotely, anywhere and anytime. Among all monitoring services pro-
2851 vided by WBM and focused on real-time or historical status of the detector, two are of particular
2852 interest for the GEM subdetector: the LastValue and the ConditionBrowser. The LastValue ser-
2853 vice consists of interactive schematic representation of the detector and a browsable tree. The
2854 last recorded values of the detector quantities (detector status, voltages, currents, gas flow, and
2855 thresholds) and environmental quantities (temperature and humidity levels) are displayed for
2856 each of the 144 GEM chambers. The ConditionBrowser allows the access to all values stored
2857 in the database for visualization. The aforementioned quantities can be plotted for any given
2858 time interval or range of run numbers or luminosity sections. Thus, patterns in behaviour and
2859 performance of the system, as well as reoccurring problems, can be easily spotted and anal-
2860 ysed. In addition, via the GEM specific WBM service, more detailed and refined plots may be
2861 produced and visualized. Via custom written queries, different parameters can be displayed
2862 and correlated for monitoring purposes. As an example, operating voltages may be displayed
2863 only when the detector status is "ON" and only when proton-proton collisions were present.
2864 All WBM plots and their underlying data are downloadable for further offline analyses.

2865 8.2.2 GEM finite state machine

2866 Detector controls are organized in a tree-like Finite State Machine (FSM) hierarchy represent-
2867 ing the logical structure of the detector, where commands flow down and states and alarms
2868 are propagated upwards. FSMs offer an easy and powerful way to model detector behaviour
2869 through the definition of a finite number of states, transitions, and actions. All the subdetec-
2870 tor control systems are integrated in a single control tree headed by the central DCS to ensure
2871 a homogeneous and coherency throughout the experiment. Therefore, states and commands
2872 for top and the conjunction nodes are fixed by CMS. The states are: ON, OFF, STANDBY, and
2873 ERROR and the commands are: ON, OFF, and STANDBY. This ensures uniformity and com-
2874 patibility with the central DCS, permitting adequate transitions between the states. During a
2875 transition between states, the FSM takes care of loading the correct parameter values and alarm
2876 settings from the configuration database. Figure 8.2 describes the FSM schema for a high volt-
2877 age channel. The "transitional" states, RAMPING UP and RAMPING DOWN, describe the
2878 situation in which one or more HV channels are ramping in voltage towards the values have
2879 been set.

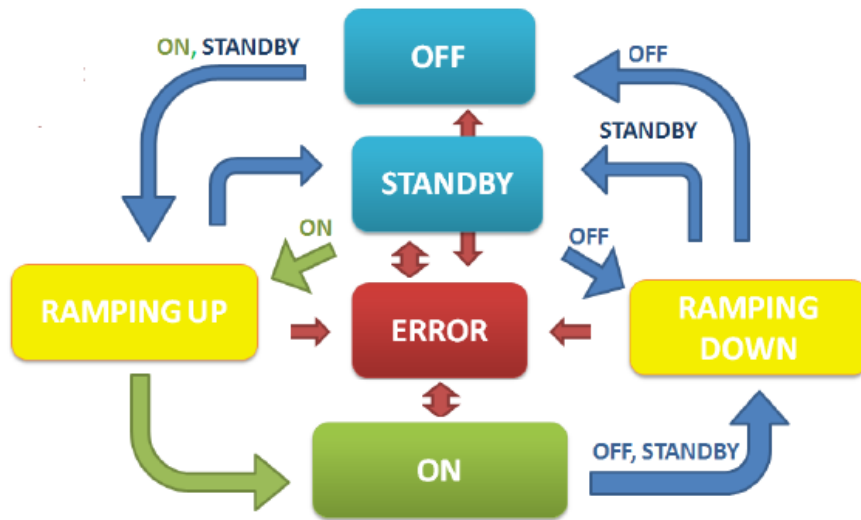


Figure 8.2: FSM schema for a high voltage (HV) channel.

2880 8.2.3 Electronic controls and monitoring

2881 The GEM electronic chain is described in Sec. 3 and Sec. 4. Monitoring the state of the electron-
 2882 ics, while taking data, is critically important. The trigger throttling system (TTS) provides the
 2883 feedback loop between the readout system and the trigger system. It functions by temporarily
 2884 reducing the L1A rate if it receives feedback that the readout system data buffers will begin to
 2885 overflow, resulting in a loss of data and possibly data corruption or readout system instability.
 2886 The system is designed in order to be able to cope with highest foreseen trigger rate. If a bot-
 2887 tleneck arises due to a malfunctioning piece of the system, it will be logged and an automatic
 2888 recovery will be attempted without sending the system into an error state. If the state stays in a
 2889 “warning” state for too long, and it can’t be automatically recovered, then an expert interven-
 2890 tion is required. If the system is sending bad or corrupted data, this will also be detected and,
 2891 whenever possible, recovered automatically without requiring a reconfiguration, possibly by
 2892 resetting and re-synching the links. Data formatting status (errors, event counters, etc.), system
 2893 buffer status, link buffer status, and link status will also be monitored, as they all provide key
 2894 information in the case of system malfunction.

2895 During normal running conditions of CMS, the electronics will undergo two steps: config-
 2896 uration and run. The configuration has to be a very quick operation, consequently all the
 2897 procedures for the electronic readiness must be happening in the initialization step, when it is
 2898 switched on, and automated.

2899 In fact, when the system is powered on, the VFAT chips will each have their parameters set to
 2900 values determined from calibration tests. The main operational parameters will be hit count
 2901 mode, the trigger mode, the mono-stable pulse length, the cycle time of the hit counter, voltage
 2902 thresholds on the comparator, and the chip latency with respect to the L1A. Additionally, for
 2903 each channel the threshold can be tuned by means of a trim DAC, and whether a particular
 2904 channel is masked or not. The optimal values will be set automatically at power on and checked
 2905 during configuration to verify that they have been properly set. All internal counters are also
 2906 reset to zero and the data buffer emptied. Calibration routines to determine the latency and
 2907 threshold of the chips (as well as the trim DACs) for the individual channels have been defined.
 2908 These need to be run few times in a year in order to ensure that the detector is operating
 2909 optimally. The calibration values will be stored in the configuration database that will serve

2910 the system in the initialization step. The configuration step is then simply translated in setting
2911 into “run mode” from “sleep mode” each chip, after which they will send data packets to the
2912 optohybrid on a received L1A.

2913 The optohybrid will process the data received from the VFAT chips. S-bits will be sent to the
2914 GE1/1-CSC trigger link, as well as the GE1/1 backend electronics. The full tracking data will
2915 be sent to the backend electronics to be checked, packaged, and sent to the readout system.
2916 The optohybrid will receive the fast commands and distribute them to the VFAT chips. On
2917 initializing the hardware, a check is done to ensure that the optical links are all active and error
2918 free. On configuring the device, counters will be reset (L1A, events received from each VFAT,
2919 events sent to the backend electronics, events sent to the trigger link, and any error counts on
2920 the links or in the data packets), and during normal running condition the link with the CSC
2921 OTMB will be enabled. During running, the Optohybrid can format the data from all VFAT
2922 chips into a common block and send it to the backend for further processing. Counters to
2923 check the integrity of the data passing through the system can be used to track the number of
2924 CRC errors and other problems in the stream.

2925 The backend electronics boards (MP7) will process the data received from several optohybrids
2926 and format it to be sent to the central DAQ system via AMC13. In addition, the central trig-
2927 ger and timing commands will be received by the backend electronics to be sent to the detector
2928 frontend. On starting the system, the communication with the frontend will be established. De-
2929 pending on the run mode (global or local), a connection to the central system as well is required.
2930 Configuration will involve resetting the counters of all fast commands received, as well as error
2931 counters and event processing counters. The GE1/1 run mode will be programmed into the
2932 MP7 cards, specifying the data readout path (whether to perform a local readout or not), the
2933 trigger source (central TTC system or possibly a local trigger source for certain types of calibra-
2934 tion runs), and other running information common for the whole GE1/1 system. Monitoring
2935 the system will involve checking errors during the formatting of the data received from the
2936 optohybrid, monitoring the status of the specific MP7 with regard to the TTC/TTS system to
2937 ensure that the whole system is in sync.

2938 GBT optical links connect the frontend electronics with the GE1/1 backend electronics and pro-
2939 vide a trigger link with the CSC subsystem (OTMB). Fast commands (TTC/TTS signals, L1A,
2940 etc.) as well as the DAQ link to the central CMS are provided to the GE1/1 μ TCA crate through
2941 the CMS standard AMC13 card. Signals coming from the central system are delivered to the
2942 MP7 boards over the μ TCA Fabric B connections. These signals are transmitted to the frontend
2943 electronics over the same bi-directional optical links that receive the tracking and trigger data
2944 from the frontend electronics. During the configuration step, the status of the various
2945 optical links will be established, and, in the case of one of the links being inactive (Optohybrid
2946 to OTMB for triggers, Optohybrid to MP7 for readout, or AMC13 to cDAQ for DAQ) the system
2947 will attempt to establish the link. If it is unable to do so at this stage, the system will attempt
2948 a recovery via a resynchronization or reset in the firmware. If this is unsuccessful, the config-
2949 uration step must fail and the faulty link be specified waiting for expert intervention. During
2950 running, the quality of the data being transmitted on the optical links between the optohybrid
2951 and the OTMB, as well as the path to the backend will be monitored for problems. If errors are
2952 detected on the optical links, this may necessitate a reset issued by the firmware, or in extreme
2953 cases, a reconfiguration of the hardware.

2954 **8.3 Data quality monitoring system**

2955 The CMS Data Quality Monitoring (DQM) framework [72] provides, within the more general
2956 CMS framework, common tools for creation, filling, storage, and visualization of histograms
2957 and scalar elements. It offers standardized algorithms for statistical tests and automated data
2958 certification. It is a set of user-defined algorithms. It is intended to be used both online, during
2959 data taking, and offline, during reconstruction and re-reconstruction stages. Its final purpose
2960 is to monitor and certify the quality of recorded data.

2961 Online DQM applications are an integral part of the event data processing. Each application,
2962 usually one per subsystem, receives event data through a dedicated Storage Manager event
2963 server. A special stream of events is used to perform DQM operations [73]. The stream con-
2964 tains detector and trigger raw data, Level-1 and High Level Trigger (HLT) summary results, in
2965 addition to HLT byproducts essential for monitoring trigger algorithms. There is neither event
2966 sorting nor handling, and no guarantee that parallel applications receive the same events. Start-
2967 ing and stopping DQM online applications is centrally managed by the RCMS.

2968 On the other hand, Offline DQM runs as part of the reconstruction process at Tier-0, of the
2969 re-reconstruction at the Tier-1s, and of the validation of software releases, simulated data, and
2970 alignment and calibration results. Despite the difference in location, data content and timing
2971 of these activities, offline monitoring is unique and formally divided into two steps. First, his-
2972 tograms are created and filled while data are processed event by event. The second step is the
2973 harvesting when histograms and monitoring information, produced in step one, are extracted
2974 and merged to yield full statistics. Efficiencies are calculated, summary plots are produced,
2975 and quality tests are performed. The automated data certification decision is taken here. The
2976 disadvantage of offline monitoring is the latency of reconstructed to raw data, which can be
2977 as long as several days. On the other hand, the advantages are substantial. All reconstructed
2978 events can be monitored and high-level quantities are available. This allows the identification
2979 of rare or slowly developing problems.

2980 **8.3.1 Architecture of the GEM DQM system**

2981 The GEM DQM system is developed within the compass of the CMS reconstruction and physics
2982 analysis software framework, CMSSW, and is based on object-oriented programming languages:
2983 C++ and Python. It has been designed to be flexible and easily customizable, since it needs to
2984 be used within different monitoring environments: online/offline DQM and standalone pro-
2985 grams for private analyses. Every data analysis and monitoring algorithm is implemented in a
2986 separate module, completely independent from the others. Each module inherits from the par-
2987 ent classes DQMEDAnalyzer and DQMEDHarvester [74] specifically designed for monitoring
2988 purposes. Modules may be added or eliminated from the monitoring sequence as needed. Dif-
2989 ferent parameter configuration files allow the modules to run on both detector and simulated
2990 data without requiring code changes and so re-compilation. The modules have been organized
2991 in a source/client structure.

2992 Source modules access information on an event-to-event basis, define the quantities to be moni-
2993 tored, and fill histograms. Event selection is performed at this level using specific trigger paths.
2994 Offline applications instead run on muon enriched samples during the event-reconstruction
2995 stage. Client modules perform the actual analyses by accessing periodically the histograms
2996 with a frequency that depends on the monitored quantity, varying from every luminosity sec-
2997 tion to once a run. Clients have the tasks of: creating summary histograms, performing quality
2998 tests, calculating alarm levels, saving the output in ROOT files, and taking a preliminary data
2999 certification decision.

3000 Histograms are organized in a hierarchical tree-like folder structure reproducing detector ge-
 3001 ometry. The parameters monitored are: single hit multiplicity, bunch crossing, number of re-
 3002 constructed hits, cluster size, occupancy, detection efficiency, detector noise, and data integrity.
 3003 These parameters are monitored for each of the 144 GEM chambers individually. This sums
 3004 to \sim thousand histograms and navigating through them is complicated for non-experts. There-
 3005 fore, special layouts containing only summary histograms are prepared for both GEM and cen-
 3006 tral DQM shifters, thus allowing the shift crew to quickly identify problems and take action.
 3007 These histograms are meaningful, not overburdened with information and equipped with a
 3008 clear set of instructions for interpreting them. Reference histograms may be superimposed and
 3009 Quality Tests (QT) are applied. QTs are standardized and integrated within the CMS DQM
 3010 framework. They include among others: comparison with reference histogram using ROOT
 3011 χ^2 algorithm and ROOT Kolmogorov algorithm, check that histogram contents are between
 3012 $(X_{min}, X_{max}) / (Y_{min}, Y_{max})$.

3013 8.3.2 Data certification

3014 The overall certification of data collected during hit operation is based on the online and offline
 3015 DQM, and on the DCS monitored information.

3016 A preliminary data certification is performed automatically within the GEM offline DQM al-
 3017 gorithms. This automatic certification is based on the results of standard quality tests applied
 3018 to the occupancy, cluster size, noise, data integrity distributions, as well as on the GEM DCS
 3019 status. The application is flexible enough to allow the expert to modify the algorithm in case
 3020 of need. The automatic certification is bound to provide as a result a number that has to range
 3021 between 0 and 1 reflecting detector performance and a quality flag, i.e. good, bad. The CMS
 3022 specification requires the quality flag to be set to bad when such a number is less than 0.95. Such
 3023 a case requires expert intervention. Results are visually displayed in a summary histogram as
 3024 shown in Fig. 8.3. The plot uses dummy data and it is presented for illustrative purpose only.

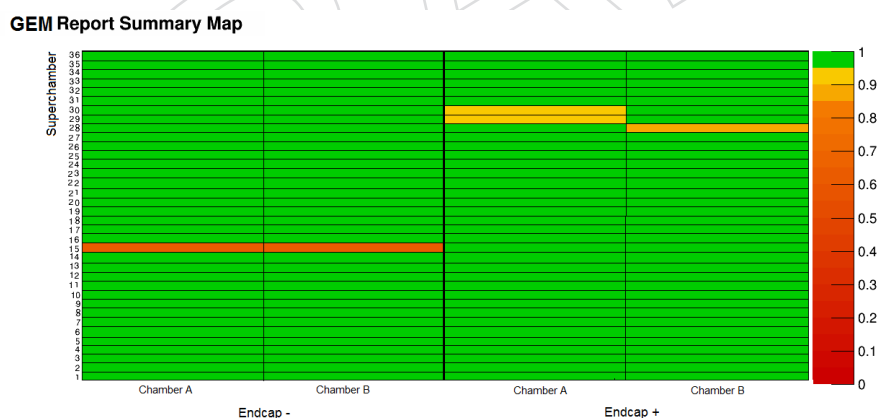


Figure 8.3: Automatic data certification results displayed in a summary report histogram. Color convention follow CMS specifications. Dummy data has been used for this plots that is here presented for illustrative purpose only.

3025 A more accurate certification is performed by both online and offline by central DQM shifters.
 3026 During the first running period Online DQM shifts took place 24/7, during detector operation
 3027 at the CMS "on-detector" control room in Cessy, France. Offline DQM shifts were carried out,
 3028 only in daytime, at the CMS control center, on the main CERN site. Shift activities are sup-
 3029 ported by regular remote shifts; two shifts per day at Fermilab (USA) and one shift per day
 3030 at DESY (Germany). Shifters analyse a limited number of summary histograms with an ex-

3031 haustive set of instructions to facilitate this task. The final list of “good” and “bad” run flags
3032 is inserted in the CMS Run Registry (RR) [75] and must be signed-off by a GEM Data Manager
3033 expert, as a final certification step, and copied to the offline condition database. The RR is the
3034 official workflow management and tracking tool used to certify collected data, to keep track of
3035 the certification results, and to make them available to the entire collaboration via a web-based
3036 user interface.

3037 **8.3.3 DQM graphical user interfaces**

3038 DQM output, which includes histograms, alarm states, and quality test results, is made avail-
3039 able in real time via a central graphical user interface (GUI) [76], accessible from the web. Being
3040 web-based, this central GUI permits users all over the world to access the data and check results
3041 without installing experiment specific software. Monitoring data is also stored to ROOT files
3042 periodically during the run. At the end of the run, final result files are uploaded to a large disk
3043 pool accessible from the central GUI. Subsequently, files are merged to larger size and backed
3044 up to tape. Recent monitoring data (several months worth) are cached on disk for easy access.
3045 The GUI was custom built to fulfil the need of shifters and experts for efficient visualization
3046 and navigation of DQM results and not meant as a physics analysis tool.

3047 The GEM Data Manager expert can access all the real-time and historical information using
3048 any browsing system delivering prompt feedback on demand.

3049 **8.4 Database management system for the GEM project**

3050 The GEM project will rely on a dedicated Database management system (DB) within the official
3051 CMS Online Master Database System (OMDS) based on ORACLE technology. The GEM DB
3052 will be in charge of four different logical functionalities:

- 3053 • The Equipment Management DB, in charge to store all information of all the basic
3054 components of the GEM system and will comply with the traceability requirements
3055 imposed by the French Agency of Nuclear Security law concerning the nuclear in-
3056 stallations, being CERN classified as an “Installation Nucleaire de Base”.
- 3057 • The Construction DB will support the GEM Chamber and Electronics construction
3058 on all the phases storing the Quality Controls test result. Data will be kept to be
3059 able to trace back all possible problems appearing in the system. A dedicated web
3060 based user interface will be deployed to allow the operators to upload and retrieve
3061 all relevant information of the construction processes.
- 3062 • The Configuration DB will be used to store all the parameters needed to set up the
3063 system into any running mode. They will include voltage settings of power supplies
3064 and the programmable parameters of the electronics.
- 3065 • The Condition DB will store data that describe the state of the GEM during oper-
3066 ation. Those data are used in the studies of the detector performance and for post
3067 mortem analysis for malfunctioning detectors.

3068 The DB architecture will be designed to account for the different usage and access of the differ-
3069 ent data. It will use the same database schema as that used for construction and online opera-
3070 tions of other CMS subdetectors. The GEM DB will consist of multiple tables that are used to
3071 map and track the detector components, and to store detector test, configuration, and monitor
3072 data. The development process involves the use of 4 instances of the database, Template DB
3073 instance (current phase), Development DB, Integration DB, and Production DB.

3074 **Chapter 9**

3075 **Project Organization, Responsibilities,**
3076 **Planning and Costs**

3077 **Editors:** The GEM Project Management

3078 **Contributors:** A. Colaleo, P. Karchin, A. Safonov, A. Sharma, M. Tytgat

3079 **9.1 Participating institutes**

3080 The CMS GEM Collaboration is currently comprised of 40 institutions in 16 countries with a
3081 total of 194 physicists, engineers, senior technicians and doctoral students. A spreadsheet is
3082 maintained, with a list of personnel by institute, accessible from the CMS GEM twiki page:
3083 <https://twiki.cern.ch/twiki/bin/view/MPGD/CmsGEMCollaboration>. It is updated regu-
3084 larly with quarterly approvals at the GEM Collaboration board.

3085 The collaboration membership by country and institute follows.

- 3086 1. Univ. Libre de Bruxelles, Brussels, **BELGIUM**
3087 P. Barria, G. De Lentdecker, M. Korntheuer, T. Lenzi, T. Maerschalk, E. Verhagen, Y. Yang,
3088 R. Yonamine, F. Zenoni
- 3089 2. Ghent Univ., Gent, **BELGIUM**
3090 S. Cauwenbergh, A. Cimmino, S. Salva, M. Tytgat, N. Zaganidis
- 3091 3. Inst. Nuc. Res. & Nuc. Energy (IRNE) Sofia, **BULGARIA**
3092 A. Aleksandar, V. Genchev, R. M. Hadjiiska, I. Plamen, M. Rodozov, M. Shopova, G. Sul-
3093 tanov
- 3094 4. Peking Univ., Beijing, **CHINA**
3095 C. Asawatangtrakuldee, Y. Ban, D. Wang, M. Wang
- 3096 5. Univ. de Los Andes, Bogota, **COLUMBIA**
3097 C. Avila, B. Gomez, J.C. Sanabria
- 3098 6. Academy of Scientific Research and Technology, Cairo, **EGYPT**
3099 Y. Assran, A. Radi
- 3100 7. Helwan University, Cairo, and Center for Theoretical Physics, Zewail City, **EGYPT**
3101 A.A. Abdelalim, W. Ahmed, R. Aly, W. Elmetenawee, A. Hassan
- 3102 8. Lappeenranta Univ. of Technology, Lappeenranta, **FINLAND**
3103 M.T. Kupiainen, J. Talvitie, T. Tuuva

- 3104 9. Atomic Energy and Alternative Energies Commission, Saclay, and Inst. of Research into
3105 the Fundamental Laws of the Universe, Saclay, **FRANCE**
3106 G. Fabrice
- 3107 10. Hubert Curien Multidisciplinary Inst. , Strasbourg, **FRANCE**
3108 J.-M. Brom, U. Goerlach, J.A. Merlin
- 3109 11. Aachen Univ., Aachen, **GERMANY**
3110 K. Hoepfner, B. Philipps, F.-P. Zantis
- 3111 12. Inst. for Particle and Nuclear Physics, Budapest, **HUNGARY**
3112 G. Bencze, G. Endroczi
- 3113 13. Inst. for Nuclear Research, Debrecen, **HUNGARY**
3114 N. Beni, S. Czellar, A. Fenyvesi, J. Molnar, Z. Szillasi
- 3115 14. National Inst. of Science Education and Research, Bhubaneswar, **INDIA**
3116 K. Mandal, P.K. Mal, S.K. Swain
- 3117 15. Panjab Univ., Chandigarh, **INDIA**
3118 J. Singh
- 3119 16. Delhi Univ., Delhi, **INDIA**
3120 A. Bhardwaj, A. Kumar, N. Mohammed, S. Ramkrishna, K. Ranjan, A.H. Shah, R.K. Shiv-
3121 puri
- 3122 17. Saha Inst. of Nuclear Physics, Kolkata, **INDIA**
3123 S. Banerjee, S. Bhattacharya, N. Majumdar, S. Mukhopadhyay, S. Roy Chowdhury
- 3124 18. Bhabha Atomic Research Center, Mumbai, **INDIA**
3125 A.K. Mohanty, L.M. Pant
- 3126 19. Univ. of Bari and National Inst. of Nuclear Physics, Bari, **ITALY**
3127 M. Abbrescia, P. Altieri, C. Calabria, C. Caputo, S. Nuzzo, R. Radogna, R. Venditti
- 3128 20. National Inst. of Nuclear Physics, Bari, **ITALY**
3129 A. Colaleo, G. de Robertis, F. Loddo, M. Maggi, A. Ranieri, C. Tamma, P. Verwilligen
- 3130 21. National Inst. of Nuclear Physics and Univ. of Bologna, Bologna, **ITALY**
3131 S. Braibant, F.R. Cavallo, M. Dallavalle, P. Giacomelli, L. Guiducci
- 3132 22. National Laboratory of Frascati, National Inst. of Nuclear Physics, Frascati, **ITALY**
3133 L. Benussi, S. Bianco, M. Caponero, M. Ferrini, D. Piccolo, G. Raffone, G. Saviano
- 3134 23. National Inst. of Nuclear Physics, Napoli, **ITALY**
3135 S. Buontempo, P. Paolucci, S. Meola
- 3136 24. National Inst. of Nuclear Physics and Univ. of Pavia, Pavia, **ITALY**
3137 C. Riccardi, P. Vitulo, A. Braghieri, A. Magnani, P. Montagna, P. Salvini, I. Vai
- 3138 25. National Inst. of Nuclear Physics and Univ. of Pisa, Pisa, **ITALY**
3139 L. Berretta, S. Lami, G. Magazzu, A. Scribano, N. Turini
- 3140 26. Kyungpook National University, Daegu, **KOREA**
3141 A. Sakharov

- 3142 27. Chonbuk National Univ., Jeonju, **KOREA**
3143 H. Kim, M.S. Ryu, Y.G. Jeng
- 3144 28. Korea Univ., Seoul, **KOREA**
3145 S. Choi
- 3146 29. Seoul National Univ., Seoul, **KOREA**
3147 U. Yang, J. Almond, G.B. Yu
- 3148 30. Univ. of Seoul, Seoul, **KOREA**
3149 K. Choi, M. Choi, H. Kim, J. Lee, J. Lee, I. Park, G. Ryu
- 3150 31. National Center for Physics, Islamabad, **PAKISTAN**
3151 W. Ahmed, I. Awan, A. Ashfaq, M.I. Asghar, H. Hoorani, S. Khan, S. Muhammad, A. Sul-
3152 tan
- 3153 32. Texas A&M Univ. - Qatar, Doha, **QATAR**
3154 M. Abi Akl, O. Bouhali, A. Castaneda, Y. Maghrbi
- 3155 33. Petersburg Nuclear Physics Inst., Gatchina, **RUSSIA**
3156 A. Vorobyev
- 3157 34. CERN, Geneva, **SWITZERLAND**
3158 D. Abbaneo, M. Abbas, P. Aspell, S. Bally, J. Bos, J. Christiansen, S. Colafranceschi, A. Conde
3159 Garcia, M.M. Dabrowski, R. De Oliveira, B. Dorney, S. Ferry, A. Marchioro, A. Mari-
3160 nov, J.A. Merlin, E. Oliveri, H. Postema, A. Puig Baranac, A. Rodrigues, L. Ropelewski,
3161 A. Sharma, J.P. Talvitie, M. van Stenis
- 3162 35. Texas A&M Univ., College Station, **UNITED STATES OF AMERICA**
3163 A. Celik, S. Dildick, W. Flanagan, J. Gilmore, T. Kamon, V. Khotilovich, S. Krutelyov,
3164 A. Safonov, A. Tatarinov
- 3165 36. Wayne State University, Detroit, **UNITED STATES OF AMERICA**
3166 A. Gutierrez, P.E. Karchin, J. Sturdy, P. Thapa, S. Zaleski
- 3167 37. Univ. of Florida, Gainesville, **UNITED STATES OF AMERICA**
3168 D. Acosta, I. Furic, A. Korytov, A. Madorsky, G. Mitselmakher
- 3169 38. Univ. of California, Los Angeles, **UNITED STATES OF AMERICA**
3170 J. Hauser, A. Peck
- 3171 39. Florida Inst. of Technology, Melbourne, **UNITED STATES OF AMERICA**
3172 V. Bhopatkar, M. Hohlmann, A. Mohapatra, M. Phipps, J. Twigger, A. Zhang

3173 9.2 Project organization

3174 The CMS GE1/1 muon upgrade is a project of the CMS GEM Collaboration in the CMS Muon
3175 Collaboration. An overview of the CMS GEM organizational structure is shown in the organ-
3176 igram of Figure 9.1. This organizational chart has evolved from 2009-2010 when the proto-
3177 collaboration was constituted from CMS-SLHC-RD-2010.02. It was comprised of active collabor-
3178 orators in detector R&D and studies for physics motivation. During 2011-2012 a revision was
3179 made with the addition of several new institutions when aspects of trigger exploitation using
3180 the detector were introduced. Finally during 2013-2014 the collaboration increased with partic-
3181 ipation in every aspect from all institutions outline above. The evolution of the collaboration

3182 and management may be seen on the twiki page:
 3183 <https://twiki.cern.ch/twiki/bin/view/MPGD/CmsGEMCollaboration>.

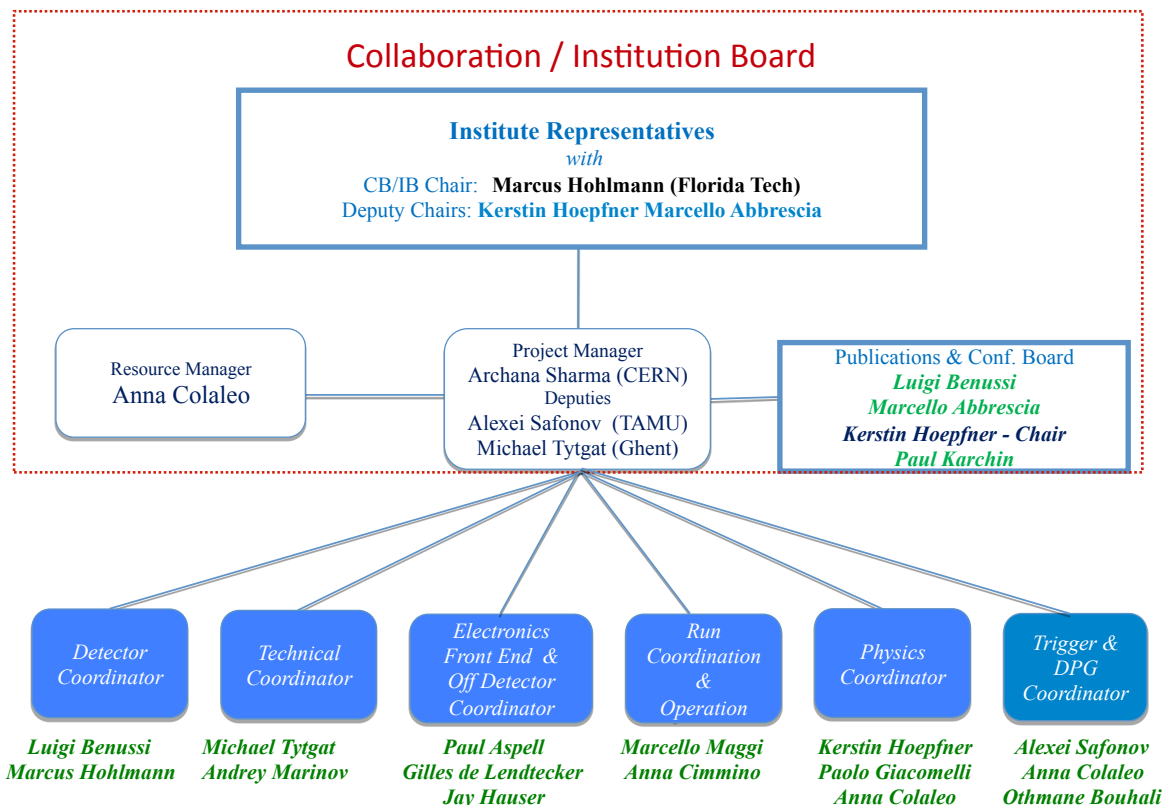


Figure 9.1: GEM collaboration management Organigram

3184 The GEM Management Board (MB) supervises, reviews progress, and defines planning and
 3185 strategy for the GEM project. It defines and manages the scope, budget, and milestones of the
 3186 project, and the sharing of responsibilities among the collaborating institutions. This is shown
 3187 in Figure 9.2 and is discussed in sect. 9.6.

3188 The GEM MB meets several times a year, typically during CMS and CMS upgrade/physics
 3189 weeks. In important areas where expertise lies outside the project (for example sophisticated
 3190 micro-electronics) matters of concern are brought to the attention of experts in the field and
 3191 solutions are sought.

3192 Overall direction of the project is provided by the GEM Institution Board (IB), composed of rep-
 3193 resentatives from each of the collaborating institutes and led by a chair and deputies. The GEM
 3194 IB meets periodically to provide guidance on technical and organizational matters. The GEM
 3195 IB provides a means of communication between the project management and the institutes.

3196 The GEM Project Manager (PM) and deputies provide the leadership to implement the goals
 3197 of the collaboration and coordinate activities with CMS Muon IB and CMS Upgrade manage-
 3198 ment. The management team includes a Resource Manager who maintains detailed records of
 3199 cost estimates, actual expenditures, and coordinates the assignment of experimental physics
 3200 responsibilities with the institute representatives.

9.3 Role of the Project Manager and Management Team

The Project Manager and the management team are selected by the institution leaders and endorsed by the collaboration Chairperson, who, along with the PM, represent the project to the CMS upgrade project office. The roles of the Project Manager and Chairperson are characterized by the following charge and deliverables.

- To lead the MB to define and manage the scope, cost and budget for the GEM upgrades, taking into account the LHC shutdown and schedules, available resources, and interests of the groups involved. In particular, this TDR reflects the management of the GE1/1 project to be installed during LS2.
- To lead the MB to define a set of project milestones and then steer the project to meet them, assuring the necessary flow of resources and information exchange throughout the project.
- To work closely in the project with the other coordinators to review technical progress, to manage the planning and strategy to deal well with problems and opportunities, to establish and maintain appropriate documentation with reliable archiving for all relevant technical specifications of parts and interfaces to ensure, QA procedures, QC procedures and logistics.
- To prepare for reviews of important technical, engineering and procurement decisions, normally chaired by CMS Upgrade and Technical Coordination.
- To chair the MB, organize meetings, agendas, objectives and follow-up with reports to the GEM and Muon Institution Boards.
- To work in partnership with the Upgrade and Muon teams to assure proper consideration of all decisions, including their impact on the Muon project as a whole, with appropriate preparation of points for endorsement by the Muon IB.
- To work closely with the GEM Resource Manager on all resource-related matters.
- To represent the GEM Upgrade in the CMS Upgrade Project Office as well as in CMS Management and LHCC meetings.
- Last but not least, the GEM MB Chairperson and Project Leader have been responsible for assembling an editorial team and publishing this TDR.

The PM and RM work to ensure that the sharing of effort is equitable across the collaboration. This assists in keeping track of the staffing of the project along with the necessary flexibility of injecting resources when needed in relevant areas.

The publications and conference committee promotes the publication of results from the CMS GEM project and their presentation in conferences. The committee assists in the review and approval of publications, conference abstracts, talk slides, posters, and conference proceedings. The committee also maintains a list of CMS GEM collaborators and authors.

The project management is assisted by coordinators in six key areas of the project: detector chambers, Technical Coordination, electronics, DAQ, operation, physics, and trigger/DPG. The detector coordinators manage the construction and testing of the GEM chambers. The technical coordinators are responsible for the planning and installation of chambers, electronics, and services at P5 and at test and preparation areas such as B904, TIF, GIF++, and test beams. The electronics coordinators manage the design and construction of on- and off-detector electronics including the front-end VFAT chips, GEBs, opto-hybrids, μ TCA readout system, trigger interface, firmware and DAQ software. Run and operations coordination includes irradiation and beam testing as well as operation at P5. The physics coordinators lead the simulation effort

3246 to assess the impact of the GE1/1 system on the physics performance of CMS in key channels
3247 in sync with ongoing CMS Upgrade as a whole. The trigger and DPG coordinators lead the
3248 development of software to simulate the GEM detectors, predict the trigger performance, and
3249 monitor the performance of the system during operation.

3250 9.4 GEM Technical Coordination Team

3251 This team is composed of two detector construction Coordinators, that lead the technical activ-
3252 ities within the project. The Coordinators act as a team to ensure the following items.

- 3253 • Realistic and detailed plans are prepared.
- 3254 • Adequate resources and supervision are committed to the different activity lines.
- 3255 • The planning is consistent with the project milestones, quality objectives and budget.
- 3256 • Progress is properly monitored across the technical activities in all centres and po-
3257 tential production sites at national institutes.
- 3258 • Technical specifications for parts and interfaces between parts of the system are es-
3259 tablished, well defined, documented and followed.
- 3260 • QA/QC procedures are established, well defined, documented and followed.
- 3261 • Information flows properly within the project, to/from the GEM MB and within the
3262 Technical Coordination Team, and that there is a central repository used to organize
3263 and archive project documents. The Coordinators convene technical steering groups
3264 of experts as necessary.

3265 9.5 Role of the Resource Manager

3266 The Resource Manager of the GEM project has the following tasks:

- 3267 • Maintaining and updating the subproject CostBook, starting initially from estimates
3268 of costs and funding, and evolving towards a detailed bookkeeping of actual ex-
3269 penses and contributions from the participating FAs
- 3270 • Elaborating and updating the cost time profile and the cost sharing among FAs.
- 3271 • Taking care, together with the Technical Coordinators and/or with the heads of
3272 Working Groups and/or the people responsible at the Production Centres, of pro-
3273 curements for the construction of the upgraded detector. Specifically, the Resource
3274 Manager is responsible along with the Project Manager, for the tendering process
3275 involved in common procurements performed centrally.
- 3276 • Reporting regularly on construction expenditures to the GEM MB, to the CMS FB,
3277 and preparing regular reports for the LHC RRB and the RRB Scrutiny Group as
3278 required.

3279 9.6 Organization of Construction work

3280 A preliminary sharing of the areas of work is shown in Figure 9.2. The horizontal rows describe
3281 the major tasks undertaken for five key areas:

3282 **Detector Hardware** - Comprising GEM foil production, chamber component procurement and
3283 QA/QC for construction and assembly of the full detector

3284 **Technical Coordination** - Comprising integration, installation and services design and com-
3285 missioning to deliver a completed operational detector at the CMS P5 cavern, with a database
3286 that tracks production and operation

3287 **Electronics and DAQ** - Comprising the development of the front-end readout (VFAT), the elec-
3288 tronics readout board (GEB), the Optohybrid with GBTs, and the uTCA-based DAQ, with trig-
3289 ger software and firmware development

3290 **Detector Operation** - Comprising the Detector Control System (DCS), Data Quality Monitoring
3291 (DQM), Web-based monitoring (WBM), and Physics validation tools (PVT)

3292 **Trigger and Detector Physics** - Comprising detector stand-alone simulation, physics studies
3293 and simulation, reconstruction, muon and trigger performance, test beam activities and data
3294 analysis

3295 **The Slice Test** - Consisting of the test described in Appendix A of this document (See CMS MB
3296 DESY Upgrade 2014).

3297 The full collaboration has been and will actively participate in all activities listed above as can
3298 be seen in the table. The tasks have been discussed extensively with the institution leaders and
3299 commitments are reflected in the resource sharing matrix, presented in Figure 9.2.

3300 9.7 Meetings

3301 The CMS Gem Collaboration holds regular weekly, biweekly, monthly and quarterly meetings
3302 documented here: <https://indico.cern.ch/category/1865/>

3303 A Coordination meeting amongst the coordinators of the six groups is held weekly where
3304 progress on the most relevant topic is discussed, issues highlighted and possible solutions sug-
3305 gested.

3306 A Detector Hardware meeting scheduled weekly for updates on detector prototypes construc-
3307 tion, performance and coordination of work in the various laboratories.

3308 A Technical Coordination meeting is held biweekly to steer and manage all technical integra-
3309 tion and engineering aspects for detector component production, electronics, DAQ and services
3310 support

3311 The GEM Weekly meetings comprise:

- 3312 • GEM reconstruction and Validation
- 3313 • Geometry description and development for simulation
- 3314 • Detector Response and Modeling
- 3315 • GEM Trigger meetings

3316 The system meeting is held biweekly as needed. Collaborators are working together at 904
3317 integration centre where daily meetings are also scheduled as needed.

3318 An electronics VFAT3 designers round table is held monthly to steer and coordinate the devel-
3319 opment of front-end electronics and related software/firmware.

3320 A GEM DAQ meeting is held biweekly to coordinate the developments of the readout systems
3321 and relevant hardware, software and firmware.

3322 In addition to the meetings listed above, the GEM Collaboration meets three or four times a

Milestone	Date
Technical Design Report	3/2015
Final Design Validation	7/2015
Final Electronics Delivery	12/2016
Component Reception at Sites	8/2016
Single Chamber Completed and reception at CERN	6/2017
Ready for installation	6/2018

Table 9.1: Major milestones for the GE1/1 LS2 construction project.

3323 year in quarterly Workshops to update and steer cross coordination in various aspects of the
3324 project.

3325 9.8 Construction schedule

3326 An overview of the construction schedule, up to installation, is shown in Figure 9.3. The con-
3327 struction is aimed for completion in time for installation in LS2, currently scheduled to begin
3328 in June 2018.

3329 The major milestones of the project are shown in Table 9.1.

3330 9.9 Costs

3331 The detailed cost estimate of the GEM GE1/1 detector has been established, with about 200
3332 individual items in the Cost Book, on four levels of a Work Breakdown Structure (WBS).

3333 The cost estimates are for M&S only and include only those items which fall into the allowed
3334 expense group as defined by the CORE (LHCC Cost Review Committee) and advised by the
3335 CMS Resource Manager and stipulated by the CMS Finance Board specifically for the CMS
3336 Upgrade project as follows.

- 3337 • Final prototype or pre-production fabrication required to validate a final design or
3338 product quality, prior to production.
- 3339 • Engineering costs incurred during production at a vendor or contractor, not at a
3340 CMS member Institution.
- 3341 • Production fabrication and construction costs, including QA and system testing dur-
3342 ing the assembly process.
- 3343 • Transportation costs, integration and installation.

3344 All quotes and estimates have been collected in calendar years 2013 and 2014. Quotes and
3345 estimates have been provided in CHF, EUR, or USD, depending on the geographical location of
3346 institutes, companies, vendors, or suppliers. In this section, all monetary values are expressed
3347 in CHF. The following conventional exchange rates have been used to convert EUR and USD
3348 to CHF:

3349 $1\text{USD} = 0.92\text{CHF}$, $1\text{EUR} = 1.23\text{CHF}$

3350 As a general procedure, the cost of an individual item is estimated by using a unit cost and an
3351 estimate of the quantity needed. The quantity is the sum of the actual quantity to be mounted
3352 on the detector, the additional quantity, varying from item to item, needed to compensate for
3353 expected yields of certain fabrication operations, and the number of spares. The number of
3354 spares is estimated based on the need to safely overcome the assembly, integration, commis-

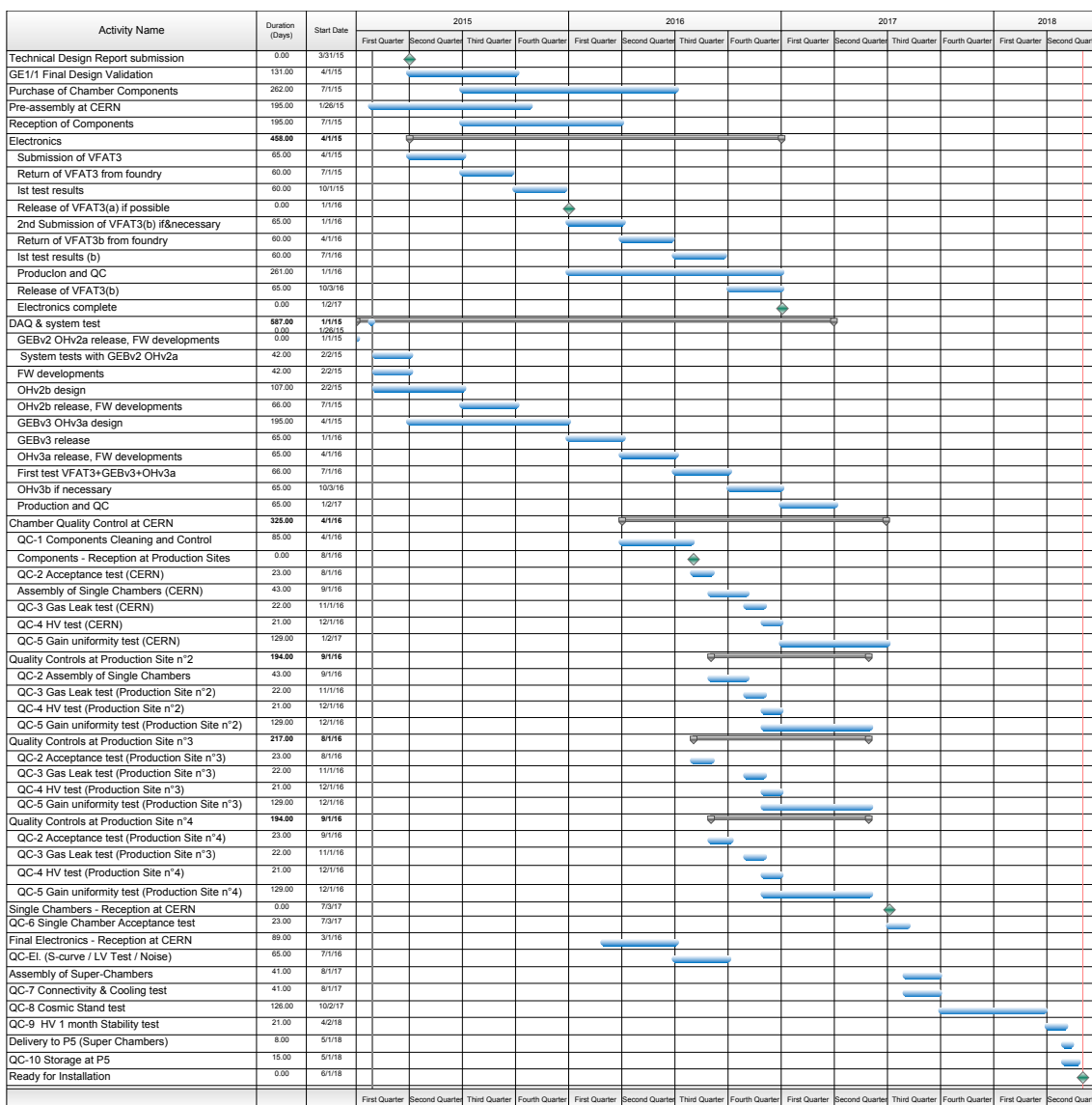


Figure 9.3: GEM GE1/1 LS2 project schedule.

3355 sioning, and installation stages, when handling of parts may result in accidental damage of
 3356 them, thus needing immediate replacement. We plan to build three additional complete cham-
 3357 bers for being ready in case of any eventuality during installation.

3358 The test bench at 904 will provide for up to six fully equipped chamber electronics, read-out
 3359 chain DAQ and trigger for final electronics as shown in Figure 5.1. The cost is 116kCHF and is
 3360 shown in Figure 9.4.

Item name	KCHF (2014)	Unit Cost	Currency of Unit Cost	Quantity of Units in CMS	Quantity of Units for Production Test Stands	Quantity of Production spares	Quantity of Units	Item Cost
Test Stand	116							
On Detector Total	40							
VFAT3 Eng Run	0	450000	CHF	0	0	0	0	0
VFAT3 Production	2	10	CHF	0	144	96	240	2400
VFAT3 additional Wafer costs	0			0	0	0	0	0
VFAT3 Hybrid	15	81	CHF	0	144	36	180	14564
GEB	14	1683	CHF	0	6	2	8	13465
Opto Hybrid	10	1184		0	6	2	8	9471
Off Detector Total	34							
MP7 (Crate incl)	26	12780	CHF	0	1	1	2	25560
Link Inter Crate	0	72	CHF	0	2	1	3	216
BI Links	8	256	CHF	0	24	6	30	7680
Uni Links	0	116	CHF	0	0	0	0	0
Power Total	42							
cables LV	1	100	CHF	0	6	0	6	600
cables HV	3	500	CHF	0	6	0	6	3000
LV supply	8	8130	CHF	0	1	0	1	8130
HV supply	10	9829	CHF	0	1	0	1	9829
LV Easy crates	2	1535	CHF	0	1	0	1	1535
HV Easy crates	2	1535	CHF	0	1	0	1	1535
AC/DC converter	5	4723	CHF	0	1	0	1	4723
mainframe	11	10627	CHF	0	1	0	1	10627
controller	1.5	1476	CHF	0	1	0	1	1476

Figure 9.4: GEM GE1/1 test bench.

3361 Following CMS guidelines for CORE costs, neither general contingency (for unexpected or un-
 3362 foreseen technical flaws or major accidents) nor financial contingency (for inflation, exchange
 3363 rate variations, or general evolution of economy or market conditions which may alter the cost

Item name	Total KCHF
GE11 Project total	3638
Chambers	845
Electronics On-Detector Total	1435
Test bench	40
GE11	1395
Electronics Off-Detector Total	334
Test bench	34
GE11	300
Power total	711
Test bench	42
GE11	669
Services	283
Integration	30

Figure 9.5: GEM GE1/1 LS2 project - CORE Cost Profile.

Item name	KCHF (2014)	Unit Cost	Currency of Unit Cost	Quantity of Units in CMS	Quantity of Units for Production Test Stands	Quantity of Production spares	Quantity of Units	Item Cost
GE11 Detector total	845							
Chamber components	799		CHF					
Drift electrodes	63	400	CHF	144	3	10	157	62832
GEM	581	3600	CHF	144	3	14	161	581040
Readout boards	126	800	CHF	144	3	10	157	125664
Cooling circuit	24	150	CHF	144	3	10	157	23562
Chamber assembly components	5	35	CHF	144	3	10	157	5498
Superchamber Assembly	6	80	CHF	72			72	5760
Storage and test stand at CERN	20	20000	CHF	1			1	20000
Shipping	20	20000	CHF	1			1	20000

Figure 9.6: GEM GE1/1 LS2 project - Detectors

3364 of procured materials and components) have been included in the estimates.

3365 The accuracy of the individual item cost estimates range from certain (i.e. a completed order
 3366 for final prototypes and/or actual cost of production site setups) down to educated guesses.
 3367 Whenever available, actual quotes already obtained from vendors and/or companies have
 3368 been used. In some cases, educated interpolation of market surveys not yet evolved to the
 3369 stage of a formal quote has been used. In other cases, careful extrapolations from similar parts
 3370 of the existing detector were carried out by experts, or groups thereof, who took care of the
 3371 corresponding parts of existing detectors.

3372 We present the estimated cost of the project: the global cost of the GEM GE1/1 Upgrade project
 3373 is estimated to be 3.6 MCHF and has been reviewed by CMS. A breakdown of the global cost
 3374 is presented in Table 9.5, with details of detector components in Table 9.6, and electronics and
 3375 power system in Table 9.7. Table 9.8 shows the costs of services needed to complete installation,
 3376 commissioning and operation in LS2.

Item name	KCHF (2014)	Unit Cost	Currency of Unit Cost	Quantity of Units in CMS	Quantity of Production spares	Quantity of Units	Item Cost
GE11 Electronics total	2364						
On Detector Total	1395						
VFAT3 Eng Run	450	450000	CHF	1	0	1	450000
VFAT3 Production	58	10	CHF	3456	2304	5760	57600
VFAT3 additional Wafer costs	22	240000		1	0	1	21600
VFAT3 Hybrid	350	81	CHF	3456	864	4320	349529
GEB	303	1683	CHF	144	36	180	302964
Opto Hybrid	213	1184		144	36	180	213098
Off Detector Total	300						0
MP7 (Crate incl)	115	12780	CHF	8	1	9	115020
Link Inter Crate	0	72	CHF	4	1	5	360
Bi Links	184	256	CHF	576	144	720	184320
Uni Links	0	116	CHF	0	0	0	0
Power Total	669						
cables LV	16	100	CHF	144	16	160	16000
cables HV	80	500	CHF	144	16	160	80000
LV supply	220	8130	CHF	24	3	27	219518
HV Supply	265	9829	CHF	24	3	27	265383
LV Easy crates	11	1535	CHF	6	1	7	10745
HV Easy crates	8	1535	CHF	4	1	5	7675
AC/DC converter	33	4723	CHF	6	1	7	33062
mainframe controller	32	10627	CHF	2	1	3	31882
	5	1476	CHF	2	1	3	4428

Figure 9.7: GEM GE1/1 LS2 project - Electronics

Item name	KCHF (2014)	Unit Cost	Currency of Unit Cost	Quantity of Units in CMS	Quantity of Production spares	Quantity of Units	Item Cost
GE11 Services total	283						
DCS	68						
DCS computers	10	5000	CHF	2	0	2	10000
Monitoring sensors	58	300	EUR	144	14	158	47520
GAS SYSTEM	165						
Control rack	15	15000	CHF	1		1	15000
Circulation pump	30	30000	CHF	1		1	30000
Mixer	30	30000	CHF	1		1	30000
Purifier	60	60000	CHF	1		1	60000
Exhaust	10	10000	CHF	1		1	10000
Distribution manifolds	5	210	CHF	24		24	5040
Connection to SGX5 supply	5	5000	CHF	1		1	5000
Connection to UGC	10	10000	CHF	1		1	10000
COOLING	50						
On disks infrastructure	50	50000	CHF	1		1	50000

Figure 9.8: GEM GE1/1 LS2 project - Services.

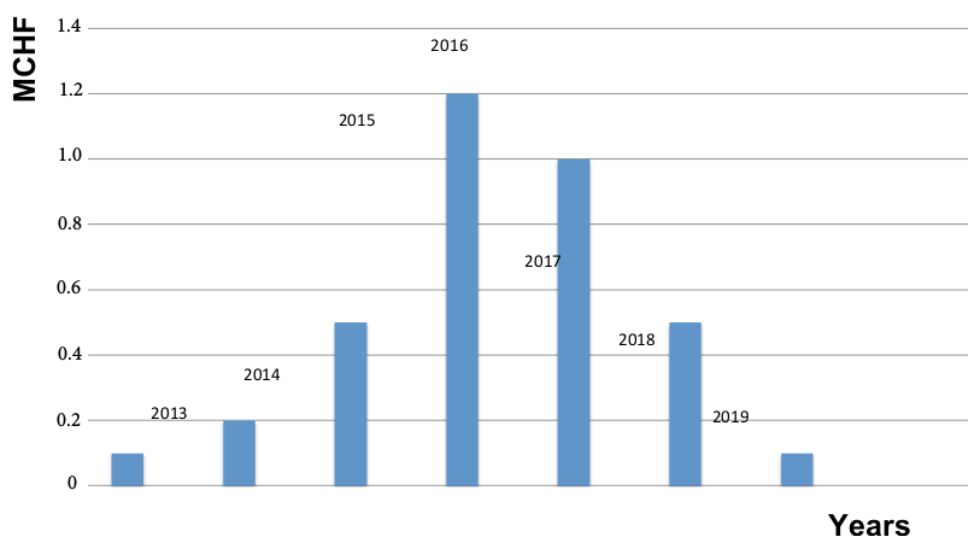


Figure 9.9: GEM GE1/1 LS2 project - Cost Profile.

3377 9.9.1 Expected funding, cost sharing and profile

3378 The global cost of the GE1/1 construction project, 3.6 MCHF, is expected to be borne by all
 3379 institutions participating in the project as shown in Section 9.1. Discussions with the Funding
 3380 Agencies are ongoing to define the sharing of the total project cost. It is expected that the
 3381 commitments will be formally made by all funding agencies when signing the Memorandum
 3382 of Understanding.

3383 It should be noted that for most institutes the total funding has already been accepted and/or
 3384 approved by the corresponding funding agencies. Indeed in order to be ready for installation
 3385 in LS2, construction of chamber prototype and electronics for test purposes and, preliminary
 3386 procurements for test bench and setting up of test facilities at the TIF and building 904, which
 3387 are part of the core cost, some funding agencies have already started their contributions.

3388 A first attempt to integrate the cost items shown in Figure 9.5 in a cost profile, following the
 3389 project schedule in Figure 9.3, is shown in Figure 9.9.

3390 This exercise has only begun. The full realisation of this planning exercise requires a good
 3391 knowledge of the funding profile. After approval, the integrated total funds available from
 3392 each of the countries participating in the project will be committed by linking the cost profile
 3393 to the composite funding profile, as requested by LHCC CORE rules.

3394 This is a work in progress and will evolve when the TDR project is approved.

3395 **Appendix A**

3396 **The GE1/1 Slice Test**

3397 **Editors:** A. Marinov, M. Tytgat

3398 **A.1 Introduction**

3399 In June 2013, CMS approved the installation of a limited number of GE1/1 chambers into the
3400 muon endcaps, in order to gain first operational experience with this new subsystem and also
3401 to demonstrate the integration of the GE1/1 chambers into the trigger. During the 2016-2017
3402 Year-End Technical Stop, 4 GE1/1 superchambers covering a 40° sector will be installed in
3403 YE1/1, at the location depicted in Figure A.1.

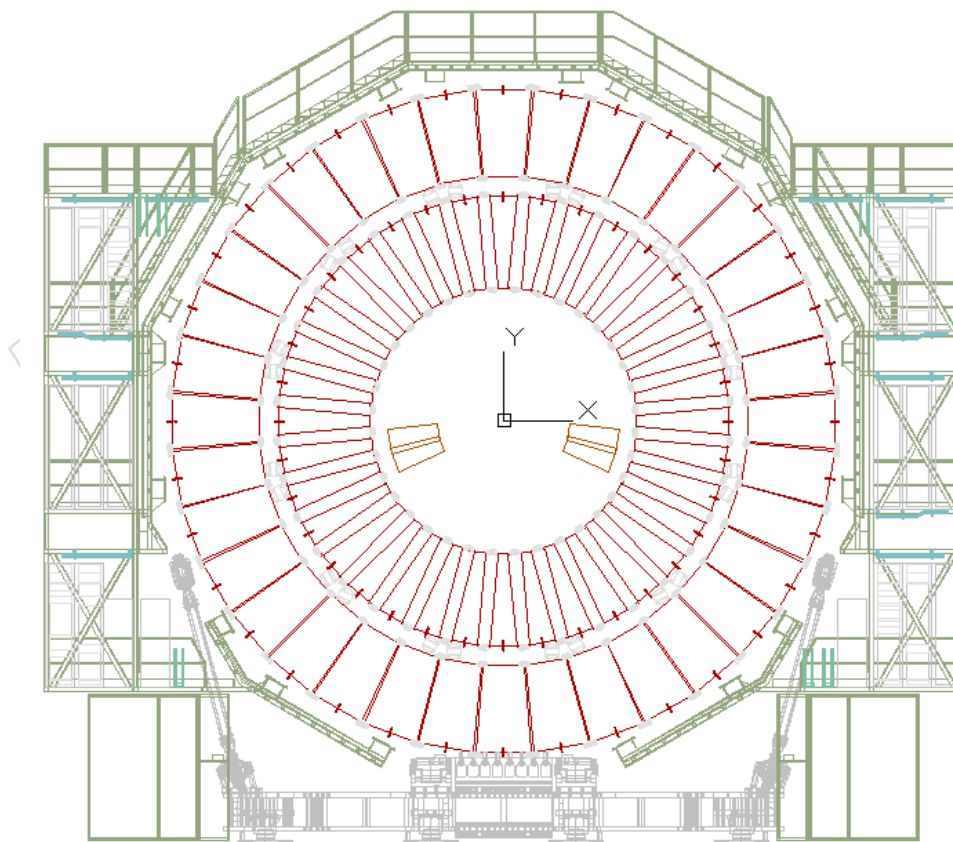


Figure A.1: Location of the Slice Test GE1/1 superchambers in YE1.

A.2 Detector configuration

3404

3405 As described in Chapter 7, during LS1, most of the required services and cabling for the GE1/1
 3406 station will be in place and tested. With few exceptions, the final GE1/1 services and cabling
 3407 configuration will be used for the Slice Test chambers as well.

3408 The HV power for the slice test chambers will be based on the single-channel HV divider option
 3409 as was used during the R&D phase of the project (see Section 2.3.6.1). In this case, only one HV
 3410 channel is required per GE1/1 chamber, or two channels per GE1/1 super-chamber. Note here
 3411 the already installed HV cables meant for a RPC RE1/1 station that so far has not been built.
 3412 These cables run from the UXC X0 HV patch panel to the GE1/1 installation slots for both the
 3413 positive and negative endcap.

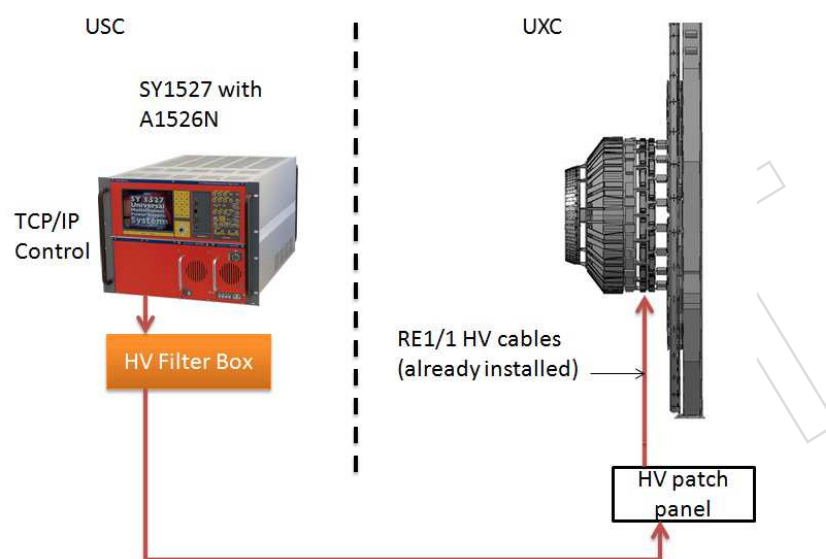


Figure A.2: Diagram of the GE1/1 powering configuration based on the HV divider.

3414 The general view of the single-channel HV powering configuration is shown in Figure A.2. It
 3415 represents a standard system based on commercial HV modules made by CAEN. As is shown
 3416 in the figure, all the HV power modules are located in the USC S1 level where the CAEN main
 3417 frame SY1527 is installed. The A1526N HV powering modules are used, which are able to
 3418 provide up to 15 kV/1mA with negative polarity. This power supply has been used in the
 3419 GE1/1 project since the beginning, both in lab measurements and beam tests. The A1526N
 3420 board has a certain noise level from its output, which needs to be cut off using a HV filter box
 3421 located close to the module.

3422 To transport the power from A1526N to the GE1/1 chambers, a multi-core HV cable of about
 3423 150 m is required between the USC and UXC caverns, which has to follow all the routing
 3424 procedures adopted by CMS.

3425 Given the installation of the Slice Test chambers at the end of 2016, the construction and com-
 3426 missioning of the GEM gas mixer will be completed latest after the Summer in 2016. For the
 3427 Slice Test, a gas flow of about 10 l/h is foreseen, for a total detector volume of about 20 l.

3428 The front-end electronics power dissipation for the Slice Test detectors is assumed to be less
 3429 than 250 W in total for the 2 superchambers. This will have a negligible impact on the presently
 3430 available YE1 cooling system.

3431 **A.3 Front-end electronics and data-acquisition**

3432 Due to the still ongoing developments of the front-end chip and GBT chip set in the coming
3433 years, it is foreseen that the readout of the chambers during the Slice Test will be close to but
3434 nonetheless slightly different from the final system that is described in Chapter 3. The on-
3435 detector electronics will be based on the VFAT2 instead of VFAT3 ASIC, and on the 2nd instead
3436 of the final (3rd) version of the GEB and opto-hybrid. The latter will already include the GBT
3437 chip set.

3438 Since the VFAT2 design is not compatible with the GBT chipset all the data (trigger and track-
3439 ing data) will transit through the front-end FPGA (Virtex 6) located on the opto-hybrid. The
3440 number of optical links per detector and the trigger data link towards the CSC TMB will be the
3441 same as in the GE1/1 system that will be installed during LS2.

3442 For the back-end electronics, the system should be the same as for the LS2 installation but with
3443 fewer components : one μ TCA crate hosting one MP7 board and one AMC13 board.

DRAFT

DRAFT

3444 Appendix B

3445 Integrated Charge Estimation

Here we briefly detail the estimation of the charge per area that will be integrated in the GE1/1 chambers over a lifetime of 20 years at the HL-LHC as stated under the design requirements in section 2.1.1. The integrated charge Q_{int} per area is given by:

$$Q_{int} = R_{max} \times n_{tot}^{ion} \times g \times e \times t_{HL-LHC}, \quad (B.1)$$

3446 where R_{max} is the maximum charged-particle hit rate per area produced by all particles incident
3447 on the chamber, n_{tot}^{ion} is the total number of ion-electron pairs produced by charged particles
3448 traversing the drift gap in the chamber, g is the gas gain of the GE1/1, e is the electron charge,
3449 and t_{HL-LHC} is the total time in seconds that the HL-LHC will be providing collisions over 20
3450 years.

3451 We use $R_{max} = 5 \text{ kHz/cm}^2$ as the rate estimate in the hottest area of the GE1/1 and $g = 2 \times 10^4$
3452 as the typical gas gain value for a Triple-GEM. In an Ar/CO₂ 70:30 gas mixture, on the average
3453 93 ion-electron pairs are produced per cm. The largest path length l in the GEM drift gap that
3454 occurs for ionizing particles when they traverse the GE1/1 is $l = d / \cos \theta$. Here $d = 0.3 \text{ cm}$ is
3455 the drift gap of the Triple-GEM and $\theta \approx 25^\circ$, which corresponds to $\eta = 1.5$, is the largest angle
3456 relative to the normal onto the chamber under which particles are incident on the GE1/1. This
3457 gives $l = 0.33 \text{ cm}$ and $n_{tot}^{ion} = 31$ ion-electron pairs in the GE1/1. Assuming that the HL-LHC
3458 will have an annual duty factor of $\approx 1/3$ as is typical for collider operations, we estimate that
3459 the chambers will be exposed to charged particles for $\approx 10^7$ seconds each year.

Multiplying these factors together, we find an estimated integrated charge per area for a projected GE1/1 lifetime of 20 years of:

$$Q_{int} \approx 5 \cdot 10^3 \text{ s}^{-1} \text{cm}^{-2} \times 31 \times 2 \cdot 10^4 \times 1.6 \cdot 10^{-19} \text{ C} \times 20 \cdot 10^7 \text{ s} = 99 \text{ mC/cm}^2 \quad (B.2)$$

3460 Gas mixtures containing in addition CF₄ in any percentage will produce very similar integrated
3461 charges because the total ionization of CF₄ (100 pairs/cm) is quite close to that of Ar (94
3462 pairs/cm) and CO₂ (91 pairs/cm). Specifically, for Ar/CO₂/CF₄ 45 : 15 : 40 the total ionization
3463 is 96 pairs/cm which gives $Q_{int} = 101 \text{ mC/cm}^2$ for the GE1/1.

DRAFT

3464 **Appendix C**

3465 **GE1/1 Project 3D Views**

3466 **Editors** Antonio Conde Garcia

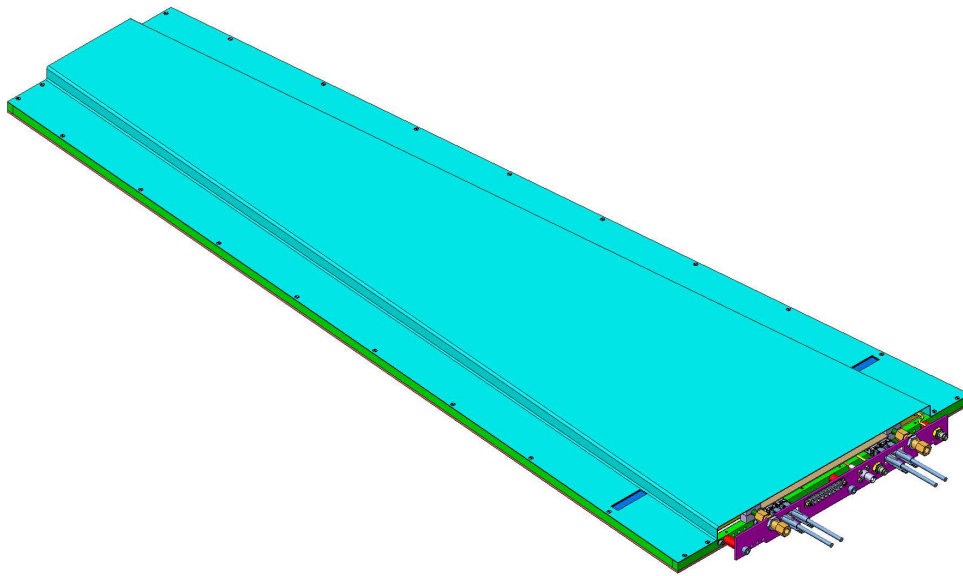


Figure C.1: GE1/1 mechanical chambers.

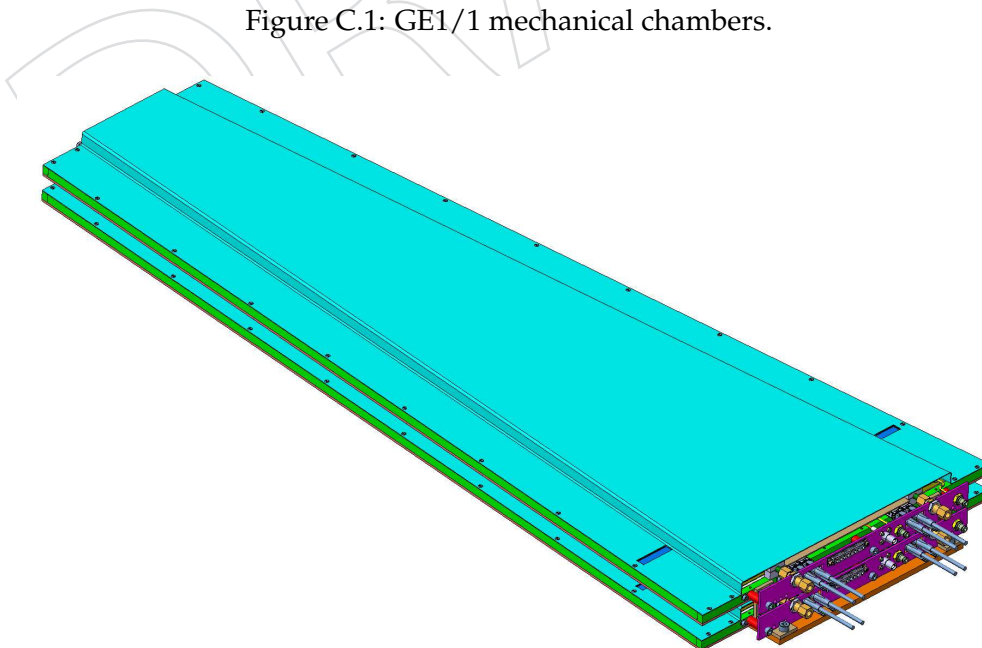


Figure C.2: GE1/1 super-chamber.

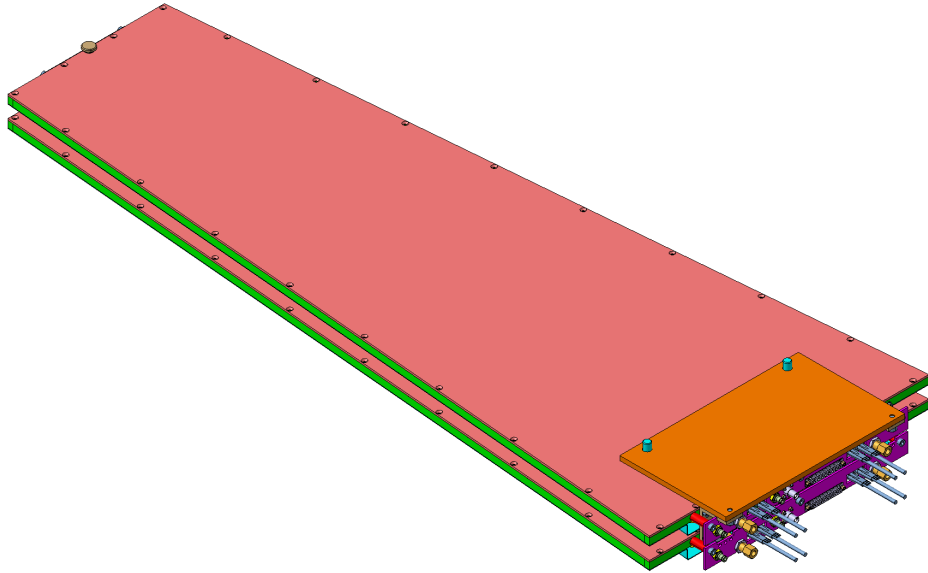


Figure C.3: GE1/1 fixations.

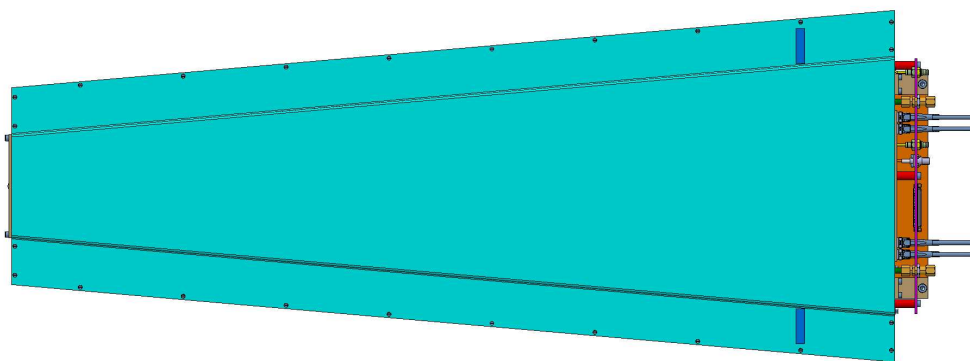


Figure C.4: GE1/1 chimney.

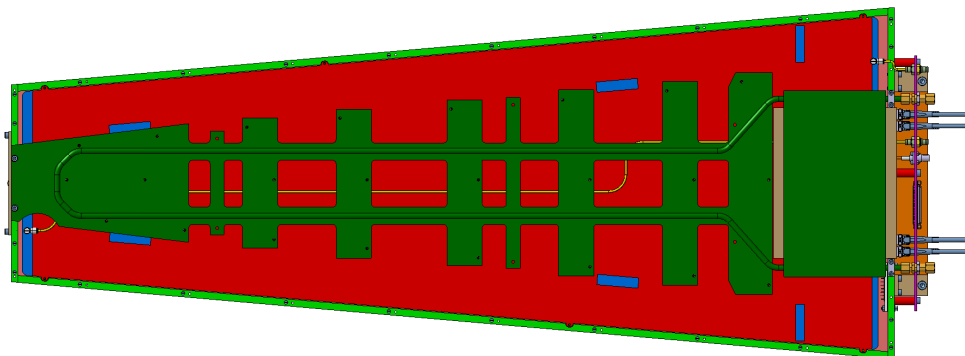


Figure C.5: GE1/1 cooling circuit.

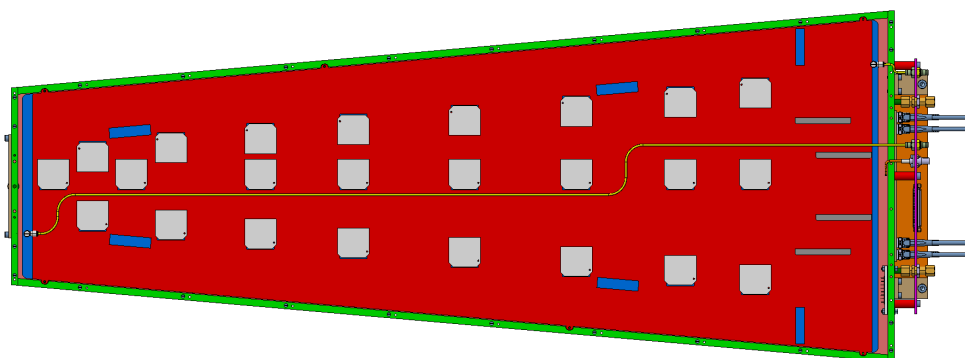


Figure C.6: GE1/1 hybrid gas pipes.

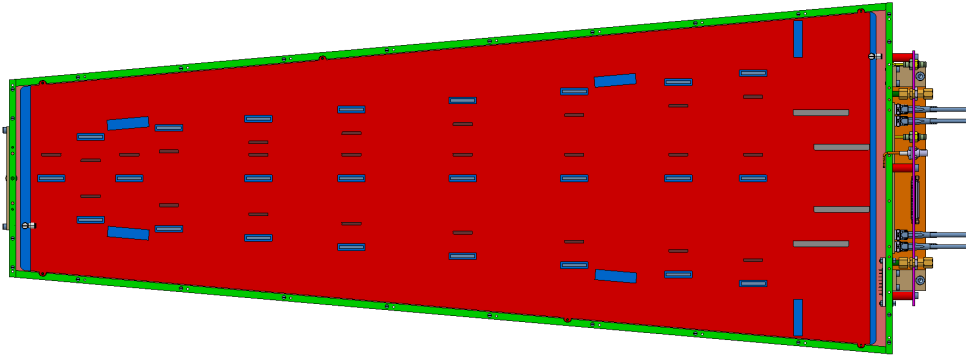


Figure C.7: GE1/1 GEB.

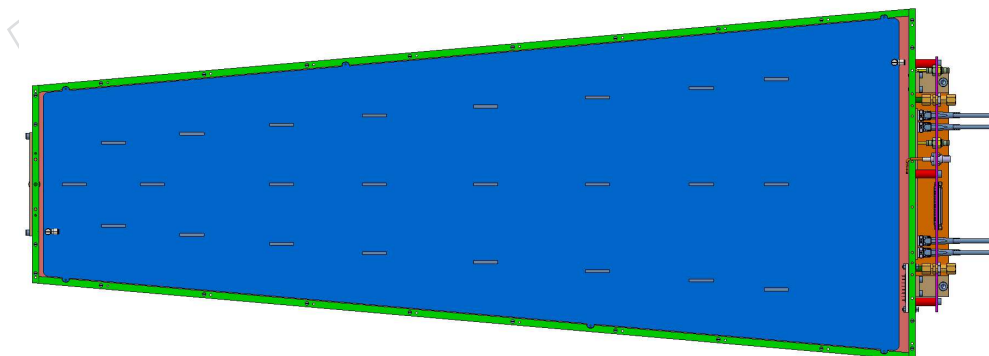


Figure C.8: GE1/1 readout board.

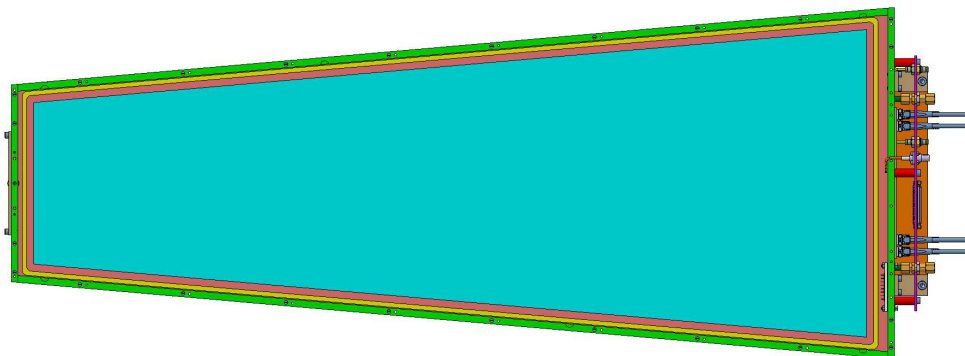


Figure C.9: GE1/1 active surface.

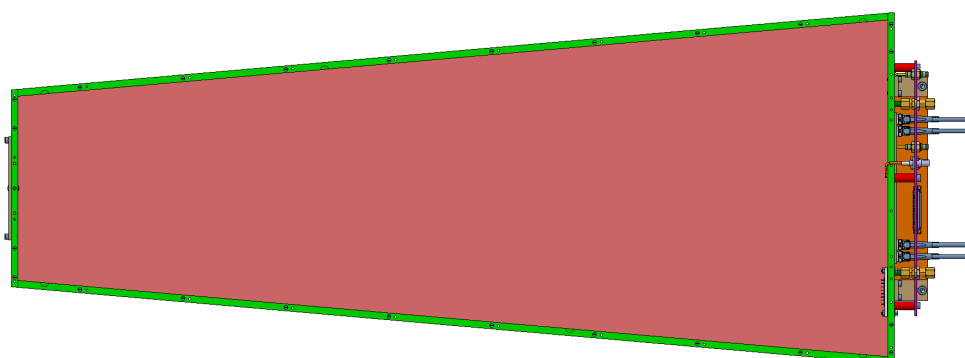


Figure C.10: GE1/1 drift board.

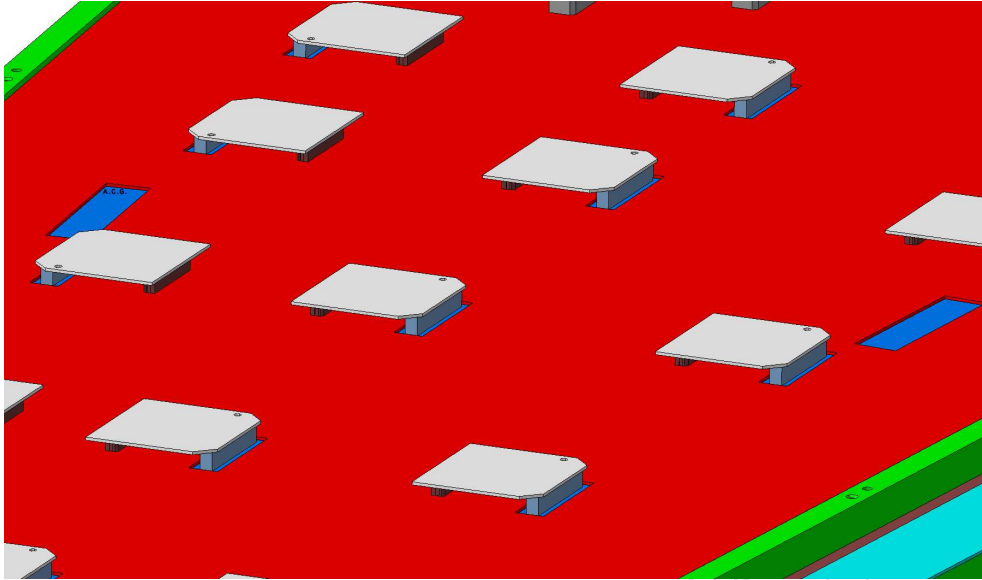


Figure C.11: GE1/1 hybrids detail.

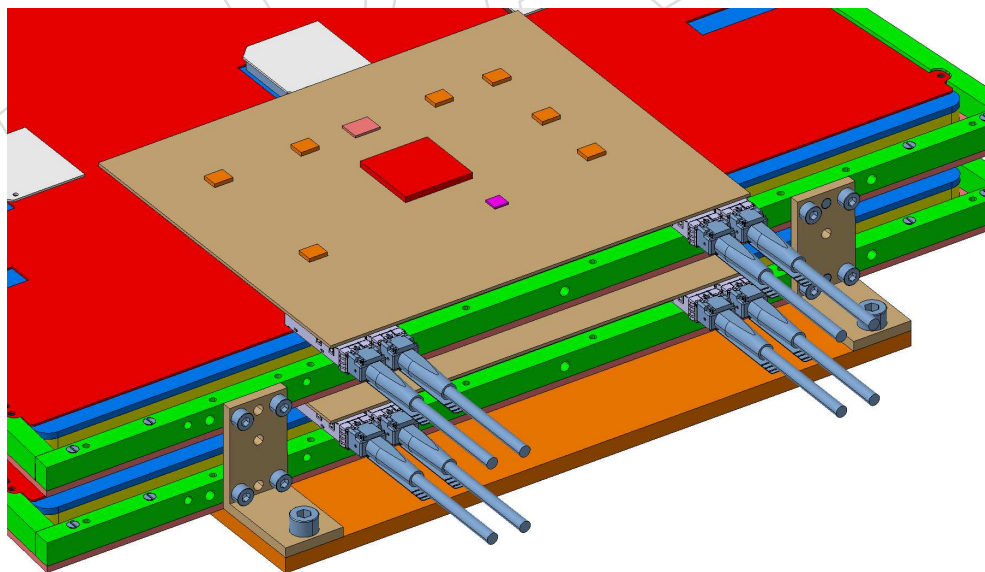


Figure C.12: GE1/1 optohybrid and fibres.

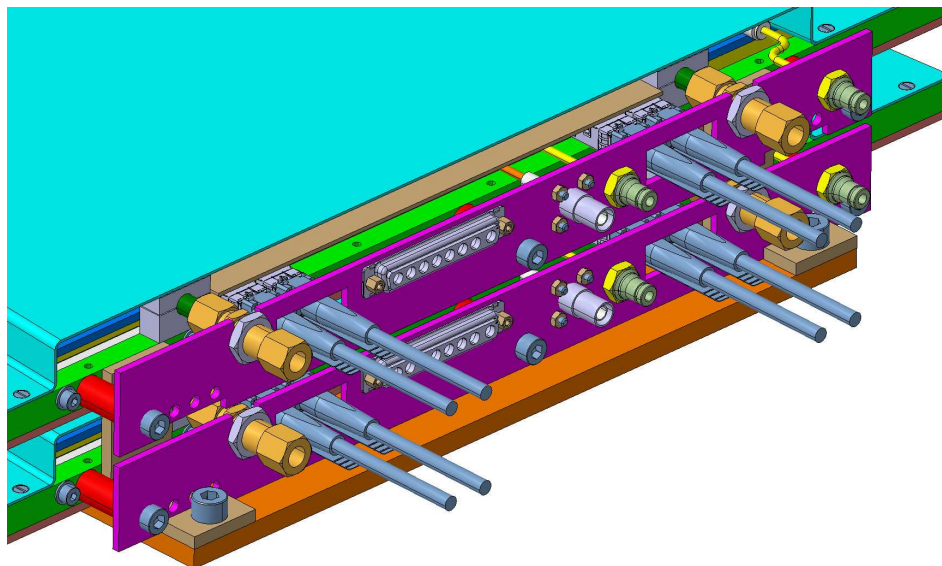


Figure C.13: GE1/1 patch-panel.

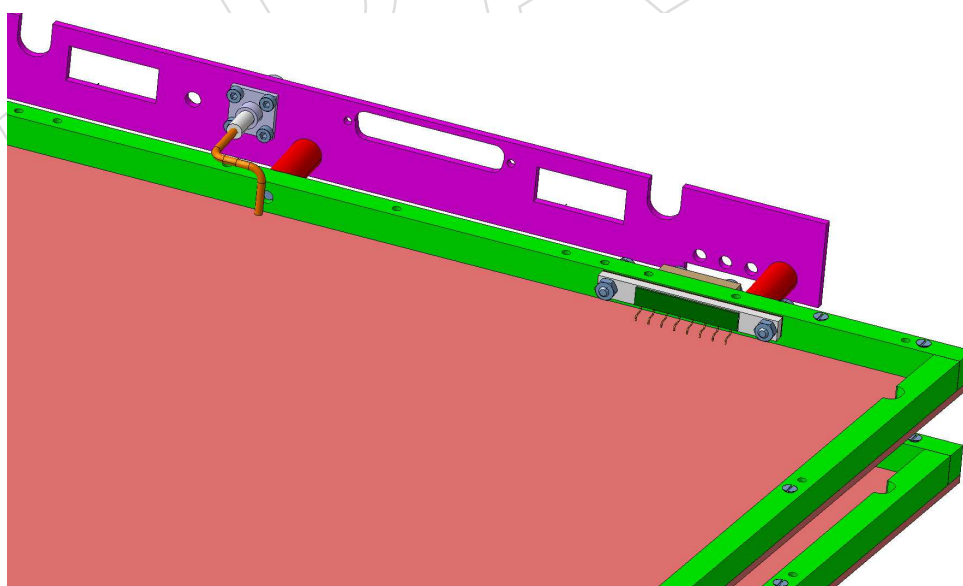


Figure C.14: GE1/1 HV divider and connectors.

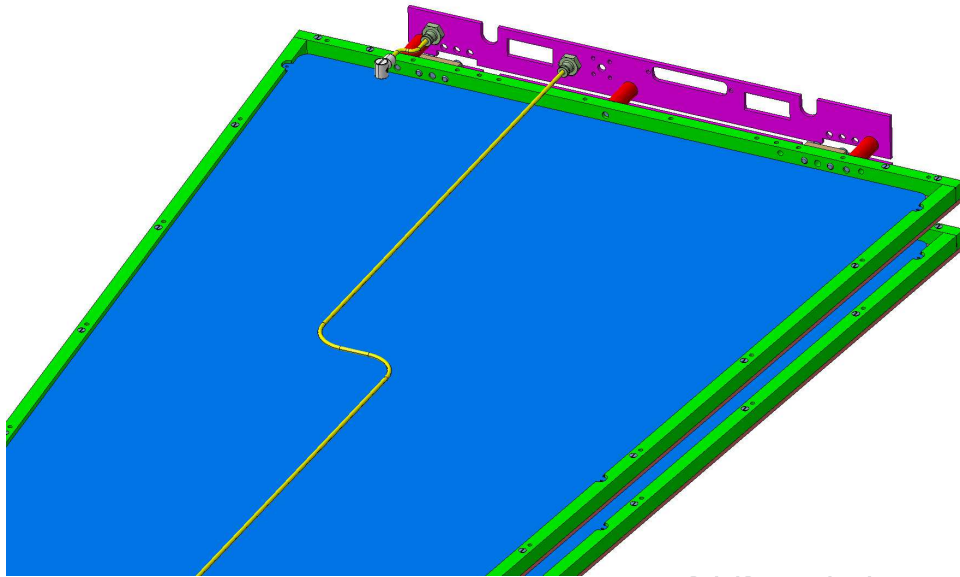


Figure C.15: GE1/1 gas conduits.

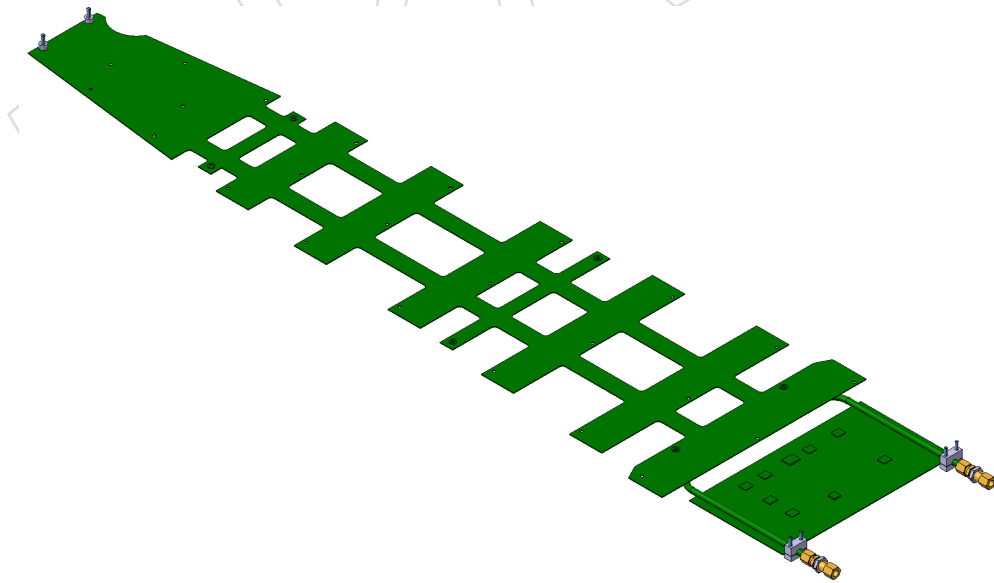


Figure C.16: GE1/1 thermal screen.

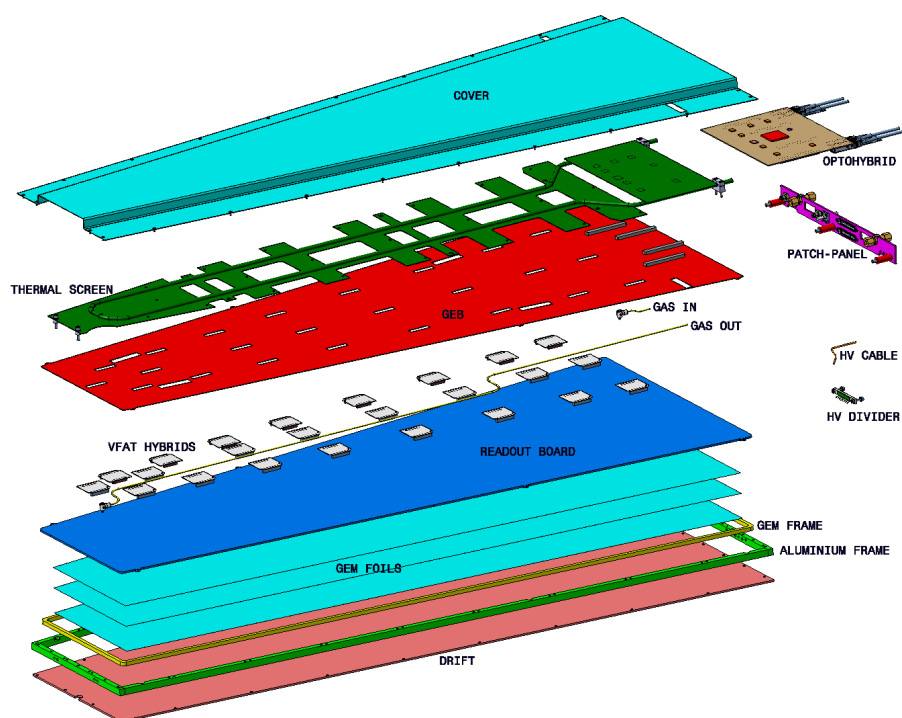


Figure C.17: GE1/1 exploded view.

DRAFT

References

-
- 3469 [1] CMS Collaboration, “CMS The Muon Project Technical Design Report”, Technical Report
3470 CERN-LHCC-1997-032, CMS-TDR-3, CERN, 1997.
- 3471 [2] CMS Collaboration, “CMS Phase 2 Technical Proposal”, technical report, CERN, 2015.
- 3472 [3] F. Sauli, “GEM: A new concept for electron amplification in gas detectors”, *Nuclear*
3473 *Instruments and Methods in Physics Research Section A: Accelerators, Spectrometers, Detectors*
3474 *and Associated Equipment* **386** (1997), no. 2–3, 531 – 534,
3475 doi:[http://dx.doi.org/10.1016/S0168-9002\(96\)01172-2](http://dx.doi.org/10.1016/S0168-9002(96)01172-2).
- 3476 [4] A. Cardini, G. Bencivenni, and P. De Simone, “The Operational Experience of the
3477 Triple-GEM Detectors of the LHCb Muon System: Summary of 2 Years of Data Taking”,
3478 *IEEE Nucl.Sci.Symp.Conf.Rec.* (2012) 759–762, doi:[10.1109/NSSMIC.2012.6551204](https://doi.org/10.1109/NSSMIC.2012.6551204).
- 3479 [5] S. Bachmann et al., “Charge amplification and transfer processes in the gas electron
3480 multiplier”, *Nucl.Instrum.Meth.* **A438** (1999) 376–408,
3481 doi:[10.1016/S0168-9002\(99\)00820-7](https://doi.org/10.1016/S0168-9002(99)00820-7).
- 3482 [6] TOTEM Collaboration, “Performance of the TOTEM Detectors at the LHC”,
3483 *Int.J.Mod.Phys.* **A28** (2013) 1330046, doi:[10.1142/S0217751X13300469](https://doi.org/10.1142/S0217751X13300469),
3484 arXiv:1310.2908.
- 3485 [7] A. Sharma, “Properties of some gas mixtures used in tracking detectors, ”,
3486 *SLAC-JOURNAL-ICEA* **16** (1998).
- 3487 [8] R. Veenhof, “Garfield, a drift chamber simulation program”, *Conf.Proc.* **C9306149** (1993)
3488 66–71.
- 3489 [9] COMPASS Collaboration, “The COMPASS experiment at CERN”, *Nucl.Instrum.Meth.*
3490 **A577** (2007) 455–518, doi:[10.1016/j.nima.2007.03.026](https://doi.org/10.1016/j.nima.2007.03.026),
3491 arXiv:[hep-ex/0703049](https://arxiv.org/abs/hep-ex/0703049).
- 3492 [10] M. French et al., “Design and results from the APV25, a deep sub-micron CMOS
3493 front-end chip for the CMS tracker”, *Nucl.Instrum.Meth.* **A466** (2001) 359–365,
3494 doi:[10.1016/S0168-9002\(01\)00589-7](https://doi.org/10.1016/S0168-9002(01)00589-7).
- 3495 [11] B. Ketzer et al., “A triple-GEM Detector with pixel readout for high-rate beam tracking in
3496 COMPASS”, *IEEE Nucl.Sci.Symp.Conf.Rec.* (2007) 242–244,
3497 doi:[10.1109/NSSMIC.2007.4436323](https://doi.org/10.1109/NSSMIC.2007.4436323).
- 3498 [12] W. Anderson et al., “Design, Construction, Operation and Performance of a Hadron
3499 Blind Detector for the PHENIX Experiment”, *Nucl.Instrum.Meth.* **A646** (2011) 35–58,
3500 doi:[10.1016/j.nima.2011.04.015](https://doi.org/10.1016/j.nima.2011.04.015), arXiv:[1103.4277](https://arxiv.org/abs/1103.4277).

- 3501 [13] B. Surrow, "The STAR forward GEM tracker", *Nucl.Instrum.Meth.* **A617** (2010) 196–198,
3502 doi:10.1016/j.nima.2009.09.012.
- 3503 [14] P. Aspell et al., "VFAT2: A front-end system on chip providing fast trigger information,
3504 digitized data storage and formatting for the charge sensitive readout of multi-channel
3505 silicon and gas particle detectors", in *Topical Workshop on Electronics for Particle Physics,*
3506 *Praque, Czech Republic, 03-07 Sept.*, pp. 292–296. 2007.
3507 doi:10.5170/CERN-2007-007.292.
- 3508 [15] D. Abbaneo et al., "Characterization of GEM Detectors for Application in the CMS Muon
3509 Detection System", *IEEE Nucl.Sci.Symp.Conf.Rec.* **2010** (2010) 1416–1422,
3510 doi:10.1109/NSSMIC.2010.5874006, arXiv:1012.3675.
- 3511 [16] D. Abbaneo et al., "Test beam results of the GE1/1 prototype for a future upgrade of the
3512 CMS high- η muon system", *IEEE Nucl.Sci.Symp.Conf.Rec.* **2011** (2011) 1806–1810,
3513 doi:10.1109/NSSMIC.2011.6154688, arXiv:1111.4883.
- 3514 [17] D. Abbaneo et al., "Beam Test Results for New Full-scale GEM Prototypes for a Future
3515 Upgrade of the CMS High-eta Muon System",
3516 doi:10.1109/NSSMIC.2012.6551293, arXiv:1211.3939.
- 3517 [18] D. Abbaneo et al., "Performance of a Large-Area GEM Detector Prototype for the
3518 Upgrade of the CMS Muon Endcap System", *IEEE Nucl.Sci.Symp.Conf.Rec.* (2014)
3519 arXiv:1412.0228.
- 3520 [19] D. Abbaneo et al., "The status of the GEM project for CMS high- η muon system",
3521 *Nucl.Instrum.Meth.* **A732** (2013) 203–207, doi:10.1016/j.nima.2013.08.015.
- 3522 [20] K. Gnanvo et al., "Detection and Imaging of High-Z Materials with a Muon Tomography
3523 Station Using GEM Detectors", doi:10.1109/NSSMIC.2010.5873822,
3524 arXiv:1011.3231.
- 3525 [21] S. Martoiu, H. Muller, A. Tarazona, and J. Toledo, "Development of the scalable readout
3526 system for micro-pattern gas detectors and other applications", *JINST* **8** (2013) C03015,
3527 doi:10.1088/1748-0221/8/03/C03015.
- 3528 [22] R. Carnegie et al., "Resolution studies of cosmic ray tracks in a TPC with GEM readout",
3529 *Nucl.Instrum.Meth.* **A538** (2005) 372–383, doi:10.1016/j.nima.2004.08.132,
3530 arXiv:physics/0402054.
- 3531 [23] T. Alexopoulos et al., "Examining the Geometric Mean Method for the Extraction of
3532 Spatial Resolution", doi:10.1088/1748-0221/9/01/P01003, arXiv:1311.2556.
- 3533 [24] M. Tytgat et al., "Construction and Performance of Large-Area Triple-GEM Prototypes
3534 for Future Upgrades of the CMS Forward Muon System", *IEEE Nucl.Sci.Symp.Conf.Rec.*
3535 **2011** (2011) 1019–1025, doi:10.1109/NSSMIC.2011.6154312, arXiv:1111.7249.
- 3536 [25] "ANSYS® Academic Research, Release 14.0". <http://www.ansys.com>.
- 3537 [26] "Garfield++ - simulation of tracking detectors".
3538 <http://garfieldpp.web.cern.ch/garfieldpp>.
- 3539 [27] M. Hohlmann, C. Padilla, N. Tesch, and M. Titov, "Aging phenomena in gaseous
3540 detectors – perspectives from the 2001 workshop", *Nuclear Instruments and Methods in*
3541 *Physics Research Section A: Accelerators, Spectrometers, Detectors and Associated Equipment*
3542 **494** (2002), no. 1-3, 179–193, doi:10.1016/S0168-9002(02)01463-8.

- 3543 [28] S. Bianco, G. Saviano, and A. Franchi, "Test for the Measurement of Diffusion Coefficient
3544 of Water in Kapton Foils for the Gem Detector of the Upgraded High-Pseudorapidity
3545 Muon Detection in CMS", *LNF Preprint INFN-13-09/LNF* (2013).
- 3546 [29] R. Guido, "CMS Trapezoidal GEM Foils Structural Analysis", *LNF Preprint LNF - 10 /*
3547 *20(IR)* (2010).
- 3548 [30] R. Guido, "CHE and Related Stresses in GEM Foils", *LNF Preprint INFN-13-11/LNF*
3549 (2013).
- 3550 [31] ASTM-International, "D570-98 Standard Test Method for Water Absorption of Plastics".
3551 <http://www.astm.org/DATABASE.CART/HISTORICAL/D570-98R05.htm>.
- 3552 [32] ASTM-International, "D882-02 Standard Test Method for Tensile properties of Thin
3553 Plastic Sheetting". <http://www.astm.org/Standards/D882.htm>.
- 3554 [33] M. Poli-Lener and G. Bencivenni, "Triple-GEM detectors for the innermost region of the
3555 muon apparatus at the LHCb experiment". PhD thesis, Roma U., Roma, 2005. Presented
3556 on 01 Dec 2005.
- 3557 [34] L. Benussi et al., "The Omega-like: A novel device using FBG sensors to position vertex
3558 detectors with micrometric precision", *Nucl.Phys.Proc.Suppl.* **172** (2007) 263–265,
3559 doi:10.1016/j.nuclphysbps.2007.08.138.
- 3560 [35] M. A. Caponero et al., "Use of fiber optic technology for relative humidity monitoring in
3561 RPC detectors", *PoS RPC2012* (2012) 073, doi:10.1088/1748-0221/8/03/T03003.
- 3562 [36] S. Grassini et al., "SiOx coated plastic fiber optic sensor for gas monitoring in RPC", *PoS*
3563 *RPC2012* (2012) 072.
- 3564 [37] D. J. Achenson, "Elementary Fluid Dynamics, ", *Oxford Applied Mathematics and*
3565 *Computing Science Series, Oxford University Press* (1990).
- 3566 [38] L. D. Landau and E. M. Lifshitz, "Fluid mechanics, Course of Theoretical Physics, 6 (2nd
3567 revised ed.), ", *Pergamon Press* (1987).
- 3568 [39] I. G. Currie, "Fundamental Mechanics of Fluids, ", *McGraw-Hill* (1974).
- 3569 [40] "The IPbus protocol". <https://svnweb.cern.ch/trac/cactus/wiki>.
- 3570 [41] P. Moreira et al., "The GBT-SerDes ASIC prototype", *Journal of Instrumentation* **5** (2010),
3571 no. 11, C11022.
- 3572 [42] CMS Collaboration, "CMS Technical Design Report for the Level-1 Trigger Upgrade",
3573 Technical Report CERN-LHCC-2013-011, CMS-TDR-012, CERN, 2013.
- 3574 [43] J. Gilmore et al., "Very forward muon trigger and data acquisition electronics for CMS:
3575 design and radiation testing", *JINST* **8** (2013) C02040,
3576 doi:10.1088/1748-0221/8/02/C02040.
- 3577 [44] P. Vichoudis et al., "The Gigabit Link Interface Board (GLIB) ecosystem", *JINST* **8** (2013)
3578 C03012, doi:10.1088/1748-0221/8/03/C03012.
- 3579 [45] D. Abbaneo et al., "A study of film and foil materials for the GEM detector proposed for
3580 the CMS muon system upgrade", *JINST* **9** (2014) C04022,
3581 doi:10.1088/1748-0221/9/04/C04022.

- 3582 [46] C.-Y. Chen and S. Dawson, “Exploring two Higgs doublet models through Higgs
3583 production”, *Phys. Rev.* **D87** (2010) 055016, doi:10.1103/PhysRevD.87.055016,
3584 arXiv:1301.0309.
- 3585 [47] J. Z. Neil Turok, “Electroweak baryogenesis in the two doublet model”, *Nucl. Phys.* **B358**
3586 (1991) 471–473, doi:10.1016/0550-3213(91)90356-3.
- 3587 [48] “Geant4 Physics Reference Manual”.
3588 [http://geant4.web.cern.ch/geant4/UserDocumentation/UsersGuides/
3589 PhysicsReferenceManual/fo/PhysicsReferenceManual.pdf](http://geant4.web.cern.ch/geant4/UserDocumentation/UsersGuides/PhysicsReferenceManual/fo/PhysicsReferenceManual.pdf).
- 3590 [49] N. Arkani-Hamed and S. Dimopoulos, “Supersymmetric unification without low energy
3591 supersymmetry and signatures for fine-tuning at the LHC”, *JHEP* **0506** (2005) 073,
3592 doi:10.1088/1126-6708/2005/06/073.
- 3593 [50] G. Giudice and A. Romanino, “Split supersymmetry”, *Nucl. Phys.* **B699** (2004) 65–89,
3594 doi:10.1016/j.nuclphysb.2004.11.048.
- 3595 [51] G. Giudice, M. Luty, H. Murayama, and R. Rattazzi, “Gaugino mass without singlets”,
3596 *JHEP* **9812** (1998) 027, doi:10.1088/1126-6708/1998/12/027.
- 3597 [52] L. Randall and R. Sundrum, “Out of this world supersymmetry breaking”, *Nucl. Phys.*
3598 **B557** (1999) 79–118, doi:10.1016/S0550-3213(99)00359-4.
- 3599 [53] N. Arkani-Hamed, D. Finkbeiner, T. Slatyer, and N. Weiner, “A Theory of Dark Matter”,
3600 *Phys. Rev.* **D79** (2009) 015014, doi:10.1103/PhysRevD.79.015014.
- 3601 [54] P. Graham, D. Kaplan, S. Rajendran, and P. Saraswati, “Displaced Supersymmetry”,
3602 *JHEP* **1207** (2012) 149, doi:10.1007/JHEP07(2012)149.
- 3603 [55] CMS Collaboration, “Evidence for the 125 GeV Higgs boson decaying to a pair of τ
3604 leptons”, *Journal of High Energy Physics* **104** (2014) doi:10.1007/JHEP05(2014)104.
- 3605 [56] CMS Collaboration, “The CMS tracker system project: Technical Design Report”,
3606 Technical Report CERN-LHCC-98-006. CMS-TDR-5, CERN, 1998.
- 3607 [57] Z. Szillási et al., “Only year of FOS measurements in CMS experiment at CERN”, *Physics*
3608 *Procedia* **37** (2012) 79.
- 3609 [58] V. Barashko et al., “Commissioning of Muon Endcap Cathode Strip Chamber
3610 High-Voltage System”, Technical Report CMS-IN-2010/032, 2010.
- 3611 [59] “Specialty fibers - DrakaElite”. [http://prysmiangroup.com/en/business_
3612 markets/markets/fibre/products/speciality-drakaelite](http://prysmiangroup.com/en/business_markets/markets/fibre/products/speciality-drakaelite).
- 3613 [60] F. Ravotti, M. Glaser, and M. Moll, “Sensor Catalogue”, Technical Report
3614 TS-NOTE-2005-02, CERN, 2005.
- 3615 [61] R. Arcidiacono et al., “CMS DCS design concepts”,.
- 3616 [62] A. Daneels and W. Salter, “What is SCADA?”, *Conf.Proc.* **C991004** (1999) 339–343.
- 3617 [63] “SIMATIC WinCC Open Architectura”. [http://www.automation.siemens.com/
3618 mcms/human-machine-interface/en/visualization-software/
3619 simatic-wincc-open-architecture/pages/default.aspx](http://www.automation.siemens.com/mcms/human-machine-interface/en/visualization-software/simatic-wincc-open-architecture/pages/default.aspx).

- 3620 [64] M. Gonzalez-Berges, “The Joint Controls project framework”, *eConf* **C0303241** (2003)
3621 THGT006, [arXiv:physics/0305128](https://arxiv.org/abs/physics/0305128).
- 3622 [65] G. Bauer et al., “The run control and monitoring system of the CMS experiment”, *PoS*
3623 **ACAT** (2007) 026, [doi:10.1088/1742-6596/119/2/022010](https://doi.org/10.1088/1742-6596/119/2/022010).
- 3624 [66] CMS Collaboration, “CMS: The TriDAS project. Technical design report, Vol. 2: Data
3625 acquisition and high-level trigger”, Technical Report CERN-LHCC-2002-026,
3626 CMS-TDR-6, CERN, 2002.
- 3627 [67] V. Brigljevic et al., “Using XDAQ in application scenarios of the CMS experiment”, *eConf*
3628 **C0303241** (2003) MOGT008, [arXiv:hep-ex/0305076](https://arxiv.org/abs/hep-ex/0305076).
- 3629 [68] S. Schmeling, B. Flockhart, S. Luders, and G. Morpurgo, “The detector safety system for
3630 LHC experiments”, *IEEE Trans.Nucl.Sci.* **51** (2004) 521–525,
3631 [doi:10.1109/TNS.2004.828631](https://doi.org/10.1109/TNS.2004.828631).
- 3632 [69] W. Badgett et al., “Web Based Monitoring in the CMS Experiment at CERN”,
3633 [arXiv:1409.1133](https://arxiv.org/abs/1409.1133).
- 3634 [70] “Axis is an XML based Web Service Framework”. <http://ws.apache.org/axis>.
- 3635 [71] “The Apache Tomcat Servlet container”. <http://tomcat.apache.org>.
- 3636 [72] L. Tuura, A. Meyer, I. Segoni, and G. Della Ricca, “CMS data quality monitoring: Systems
3637 and experiences”, *J.Phys.Conf.Ser.* **219** (2010) 072020,
3638 [doi:10.1088/1742-6596/219/7/072020](https://doi.org/10.1088/1742-6596/219/7/072020).
- 3639 [73] CMS Collaboration, “Commissioning of the CMS High-Level Trigger with Cosmic Rays”,
3640 *JINST* **5** (2010) T03005, [doi:10.1088/1748-0221/5/03/T03005](https://doi.org/10.1088/1748-0221/5/03/T03005),
3641 [arXiv:0911.4889](https://arxiv.org/abs/0911.4889).
- 3642 [74] “Migration of the DQM and Validation code to be Thread Safe”.
3643 <https://twiki.cern.ch/twiki/bin/viewauth/CMS/ThreadedDQM>.
- 3644 [75] CMS Collaboration, “CMS Run Registry: Data Certification Bookkeeping and Publication
3645 System”, Technical Report CMS-CR-2011-020, CERN, Geneva, Jan, 2011.
- 3646 [76] L. Tuura, G. Eulisse, and A. Meyer, “CMS data quality monitoring web service”,
3647 *J.Phys.Conf.Ser.* **219** (2010) 072055, [doi:10.1088/1742-6596/219/7/072055](https://doi.org/10.1088/1742-6596/219/7/072055).